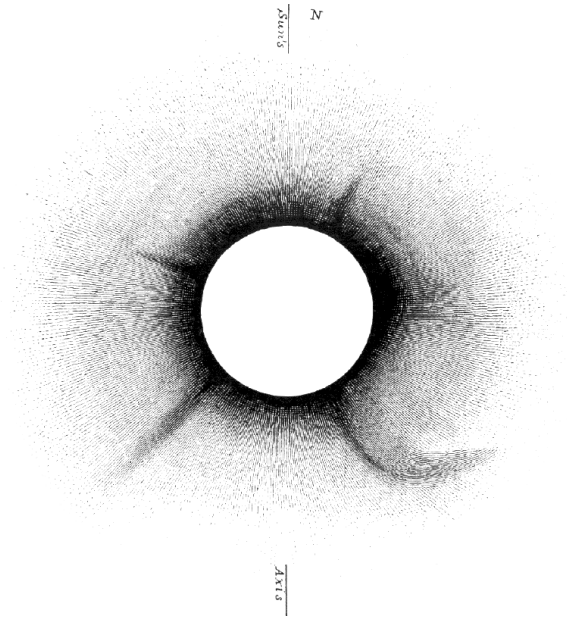

Multipoint observations of ICMEs in the inner heliosphere

Forbush decreases and remote sensing



DISSERTATION

zur Erlangung des Doktorgrades
der Mathematisch-Naturwissenschaftlichen Fakultät
der Christian-Albrechts-Universität zu Kiel

vorgelegt von

Johan Lauritz Freiherr von Forstner

– Kiel, Dezember 2020 –

Johan Lauritz Freiherr von Forstner:
Multipoint observations of ICMEs in the inner heliosphere
Forbush decreases and remote sensing
© Dezember 2020

TITELBILD / COVER PICTURE:

Das Titelbild zeigt eine Skizze der Sonnenkorona während der totalen Sonnenfinsternis am 18.07.1860 von F. A. Oom. Es handelt sich dabei vermutlich um eine der ersten Beobachtungen eines koronalen Massenauswurfs (CME) überhaupt, und zusammen mit der im Dezember 2020¹ eine der wenigen solchen Beobachtungen während einer Sonnenfinsternis. Basierend auf Ranyard (1879, S. 551). / The cover picture shows a drawing of the solar corona by F. A. Oom during the total solar eclipse of July 18, 1860. This is likely one of the first observations of a coronal mass ejection (CME), and together with the one in December 2020¹ one of the few such observations during a solar eclipse. Adapted from Ranyard (1879, page 551).

¹ see <https://apod.nasa.gov/apod/ap210107.html>

ERSTER GUTACHTER (SUPERVISOR):
Prof. Dr. Robert F. Wimmer-Schweingruber

ZWEITER GUTACHTER :
Prof. Dr. Wolfgang J. Duschl

TAG DER MÜNDLICHEN PRÜFUNG:
16. Februar 2021

ZUM DRUCK GENEHMIGT:
16. Februar 2021

ABSTRACT

Coronal mass ejections (**CMEs**) are clouds of plasma and magnetic field regularly ejected from the Sun at high speeds that propagate out into interplanetary space. These events are one of the most important space weather phenomena. Their strong and turbulent magnetic field can cause disruptions of spacecraft electronics as well as terrestrial infrastructure, and they can be associated with the acceleration of energetic particles, which may cause increased radiation exposure, e.g. for astronauts. To be able to validate and consequently improve theoretical models predicting the arrival of interplanetary **CMEs** (**ICMEs**) at Earth and other locations in the heliosphere, it is important to employ many different data sources measuring the various signatures of **ICMEs** at different locations, so that their temporal and radial evolution can be studied. These investigations are also significantly aided by observations from remote sensing telescopes, which can directly observe the global structure of the **ICMEs** and track them out to large radial distances.

The studies presented in this thesis introduce Mars into the framework of routinely available locations for the in situ observation of space weather. Here, **ICMEs** can be detected using Forbush decrease measurements by the Radiation Assessment Detector (**RAD**) onboard the Mars Science Laboratory rover *Curiosity*. Forbush decreases are short-term decreases in the galactic cosmic ray flux caused by the magnetic structure of the **ICME** partly shielding away the cosmic rays. The measurements of these Forbush decreases are utilized in this thesis to determine **ICME** arrival times for statistical studies of events seen at two planets, Earth and Mars, or at one of the two **STEREO** spacecraft and Mars, during close longitudinal alignment. The measurements show for the first time that fast **ICMEs** can continue to decelerate beyond the orbit of Earth due to their interaction with the slower ambient solar wind. Using remote sensing observations from the **STEREO** heliospheric imagers, we study additional **ICMEs** that hit Mars and benchmark the accuracy of different approaches for the analysis of these heliospheric imager data. Subsequently, the Forbush decrease data for the thereby cataloged events are further investigated to infer not only the arrival time, but also more information about the radial evolution of the **ICME** properties by comparison with analytical modeling approaches.

Finally, two case studies are performed: First, the major space weather events of September 2017 and their impact on Mars are examined, including the investigation of the solar energetic particle events and three associated **CMEs** that interacted and merged on their way towards Mars. Second, the first in situ observations of an **ICME** at the Solar Orbiter spacecraft, which launched in February 2020, are presented. In this study, we describe the capabilities of the Solar Orbiter's High Energy Telescope for high-resolution observations of Forbush decreases and use its measurements in combination with a reverse modeling approach to show that the expansion of the **ICME** was non-uniform, possibly due to interaction with a following solar wind stream interaction region.

ZUSAMMENFASSUNG

Koronale Massenauswürfe (*coronal mass ejections*, **CMEs**) sind magnetisierte Plasmawolken, die die Sonne regelmäßig mit hoher Geschwindigkeit ausstößt und die sich anschließend im interplanetaren Raum ausbreiten. Sie gehören zu den wichtigsten Phänomenen des sogenannten Weltraumwetters. Ihr starkes und turbulentes Magnetfeld kann für Störungen bei Satellitenelektronik sorgen oder sogar Infrastruktur auf der Erde beschädigen. Zusätzlich stehen **CMEs** häufig auch im Zusammenhang mit der Beschleunigung von hochenergetischen Teilchen, die beispielsweise bei Astronauten für eine erhöhte Strahlendosis sorgen können. Um theoretische Modelle, die die Ankunftszeit von interplanetaren **CMEs** (**ICMEs**) an der Erde oder anderen Orten im Sonnensystem vorhersagen, besser überprüfen und daraufhin auch verbessern zu können, ist es wichtig, Daten von möglichst vielen Messinstrumenten einzubeziehen. So können unterschiedliche Merkmale von **ICMEs** an mehreren Orten im Sonnensystem gemessen und damit deren zeitliche und radiale Entwicklung untersucht werden. Ebenso hilfreich für diese Untersuchungen sind bildgebende Teleskope, die die globale Struktur der **ICMEs** direkt beobachten und sie weit hinaus in den interplanetaren Raum verfolgen können.

Die in dieser Dissertation vorgestellten Forschungsarbeiten führen den Mars als weiteren durchgehend verfügbaren Beobachtungspunkt im Rahmen der In-situ-Beobachtung des Weltraumwetters ein. Hier können **ICMEs** mithilfe von sogenannten Forbush decreases detektiert werden, die in den Messungen des Radiation Assessment Detector (**RAD**) an Bord des Rovers *Curiosity* (Mars Science Laboratory) erscheinen. Hierbei handelt es sich um kurzzeitige Abschwächungen der galaktischen kosmischen Strahlung, die die magnetische Struktur der **ICMEs** durch Abschirmung hervorruft. Die Messungen solcher Forbush decreases werden hier verwendet, um die Ankunftszeiten von **ICMEs**, die nacheinander Erde und Mars treffen, oder alternativ zuerst eine der **STEREO**-Sonden und dann den Mars, statistisch zu untersuchen. Die Messungen zeigen zum ersten Mal, dass schnelle **ICMEs** auch über die Erdbahn hinaus durch die Wechselwirkung mit dem umgebenden langsameren Sonnenwind weiter abgebremst werden. Mithilfe der bildgebenden Teleskope auf **STEREO**, den sogenannten Heliospheric Imagers, untersuchen wir weitere **ICMEs** die den Mars getroffen haben und überprüfen damit die Genauigkeit verschiedener Methoden für die Analyse dieser Bilddaten. Anschließend werden die Forbush-decrease-Messungen für die so katalogisierten **ICMEs** noch genauer untersucht, um neben der Ankunftszeit durch den Vergleich mit analytischen Modellen noch weitere Informationen über die radiale Entwicklung der **ICMEs** zu gewinnen.

Daraufhin werden noch zwei Fallstudien vorgestellt: Zunächst werden die starken Weltraumwetter-Ereignisse im September 2017 und ihre Auswirkungen auf dem Mars vorgestellt – hier werden neben den solaren Teilchenereignissen auch drei dazugehörige **CMEs** untersucht, die zusammentreffen und sich auf dem Weg zum Mars vereinigen. Zuletzt werden die ersten Messungen eines **ICMEs** mit der

Raumsonde Solar Orbiter vorgestellt, die im Februar 2020 gestartet ist. In dieser Studie zeigen wir, wie mit dem High Energy Telescope an Bord von Solar Orbiter Forbush decreases mit hoher Auflösung gemessen werden können, und rekonstruieren die Daten des beobachteten Forbush decrease mit einem theoretischen Modell. Die Ergebnisse zeigen, dass der ICME ein ungleichmäßiges Expansionsverhalten zeigt, möglicherweise durch den Einfluss einer nachfolgenden Sonnenwind-Wechselwirkungsregion (*stream interaction region*).

PUBLICATIONS

This is a list of the peer-reviewed publications that are relevant in the context of this thesis and are reprinted therein. A list of all publications I have contributed to can be found in [Appendix C](#).

USING FORBUSH DECREASES TO DERIVE THE TRANSIT TIME OF ICMEs PROPAGATING FROM 1 AU TO MARS

Freiherr von Forstner, J. L., J. Guo, R. F. Wimmer-Schweingruber, D. M. Hassler, M. Temmer, M. Dumbović, L. K. Jian, J. K. Appel, J. Čalogović, B. Ehresmann, B. Heber, H. Lohf, A. Posner, C. T. Steigies, B. Vršnak, and C. J. Zeitlin, *Journal of Geophysical Research: Space Physics*, 123, 1, pages 39–56 (2018), DOI: [10.1002/2017JA024700](https://doi.org/10.1002/2017JA024700)

Own contribution: 90%

TRACKING AND VALIDATING ICMEs PROPAGATING TOWARD MARS USING STEREO HELIOSPHERIC IMAGERS COMBINED WITH FORBUSH DECREASES DETECTED BY MSL/RAD

Freiherr von Forstner, J. L., J. Guo, R. F. Wimmer-Schweingruber, M. Temmer, M. Dumbović, A. Veronig, C. Möstl, D. M. Hassler, C. J. Zeitlin, and B. Ehresmann, *Space Weather*, 17, 4, pages 586–598 (2019), DOI: [10.1029/2018SW002138](https://doi.org/10.1029/2018SW002138)

Own contribution: 90%

COMPARING THE PROPERTIES OF ICME-INDUCED FORBUSH DECREASES AT EARTH AND MARS

Freiherr von Forstner, J. L., J. Guo, R. F. Wimmer-Schweingruber, M. Dumbović, M. Janvier, P. Démoulin, A. Veronig, M. Temmer, A. Papaioannou, S. Dasso, D. M. Hassler, and C. J. Zeitlin, *Journal of Geophysical Research: Space Physics*, 125, 5, e2019JA027662 (2020), DOI: [10.1029/2019JA027662](https://doi.org/10.1029/2019JA027662) Own contribution: 80%

ANALYSIS OF THE RADIATION HAZARD OBSERVED BY RAD ON THE SURFACE OF MARS DURING THE SEPTEMBER 2017 SOLAR PARTICLE EVENT

Zeitlin, C., D. M. Hassler, J. Guo, B. Ehresmann, R. F. Wimmer-Schweingruber, S. C. R. Rafkin, **J. L. Freiherr von Forstner**, H. Lohf, T. Berger, D. Matthiä, and G. Reitz, *Geophysical Research Letters*, 45, 12, pages 5845–5851 (2018), DOI: [10.1029/2018GL077760](https://doi.org/10.1029/2018GL077760) Own contribution: 10%

MODELING THE EVOLUTION AND PROPAGATION OF 10 SEPTEMBER 2017 CMEs AND SEPs ARRIVING AT MARS CONSTRAINED BY REMOTE SENSING AND IN SITU MEASUREMENT

Guo, J., M. Dumbović, R. F. Wimmer-Schweingruber, M. Temmer, H. Lohf, Y. Wang, A. Veronig, D. M. Hassler, L. M. Mays, C. Zeitlin, B. Ehresmann, O. Witasse, **J. L. Freiherr von Forstner**, B. Heber, M. Holmström, and A. Posner, *Space Weather*, 16, 8, pages 1156–1169 (2018), DOI: [10.1029/2018SW001973](https://doi.org/10.1029/2018SW001973) Own contribution: 10%

RADIAL EVOLUTION OF THE APRIL 2020 STEALTH CORONAL MASS EJECTION BETWEEN 0.8
AND 1 AU: A COMPARISON OF FORBUSH DECREASES AT SOLAR ORBITER AND EARTH

Freiherr von Forstner, J. L., M. Dumbović, C. Möstl, J. Guo, A. Papaioannou, R. Elftmann, Z. Xu, J. C. Terasa, A. Kollhoff, R. F. Wimmer-Schweingruber, J. Rodríguez-Pacheco, A. J. Weiss, J. Hinterreiter, T. Amerstorfer, M. Bauer, A. V. Belov, M. A. Abunina, T. Horbury, E. E. Davies, H. O'Brien, R. C. Allen, G. B. Andrews, L. Berger, S. Boden, I. Cernuda Cangas, S. Eldrum, F. Espinosa Lara, R. Gómez-Herrero, J. R. Hayes, G. C. Ho, S. R. Kulkarni, W. J. Lees, C. Martín, G. M. Mason, D. Pacheco, M. Prieto Mateo, A. Ravanbakhsh, O. Rodríguez Polo, S. Sánchez Prieto, C. E. Schlemm, H. Seifert, K. Tyagi, and M. Yedla, *A&A* (2021), doi: [10.1051/0004-6361/202039848](https://doi.org/10.1051/0004-6361/202039848)

Own contribution: 80%

CONTENTS

1	INTRODUCTION	1
1.1	Particles in the heliosphere	1
1.2	Space Weather events and their detection	3
1.3	Coronal mass ejections	4
1.4	Forbush decreases	6
1.5	Motivation	9
2	INSTRUMENTATION	11
2.1	The MSL Radiation Assessment Detector	11
2.2	The Solar Orbiter High Energy Telescope	14
2.3	Neutron monitor measurements	17
2.4	The STEREO Heliospheric Imagers	18
3	STUDIES OF ICME ARRIVAL TIMES AT 1 AU AND MARS USING FORBUSH DECREASES	23
3.1	Opposition phases	23
3.1.1	Using Forbush Decreases to Derive the Transit Time of ICMEs Propagating from 1 AU to Mars (Publication JGR–Space Physics 2018)	25
3.1.1.1	Introduction	25
3.1.1.2	Methods and Data	27
3.1.1.3	Results and Discussion	30
3.1.1.4	Conclusion	37
3.1.1.5	Appendix A: Cross-Correlation Analysis Plots for Each Event	38
3.1.1.6	References	41
3.2	Heliospheric imager observations	43
3.2.1	Tracking and Validating ICMEs Propagating Toward Mars Using STEREO Heliospheric Imagers Combined With Forbush Decreases Detected by MSL/RAD (Publication Space Weather 2019)	44
3.2.1.1	Introduction	44
3.2.1.2	Data and Methods	45
3.2.1.3	Results and Discussion	47
3.2.1.4	Conclusions and Outlook	53
3.2.1.5	References	54
4	COMPARING FORBUSH DECREASE PROPERTIES AT EARTH AND MARS	57
4.1	Comparing the Properties of ICME-Induced Forbush Decreases at Earth and Mars (Publication JGR–Space Physics 2020)	58
4.1.1	Introduction	58
4.1.2	Data Sources and Catalogs	59
4.1.3	Definitions and Methodology	63
4.1.4	Results and Discussions	65
4.1.5	Conclusions and Outlook	74

4.1.6	Appendix A: Location of m_{\max} Within the ICME Substructures	74
4.1.7	References	76
5	MAJOR SPACE WEATHER EVENTS: THE EVENTS OF SEPTEMBER 2017	79
5.1	Analysis of the radiation hazard observed by RAD on the surface of Mars during the September 2017 solar particle event (Publication GRL 2018)	81
5.1.1	Introduction	81
5.1.2	Triggering and Data Acquisition	81
5.1.3	Results	82
5.1.4	Conclusions	86
5.1.5	References	87
5.2	Modeling the Evolution and Propagation of 10 September 2017 CMEs and SEPs Arriving at Mars Constrained by Remote Sensing and In Situ Measurement (Publication Space Weather 2018)	89
5.2.1	The Flare, CMEs, and GLE 72: Close to the Sun	90
5.2.2	The Interplanetary Trajectory and Interaction of Three CMEs Modeled by the DBM	93
5.2.3	Shock Kinematics and Propagation Toward Earth and Mars: Data-Constrained DBM	95
5.2.4	The Shock and ICME Arrival at Mars and Earth: Modeled Results and In Situ Observations	96
5.2.5	SEPs Arriving at Earth, Mars, and STA and the Indication of the Shock and Stream Interaction Region Propagation	97
5.2.6	Summary and Conclusion	99
5.2.7	Appendix A: References of the Measurements and Databases Employed in This Study	100
5.2.8	References	101
6	CASE STUDY: FIRST CME SEEN AT SOLAR ORBITER	103
6.1	Radial Evolution of the April 2020 Stealth Coronal Mass Ejection between 0.8 and 1 AU: A Comparison of Forbush Decreases at Solar Orbiter and Earth (Publication A&A 2021)	105
6.1.1	Introduction	105
6.1.2	Data Sources	106
6.1.3	Methods	109
6.1.4	Results	109
6.1.5	Discussion and conclusions	115
6.1.6	References	118
7	SUMMARY AND OUTLOOK	121
	BIBLIOGRAPHY	123
A	ISOTROPIC SIMULATION OF THE HIGH ENERGY TELESCOPE WITH THE SOLAR ORBITER SPACECRAFT MODEL	133
A.1	Isotropic simulation of HET	134
A.2	The spacecraft model	134
A.3	Analysis of the simulation results	137
B	IMPLEMENTATION OF THE GRADUATED CYLINDRICAL SHELL MODEL IN PYTHON	141

B.1	GCS geometry	143
B.2	Graphical user interface	143
B.3	Validation	146
C	LIST OF PUBLICATIONS	149

LIST OF FIGURES

Figure 1	Spectra of oxygen ions in the near-Earth interplanetary space	1
Figure 2	Sketch of some of the particle populations in the heliosphere	2
Figure 3	Examples of CME and ICME signatures	4
Figure 4	Illustration of ICMEs and Forbush decreases	8
Figure 5	Photo of the RAD sensor head	11
Figure 6	Schematic diagram of the RAD sensor head	12
Figure 7	EPD energy coverage	15
Figure 8	HET sensor head	16
Figure 9	Fields of view of the STEREO SECCHI telescopes	20
Figure 10	STEREO-A HI images of the April 15, 2020 CME	22
Figure 11	Density model of the Solar Orbiter spacecraft	135
Figure 12	HET simulation setup with spacecraft model	138
Figure 13	Response functions of HET C detector single counters	139
Figure 14	Illustration of the GCS model	141
Figure 15	Results of the functions from GCS-Python	144
Figure 16	Screenshot of the GCS Python GUI	145
Figure 17	Validation of the GCS Python implementation	147

LIST OF TABLES

Table 1	Properties of the STEREO SECCHI telescopes	19
Table 2	Details of the spacecraft model used for the HET simulation	136
Table 3	GCS parameters for Figure 17	146

ACRONYMS

ACE	Advanced Composition Explorer
API	Application Programming Interface
CAD	computer-aided design
CIR	corotating interaction region
CME	coronal mass ejection (see Section 1.3)
CRaTER	Cosmic Ray Telescope for the Effects of Radiation (onboard LRO)
DBM	drag-based model (for CME propagation, Vršnak et al., 2013)
DSCOVR	Deep Space Climate Observatory
EPD	Energetic Particle Detector (onboard SolO)
EPHIN	Electron Proton Helium Instrument (onboard SOHO)
EPT	Electron Proton Telescope (part of EPD onboard SolO)
EUHFORIA	European Heliospheric Forecasting Information Asset (heliospheric MHD model, Pomoell and Poedts, 2018)
EUV	extreme ultraviolet
FD	Forbush decrease (see Section 1.4)
ForbMod	Forbush decrease model for flux rope ICMEs (Dumbović et al., 2018a , 2020)
FOV	field of view
GCR	galactic cosmic ray
GCS	graduated cylindrical shell (CME model, see Appendix B)
Geant4	Geometry and Tracking 4 (simulation toolkit, Agostinelli et al., 2003)
GLE	ground level enhancement
GSM	Global Survey Method
GUI	graphical user interface
HEE	Heliocentric Earth Ecliptic (coordinate system)
HELCASTS	Heliospheric Cataloguing, Analysis and Techniques Service (https://www.helcats-fp7.eu/)
HET	High Energy Telescope (part of EPD onboard SolO , or onboard STEREO)
HI	heliospheric imager (e.g. part of SECCHI onboard STEREO)
HSS	high speed stream
ICME	interplanetary coronal mass ejection

IDL	Interactive Data Language (programming language)
IMF	interplanetary magnetic field
ISM	interstellar medium
ICME	interplanetary coronal mass ejection
JSON	JavaScript Object Notation (data format)
LASCO	Large Angle and Spectrometric Coronagraph Experiment (onboard SOHO)
LET	linear energy transfer
LRO	Lunar Reconnaissance Orbiter
MAVEN	Mars Atmosphere and Volatile Evolution
MHD	magnetohydrodynamic
MIP	minimally ionizing particle
NMDB	Neutron Monitor Database
MSL	Mars Science Laboratory
NOAA	National Oceanic and Atmospheric Administration
PCB	printed circuit board
PDB	propagating diffusive barrier (FD model, Wibberenz et al., 1998)
PSP	Parker Solar Probe
RAD	Radiation Assessment Detector (onboard MSL)
REMS	Rover Environmental Monitoring Station (onboard MSL)
SDO	Solar Dynamics Observatory
SECCHI	Sun Earth Connection Coronal and Heliospheric Investigation (remote sensing instrument suite onboard STEREO)
SEP	solar energetic particle
SIR	stream interaction region
SIS	Suprathermal Ion Spectrograph (part of EPD onboard Solo)
SOHO	Solar and Heliospheric Observatory
Solo	Solar Orbiter
STEP	Suprathermal Electrons and Protons (part of EPD onboard Solo)
STEREO	Solar Terrestrial Relations Observatory
TID	total ionizing dose

INTRODUCTION

1.1 PARTICLES IN THE HELIOSPHERE

Our heliosphere is a vast region in space embedded in the interstellar medium (ISM), which encompasses all solar system planets and extends far beyond even the Kuiper belt. It is filled with a thin plasma consisting of various populations of particles, many of which originate from the Sun itself. These populations can be identified in Figure 1 (based on measurements by Mewaldt et al., 2001), shown as an energy spectrum that extends over more than 7 orders of magnitude on the energy scale and about 20 orders of magnitude on the intensity scale. The by

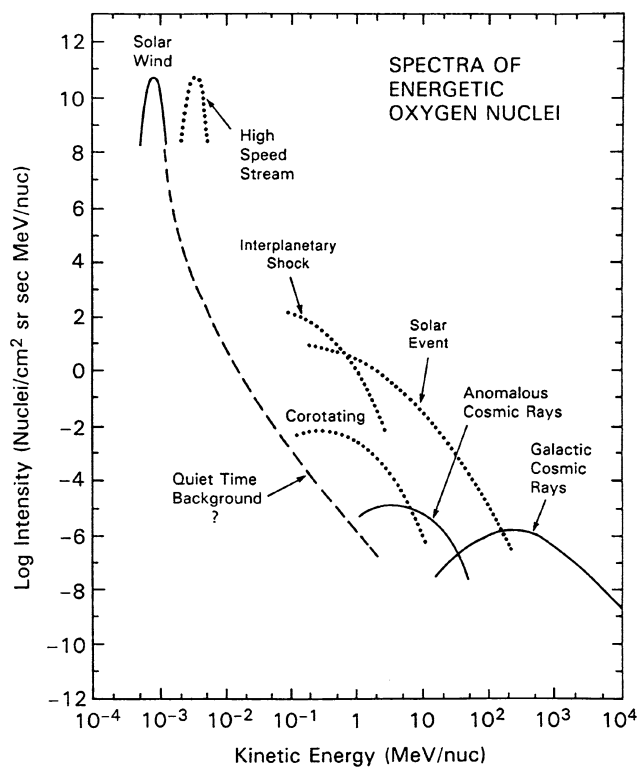


Figure 1: Typical spectra of oxygen ions in the near-Earth interplanetary space, showing the contributions of different populations. Other particle species show similarly shaped spectra when plotted as a function of energy per nucleon (adapted from <http://helios.gsfc.nasa.gov/ace/gallery.html>, based on Mewaldt et al., 2001).

far most abundant population is the solar wind, a steady flow of plasma that is emitted from the Sun radially and fills the heliosphere. In the near-Earth space at one astronomical unit (AU), the slow solar wind typically reaches speeds between 300 km/s and 500 km/s. Due to its low pressure, and therefore high plasma β , it carries the solar magnetic field with it and creates the interplanetary magnetic

field (**IMF**). As the Sun rotates, the **IMF** forms an Archimedian spiral, which was named Parker spiral after Eugene N. Parker, who first developed this model of the solar wind (Parker, 1958).

However, our Sun is an active star, and thus the flow of particles is not simply constant. The variability is driven by the 11-year solar cycle, a recurring reversal of the solar magnetic field that is associated with enhancements in solar activity (solar maximum) due to the increased amount of magnetic stress and reconnection processes, and low-activity periods inbetween (solar minimum). Coronal holes, which are colder and therefore darker regions forming on the Sun, emit faster solar wind streams with speeds above approximately 600 km/s. These high speed streams (**HSS**), which are located right next to the (slow) solar wind in **Figure 1**, then interact with the neighboring streams of slower wind due to their different Parker spiral curvature and form a stream interaction region (**SIR**, e.g. Richardson, 2018), as shown in **Figure 2**. **SIRs** are flanked by interplanetary shocks on each side,

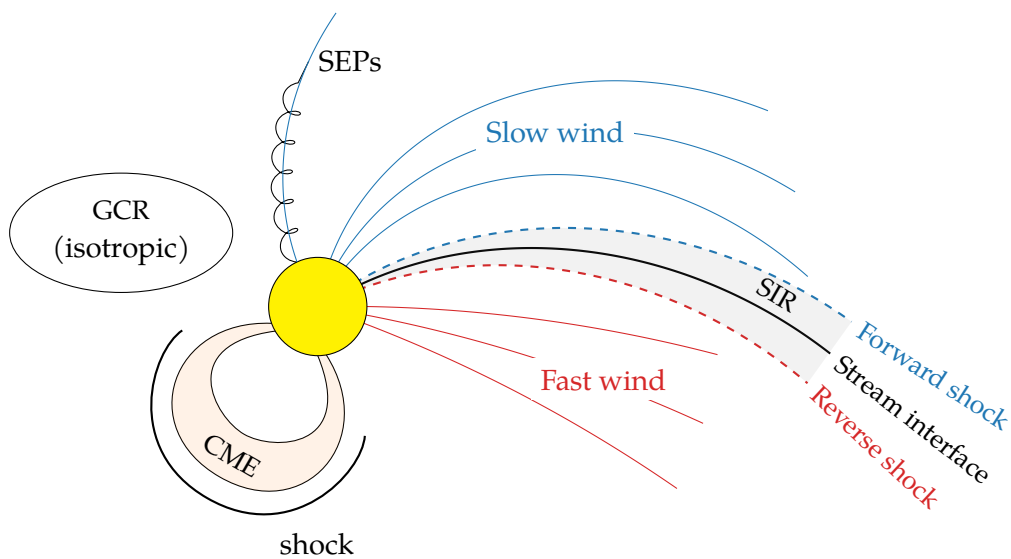


Figure 2: Sketch of some of the particle populations in the heliosphere: slow and fast solar wind, **SIRs**, **CMEs**, **SEPs**, shocks, and **GCRs**.

the so-called forward and reverse shocks. If a coronal hole stays stable for a longer time, these interaction regions can be observed recurrently in each solar rotation (i.e., every ~ 27 days when observed from Earth), in which case they are called corotating interaction regions (**CIRs**). Furthermore, active regions on the Sun can occasionally produce solar flares, sudden and intense emissions of photons often associated with the release of high-energy (\sim MeV) solar energetic particles (**SEPs**, e.g. Reames, 1990), as shown in the central area of **Figure 1**. **SEPs** then quickly propagate out into the heliosphere from their source region, typically following the **IMF** lines, as shown in **Figure 2**. Solar flares are believed to be powered by the reconnection of magnetic field lines at the Sun, which leads to the release of energy and acceleration of particles. These events often also coincide with the eruption of plasma from the solar corona in the form of a coronal mass ejection (**CME**) at speeds up to a few thousand km/s. Just like the solar wind, **CMEs** carry a magnetic field with them when they propagate away from the Sun. Due to their high speed,

an interplanetary shock can form in front of the **CME**, followed by a turbulent sheath region. This shock can also be efficient at accelerating additional particles to higher energies, similar to **SEPs** accelerated directly at the Sun.

The high end of the energy spectrum (**Figure 1**) from tens of MeV to GeV is dominated by galactic cosmic rays (**GCRs**), charged particles originating from outside the heliosphere produced e.g. in stellar supernovae and entering it with a relatively constant and isotropic flux. Within the heliosphere, the flux of these high-energy particles is modulated by various effects: On large timescales, the variation of the **IMF** intensity during the 11-year solar cycle modulates the **GCRs** observed in the inner solar system, so that the average **GCR** flux is higher at solar minimum than at solar maximum (Fisk, 1980). In addition, there are short-term modulations of **GCR** due to magnetic structures in the solar wind, such as **CMEs** and **SIRs/CIRs**. These are the so-called Forbush decreases, which will be the main focus of this thesis and will be further described in **Section 1.4**.

1.2 SPACE WEATHER EVENTS AND THEIR DETECTION

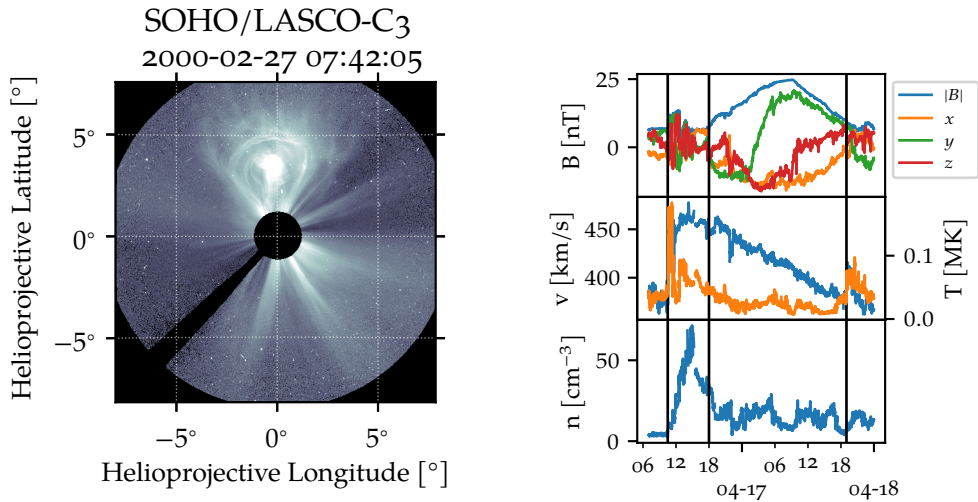
As defined by the U.S. National Space Weather Program, the term *space weather* refers to “conditions on the Sun and in the solar wind, magnetosphere, ionosphere and thermosphere that can influence the performance and reliability of spaceborne and ground-based technological systems and endanger human life or health” (OFCM, 1995). The aforementioned large-scale heliospheric events, such as **SEPs**, **CMEs** and **CIRs** are all relevant to space weather. For example, the increased radiation exposure due to accelerated energetic particles can be dangerous for astronauts. Additionally, the enhanced and turbulent magnetic fields impacting spacecraft or disturbing the Earth’s magnetosphere in a so-called geomagnetic storm can cause disruptions of spacecraft electronics or of electricity grids on the ground.

Thus, space weather research is focused on enhancing the understanding of these events in order to be able to more accurately predict their occurrence and propagation, including the onset time at Earth (or other locations in the solar system) and their intensity. In the past, the investigation of heliospheric events has been mostly based on two kinds of measurements: First, remote sensing observations of the Sun and its vicinity, such as extreme ultraviolet (**EUV**) images, magnetograms and white-light coronagraph images, are available from spacecraft near Earth such as the Solar and Heliospheric Observatory (**SOHO**) and the Solar Dynamics Observatory (**SDO**). Second, in situ observations, such as solar wind plasma measurements and magnetometers, can also be obtained from spacecraft located at the L_1 Lagrange point, including **SOHO**, the Advanced Composition Explorer (**ACE**), Wind, and the Deep Space Climate Observatory (**DSCOVR**). In the last two decades, these observations have been complemented by in situ measurements from deep space heliophysics missions, such as from the two Solar Terrestrial Relations Observatory (**STEREO**) spacecraft orbiting the Sun near 1 AU as well as the recent Parker Solar Probe (**PSP**) and Solar Orbiter (**SoHO**) missions, which are starting to provide valuable data from extremely close to the Sun with a larger variety of instruments and higher resolution than the Helios mission in

the 1970s. In addition to observing the Sun and its corona, these missions also facilitate imaging observations of the interplanetary space using the wide field of view of their heliospheric imagers (HIs). These can be used to directly track CMEs all the way out to Earth (see Section 2.4).

1.3 CORONAL MASS EJECTIONS

As mentioned in Section 1.1, CMEs are large-scale eruptions of plasma from the Sun that propagate outward into the heliosphere. They are often associated with flares and believed to be driven by reconnection of the coronal magnetic field (see e.g. Forbes, 2000 and Kusano et al., 2012). CMEs occur relatively frequently, on average every 4 days at solar minimum and 2.5 to 3 times per day at solar maximum (Webb and Howard, 1994). The properties of CMEs have a large variability: For example, their speeds can range between 20 km/s and 2000 km/s, where the average is at about 400 km/s and faster CMEs are more likely to occur near solar maximum. Also, their longitudinal extent can vary: Very narrow (5°) and very wide (120°) cases have been observed, with the average being around 50° (Cane, 2000). A classic example of a CME observed by the C3 coronagraph of the SOHO Large Angle and Spectrometric Coronagraph Experiment (LASCO) is shown in Figure 3a. The black circle in the center of the coronagraph image is the occulter that covers the solar disk, and the CME appears over the solar north pole as the source region is located far north of the solar equator in this case (at $\sim 30^\circ$ latitude).



(a) CME observed by the SOHO/LASCO C3 coronagraph on February 27, 2000. (b) ICME signatures in ACE magnetic field and plasma data on April 17, 1999.

Figure 3: Examples of CME/interplanetary coronal mass ejection (ICME) signatures in remote sensing and in situ data.

When the in situ counterparts of CMEs are observed in interplanetary space, in contrast to remote sensing observations close to the Sun, they are often referred to as an interplanetary CMEs (ICMEs). Common ICME signatures include a low proton temperature and density, an enhanced and often smoothly rotating magnetic field (magnetic cloud / flux rope), bidirectional electron streaming as well as

the modulation of some elemental abundance ratios (Richardson and Cane, 1995; Zurbuchen and Richardson, 2006; Wimmer-Schweingruber et al., 2006). Examples of these signatures, mainly the low temperature and density as well as the smooth magnetic field rotation, are shown in Figure 3b as observed by the ACE spacecraft — the ICME ejecta is located between the second and third vertical line, whose positions are taken from the list by Richardson and Cane (2010). As a CME’s magnetic ejecta is often propagating at a higher velocity than the surrounding solar wind plasma, a turbulent region of compressed plasma, called the sheath, typically forms in front of these CMEs. While additional solar wind plasma can be accumulated into the sheath from the front, causing it to grow over time, this effect can also be counteracted by lateral flow away from the CME apex and magnetic reconnection with the ejecta (see e.g. Siscoe and Odstrcil, 2008; Manchester et al., 2005; Janvier et al., 2019). When the CME exceeds the local magnetosonic speed, a shock forms in front of the sheath, which is then observed as an abrupt change in most of the parameters that are measured in situ, such as the magnetic field, plasma velocity and density. This is also seen in Figure 3b, where the shock (first vertical line) is associated with jumps in all measured quantities and the following sheath region shows a highly compressed and turbulent plasma.

Especially since the availability of HI observations, it has become evident that the structures observed near the Sun and in interplanetary space are directly linked. Consequently, the lines between the terms CME and ICME have become more blurred, and many authors have begun to use the term CME for both the remote sensing and in situ observed phenomena.

Many efforts have been made to develop models that describe the propagation of CMEs in the heliosphere and predict their arrival times at different locations, taking into account the interaction with the surrounding ambient solar wind and other interplanetary structures, such as SIRs and other CMEs. Most of these models can be divided into two basic classes: magnetohydrodynamic (MHD) simulations and empirical models. One of the most widely used MHD models in this field is the Wang-Sheeley-Argé ENLIL with cone model (WSA-ENLIL+Cone) developed by Odstrcil et al. (2004). WSA-ENLIL simulates the solar wind propagation in the heliosphere based on magnetogram observations of the Sun and a potential field source surface model of the coronal magnetic field (WSA model) within $21.5 R_{\odot}$, which is then used as the inner boundary of the MHD simulation (ENLIL). CMEs can be injected into the MHD model as dense cone-shaped hydrodynamic bubbles starting from the inner boundary at $21.5 R_{\odot}$. The input parameters, such as the CME velocity, direction and size are typically derived manually from coronagraph observations, e.g. using the graduated cylindrical shell (GCS, Thernisien, 2011) model, which is further described in Appendix B.

As it has long been known that the strongest geomagnetic storms are typically caused by ICMEs with a strong southward magnetic field (negative B_z , see e.g. Russell et al., 1974) and the hydrodynamic cones used in the WSA-ENLIL+Cone are just bubbles of enhanced density with no inherent magnetic field, it became clear that more sophisticated models are needed for predicting the in situ magnetic field. Therefore, in the recent years, a new heliospheric MHD model named the European Heliospheric Forecasting Information Asset (EUHFORIA, Pomoell and

Poedts, 2018) has been developed, which initially used the same cone model for describing the CMEs, but was later adapted with a new *spheromak* model (Scolini et al., 2019), which includes the magnetic field of the CME and thus has substantially improved the predictions of the magnetic field observations at Earth.

On the other hand, there are simple empirical models of CME propagation, such as the analytical drag-based model (DBM, Vršnak et al., 2013). The DBM is used to calculate the ICME arrival time at different points in space, it does not predict any of the solar wind plasma or magnetic field properties. The model is based on the well-known effect that due to the interaction of CMEs with the ambient solar wind, the CME velocity v tends to approach the solar wind speed w over time, apparently following a “drag force”. In reality, these forces are not caused by actual collision of particles, but transported in the form of MHD waves and turbulence generated in the plasma (see e.g. Cargill et al., 1996; Owens and Cargill, 2004, for details). DBM describes the acceleration a of the CME in the mathematical form of a simple aerodynamic drag equation with an empirical drag coefficient Γ , where the solar wind speed w is given as a fixed input parameter:

$$a = -\Gamma(v - w)|v - w| \quad (1)$$

The advantage of such a simple model is that its results are much quicker to calculate (e.g., in real time prediction environments) and it requires less input parameters. It can also be employed in a reverse modeling approach, where the model is fitted to the observed arrival times in order to determine the drag parameter (Žic et al., 2015). Furthermore, the analytical form and fast computation time of the model allow to easily propagate the uncertainties of the input parameters, either analytically or with an ensemble modeling technique (DBEM) as proposed by Dumbović et al. (2018b).

As has been shown in statistical studies, e.g. by Vršnak et al. (2014) and Dumbović et al. (2018b) and others referenced therein, it seems that all these common modeling approaches, both empirical and MHD, show a surprisingly similar performance when it comes to the prediction of arrival times, with a mean absolute error on the order of 10 h for large representative samples of CMEs arriving at Earth. Even other independent approaches such as recent studies that successfully predicted arrival times using convolutional neural networks solely based on coronagraph images (without any manual intervention for the extraction of parameters) (Wang et al., 2019) have not yet been able to significantly surpass this accuracy, even though this would be desirable for space weather forecasting purposes. This suggests that more measurements at different heliospheric locations will need to be incorporated into such models in the future — both to provide additional input parameters from observations close to the Sun and to create a larger sample size of in situ data for better calibration of the models.

1.4 FORBUSH DECREASES

Forbush (1937) and Hess and Demmelair (1937) first discovered short-term decreases in the GCR intensity at Earth using ionization chambers, where decreases were detected at multiple locations simultaneously and coincided with

geomagnetic storms. These decreases, which are routinely measured today using ground-based neutron monitors or spaceborne energetic particle detectors, were later named Forbush decreases (FDs) in honor of their discoverer. It was found that FDs are not caused by the geomagnetic field variations themselves (as they are even observed in the polar regions), but rather have an interplanetary origin (see e.g. Lockwood, 1971, and references therein). There are two types of FDs: The so-called recurrent decreases, which are induced by CIRs and therefore reoccur after one solar rotation (~ 27 days), and the non-recurrent decreases caused by CMEs. In both cases, the turbulent magnetic field of the shocks and sheaths associated with CMEs or CIRs as well as the strong magnetic field of a CME flux rope can shield away part of the GCRs, so that the intensity is decreased during the passage of this structure. Especially in the case of CMEs, the decrease phase is usually short ($\lesssim 1$ day), while the recovery to the previous GCR intensity (for isolated events) can take multiple days up to about a week. The onset typically corresponds well with the arrival of the CME or shock/sheath structure. For CMEs that drive a shock, a two-step decrease can sometimes be observed, with the first step caused by the shock/sheath region and the second by the magnetic ejecta — this classical picture is illustrated by Figure 4. However, when the resolution of the GCR measurements is not high enough, the second step may not be clearly separable for all events associated with a shock. Typical amplitudes of FDs can range from a few percent up to more than 10 % depending on the event, but this varies significantly depending on which GCR energies are observed: Lower energy particles are modulated more easily and thus show larger FDs (e.g. Lockwood, 1971; Lockwood et al., 1991).

Over time, multiple models have been proposed to describe FDs caused by different magnetic structures, and these are often based on a diffusion equation. For example, the propagating diffusive barrier model (PDB, Wibberenz et al., 1998) can be used to describe a shock that acts as a barrier through which GCRs cannot diffuse as easily as in the ambient solar wind. This creates a “shadow” within and behind the shock in which the GCR intensity is decreased. The Forbush decrease model for flux rope ICMEs (ForbMod) developed by Dumbović et al. (2018a) builds on top of this approach to model FDs caused by flux rope CMEs by combining the diffusion process with an expanding cylindrical flux rope structure. In this case, the flux rope initially does not contain any GCRs close to the Sun, and they can gradually diffuse into it (perpendicular to the magnetic field) over time. The time evolution of the GCR density within the flux rope is determined by the interplay of its self-similar expansion and the efficiency of the GCR diffusion. In a following article (Dumbović et al., 2020) the model was combined with empirical equations for the energy dependence of the diffusion process, so that FDs measured using different instruments can be modeled by taking into account their response functions. ForbMod has been applied in two of the publications included in this dissertation (Freiherr von Forstner et al., 2020, 2021) and further details about its derivation are given in these publications.

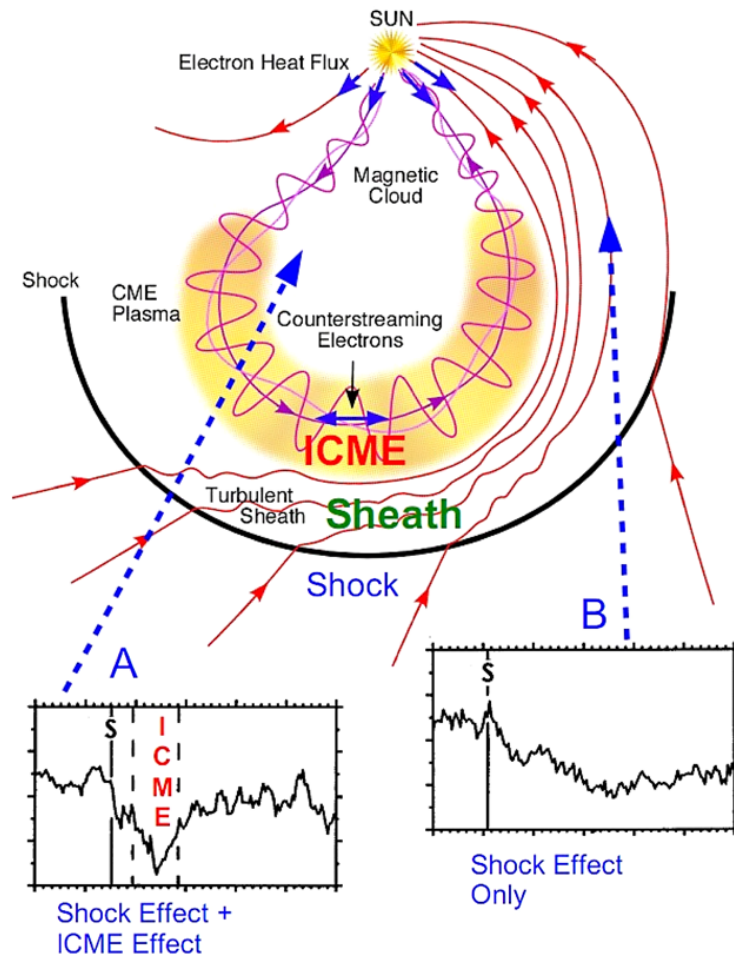


Figure 4: Illustration of an ICME that drives a shock and the FDs it causes at two locations A and B (marked by the blue dashed arrows). A classical two-step Forbush decrease is seen at location A, where both the shock/sheath and the magnetic cloud pass. At location B, only a single-step Forbush decrease is observed because only the shock is seen here. The red and pink arrows indicate selected magnetic field lines. Source: Richardson and Cane (2011, Figure 1), reprinted by permission from Springer Nature.

1.5 MOTIVATION

To better understand the propagation of ICMEs in the heliosphere, their radial evolution and impacts on Earth, it is essential to make measurements not only in situ at Earth, but from as many locations as possible. This allows us to validate and calibrate modeling approaches and thus improve our forecasting capabilities. The necessary observations include both in situ measurements at different locations on the ICME's trajectory, e.g., as an upstream monitor on the Sun-Earth line to give early warning of an approaching ICME, as well as remote sensing observations from viewpoints not hit by the CME (e.g., away from the Sun-Earth line) to better understand the global CME characteristics. Measurements at other locations also become increasingly relevant not only for Earth, but likewise for the large amount of operating and planned space missions (including human spaceflight to Mars in the next decades), which are also in need of space weather forecasting for ensuring the safety of spacecraft and astronauts.

Several spacecraft with appropriate plasma and magnetic field measurements for these purposes are already available. However, on missions not primarily focused on heliophysics, such as planetary missions, these instruments are typically absent or provide only limited data. Incorporating these missions into the framework of space weather observations would nonetheless be interesting, so that they could serve as additional in situ viewpoints. Especially in these cases, it is sensible to use FDs as an alternative method for the detection of ICMEs — these can be measured with particle detectors, which are available on many additional spacecraft. For example, the Radiation Assessment Detector (RAD) instrument on the Mars Science Laboratory (MSL) mission, which will be introduced in Section 2.1, is the only instrument that provides continuous measurements of space weather at Mars through its FD observations — other missions orbiting the planet such as Mars Express (2003) and Mars Atmosphere and Volatile Evolution (MAVEN, 2014) carry some plasma and/or magnetic field instruments, but only have limited coverage as their orbits cross below Mars's bow shock, so that the upstream solar wind cannot be observed all the time.

This thesis will present the first systematic studies of Forbush decreases caused by ICMEs at Mars using the RAD cosmic ray data. The measured CME arrival times at Mars as well as remote sensing data from STEREO-HI will be inspected to validate different approaches for the modeling of ICME propagation (as introduced in Section 1.3). Furthermore, it will be explored whether it is possible to derive more information about the CME evolution than just the arrival times from the FD observations by applying the analytical models introduced in Section 1.4 in a reverse modeling approach. Furthermore, some case studies of notable space weather events that were associated with FDs will be conducted.

In Chapter 2, a detailed overview of the most important instruments employed in these studies and their data products will be given. The following chapters present several peer-reviewed publications that study ICME arrival times at 1 AU and Mars using FDs and remote sensing observations (Chapter 3) as well as additional properties of FDs at Earth and Mars and their implications for CME radial evolution (Chapter 4). Additional articles in Chapter 5 provide a case study

of a major **SEP** event at Mars in September 2017 that was associated with multiple **ICMEs**. Moreover, the recently submitted article included in **Chapter 6** shows an analysis of the first **ICME** observed at the Solar Orbiter spacecraft in April 2020 and the corresponding **FD** detected by its High Energy Telescope (**HET**). **Chapter 7** subsequently gives a summary of the studies presented in the publications. The following three appendices describe certain technical aspects of these studies in more detail, such as the derivation of response functions for the **HET** (**Appendix A**) and the development of a new software implementation of the **GCS** model for the reconstruction of **CMEs** in remote sensing observations (**Appendix B**). Finally, **Appendix C** presents a list of all publications that I have contributed to, including those that are not included within this dissertation as they do not directly fit into the logical flow.

INSTRUMENTATION

2.1 THE MSL RADIATION ASSESSMENT DETECTOR

Built in a cooperation between the University of Kiel and Southwest Research Institute, the Radiation Assessment Detector (**RAD**, Hassler et al., 2012) instrument onboard the Mars Science Laboratory (**MSL**, Grotzinger et al., 2012) mission provided the first-ever direct radiation measurements on the surface of Mars. It is designed to measure both charged and neutral particles, and calculate particle spectra as well as dosimetric quantities, such as the total ionizing dose (**TID**) rate and linear energy transfer (**LET**) spectra. This aligns with its main science objectives, which include the characterization of energetic particle spectra on the surface of Mars (galactic cosmic rays (**GCRs**) and solar energetic particles (**SEPs**)) and the determination of the radiation hazard for past or present life on Mars or for future human Mars missions. Consequently, **RAD** has not only been continuously measuring the radiation environment on the Martian surface since the *Curiosity* rover's landing on August 6, 2012, but has also been active during the most part of its 9-month flight to Mars (the so-called cruise phase) to evaluate the radiation dose that astronauts would be exposed to when traveling to Mars.



Figure 5: A photo of the **RAD** sensor head before it was mounted on the **MSL** spacecraft. The red protection cap was removed after installation on the rover. Source: NASA/JPL-Caltech/SwRI

The **RAD** sensor head (shown in **Figure 5**) is mounted on the top deck of the rover, pointing along the z axis of **RAD**, i.e. towards the zenith. It is composed of three hexagonal silicon solid-state detectors (A, B, and C) with a thickness of $300\ \mu\text{m}$ each, mounted in a stack to form a charged particle telescope (**Figure 6**) with an opening angle of about 60° . Each detector is divided into an inner and

an outer segment. The D detector, a cesium iodide (CsI) scintillator in the shape of a truncated hexagonal pyramid, is situated directly below the charged particle telescope. Its shape is designed to align with the inner segment of C and follows the opening angle of the charged particle telescope (shown with dashed lines in Figure 6). The E detector, a plastic scintillator which is located below D, is mainly responsible for neutral particle detection. D and E are surrounded by another plastic scintillator (F), which is used as an anticoincidence shield to reject ions that enter D or E from the sides.

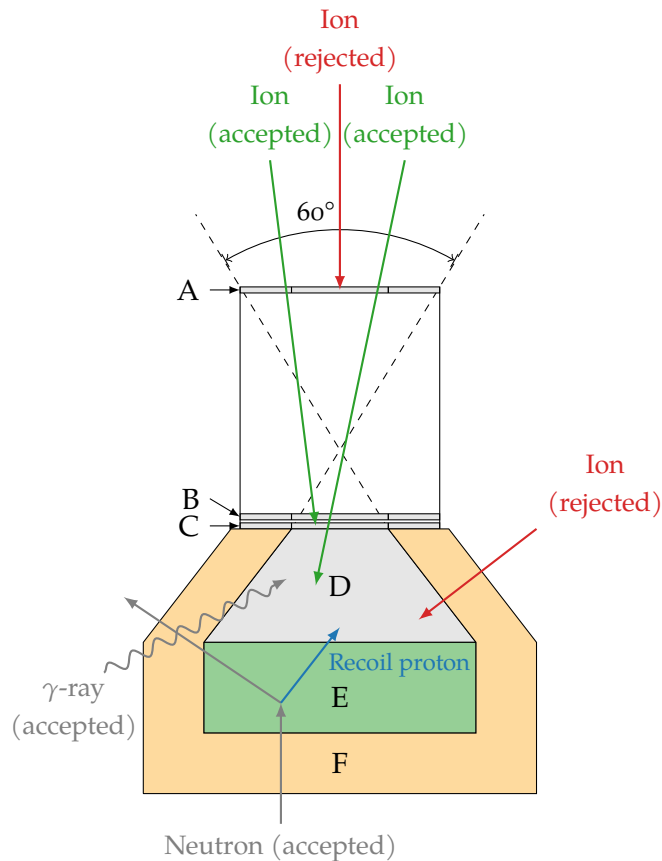


Figure 6: Schematic diagram of the RAD sensor head. Red, green, blue and gray arrows show possible trajectories of charged and neutral particles through the detectors. Based on Hassler et al. (2012), Fig. 7b

For the detection of charged particles, RAD requires an energy deposit in at least the A and B detector, which sets the lower limit for the particle's kinetic energy to e.g. 6 MeV for protons. Higher energy charged particles penetrate the B detector and stop in C, D, or E, where the high stopping power of the D detector allows for a large energy range, e.g. up to 95 MeV for stopping protons. For stopping charged particles, the charge and the total kinetic energy can be determined from the two measured quantities, the total deposited energy E in all triggered detectors and the LET (deposited energy per path length) dE/dx in one of the detectors. This common principle is called the dE/dx - E method and has been in use in numerous instruments since the IMP-1 mission in the 1960s (McDonald and Ludwig, 1964).

Higher energy charged particles, which penetrate the whole **RAD** sensor, cannot be analyzed using this technique, as the total energy E is not measured directly in this case. Up to a few hundred MeV per nucleon, particles can still be partially analyzed as their **LET** is slightly different at the top and bottom ends of the telescope. In this case, the **LET** ratio between the top and bottom can be used to infer the approximate kinetic energy of the incoming particle. For even higher energy particles, the so-called minimally ionizing particles (**MIPs**), there is no significant change in the **LET**, so only the charge and **LET** can be determined, but not the primary energy.

The D and E detectors are both, to different degrees, also sensitive to neutral particles. Being a CsI scintillator, D can detect secondary electrons produced by γ -rays effectively, while neutrons hitting E can interact with the hydrogen atoms in the plastic to produce recoil protons. An inversion method that takes all these interaction processes into account is then used to derive neutral particle spectra (Köhler et al., 2011).

Being an instrument with a rather low mass (1.6 kg) and volume, the observation of short-term and low-amplitude **GCR** variations such as Forbush decreases with **RAD** is only possible when measuring particles that enter the sensor head from all directions, as the restricted opening angle of the charged particle telescope decreases the count rate too much. In this case, the dose rate data products of **RAD** can be used, which are available for the B and E detectors. The E detector is best suited for this purpose due to its larger volume and therefore better statistics. The dose in a detector is calculated as

$$D = \frac{E_{\text{dep}}}{m}, \quad (2)$$

i.e. the total energy deposited in the detector divided by its mass, and typically given in units of Gy = J/kg. The dose rate is its time derivative, so it is given in Gy/s (or $\mu\text{Gy}/\text{day}$, for the order of magnitude that is typically observed on planets). In comparison to a simple count rate, where each detected particle increases the counter by one, particles stopping in the detector typically contribute more to the dose rate than penetrating particles, as the former deposit all their energy.

Because **RAD** is located on the surface of Mars, incoming primary **GCR** and **SEP** particles first need to travel through the Martian atmosphere before reaching the **RAD** detectors. In this process, some particles are shielded away, while others can generate secondary particles by interacting with the particles in the atmosphere. Thus, the radiation environment observed by **RAD** is a mix of primary and secondary particles, and **RAD** measurements cannot be directly compared to deep-space detectors without taking into account the atmospheric response functions (see e.g. Guo et al., 2017a, 2019). For example, **SEP** events need a certain minimum energy to be observed on ground, so **RAD** only sees the most intense events as a ground level enhancement (**GLE**).

The atmospheric pressure measured by the Rover Environmental Monitoring Station (**REMS**) instrument onboard **MSL** shows a significant daily variation of about $\pm 5\%$ (Haberle et al., 2014) due to the considerable temperature changes between day and night — for comparison, the diurnal pressure variations on Earth are at least an order of magnitude lower (e.g. Le Blancq, 2011). These pressure

variations also influence the **RAD** measurements, as they affect the column mass of the atmosphere above **MSL**, and thus change the amount of secondary particles generated in the atmosphere. A clear correlation between dose rate and pressure was observed by Guo et al. (2017a). These diurnal variations show amplitudes up to $\sim 2.5\%$, and this needs to be taken into account when observing short-term variations of the **GCR**, which are typically on a similar order of magnitude. The easiest solution would be to average the dose rate measurements over one solar day (sol) but this would significantly increase the uncertainty for the onset time definition of events such as Forbush decreases (**FDs**). Instead, a spectral notch filter can be applied to the data to filter out the 1 sol frequency and harmonics. This method was described in detail by Guo et al. (2017b) and is also used for most **RAD** data shown within this thesis. These considerations about atmospheric effects of course do not apply to the cruise phase data, where **RAD** was relatively lightly shielded by the surrounding **MSL** spacecraft (Zeitlin et al., 2013; Guo et al., 2015) and no diurnal effects were observed.

2.2 THE SOLAR ORBITER HIGH ENERGY TELESCOPE

The ESA Solar Orbiter spacecraft (**Solo**, Müller et al., 2020) was launched successfully on February 10, 2020. During its mission, it will travel as close to the Sun as 0.27 AU and provide valuable measurements of all kinds of solar events with its comprehensive remote sensing and in situ instrument suite. The Energetic Particle Detector investigation (**EPD**, Rodríguez-Pacheco et al., 2020) onboard **Solo**, a collaboration of the University of Kiel, the University of Alcalá and the Johns Hopkins University APL, is comprised of four instruments, covering the whole energetic particle spectrum from a few keV up to several hundreds of MeV (Figure 7). The lowest energies of electrons and protons, from a few keV (slightly above the solar wind bulk) up to 80 keV, are measured by the Suprathermal Electrons and Protons (**STEP**) telescope, which is followed by the Electron Proton Telescope (**EPT**) for medium energies up to ~ 6 MeV for protons and 450 keV for electrons. Both **EPT** and **STEP** mainly measure electrons and protons, but cannot distinguish between protons and heavier ion species. Hence, they are supplemented with the Suprathermal Ion Spectrograph (**SIS**), a time-of-flight based instrument that measures 12 ion species from H to Fe between 14 keV/nuc and 20.5 MeV/nuc. The highest energies of electrons and all ion species are covered by the High Energy Telescope (**HET**), whose measurements are, similarly to **MSL/RAD** (Section 2.1), based on the $dE/dx-E$ method.

The double-ended **HET** sensor head is shown in Figure 8a. Two of these sensors are installed on the side decks of the **Solo** spacecraft to provide four viewing directions: sunward, antisunward, north and south. The sunward and antisunward fields of view (**HET 1**) are pointed 35° away from the radial direction within the ecliptic, which corresponds to the nominal Parker spiral direction, while the north and south fields of view (**HET 2**) are pointed out of the ecliptic. The **HET** telescopes each consist of four silicon solid-state detectors (**A1**, **B1**, **B2**, **A2**) and a bismuth germanium oxide ($\text{Bi}_4\text{Ge}_3\text{O}_{12}$, **BGO**) scintillator (**C**) in the center. This setup is similar

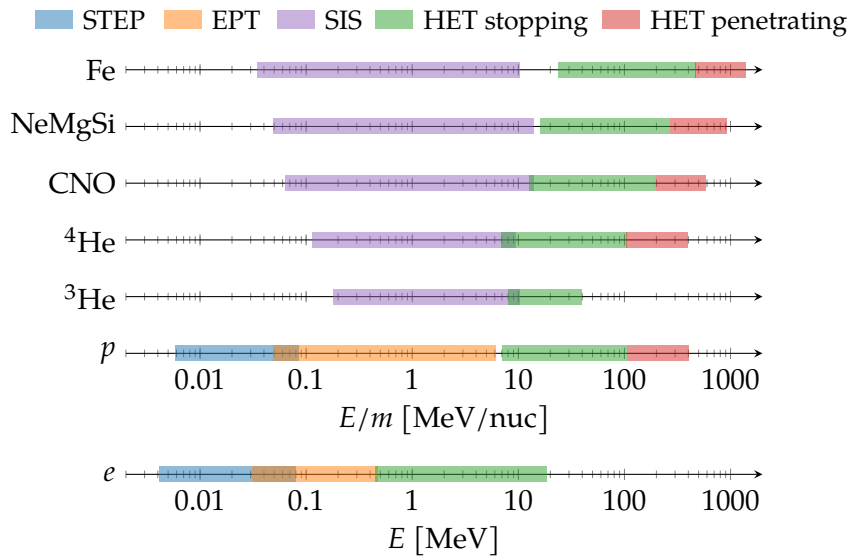
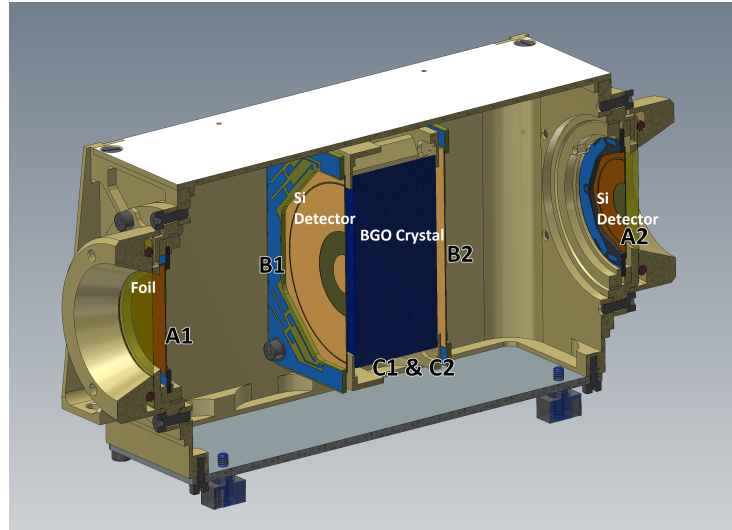
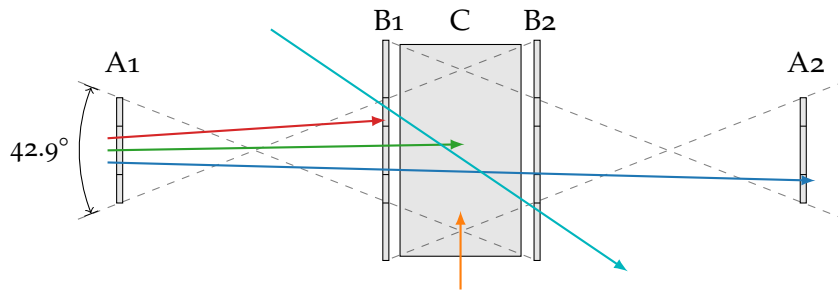


Figure 7: Energy coverage of the different sensors in the SolO EPD suite for electrons and different ion species, based on the current science data products as of October 2020. This is an updated and enhanced version of Figure 3 from Rodríguez-Pacheco et al. (2020). In the case of the CNO and NeMgSi groups, the responses for carbon and neon were taken as an example, the other species differ only slightly. For simplicity, SIS protons, EPT stopping helium as well as EPT penetrating data products, which overlap with other measurements, are excluded from this plot. For the penetrating data products of HET, the highest energy bin (as given by Elftmann, 2020, Appendix A) is not included, as its coverage extends to infinity.

to RAD, though there is no second plastic scintillator for the detection of neutral particles.



(a) CAD rendering of the HET sensor head. Adapted from Rodríguez-Pacheco et al. (2020), Fig. 31.



(b) Schematic diagram of the HET sensor head. Exemplary particle trajectories ending up in different data products are shown by the arrows: stopping in B, stopping in C, penetrating, GCR channel, C single counter.

Figure 8: HET sensor head

Charged particles that enter through one of the A detectors and then stop in B or C are measured in the HET data products for stopping particles, which are defined using the ABnC and ABC coincidence conditions (as shown in red and green in Figure 8b). These particles are fully analyzed using the $dE/dx-E$ method, i.e. their primary energy and charge can be directly determined. Ions with higher energies (e.g. ≥ 100 MeV/nuc for protons and helium) penetrate the whole telescope (ABCBA coincidence, shown in blue in Figure 8b). In this case, as with the penetrating particles in RAD, the particles are not fully analyzed. Still, up to a few hundred MeV/nuc, the particle direction and primary energy can be estimated based on the different LET at each end of the telescope (e.g. in the A1 and A2 detectors).

Similarly to RAD, these energy-resolved stopping and penetrating particle data products are very useful for SEP events as well as to calculate longterm GCR spectra, but they do not have high enough count rates to study short-term variations

of the **GCR**. Alternatively, **HET** also produces a data product using the BCB coincidence (irrespective of the A detectors, shown in turquoise in **Figure 8b**), which significantly increases the opening angle at the cost of lower energy resolution and no separation of particle species. For this data product, only a 1D histogram of the energy deposit in C is stored. In addition, basic single detector count rates (level 1 trigger rates) without any coincidence conditions applied are available in **HET**'s housekeeping data, which include particles entering **HET** from any direction. In this case, the count rates for the C detector are best suited for measuring short-term variations due to the large volume of C. The response function of this single detector counter is derived in **Appendix A**.

Further details about the design of the **HET** instrument, the definition of its data products and their calibration can be found in Elftmann (2020).

2.3 NEUTRON MONITOR MEASUREMENTS

First developed in the 1950s (see e.g. Simpson, 2000), ground-based neutron monitors have historically been the most widely available instrument for the measurement of the cosmic ray flux at Earth. Neutron monitors measure secondary neutrons generated by the primary **GCR** and **SEP** particles in the Earth's atmosphere. They are typically large and heavy instruments, as one or more large tubes of lead are needed to achieve a sufficiently large detection efficiency for high-energy neutrons. Within a decade, such devices had been deployed at numerous locations around the globe, and many of them have been producing measurements almost continuously until the present day. Today, data from the global network of more than 50 neutron monitors (e.g. Moraal et al., 2000) are archived at the Neutron Monitor Database (**NMDB**, Steigies, 2009)¹, and many of these stations are also providing realtime data through **NMDB**.

Similar to **RAD** on Mars (**Section 2.1**), neutron monitor measurements are influenced by the Earth's atmosphere, but also by the magnetic field, which is negligible at Mars. Thus, any cosmic ray particle needs a certain minimum energy, the so-called cutoff energy, to be able to pass through the magnetosphere and produce a secondary neutron in the atmosphere, which then reaches the ground and can be detected by a neutron monitor. The atmospheric effect is mainly dependent on the altitude as well as the atmospheric pressure, while the magnetospheric effect depends on the geographic location, particularly the latitude. At the poles, where the magnetic field lines are nearly vertical, the magnetic cutoff decreases to zero, and thus the atmospheric effect is dominant in this case.

The cutoff energy is often also expressed in terms of a rigidity

$$R = \frac{pc}{q}, \quad (3)$$

a quantity which is given in units of volts (V). p is the particle's momentum, q its charge and c the speed of light. The benefit of using rigidities instead of (kinetic) energies is that particles with the same rigidity also have the same gyroradius in the magnetic field independent of the particle species. Using relativistic relations,

¹ <https://www.nmdb.eu>

R can be rewritten in terms of the particle's charge $q = Ze$, rest mass m_0 and kinetic energy E_{kin} as:

$$R = \frac{1}{Ze} \sqrt{E_{\text{kin}}(E_{\text{kin}} + 2m_0c^2)} \quad (4)$$

(see e.g. Moraal, 2013, for the detailed derivation), which approaches $R \approx E_{\text{kin}}/(Ze)$ for highly relativistic particles ($E_{\text{kin}} \gg m_0c^2$). So, for example, a 100 GeV proton ($Z = 1$) has a rigidity of approximately 100 GV.

Magnetic cutoff rigidities and the resulting response functions for neutron monitors, which take both the magnetospheric and the atmospheric effect into account, have been calculated by e.g. Clem and Dorman (2000), Shea and Smart (2001), and Smart and Shea (2008). The South Pole Neutron Monitor, located at the geographic south pole (90° S) and 2820 m altitude — next to the Amundsen-Scott research station — is the most sensitive neutron monitor station, as its magnetic cutoff is negligible and the atmospheric cutoff is also lower than at sea level. This makes it especially well suited for the detection of FDs, as they typically have larger amplitudes at lower energies (see Section 1.4). The South Pole Neutron Monitor will be used multiple times in this thesis to provide FD observations at Earth that can be compared to the Mars or SolO data.

In addition to using single neutron monitors, an inversion method has also been developed to reconstruct the variation of the GCR flux at a certain rigidity above the atmosphere and magnetosphere from the global network of neutron monitors. This so-called Global Survey Method (GSM) produces results that are independent of the characteristics of a single neutron monitor station. It is described in detail by Belov et al. (2018), and is used e.g. as a basis for the extensive catalog of Forbush decreases at Earth compiled by the Russian Space Weather Prediction Center (IZMIRAN)², which is also employed in this thesis for statistical studies in the publication by Freiherr von Forstner et al. (2020).

2.4 THE STEREO HELIOSPHERIC IMAGERS

Launched in 2006, the Solar Terrestrial Relations Observatory (STEREO, Russell, 2008) is a NASA mission that enabled a stereoscopic view of the Sun for the first time. It consists of two largely identical spacecraft that were placed in an orbit around the Sun at distances close to 1 AU, carrying both in situ and remote sensing instruments. The STEREO-A (Ahead) spacecraft is placed a bit closer to the Sun than Earth, while STEREO-B (Behind) is a bit farther away. This caused the two spacecraft to slowly drift away from Earth, as A orbits the Sun slightly faster than Earth, and B slightly slower. 5 years later, the spacecraft were separated by 180° in longitude, and this made it possible to observe all sides of the Sun (except the poles) simultaneously for the first time. In 2015, the two spacecraft reached a solar conjunction, passing behind the Sun as seen from Earth, and are coming closer to Earth again ever since. Their next close approach to Earth is expected in 2023, 17 years after launch.

With a planned mission duration of only 2 years, the STEREO spacecraft were never designed to survive a solar conjunction, during which communication with

² <http://spaceweather.izmiran.ru/eng/dbs.html>

Earth is not possible for several months, so significant configuration changes were necessary in the flight software. Unfortunately, while testing the new configuration designed for the solar conjunction phase, communications with the **STEREO-B** spacecraft were lost on October 1, 2014, so since this date, science data are only available from **STEREO-A**. It is believed that this was due to a temporary failure of the star tracker coinciding with incorrect data transmitted from one of the gyroscopes, causing the spacecraft to start spinning while it fired its thrusters in an attempt to compensate for the perceived rotation (Ossing et al., 2018). In this state, the spacecraft battery drained quickly as the solar panels were pointed toward the Sun only for a fraction of the time. The communications link to the spacecraft was restored for a few weeks in 2016, but the following attempt to re-stabilize the spacecraft was unsuccessful and connection was lost again. Recovery will be re-attempted when **STEREO-B** comes closer to Earth in the next few years.

Apart from three in situ experiments investigating the local solar wind plasma, energetic particles, magnetic fields and radio waves, the scientific payload onboard the **STEREO** spacecraft also includes the Sun Earth Connection Coronal and Heliospheric Investigation (**SECCHI**, Howard et al., 2008), a suite of remote sensing instruments consisting of five telescopes (Table 1) with different fields of view (from the solar disk to almost 90°) and wavelengths (extreme ultraviolet (**EUV**) and visible light, “white light”). The **EUV** imager (**EUVI**) observes the solar disk directly in four different wavelength bands, while the white-light coronagraphs **COR1** and **COR2** use an occulting disk in their center to cover the solar disk and observe the surrounding corona. Similar types of instruments have already been available from the Earth point of view, e.g. on the Solar and Heliospheric Observatory (**SOHO**) spacecraft launched in the 1990s and its predecessors. On the other hand, the heliospheric imagers (**HI**, Eyles et al., 2009) are a relatively new type of instrument that had first been demonstrated in 2003 with the Solar Mass Ejection Imager (**SMEI**, Eyles et al., 2003) onboard the *Coriolis* spacecraft. These white-light telescopes provide a very wide field of view between 4° and 88.7° from the Sun in the ecliptic plane and up to $\pm 35^\circ$ in the perpendicular direction. With these data, coronal mass ejections (**CMEs**) can be directly tracked from near the Sun out into interplanetary space. In contrast to the other telescopes, the **HI**s have rectangular fields of view directed away from the Sun towards one side — therefore, the **STEREO** spacecraft are always rotated so that the **HI**s can best observe the Sun-Earth line.

Telescope	Description	Wavelength	Field of view
EUVI	EUV imager	171 Å, 195 Å, 284 Å, 304 Å	$0 R_\odot$ to $1.7 R_\odot$
COR1	inner coronagraph	white light	$1.4 R_\odot$ to $4 R_\odot$
COR2	outer coronagraph	white light	$2.5 R_\odot$ to $15 R_\odot$
HI1	heliospheric imager 1	white light	4° to 24°
HI2	heliospheric imager 2	white light	18.7° to 88.7°

Table 1: Properties of the **STEREO SECCHI** telescopes.

Figure 9 demonstrates the different fields of view of the SECCHI instruments. This composite image, which was constructed using the SunPy software toolkit (The SunPy Community et al., 2020), shows the April 15, 2020 CME (see also Chapter 6 / Freiherr von Forstner et al., 2021), which has just entered the HI1 field of view at this time. In addition, signatures of four solar system planets (Venus, Earth, Jupiter and Saturn) can be seen in the HIs telescopes, as well as the diagonal band of the Milky Way in HI2. The near-vertical trails in the HI images are an instrumental artifact caused by the high relative brightness of the planets and some stars in combination with the column-wise sensor readout and the lack of a mechanical shutter.

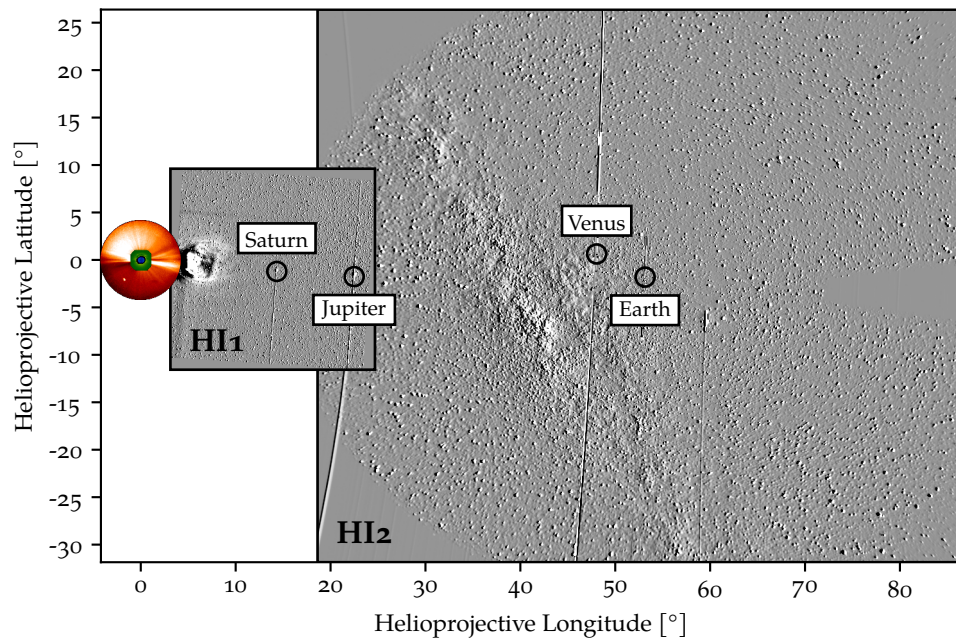


Figure 9: Composite image demonstrating the fields of view of the STEREO SECCHI telescopes EUVI, COR1, COR2 (blue, green and red areas on the left side), and HI1 and HI2. HI images are shown as running difference images, while COR and EUVI are direct images. This image features the April 15, 2020 CME, some planets as well as the Milky Way (diagonal band across the HI2 image).

CMEs appear in the HI telescopes due to Thomson scattering: Sunlight is scattered by free electrons in the solar wind plasma, and regions of enhanced density, such as CMEs and the shocks driven by them, appear as brighter structures in the images. To make these transients more clearly visible, long exposure times on the order of 20 minutes to 1 hour are needed, and difference images are often used to further highlight the moving structures. In theory, the 88.7° field of view would allow the HIs to track CMEs all the way out to Earth under most conditions. However, in practice, the CME structures become more faint during the propagation as their density and velocity decreases. Also, CMEs not directed towards Earth are not always covered by HI, as these may also occur on the opposite side of the Sun (e.g. the left side of Figure 9).

To routinely reconstruct the trajectories of CMEs in the HI observations, the 2D images are typically transformed into so-called J-maps, a technique which was originally developed by Sheeley et al. (1999) and first applied to STEREO-HI data by Rouillard et al. (2008) and Davies et al. (2009): After subtraction of backgrounds and the calculation of running difference images, a 1D slice is extracted from each HI image in the time period of interest, usually close to the ecliptic plane. For each consecutive point in time, these slices are then rotated by 90° and concatenated into a new 2D plot, where time is on the x axis and the heliographic longitude, which in this case is named the *elongation angle* ϵ , is on the y axis. Moving structures, such as CME or shock fronts, then appear as bright streaks in the J-map, which extend from the bottom (low elongation) out to larger elongations (see Figure 10c for an example). Depending on the CME direction and the evolution of its velocity, these structures can often resemble a (rotated) letter J, hence the corresponding naming of this type of plot. This is not the case in the example in Figure 10c, as this slow CME propagates at a nearly constant speed and produces a more or less straight line in the J-map. By tracing the structures in the J-map images, the time-elongation profile $\epsilon(t)$ can then easily be reconstructed.

The more challenging part is to use this measurement to calculate the actual CME trajectory, i.e. the time profile of the radial distance $r(t)$ from the Sun. To solve this problem unambiguously, some assumptions need to be made, as the Thomson-scattered HI image accumulates the electron density along the line of sight, which contains points at different heliospheric longitudes and radial distances. This means that the geometric shape of the CME needs to be known to derive the position of the apex from the images. Multiple techniques have been developed to address this issue in different ways, starting with single-spacecraft approaches that also need to make assumptions about the CME longitude (Howard et al., 2006; Kahler and Webb, 2007; Lugaz et al., 2009; Davies et al., 2012), followed by approaches that take into account the measurements from both STEREO spacecraft at the same time to triangulate the CME location (Liu et al., 2010a,b; Lugaz et al., 2010; Davies et al., 2013). Of course, the latter can only be used for events observed by both spacecraft simultaneously, before the loss of connection to STEREO-B in 2014. A detailed overview of these reconstruction methods and the corresponding mathematical expressions was given in Section 3.3.2 of Freiherr von Forstner (2018). The single-spacecraft reconstruction methods are also summarized in Section 2.3 and Figure 2 of Freiherr von Forstner et al. (2019), which is reprinted in Chapter 3 of this thesis.

The Heliospheric Cataloguing, Analysis and Techniques Service (HELCASTS)³ has systematically cataloged and analyzed all CMEs detected by the STEREO-HI telescopes and provides these data on their website. This database will serve as the basis for most HI-related studies in this thesis. As an example, the images and J-map provided by HELCASTS for the April 15, 2020 CME observed by STEREO-A are shown in Figure 10. The corresponding data and reconstruction results can be found under the ID HCME_A__20200415_01 in the HELCASTS catalogs.

³ <https://www.helcats-fp7.eu/>

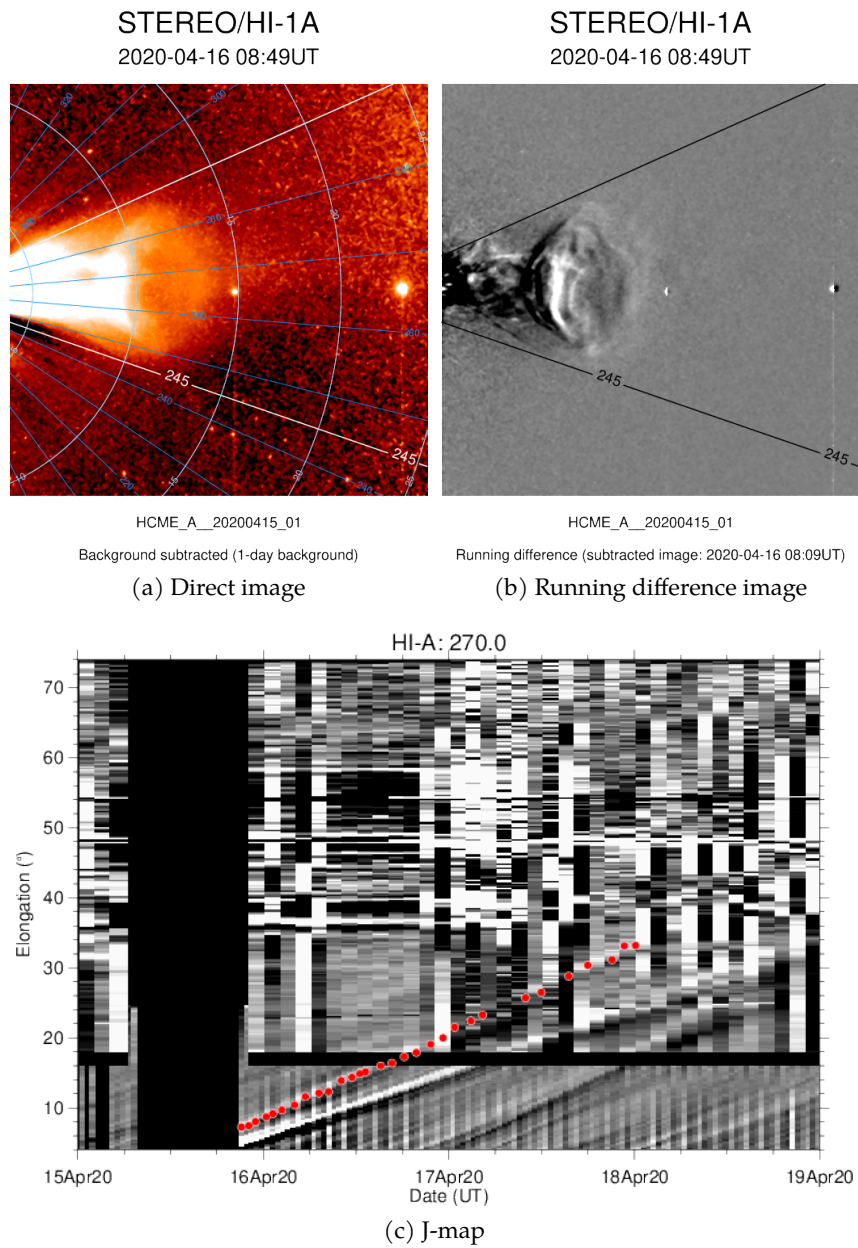


Figure 10: STEREO-A HI images of the April 15, 2020 CME generated by the HELCATS project. In the J-map, the CME trajectory was marked with red dots.

STUDIES OF ICME ARRIVAL TIMES AT 1 AU AND MARS USING FORBUSH DECREASES

3.1 OPPOSITION PHASES

An interesting constellation to study the propagation of interplanetary coronal mass ejections (ICMEs) is the so-called opposition, where two planets (or spacecraft) are closely aligned in heliospheric longitude. Near these oppositions, CMEs that are seen in situ at one of these locations are most likely to be seen at the other as well, which allows to investigate their radial evolution.

Some previous studies, such as the model proposed by Gopalswamy et al. (2001) — a predecessor of the drag-based model (DBM, see Section 1.3) — have stated that the deceleration of fast coronal mass ejections (CMEs) due to their interaction with the slower ambient solar wind ceases before 1 AU, e.g. at distances between 0.75 AU and 0.85 AU. Winslow et al. (2015) have validated this hypothesis using measurements at Mercury and Wang et al. (2005) have shown measurements from the *Ulysses* spacecraft, mostly far beyond 1 AU, that show no significant deceleration. However, observations at Mars, which is located at a heliocentric distance of ~ 1.5 AU have not been included in such investigations so far.

In the case of Earth and Mars, whose orbital periods are 365 and 687 days, respectively, an opposition occurs approximately every 2.1 years. Since the *Curiosity* rover's landing on Mars in August 2012, there were four such oppositions: In April 2014, May 2016, July 2018, and October 2020. The following study will present the first statistical study of ICMEs and the associated Forbush decreases (FDs) during the first two of these opposition periods, and during oppositions of Mars with one of the two Solar Terrestrial Relations Observatory (STEREO) spacecraft in 2012 and 2013. The FDs were detected at the two locations using the Mars Science Laboratory Radiation Assessment Detector (MSLs/RADs, Section 2.1), the South Pole neutron monitor at Earth (Section 2.3) and the STEREO High Energy Telescope (HET). These datasets were then used to derive the ICME propagation time between 1 AU and Mars. In the study, we compare the derived transit speed between 1 AU and Mars to the in situ measured velocity at 1 AU as well as the launch speed at the Sun to show that fast ICMEs still decelerate beyond 1 AU. Comparisons with the WSA-ENLIL+Cone and DBM models are also performed to investigate their accuracy for predicting ICME arrival times at Mars.

The following article is reproduced from Freiherr von Forstner et al. (2018) with permission from Journal of Geophysical Research: Space Physics, ©American Geophysical Union:

USING FORBUSH DECREASES TO DERIVE THE TRANSIT TIME OF ICMEs PROPAGATING FROM 1 AU TO MARS

Freiherr von Forstner, J. L., J. Guo, R. F. Wimmer-Schweingruber, D. M. Hassler, M.

Temmer, M. Dumbović, L. K. Jian, J. K. Appel, J. Čalogović, B. Ehresmann, B. Heber, H. Lohf, A. Posner, C. T. Steigies, B. Vršnak, and C. J. Zeitlin, *Journal of Geophysical Research: Space Physics*, 123, 1, pages 39–56 (2018), DOI: [10.1002/2017JA024700](https://doi.org/10.1002/2017JA024700)

Own contribution: 90%

RESEARCH ARTICLE

10.1002/2017JA024700

Key Points:

- The interplanetary propagation of 15 CMEs is studied based on a cross-correlation analysis of Forbush decreases at 1 AU and Mars
- The speed evolutions of the ICMEs are derived from observations, indicating that most of them are slightly decelerated even beyond 1 AU
- Model-predicted ICME arrival times at Mars could be improved by using ICME parameters measured at 1 AU

Correspondence to:

J. Guo,
guo@physik.uni-kiel.de

Citation:

Freiherr von Forstner, J. L., Guo, J., Wimmer-Schweingruber, R. F., Hassler, D. M., Temmer, M., Dumbović, M., ... Zeitlin, C. J. (2018). Using Forbush decreases to derive the transit time of ICMEs propagating from 1 AU to Mars. *Journal of Geophysical Research: Space Physics*, 123, 39–56. <https://doi.org/10.1002/2017JA024700>

Received 23 AUG 2017

Accepted 18 DEC 2017

Accepted article online 3 JAN 2018

Published online 18 JAN 2018

Using Forbush Decreases to Derive the Transit Time of ICMEs Propagating from 1 AU to Mars

Johan L. Freiherr von Forstner¹ , Jingnan Guo¹ , Robert F. Wimmer-Schweingruber¹, Donald M. Hassler^{2,3}, Manuela Temmer⁴ , Mateja Dumbović⁴, Lan K. Jian^{5,6} , Jan K. Appel¹ , Jaša Čalogović⁷, Bent Ehresmann², Bernd Heber¹ , Henning Lohf¹, Arik Posner⁸, Christian T. Steigies¹, Bojan Vršnak⁷, and Cary J. Zeitlin⁹

¹Institute of Experimental and Applied Physics, University of Kiel, Kiel, Germany, ²Southwest Research Institute, Boulder, CO, USA, ³Institut d'Astrophysique Spatiale, University Paris Sud, Orsay, France, ⁴Institute of Physics, University of Graz, Graz, Austria, ⁵Department of Astronomy, University of Maryland, College Park, MD, USA, ⁶Heliophysics Science Division, NASA Goddard Space Flight Center, Greenbelt, MD, USA, ⁷Hvar Observatory, Faculty of Geodesy, University of Zagreb, Zagreb, Croatia, ⁸NASA Headquarters, Washington, DC, USA, ⁹Leidos, Houston, TX, USA

Abstract The propagation of 15 interplanetary coronal mass ejections (ICMEs) from Earth's orbit (1 AU) to Mars (~1.5 AU) has been studied with their propagation speed estimated from both measurements and simulations. The enhancement of magnetic fields related to ICMEs and their shock fronts causes the so-called Forbush decrease, which can be detected as a reduction of galactic cosmic rays measured on ground. We have used galactic cosmic ray (GCR) data from in situ measurements at Earth, from both STEREO A and STEREO B as well as GCR measurements by the Radiation Assessment Detector (RAD) instrument on board Mars Science Laboratory on the surface of Mars. A set of ICME events has been selected during the periods when Earth (or STEREO A or STEREO B) and Mars locations were nearly aligned on the same side of the Sun in the ecliptic plane (so-called opposition phase). Such lineups allow us to estimate the ICMEs' transit times between 1 and 1.5 AU by estimating the delay time of the corresponding Forbush decreases measured at each location. We investigate the evolution of their propagation speeds before and after passing Earth's orbit and find that the deceleration of ICMEs due to their interaction with the ambient solar wind may continue beyond 1 AU. We also find a substantial variance of the speed evolution among different events revealing the dynamic and diverse nature of eruptive solar events. Furthermore, the results are compared to simulation data obtained from two CME propagation models, namely the Drag-Based Model and ENLIL plus cone model.

Plain Language Summary Eruptions from the Sun often containing a shock front followed by a magnetic ejecta may cause a depression in the omnipresent cosmic rays that can now be observed at Mars thanks to the radiation assessment detector (RAD) on board the Mars Science Laboratory. When both Earth (or other spacecraft like STEREOs that are located at Earth orbit) and Mars are closely aligned on the same side of the Sun, we have a great opportunity to observe such eruptions passing by and affecting both planets. Based on measurements from both Earth orbit and Mars, we have studied 15 solar events and their properties such as the speed and its evolution from the Sun to Mars. We found that most of these eruptions slow down considerably during their propagation from the Sun to Earth orbit and even beyond all the way to Mars.

1. Introduction

It is currently well accepted that coronal mass ejections (CMEs), magnetized plasma clouds expelled from the Sun, may have severe impact on Earth, robotic missions on other planets, and spacecraft electronics. A better understanding of the interplanetary propagation of CMEs is very important to gain a deeper understanding of the heliosphere and the Sun itself, and to improve space weather forecasting.

ICMEs are regularly observed using both remote sensing images (coronagraph and heliospheric imaging instruments) and in situ measurements of plasma and magnetic field quantities (e.g., Richardson & Cane, 1995; Wimmer-Schweingruber et al., 2006). Another common in situ method to detect ICMEs employs the

observation of Forbush decreases (FD, first observed by Forbush, 1937; Hess & Demmelair, 1937 and also studied by, e.g. Burlaga et al., 1985; Cane, 2000; Kumar & Badruddin, 2014; Lockwood, 1971; Zhao & Zhang, 2016) in measurements of galactic cosmic rays (GCRs) caused by the magnetic field structure embedded in the ICME passing by.

ICMEs do not necessarily consist only of the magnetized ejecta (which, depending on its geometry, can also be called “magnetic cloud” or “flux rope”), but in many cases also drive an interplanetary shock in front of them, separated by a turbulent sheath region. Forbush decreases can occur during the passage of the sheath region (after the shock arrival) as well as the ejecta, which is described to be the cause of a two-step structure, for example, by Cane (2000). However, recent studies such as Jordan et al. (2011) and Masias-Meza et al. (2016) have found that even though the ejecta is effective at decreasing the GCR intensity, an ICME with a shock does not necessarily produce a clear two-step structure in the FD and that the shock arrival is much more likely to produce an abrupt drop in the GCR intensity than the ejecta. When multiple CMEs are ejected from the Sun in a short period of time, they can interact with each other during their propagation and form complex structures, which also affects the corresponding Forbush decrease (e.g., Maričić et al., 2014).

The interplanetary propagation of ICMEs is strongly influenced by the ambient solar wind. This leads to either a deceleration or acceleration depending on the relative speed of the ICME to the ambient solar wind speed (e.g., Gopalswamy et al., 2001; Vršnak et al., 2004; Vršnak & Žic, 2007). As most CMEs launched from the Sun are faster than the ambient solar wind, this more often results in deceleration rather than acceleration. With a large amount of imaging and in situ instruments available on spacecraft especially near Earth’s orbit, extensive studies of the evolution of CMEs during their eruption at the Sun and their propagation up to 1 AU have been carried out. Heliospheric imaging instruments, for example, on board the two *Solar Terrestrial Relations Observatory* (STEREO) spacecraft allow a continuous tracking of ICMEs up to 1 AU (e.g., Lugaz et al., 2012; Möstl et al., 2014; Wood et al., 2017). Additionally, spacecraft such as *Ulysses* (e.g., Jian et al., 2008; Wang et al., 2005) and *Voyager* (e.g., Liu et al., 2014) have provided ICME observations at locations in the outer solar system. Based on the results from Wang et al. (2005) and their own studies of ICMEs seen at Mercury and Earth, Winslow et al. (2015) stated that the deceleration of most ICMEs should cease at approximately 1 AU.

With the *Curiosity* rover of NASA’s *Mars Science Laboratory* (MSL) mission (Grotzinger et al., 2012), another device capable of registering Forbush decreases is available on the surface of Mars (at approximately 1.5 AU) since its landing on 6 August 2012. Its *Radiation Assessment Detector* (RAD) instrument (Hassler et al., 2012) has been continuously measuring GCR particles on the surface of Mars since then. MSL/RAD was already used for observations of ICMEs through Forbush decreases, for example, by Witasse et al. (2017).

In situ observations of ICMEs at Mars are also possible using instruments on the *Mars Atmosphere and Volatile Evolution* (MAVEN) spacecraft that is in orbit around Mars. But it only arrived at Mars in September 2014, so a time period of 2 years after MSL’s arrival cannot be studied using MAVEN data. For this reason, we have not yet incorporated MAVEN data in this study, but we plan to do so in the future as the number of ICMEs observed by MAVEN increases. A first study involving a comparison of ICME measurements at MAVEN and MSL/RAD can be found in Guo, Lillis, et al. (2017).

At times where Mars and either Earth or the STEREO A or STEREO B spacecraft have a low separation in their heliospheric longitudes, that is, they nearly form a straight line with the Sun, we have a better chance of observing the same ICMEs at both 1 AU and Mars using in situ data. These times are the oppositions of Mars observed from Earth and the STEREO spacecraft, respectively. We define an *opposition phase* to be the period where the absolute value of the longitudinal separation $\Delta\varphi$ between Mars and Earth (or STEREO) is smaller than a fixed value $\Delta\varphi_{\max}$, which for this study is set to 30° , keeping the probability that ICMEs are observed at both locations reasonably high, but at the same time not restricting the number of ICME candidates too much. The latitudinal separations between Earth, the STEREO spacecraft, and Mars are generally only a few degrees at most and therefore not taken into account. Yashiro et al. (2004) found that the average angular width of CMEs is between 47° and 61° , which supports that choosing $\Delta\varphi_{\max} = 30^\circ$ is reasonable. Figure 1 illustrates the opposition phases and the definition of $\Delta\varphi_{\max}$.

These multispacecraft observations of ICMEs during the opposition phases allow us to determine ICMEs’ traveltimes between the radial distances of 1 AU and ~ 1.5 AU from the Sun. They can be used to compare the resulting transit speed with measurements at 1 AU to determine the amount of deceleration or acceleration.

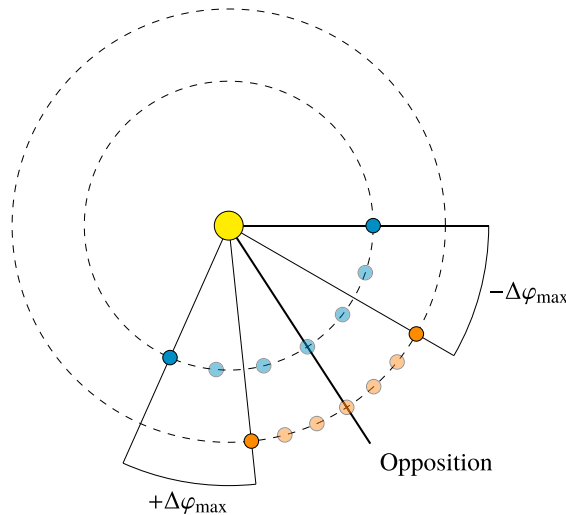


Figure 1. The opposition phases for this study are defined by the longitudinal separation of Earth (or STEREO) and Mars being between $-\Delta\phi_{\max}$ and $+\Delta\phi_{\max}$. The bold diagonal line marks the opposition itself.

To be able to derive the propagation time of an ICME between the two observation locations, we assume that the same part of the ICME is observed at both places, or alternatively that the ICME's shape has a sufficient amount of radial symmetry between the two longitudes where it is observed. The probability that this assumption holds true is obviously higher for smaller longitudinal separations of the two observers, which is another reason why we chose a small angle for $\Delta\phi_{\max}$. A sophisticated study of the ICMEs' shapes could only in theory be done with a significantly higher number of observation locations or using 3-D reconstruction techniques based on stereoscopic imaging techniques, where the former drastically reduces the amount of ICME candidates and the latter can currently only be done up to approximately 1 AU, for example, with the heliospheric imagers at both STEREO spacecraft (e.g., Liu et al., 2010).

2. Methods and Data

2.1. Data

Table 1 shows the opposition periods between CURIOSITY's landing in August 2012 and the end of 2016, as defined in Figure 1. Oppositions of Earth and Mars are included as well as those with the STEREO spacecraft.

We used the ICME list by Richardson and Cane (2010) (<http://www.srl.caltech.edu/ACE/ASC/DATA/level3/icmetable2.htm>) as a basis for finding the ICME-caused Forbush decreases at Earth and a similar list by Jian et al. (2013) for ICMEs at STEREO A and STEREO B.

Communication with the STEREO B spacecraft was lost on 1 October 2014 and a recovery attempt in summer 2016 was not successful. Therefore, data from its 2015 opposition with Mars are not available. Additionally, because of the solar conjunction in 2015, the Plasma and Suprathermal Ion Composition (PLASTIC) instrument on board STEREO A was turned off and there is no plasma data for the second STEREO A and Mars opposition phase. For these reasons, we excluded the two 2015 opposition phases, leaving us with the four opposition periods to investigate in this study.

For the two oppositions of Earth and Mars, we retrieved count rate data from the Neutron Monitor Database (<http://nmdb.eu>). We chose the South Pole neutron monitor, which has a low cutoff rigidity (with an effective vertical cutoff rigidity of 0.1 GV) due to its geographic location. This was then used together with the RAD dose rate data to apply the cross-correlation method, which will be described in section 2.3.

For the STEREO oppositions, we replaced the neutron monitor count rates with measurements from the High Energy Telescope (HET) instruments available on both STEREO spacecraft (von Rosenvinge et al., 2008), which measure the flux of high-energy charged particles. While in situ observations of ICMEs at the STEREO spacecraft are also possible using magnetometer and plasma data (as has been used to identify ICMEs in the lists employed in our study), Forbush decreases in the HET data allow for a more direct comparison to the RAD data at Mars.

The publicly available HET data include measurements of protons with kinetic energies between 13.6 and 100 MeV and electrons between 0.7 and 4.0 MeV, with each of these ranges subdivided into multiple

Table 1
Opposition Periods Considered for This Study

Opposition type	Date		
	Start	Opposition	End
STEREO B and Mars	2012-8-22	2012-11-28	2013-2-5
STEREO A and Mars	2013-5-21	2013-7-19	2013-9-12
Earth and Mars	2014-2-13	2014-4-8	2014-6-10
Earth and Mars	2016-3-20	2016-5-22	2016-8-5

Note. The start and end dates of the $\pm 30^\circ$ periods and the actual date of the opposition are given. Dates are formatted as year/month/day.

energy bins. We chose the 23.8 and 100 MeV proton range, which appeared to show the Forbush decreases reasonably well for this study. In some cases (event numbers 1, 2, 4, 5, 7, and 9), we chose to only use the highest-energy channel (60 and 100 MeV) instead because there were solar energetic particles (SEP) coinciding with the ICME arrival at STEREO, resulting in a much higher particle flux instead of FDs in the lower HET channels.

2.2. RAD Data and Compensating for the Diurnal Variations

RAD/MSL is an energetic particle detector, and it has been carrying out radiation measurements on the surface of Mars since the landing of MSL in August 2012 (Ehresmann et al., 2014; Guo et al., 2015; Guo, Slaba, et al., 2017; Hassler et al., 2014; Köhler et al., 2014; Rafkin et al., 2014; Wimmer-Schweingruber et al., 2015). On the surface of Mars, RAD measures a mix of primary GCRs or SEPs and secondary particles generated in the atmosphere including both charged and neutral particles. Due to the shielding of the atmosphere, such particles are mostly equivalent to primary GCR/SEP with energies larger than ~ 100 MeV/nuc. The radiation dose rates contributed by surface particles are measured in two detectors—a silicon detector and a plastic scintillator—and the latter has better statistics due to a larger geometric factor and is a very good proxy for studying GCR fluence and its temporal variations.

RAD's GCR dose rate measurements on the surface of Mars show a considerable amount of periodic variation (about $\pm 5\%$) with a frequency of 1 sol and its harmonics, which is caused by the variation of temperature and therefore atmospheric pressure during the course of the Martian day. This effect was analyzed by Rafkin et al. (2014), and its intensity varies for different fluxes of primary and secondary GCR particles.

Guo, Slaba, et al. (2017) found that the magnitude of this diurnal effect is not constant but rather influenced by the solar modulation of the primary GCRs; direct subtracting of the pressure effect during an FD event is therefore not feasible. To reliably detect Forbush decreases in this data, we process the data using a notch filter (Parks & Burrus, 1987) that significantly reduces the diurnal variations in the data but keeps other influences—such as Forbush decreases—intact. A more detailed description of the implementation of this method is shown in Guo, Lillis, et al. (2017).

2.3. Cross-Correlation Analysis

We assume that the traveltime of the ICMEs between 1 AU and Mars corresponds to the delay time between the onset of Forbush decreases detected at these two locations. To determine this delay, we use a method based on the cross-correlation function (CCF), assuming that Forbush decreases at 1 AU and Mars from the same ICME should have similar characteristics, such as being a one- or two-step decrease. An advantage of this method is that it allows to determine the traveltime without needing to define exact onset times at both Earth and Mars, which can be difficult when the Forbush decrease is weak and/or rather complex.

For the analysis, a ± 1 sol window (a sol is a solar day on Mars, 1 sol ≈ 24 h 40 m) around the given ICME onset time at 1 AU $t_{1\text{ AU}}$ is selected from the GCR data at 1 AU, which includes a Forbush decrease at this time. The rather small window makes sure that we only compare the actual decrease, so that a difference in the following recovery period should not affect the results. The normalized cross-correlation function of the 1 AU data with the filtered RAD dose rate data (see details in section 2.2) is then calculated in this window. It is a measure for the correlation between the two data sets when one is shifted in time by a lag τ . For discrete measurements $f[m]$ and $g[m]$, the normalized cross-correlation function is defined as

$$(f \star g)[n] \doteq \frac{1}{m_{\max} - m_{\min}} \sum_{m=m_{\min}}^{m_{\max}} f'[m] g'[m+n], \quad (1)$$

where the lag τ is represented by a number of data points n , the range $[m_{\min}, m_{\max}]$ is the aforementioned ± 1 sol window, and the normalized functions f' and g' are defined as

$$\begin{aligned} f'[m] &\doteq \frac{f[m] - \bar{f}}{\sigma_f}, \\ g'[m] &\doteq \frac{g[m] - \bar{g}}{\sigma_g}. \end{aligned} \quad (2)$$

where σ_f and σ_g are standard deviations of $f[m]$ and $g[m]$ in the range $[m_{\min}, m_{\max}]$, respectively.

The value of τ where $(f \star g)$ assumes its maximum in a reasonable range $\tau \in [0, \Delta t_{\max}]$ is considered to be the ICME's traveltime T between 1 AU and Mars. We fit the cross-correlation function's peak with a Gaussian distribution to estimate the error of T .

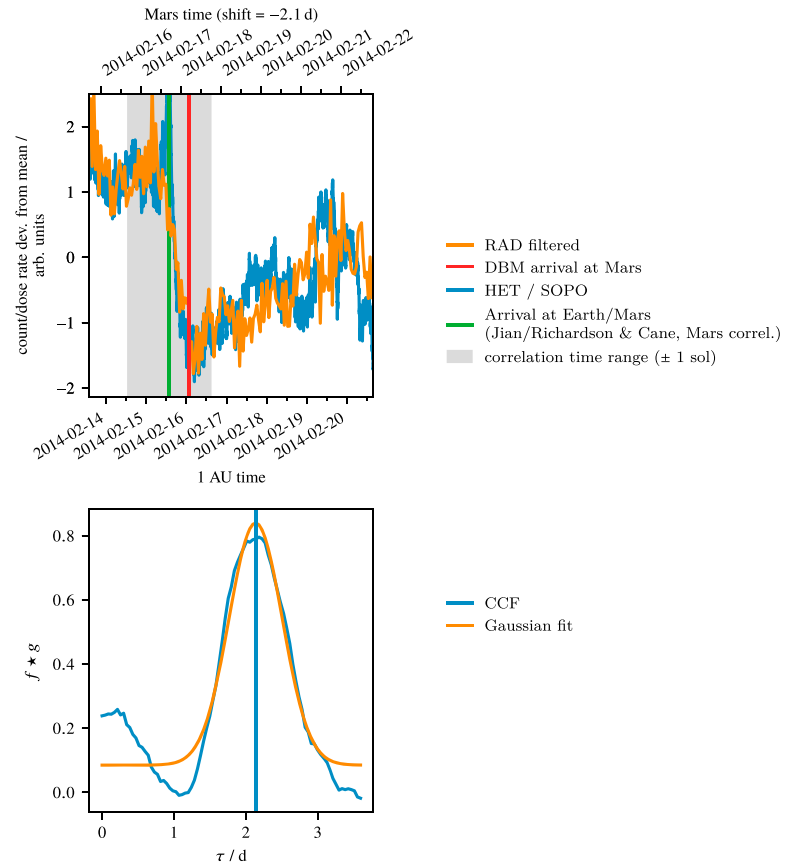


Figure 2. Example of an application of the cross-correlation method. (top) The count rate data from the South Pole neutron monitor with the ICME disturbance time from the Richardson and Cane ICME list marked by the green bar. In the same panel, the RAD dose rate data (filtered using the method described in section 2.2 and shifted back in time by the best fitted CCF lag time) are shown, together with the onset time calculated using the Drag-Based Model (DBM) (red bar). (bottom) The cross-correlation function (CCF) of the two data sets plotted over the time lag τ , fitted with a Gaussian function to obtain the estimated traveltime T and its uncertainty. The window used for calculating the CCF is displayed in Figure 2 (top) with a light gray color. In this example, the resulting ICME traveltime is 2.14 ± 0.37 days, which is slightly shorter than the 2.6 days calculated using the DBM (explained later in section 3.3).

Figure 2 shows an example of an application of the cross-correlation method applied to the ICME that arrived at Earth on 15 February 2014. The implication of these results will be discussed in section 3.1.

The GCR data in Figure 2 is scaled so that the correlation between the two data sets is more clearly shown. Specifically, we subtract the mean value in the shown time range from the measurements and then divide the results by their standard deviations. For some events at the STEREO spacecraft, we adjusted the scaling of the HET flux rate data manually as the calculation of the mean and standard deviation was affected by strong increases in the data related to SEP events shortly before or after the ICME arrival. This was done by calculating the mean and standard deviation in a smaller ± 16 h period around $t_{1 \text{ AU}}$ instead of the whole range of the plot. Additionally, in one case (event 1) we needed to decrease the size of the window in which the correlation is calculated to ± 0.75 sol instead of ± 1 sol to make sure that the SEP event does not influence the result of the cross-correlation analysis.

Note that we are not comparing the magnitude of the Forbush decreases at 1 AU and Mars, which would be an interesting study in the future. However, it needs to be considered that both the neutron monitor

measurements and RAD dose rate are influenced by the atmosphere and/or magnetosphere of two different planets, which makes the comparison more complicated than simply assessing the relative drop ratios in the two data sets.

3. Results and Discussion

3.1. Results

In total, 43 ICMEs were observed during the four opposition periods, according to the Richardson/Cane (Richardson & Cane, 2010) and Jian (Jian et al., 2013) lists. However, not all of them caused visible Forbush decreases in our data sets at 1 AU and/or Mars—probably because (a) FDs can be very weak in comparison to the background oscillations, for example, due to low ICME speeds and/or magnetic field strengths; (b) the ICME missed one of the observation points, for example, due to (1) the angular width of the ICME is not covering the longitudinal separation of 1 AU and Mars observers (up to $\pm 30^\circ$) and/or (2) a significant deviation of the propagation direction; (c) a gap occurring in the data at one of the observation locations; or (d) a strong solar energetic particle (SEP) event seen at STEREO does not allow us to see the FD even when selecting only the highest-energy channels.

Additionally, a considerable amount of ICMEs were ejected from the Sun in quick succession and possibly interacted or merged with each other during their propagation, which makes the cross-correlation analysis very difficult. One example for this is a series of five events in early February 2014 at Earth, where only the first event could be analyzed sufficiently well using the cross-correlation method as its distance to the others was larger and it had the strongest FD.

We therefore only kept the events in the study where the onset time from the list corresponded to a clear FD at 1 AU and where a convincing correspondence to a FD at Mars could be found using the cross-correlation analysis. For the 15 remaining events, we are most confident that the cross-correlation method picked up the Forbush decreases corresponding to the same ICME in the data sets at both locations.

In total, 14 events had no or only weak Forbush decreases at at least one of the observation locations causing a high uncertainty in the cross-correlation method results; 10 events were dropped due to a merging of multiple ICMEs, 3 FDs at STEREO could not be seen due to a coinciding SEP event; and one event could not be analyzed due to a gap in the RAD data. A comparison of the speeds v_{\max} listed in the Richardson and Cane/Jian lists of the full set of 43 events to our selection of 15 events shows that both nearly have the same average value of 476 km s^{-1} and 475 km s^{-1} , respectively, so it seems that we did not select a set of particularly fast ICMEs.

The Richardson/Cane and Jian lists include arrival times for multiple ICME features: The disturbance arrival time (which refers to the arrival of a shock), the ICME plasma arrival time, and the ICME end time. For the ICMEs where the disturbance arrival time was listed, we used it as the basis for the cross-correlation method because as explained in section 1, the shock is most likely to cause the FD. For the remaining events, we used the ICME plasma arrival time.

In fact, the choice of the onset time used at Earth hardly affects our study of the propagation time as it is only used to determine the position of the ± 1 sol window (which is sufficiently large in comparison to the onset time precision) in which the cross-correlation function is calculated. Nevertheless, in a few cases (events 11–13) the onset times were manually corrected “by eye” by amounts of up to a few hours to better reflect the beginning of the Forbush decrease in the in situ data at Earth, which is not necessarily equal to the start of the disturbance or ICME start given in the lists.

Table 2 shows the basic data and the results of the cross-correlation method for all the ICMEs in this study. Figures A1–A5 in Appendix A include the corresponding plots of the in situ data and CCF.

As explained in section 2.3, due to the uncertainties in the data, the CCF was fitted with a Gaussian distribution to both enhance the detection of the maximum and obtain an estimation of the error. This method works reasonably well most of the time, but in some cases (e.g. events 9 and 14), the CCF shows a relatively wide peak, overlaid by one or multiple narrow peaks. Especially in these cases, the error might have been overestimated by the fit, which generally follows the wide peak.

For each ICME, the ratio $\bar{v}/v_{1 \text{ AU}}$ was calculated and shown Table 2, where $v_{1 \text{ AU}}$ is the measured maximum speed of the ICME at 1 AU, obtained from the Richardson/Cane and Jian lists (v_{\max} column—maximum solar wind speed during the passing of the ICME and shock/sheath), which presumably corresponds to the propagation speed of the shock (if present) or the ejecta; and \bar{v} is the average speed of the ICME between 1 AU and

Table 2
Table of All the ICMEs Examined in This Study

ICME	Obs S/C	Observations					Cross-correlation method results			
		$t_{1 \text{ AU}}$ (UTC)	$v_{1 \text{ AU}}$ /km s ⁻¹	Δr /AU	v_{launch} /km s ⁻¹	v_{sw} /km s ⁻¹	T_{correl} /days	$t_{\text{Mars}} = t_{1 \text{ AU}} + T_{\text{correl}}$ (UTC)	\bar{v} /km s ⁻¹	$\frac{\bar{v}}{v_{1 \text{ AU}}}$
1	STB	2012-9-25 16:26	740.0	0.407	1056	389±12	1.24±0.23	2012-9-26 22:13	567±103	0.77±0.14
2	STB	2012-10-17 06:57	365.0	0.369	960	295±5	2.05±0.33	2012-10-19 08:16	311±51	0.85±0.14
3	STB	2012-10-25 19:10	435.0	0.357	380	297±5	2.31±0.66	2012-10-28 02:39	267±76	0.61±0.17
4	STB	2012-11-11 13:36	512.0	0.334	710	333±22	1.33±0.46	2012-11-12 21:27	436±150	0.85±0.29
5	STB	2012-11-19 09:50	505.0	0.326	643	344±6	1.50±0.54	2012-11-20 21:47	377±137	0.75±0.27
6	STB	2012-11-28 03:36	347.0	0.318	440	331±7	1.46±0.27	2012-11-29 14:32	378±71	1.09±0.20
7	STA	2013-5-29 12:20	480.0	0.516	879	398±20	2.53±0.37	2013-6-1 00:57	354±51	0.74±0.11
8	STA	2013-6-27 16:17	397.0	0.551	732	343±20	2.53±0.48	2013-6-30 04:54	377±72	0.95±0.18
9	STA	2013-7-25 06:12	545.0	0.584	1000	325±23	2.57±0.56	2013-7-27 19:50	393±85	0.72±0.16
10	STA	2013-8-10 15:00	453.0	0.603	375	367±15	2.57±0.24	2013-8-13 04:38	407±38	0.90±0.08
11	EARTH	2014-2-15 13:45	450	0.669	620	342±10	2.14±0.37	2014-2-17 17:07	541±93	1.20±0.21
12	EARTH	2014-4-5 19:00	500	0.624	450	419±22	1.84±0.72	2014-4-7 15:10	587±230	1.17±0.46
13	EARTH	2014-4-18 19:00	500	0.609	396	366±30	2.40±0.71	2014-4-21 04:32	440±131	0.88±0.26
14	EARTH	2016-3-20 07:00	430	0.602		432±19	3.00±0.61	2016-3-23 06:55	348±71	0.81±0.16
15	EARTH	2016-8-2 14:00	460	0.418	350	350±18	2.40±0.53	2016-8-4 23:32	302±66	0.66±0.14
Average			475	0.486	642	355±4	2.12±0.13		406±27	0.86±0.06

Note. The second column shows the spacecraft or planet at 1 AU where the ICME was observed (STEREO A, STEREO B, or Earth), and the third column contains the ICME arrival time $t_{1 \text{ AU}}$ at this location according to the Richardson/Cane or Jian list (disturbance start time if available, otherwise ICME start time). The fourth column states the speed $v_{1 \text{ AU}}$, also taken from the Richardson/Cane and Jian lists (v_{max}). Δr is the radial distance between Earth and Mars or the STEREO spacecraft and Mars, respectively, at the time $t_{1 \text{ AU}}$. The next two columns include the CME launch speed v_{launch} used for simulation purposes and the average ambient solar wind speed v_{sw} in 3 days before the ICME arrival at 1 AU. T_{correl} is the estimated traveltime obtained from the cross-correlation method. The arrival time at Mars t_{Mars} was calculated under the assumption that $t_{1 \text{ AU}}$ is correct, and \bar{v} is the average ICME speed between Earth orbit and Mars calculated from T_{correl} and Δr . The final column shows the ratio $\bar{v}/v_{1 \text{ AU}}$. The last row shows the average values (if applicable) for all events together.

Mars calculated from the traveltime obtained from the cross-correlation method and the radial distance Δr between Earth (or the STEREO spacecraft) and Mars:

$$\bar{v} = \frac{\Delta r}{T_{\text{correl}}}. \quad (3)$$

Additionally, if we assume that the acceleration a of the ICME between 1 AU and Mars is constant, we can calculate it from the traveltime T_{correl} and the measured speed at 1 AU using the following considerations: With $v(t) = v_{1 \text{ AU}} + at$, the mean speed \bar{v} (as given in equation (3)) can also be expressed as

$$\bar{v} = \frac{\int_0^{T_{\text{correl}}} v(t) dt}{T_{\text{correl}}} = v_{1 \text{ AU}} + \frac{1}{2} a T_{\text{correl}}.$$

Equating this expression with the one from equation (3) and solving for a give

$$a_{1 \text{ AU}, \text{Mars}} = 2 \left(\frac{\Delta r}{T_{\text{correl}}^2} - \frac{v_{1 \text{ AU}}}{T_{\text{correl}}} \right). \quad (4)$$

This value was also calculated for all events and included in Table 2. Similarly, the mean acceleration between a radial distance of $21.5 R_{\odot}$ from the Sun and the arrival at 1 AU, $a_{\text{Sun}, 1 \text{ AU}}$, was calculated using the speed at $21.5 R_{\odot}$ obtained from the Database of Notifications, Knowledge, Information (DONKI) database (section 3.3) and the traveltime between those locations. In the case of ICME 2, the launch speed of 480 km s^{-1} from the DONKI database was changed to the more reasonable value of 960 km s^{-1} reported in the SOHO/LASCO CME catalog for the calculation of the acceleration. The DONKI value of 480 km s^{-1} led to a negative, unphysical result for the drag parameter Γ calculated in section 3.4. For the other events, the difference between the DONKI and SOHO/LASCO catalogs was much less significant.

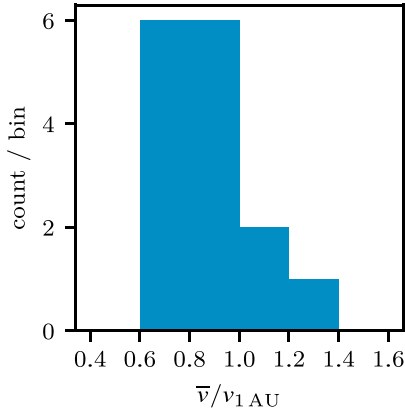


Figure 3. Histogram of ICME speed changes between 1 AU and Mars. Plotted is the ratio of the calculated mean speed between 1 AU and Mars over the measured speed at 1 AU.

3.2. Statistical Analysis

In Figure 3, we show a histogram of the ratio $\bar{v}/v_{1\text{AU}}$ for the 15 ICMEs. On average, we get a value of

$$\left\langle \frac{\bar{v}}{v_{1\text{AU}}} \right\rangle = 0.86 \pm 0.06,$$

which indicates that the average ICME in our sample decelerates slightly during its propagation between 1 and 1.5 AU.

Considering the calculated standard deviations σ of the $\bar{v}/v_{1\text{AU}}$ values (included in Table 2) and using a 1σ confidence interval, we can say that eight ICMEs (53% of our sample of ICMEs) decelerated ($\bar{v}/v_{1\text{AU}} + \sigma < 1$) and no ICME accelerated ($\bar{v}/v_{1\text{AU}} - \sigma > 1$) while the seven remaining events showed neither a clear deceleration nor acceleration. We calculated the mean and standard deviation of $v_{1\text{AU}}$ of our 15 events to be 466.9 km s^{-1} and 84.5 km s^{-1} , respectively, while the mean and standard deviation of $v_{1\text{AU}}$ of all ICMEs in the Richardson and Cane list from 2012 until 2016 (123 events) are 489.2 km s^{-1} and 114.2 km s^{-1} . Despite of the small sample of our events, the $v_{1\text{AU}}$ measurements seem to suggest that they are good

in representing the average ICME speeds at 1 AU. However, we still note that our derived probabilities of the changing of ICME speeds should be applied with caution because (a) our accuracy is not high enough to find out the exact speed change of the remaining seven events, and (b) the geometry of the ICME may affect our results, which will be discussed in more detail later (see also Figures 5 and 6).

As the deceleration of ICMEs is believed to be related to the ambient solar wind speed, we also compared the $\bar{v}/v_{1\text{AU}}$ values to the solar wind speed v_{sw} in Figure 4, using data from the *Solar Wind Electron, Proton, and Alpha Monitor* (SWEPAM) instrument (McComas et al., 1998) on the *Advanced Composition Explorer* (ACE) spacecraft (Stone et al., 1998) located at the L1 point near Earth and the *Plasma and Suprathermal Ion Composition* (PLASTIC) (Galvin et al., 2008) instruments on the two STEREO spacecraft. The value we used for v_{sw} is the average value of the solar wind speed measurements in a 1 day window before the ICME/disturbance arrival time at 1 AU, and its standard deviation was used for the error bars.

Most ICME speeds at 1 AU are larger than the ambient solar wind speed, which can be seen on the x axis in Figure 4. Slightly different from previous findings, \bar{v} (the average transit speed between 1 AU and Mars) is generally smaller than $v_{1\text{AU}}$ (which corresponds to a deceleration of the ICME), as visible on the y axis, apart from 3 cases where the error bars are also very large. Our results tend to show that lower ambient solar wind speeds compared to the ICME speed generally result in more deceleration even beyond 1 AU, as expected.

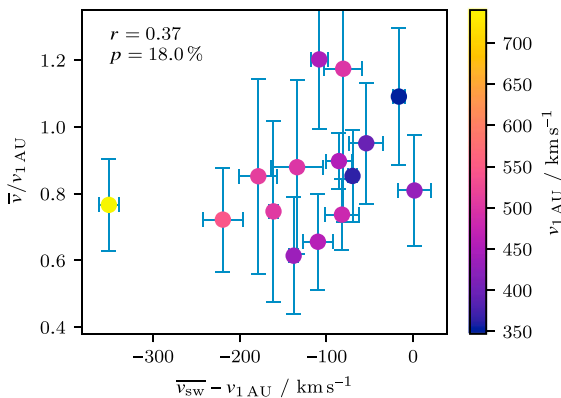


Figure 4. Comparison of the ratio $\bar{v}/v_{1\text{AU}}$ to $v_{\text{sw}} - v_{1\text{AU}}$, where v_{sw} is the ambient solar wind speed measured at ACE. The colors show the initial speed of the ICME at $v_{1\text{AU}}$. The Pearson correlation coefficient r and the probability p that such a data set was produced by an uncorrelated system are displayed in the plot.

However, there is a considerable amount of variance in the data points, which is reflected by the Pearson correlation coefficient $r = 0.37$ in Figure 4 not being very high. This variance can possibly be due to the determined speed \bar{v} being influenced by the geometry of the ICME: In general, the propagation of different parts of the ICME can be affected differently by ambient solar wind conditions and the interaction with other structures, such as stream interaction regions (SIRs)/corotating interaction regions (CIRs) and other ICMEs, potentially resulting in a variation of the ICMEs' geometric shape. This could lead to a radial asymmetry of the ICME resulting in larger uncertainties in our analysis especially when the two observers have a bigger longitudinal separation. A demonstration of this influence is also shown as a cartoon in Figure 5, together with an example of the ENLIL model result in Figure 6 (explained later in section 3.3) for ICME 11 where we suspect that this effect led to the ratio $\bar{v}/v_{1\text{AU}}$ being 1.20 ± 0.21 . Another example is visible in Figure 9, where ICME 12 is merging with an SIR structure, possibly leading to a slight "acceleration," $\bar{v}/v_{1\text{AU}} = 1.17 \pm 0.46$. Similar effects have been observed previously by Priše et al. (2015) and Winslow et al. (2016).

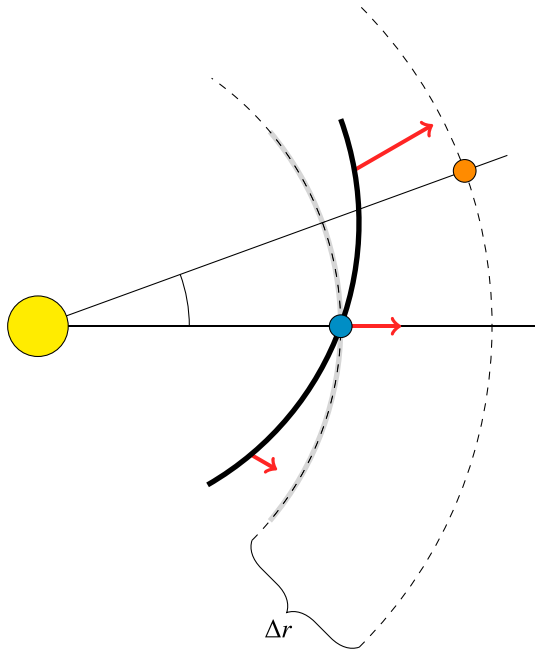


Figure 5. Cartoon illustration of the possible influence of the ICME shape on the measured speeds when the two observation locations are not perfectly aligned in their heliospheric longitudes. In this case, the inclined shape causes a perceived “speedup” of the ICME between Earth and Mars even if the actual speed of the ICME stays constant.

Another comparison can be made to the mean acceleration values that we calculated for the travel between $21.5 R_{\odot}$ and 1 AU ($a_{Sun,1 AU}$) and between 1 AU and Mars ($a_{1 AU, Mars}$) as shown in Figure 7. The acceleration was calculated using equation (4), which depends on T_{correl}^2 , amplifying the error bars. The big variations of a shown in the figure indicate that ICMEs are very dynamic and their propagation depends on various properties, such as the different ambient solar wind conditions at different parts of the ICME and the interaction with other heliospheric structures. Our results suggest that the dynamics of the propagation continue to evolve beyond 1 AU and that, although the acceleration values up to and after 1 AU tend to be related (supported by a Pearson correlation coefficient of $r = 0.29$), the acceleration is hardly a constant value. This is because (a) the ambient environment that the ICME travels through fluctuates due to the time-varying structures of the heliosphere (as shown, e.g., by Temmer et al., 2011) and (b) the ambient solar wind conditions vary throughout the heliosphere, thus diversely affecting the same ICME at different locations.

We have also marked the four quadrants in the plot, showing which ICMEs kept decelerating before and after 1 AU (lower left quadrant) and which changed from acceleration to deceleration (lower right) or the other way round (upper left). There are no ICMEs that accelerated before and after 1 AU (upper right quadrant), and two cases that “accelerated” between 1 AU and Mars were addressed above (events 11 and 12). There are also two ICMEs that seem to have accelerated between the Sun and 1 AU, that is, event numbers 10 and 15, which have very low launch speeds reported (below 400 km s^{-1} in the DONKI list, as well as even lower values in the SOHO/LASCO and CACTus (Computer Aided CME Tracking) databases). These could of course be physical but might also be due to the projection effect used in the image-based remote sensing analysis used to derive the launch speed. As the current paper is not focusing on the launch properties of the CMEs we did not pursue this matter further.

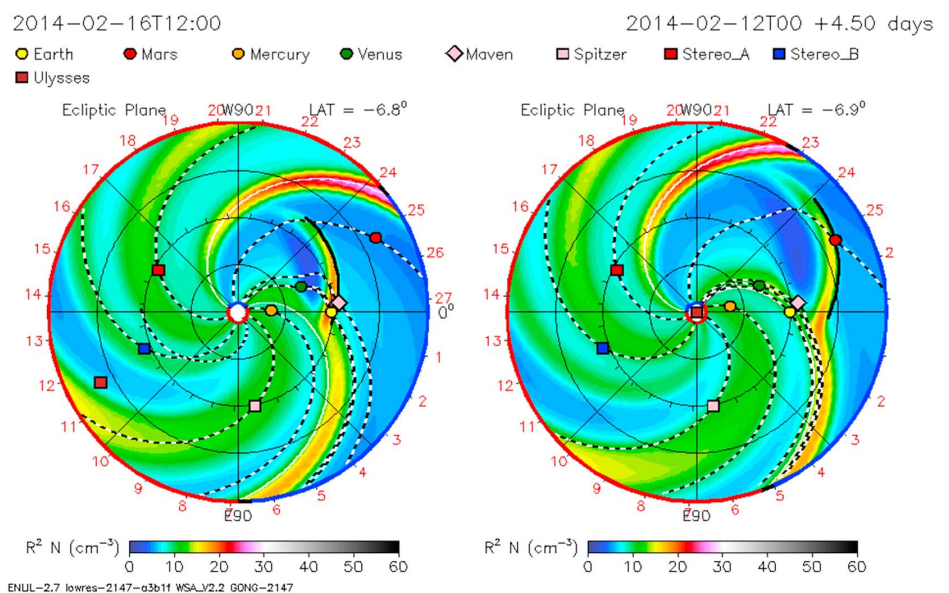


Figure 6. ENLIL simulation for the 15 February 2014 ICME, showing the same effect that was illustrated in Figure 5 (left, arrival at Earth; right, arrival at Mars). The CME front was emphasized manually using a black line.

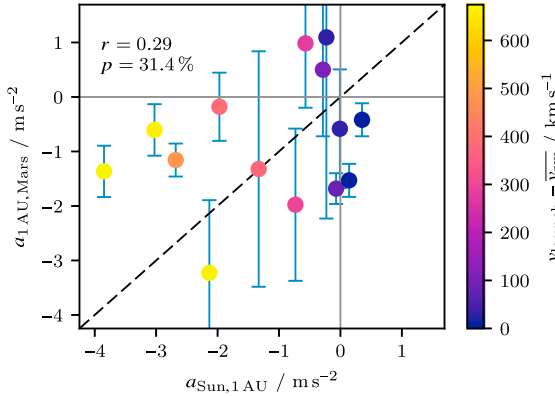


Figure 7. Comparison of the acceleration $a_{\text{Sun}, 1 \text{ AU}}$ between $21.5 R_{\odot}$ and the arrival at 1 AU and $a_{1 \text{ AU}, \text{ Mars}}$ between the arrival at 1 AU and the arrival at Mars. The Pearson correlation coefficient r and the probability p that such a data set was produced by an uncorrelated system are displayed in the plot. The diagonal line marks where the accelerations would be equal, and the gray lines divide the four quadrants of the plot.

In Figure 8, we correlated the acceleration between the Sun and 1 AU with the launch speed (left) and the acceleration between 1 AU and Mars with the speed at 1 AU (right). Both plots show that a stronger deceleration is correlated with higher ICME speeds, which is supported by high Pearson correlation coefficients of $r = -0.94$ and -0.64 and low corresponding probabilities $p = 0.0\%$ and 1.5% for uncorrelated data, respectively. Again, the error bars in Figure 8 (right) are large due to the dependence of a on T_{correl}^2 . Comparing our results for the acceleration with the values that Richardson (2014) obtained for ICMEs propagating from Earth to the *Ulysses* spacecraft (shown in their Figure 22 in a similar manner as our Figure 8), which was at a distance of between 3.74 and 5.41 AU from the Sun at that time, we find that our average deceleration value of $(0.81 \pm 0.33) \text{ m s}^{-2}$ is much larger than their values of up to 0.1 m s^{-2} . This suggests that the deceleration becomes weaker at a larger radial distance beyond Mars, thus resulting in a lower average value between Earth and *Ulysses*.

3.3. WSA-ENLIL+Cone Model

The Wang-Sheeley-Argge (WSA) ENLIL model (Odstrcil et al., 2004) is a widely used tool to predict solar wind propagation in the heliosphere. It is based on an MHD simulation and can be combined with a cone model to

describe the propagation of ICMEs. Using the *Space Weather Database of Notifications, Knowledge, Information* (DONKI, <https://kauai.ccmc.gsfc.nasa.gov/DONKI/>), which is based on coronagraph observations of CMEs close to their launch from the Sun, we matched most of the ICMEs in our study to WSA-ENLIL+Cone model simulation results provided by the Community Coordinated Modeling Center (CCMC) (<https://ccmc.gsfc.nasa.gov/missionsupport/>). In some cases, there are multiple ENLIL results for the same ICME (using slightly different input parameters)—in that situation, we chose the one that gave the best 1 AU arrival time compared to the observations from the Richardson and Cane or Jian lists, respectively. In one case (ICME 14 in Table 3), we did not find any event output in the DONKI database that would possibly match the observed arrival time at 1 AU. Figure 9 shows a graphical representation of an ENLIL simulation result, specifically the ICME arriving at Earth on 5 April 2014 and at Mars on 7 April 2014, respectively (ICME 12 in Table 3).

To compare our measured ICME traveltimes to the ENLIL model results, we applied the cross-correlation method described in section 2.3 to the plasma number density n at Earth (or STEREO) and Mars obtained from the model. This gives us another time lag value, which is considered to be the traveltime that the ENLIL model predicts. In most cases, due to the smooth nature of the simulated data, the uncertainty of the traveltime is smaller than for the one obtained from measured Forbush decreases.

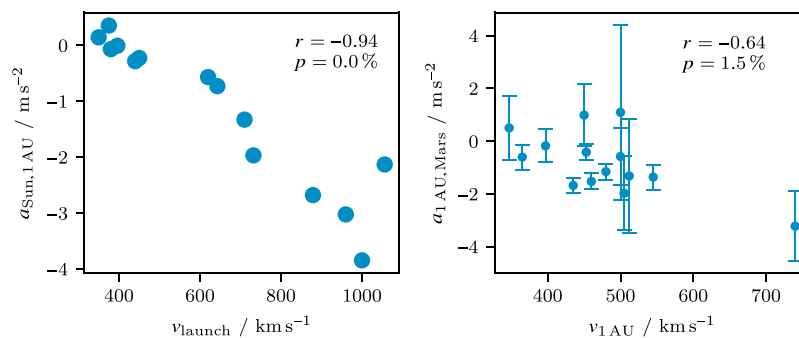


Figure 8. Comparison of the (right) acceleration $a_{1 \text{ AU}, \text{ Mars}}$ between the arrival at 1 AU and the arrival at Mars with the speed $v_{1 \text{ AU}}$ and the (left) acceleration $a_{\text{Sun}, 1 \text{ AU}}$ between $21.5 R_{\odot}$ and the arrival at 1 AU with the speed v_{launch} of the ICME at $21.5 R_{\odot}$. The Pearson correlation coefficients r and the probabilities p that such data sets were produced by an uncorrelated system are displayed in the plots.

Table 3
Table of All the ICMEs Examined in This Study

ICME	Repetition from Table 2			Acceleration		Model input and results			
	Obs S/C	t_1 AU (UTC)	T_{correl} /days	a_1 AU, Mars /m s ⁻²	$a_{\text{Sun, 1 AU}}$ /m s ⁻²	$t_{21.5 R_{\odot}}$ (UTC)	T_{ENLIL} /days	T_{DBM} /days	$\Gamma_{\odot-1 \text{ AU}}$ /10 ⁻⁷ km ⁻¹
1	STB	2012-9-25 16:26	1.24±0.23	-3.2±1.3	-2.13	2012-9-23 18:58	1.03±0.14	1.0	0.082±0.004
2	STB	2012-10-17 06:57	2.05±0.33	-0.60±0.47	-3.03	2012-10-14 08:45	1.54±0.26	2.1	0.224±0.006
3	STB	2012-10-25 19:10	2.31±0.66	-1.68±0.28	-0.07	2012-10-21 03:59	1.28±0.34	2.5	0.058±0.006
4	STB	2012-11-11 13:36	1.33±0.46	-1.3±2.2	-1.33	2012-11-8 07:21	1.33±0.23	1.8	0.17±0.03
5	STB	2012-11-19 09:50	1.50±0.54	-2.0±1.4	-0.73	2012-11-16 06:32	0.94±0.19	1.7	0.138±0.007
6	STB	2012-11-28 03:36	1.46±0.27	0.5±1.2	-0.29	2012-11-23 17:17	1.46±0.28	1.6	0.7±0.2
7	STA	2013-5-29 12:20	2.53±0.37	-1.16±0.30	-2.68	2013-05-26 22:58	1.37±0.25	1.9	0.34±0.05
8	STA	2013-6-27 16:17	2.53±0.48	-0.18±0.63	-1.97	2013-6-24 08:08	1.97±0.41	2.6	0.40±0.07
9	STA	2013-7-25 06:12	2.57±0.56	-1.37±0.47	-3.85	2013-7-22 09:55	1.97±0.44	2.1	0.19±0.02
10	STA	2013-8-10 15:00	2.57±0.24	-0.42±0.30	0.35	2013-8-7 02:53	2.57±0.26	2.4	-2±1
11	EARTH	2014-2-15 13:45	2.14±0.37	1.0±1.2	-0.57	2014-2-12 18:51	2.01±0.32	2.6	0.15±0.02
12	EARTH	2014-4-5 19:00	1.84±0.72	1.1±3.3	-0.23	2014-4-2 00:19	2.53±0.30	2.4	0.7±0.6
13	EARTH	2014-4-18 19:00	2.40±0.71	-0.6±1.1	-0.01	2014-4-14 19:44	2.35±0.23	2.2	0.01±0.01
14	EARTH	2016-3-20 07:00	3.00±0.61	-0.63±0.42				3.0	
15	EARTH	2016-8-2 14:00	2.40±0.53	-1.53±0.30	0.14	2016-7-29 08:50	2.31±0.24	3.1	-0.5±0.3
Average			2.12±0.13	-0.81±0.33	-1.17		1.76±0.08	2.2	0.13
				$\sigma = 1.11$	$\sigma = 1.29$				

Note. This table supplements the data from Table 2 with the average acceleration values calculated using equation (4), the time $t_{21.5 R_{\odot}}$ used for the ENLIL simulations, the traveltime T_{ENLIL} calculated from the ENLIL model results and the traveltime T_{DBM} calculated using DBM by propagating the ICME from 1 AU to Mars (section 3.3) using a drag parameter of $\Gamma = 0.1 \times 10^{-7} \text{ km}^{-1}$. The last column shows an estimation of the actual drag parameter for this event between the Sun and 1 AU calculated using the observation values as described at the end of section 3.4, where the average displayed in the bottom row is weighted using the inverse errors. The acceleration values of events 10 and 15 are very small with absolute errors similar to the others, which makes the errors of Γ large. However, due to the weighted mean calculation, these two values only have a very small influence on the mean Γ value for all events shown in the last row. Γ values for the propagation between 1 AU and Mars are not shown; their uncertainties are so large that the values are not meaningful. For Event 15, there is a negative Γ value because the speed at 1 AU is larger than the launch speed, which is very low both in the DONKI and CACTUS ICME catalogs. Dates are formatted as year/month/day.

In Figure 10 (top left), we compare the traveltimes calculated by the ENLIL model with the ones obtained from the in situ data in this work. Both traveltimes are also listed in Tables 2 and 3. For many events, ENLIL seems to predict a slightly faster propagation. Results for faster ICMEs (e.g., the 28 November 2012 ICME at STEREO B—ICME 6 in Tables 2 and 3) seem to agree quite well, while the slower events show larger differences. This might be the result of slower ICMEs being exposed to the disturbances in the interplanetary space for a longer time, thus accumulating a larger amount of possible uncertainties in the model. However, a more systematic statistical study based on more events should be carried out in the future to draw a solid statement on this matter.

We also calculated the mean difference between the results

$$\langle T_{\text{ENLIL}} - T_{\text{correl}} \rangle = -7 \pm 11 \text{ h}$$

and the average absolute difference

$$\langle |T_{\text{ENLIL}} - T_{\text{correl}}| \rangle \approx 10 \text{ h.}$$

The error given here is the standard error of the mean, not the standard deviation.

3.4. Drag-Based Model

A simpler model for the propagation of ICMEs is the Drag-Based Model (DBM), described in Vrřnak et al. (2013) and Źic et al. (2015). The DBM is based on the assumption that beyond a distance of approximately $20 R_{\odot}$, the dominating influence on ICMEs is an “aerodynamic” drag force with an empirically determined drag

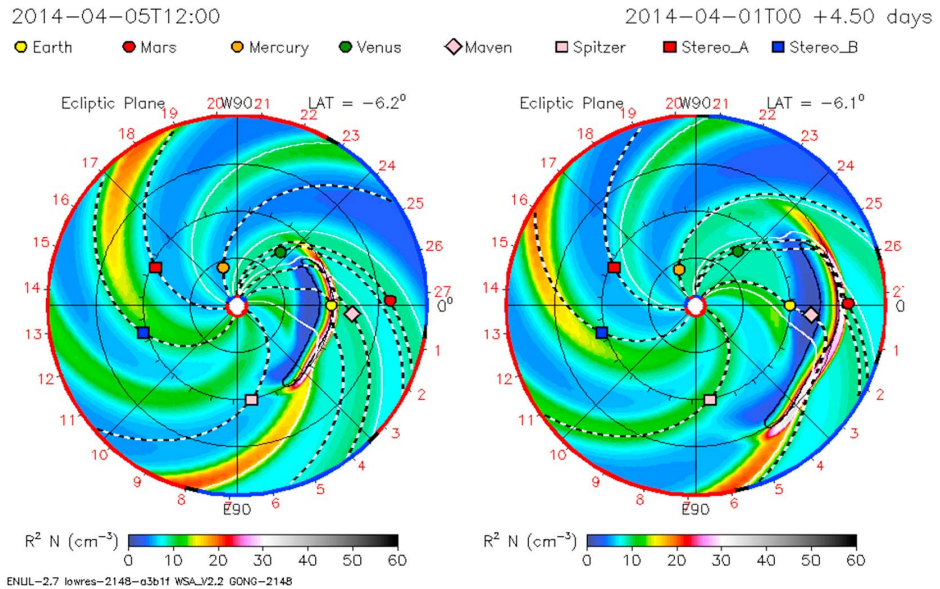


Figure 9. Example of an ENLIL simulation result for the 5 April 2014 ICME (left, arrival at Earth; right, arrival at Mars).

parameter Γ . The main difference between DBM and ENLIL is that the former does not employ numerical MHD simulations—the drag equations can be solved analytically. Therefore, the simulation is computationally inexpensive.

Vršnak et al. (2014) already compared results from DBM and ENLIL simulations and found that the ICME arrival times at Earth predicted by the two models generally agree quite well with average absolute-value difference of below 8 h. For these results, drag parameter values between $\Gamma = 0.1 \times 10^{-7}$ and $0.2 \times 10^{-7} \text{ km}^{-1}$ and solar wind speeds between $w = 400$ and 500 km s^{-1} were used as an input for the DBM.

We apply the DBM model in such a way that the propagation of ICMEs is simulated starting from 1 AU, where the in situ measurement of the ICME is used as input, thus avoiding the uncertainty of the propagation from the Sun up to 1 AU. As the input for DBM, we used the local ICME speed ($v_{1 \text{ AU}}$) and the ambient solar wind speed for each event measured at ACE or STEREO as described in section 3.1. The drag parameter Γ was chosen to be $0.1 \times 10^{-7} \text{ km}^{-1}$, which is a low value that is commonly used for describing the propagation of the interplanetary shock associated with an ICME. We chose this value because the shock is related to the first step of the Forbush decrease (e.g., Cane, 2000). Assuming that the ICME propagates outward radially, the ICMEs' half widths and the heliospheric longitudes of their propagation directions were taken from the DONKI database entries, as previously done for the ENLIL model (as such information is not available at 1 AU).

The arrival times at Mars predicted by DBM are marked in Figure 2 as well as Figures A1–A5 in Appendix A. Additionally, Figure 10 (top right) compares the traveltimes predicted by DBM to the results of the correlation method, and Figure 10 (top left) compares the two models, ENLIL and DBM.

The mean difference and mean absolute difference between the results are the following:

$$\begin{aligned} \langle T_{\text{DBM}} - T_{\text{correl}} \rangle &= (1 \pm 9) \text{ h} \\ \langle |T_{\text{DBM}} - T_{\text{correl}}| \rangle &\approx (7) \text{ h} \\ \langle T_{\text{DBM}} - T_{\text{ENLIL}} \rangle &= (9 \pm 10) \text{ h} \\ \langle |T_{\text{DBM}} - T_{\text{ENLIL}}| \rangle &\approx 11 \text{ h}. \end{aligned}$$

On average, DBM gives slightly better results than ENLIL for these events, even though the amount of variance is similar. Probably, this is primarily due to the fact that we could use DBM for propagation from 1 AU to Mars instead of from the Sun.

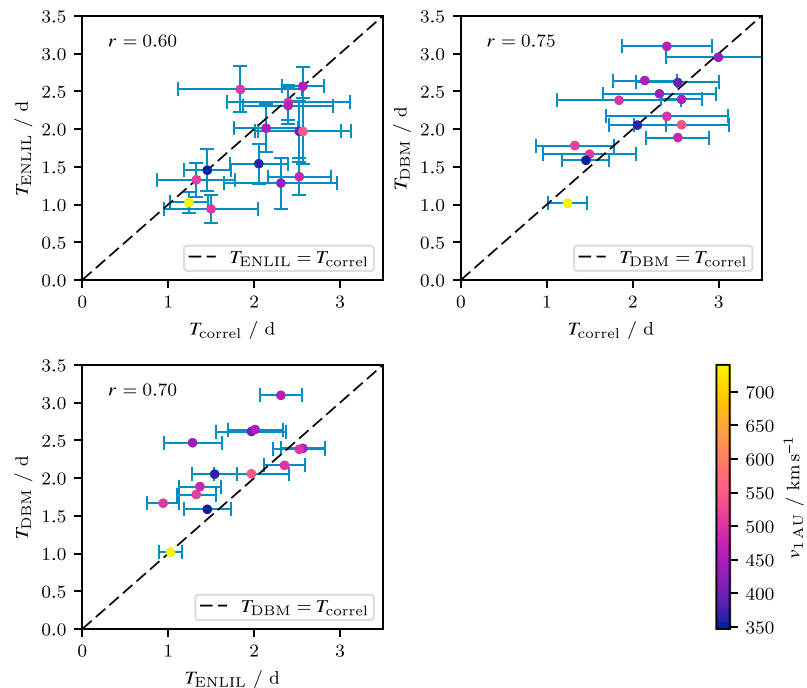


Figure 10. Plots comparing the ICME traveltimes between 1 AU and Mars determined using the cross-correlation method and calculated by ENLIL or DBM. The diagonal line marks where the traveltimes would be equal. The Pearson correlation coefficient r is noted in the top left corner.

The agreement between the DBM and ENLIL models is similar to the one of ENLIL, and the correlation method results with an average absolute-value difference slightly above the value of 8 h determined by Vršnak et al. (2014) for the propagation up to 1 AU. This difference seems reasonable as the propagation from the Sun out to Mars (~ 1.5 AU) takes a longer time and can therefore introduce a larger amount of error.

Under the assumption that the acceleration a of an ICME stays constant between the Sun and 1 AU and between 1 AU and Mars and with a simplified, one-dimensional version of DBM (disregarding the influence of the geometric shape of the ICME), we also tried to derive the actual values of the drag parameter Γ based on the observations and our calculated a values by solving the following equation (cf. Vršnak et al., 2013, equation (1))

$$a = -\Gamma(v_{\text{ICME}} - v_{\text{sw}})|v_{\text{ICME}} - v_{\text{sw}}| \quad (5)$$

for Γ .

Using the average speed $v_{\text{ICME}} = (v_{\text{launch}} + v_{1 \text{ AU}})/2$ and $a = a_{\text{Sun}, 1 \text{ AU}}$ (from Table 2), we get an estimation of Γ between the Sun and 1 AU, which is given in Table 3. By calculating a weighted average using the inverse errors of these Γ values, we obtain a result of $0.09 \times 10^{-7} \text{ km}^{-1}$, which shows that our assumption of $\Gamma = 0.1 \times 10^{-7} \text{ km}^{-1}$ was reasonable. Nonetheless, we note that the variance of Γ for different events is considerable, which reflects the dynamic and variant nature of ICMEs and suggests that the approximated constant value of Γ in DBM may result in uncertainties in the modelling procedure. The same Γ values could also be calculated between 1 AU and Mars using $v_{\text{ICME}} = \bar{v}$ and $a = a_{1 \text{ AU}, \text{ Mars}}$; however, the results have propagated uncertainties that are too large to be meaningful.

4. Conclusion

We have described a method to determine the traveltime of ICMEs between two heliospheric locations using the cross-correlation function of two in situ data sets and applied it to 15 ICMEs and their Forbush decreases

observed at Earth or the STEREO spacecraft and Mars close to their oppositions between 2012 and 2016. The method gives meaningful results in most cases apart from periods when ICMEs interact with each other and/or with SIRs/CIRs.

The results were used as the basis for this first statistical study of ICME-caused FDs observed at both 1 AU and 1.5 AU. It was found that the average ICME in our sample slightly decelerated during its propagation between 1 AU and 1.5 AU. Additionally, the results support that slower ambient solar wind speeds in comparison to the maximum ICME speed lead to a larger amount of deceleration. More studies based on a higher number of events in the future would help to better quantify these results.

The traveltimes between 1 AU and Mars obtained for the 15 events were compared with results from the ENLIL and DBM models. To derive traveltimes from the interplanetary plasma number density data output by ENLIL for different locations, the same cross-correlation method was used. On average, ENLIL predicts a faster propagation from 1 AU to Mars, but the ENLIL results seem to be less accurate for slower ICMEs in the study, which might be an effect of accumulation of uncertainties during the longer traveltime.

Additionally, the observations were compared to results from the Drag-Based Model. Unlike ENLIL, we could use the observations at 1 AU as the basis for DBM and simulate the propagation from 1 AU to Mars. Avoiding the uncertainties of the propagation close to the Sun, this led to a slightly better agreement with the observations at Mars.

This highlights the importance of space weather modeling taking into account not only information about the launch of CMEs at the Sun but also the in situ measurements farther away, for example, at 1 AU, to improve forecasts for space weather hazards for robotic missions positioned beyond 1 AU. With future missions, such as Solar Orbiter and the Parker Solar Probe, we will have more measurements available at solar distances of less than 0.3 AU, which should be exploited as an input for modeling of space weather scenarios.

Appendix A: Cross-Correlation Analysis Plots for Each Event

The results based on the cross-correlation method for all the ICMEs in this study are presented in this appendix.

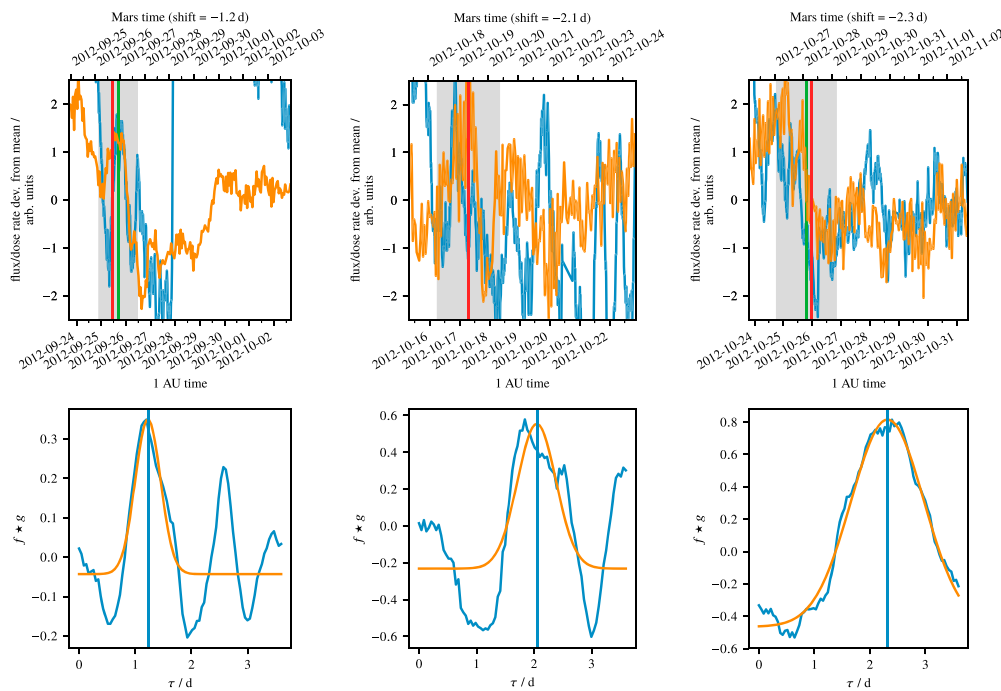


Figure A1. Plots showing the application of the cross-correlation method to every single ICME in the study. These are Events 1 to 3 (all observed at STEREO B and Mars). The legend for the plots is in Figure 2.

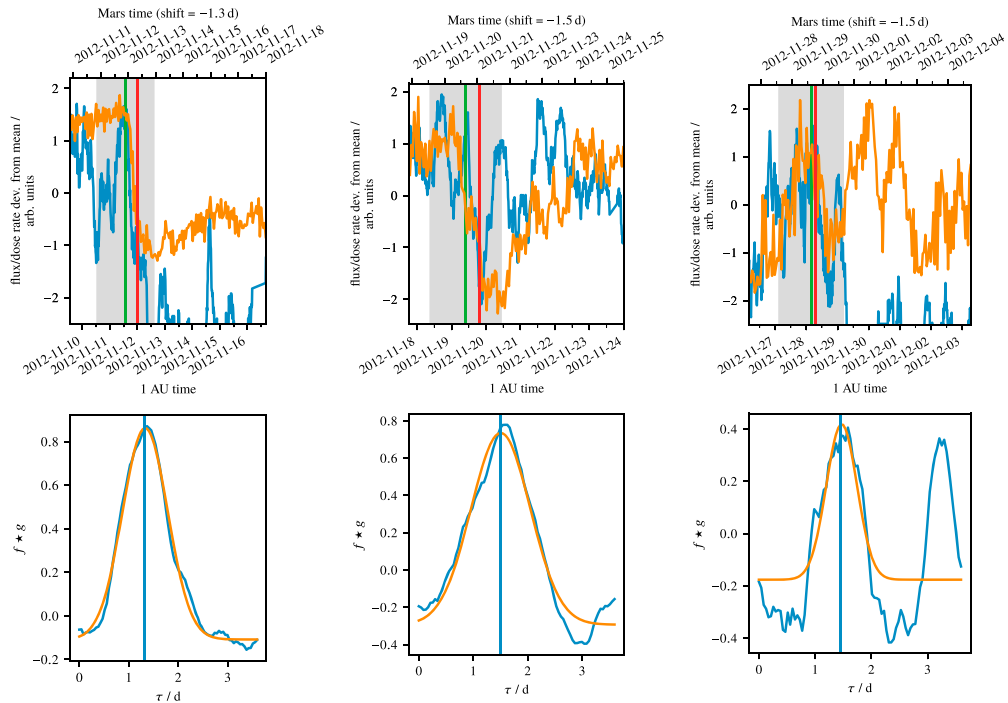


Figure A2. Plots showing the application of the cross-correlation method to every single ICME in the study. These are Events 4 to 6 (all observed at STEREO B and Mars). The legend for the plots is in Figure 2.

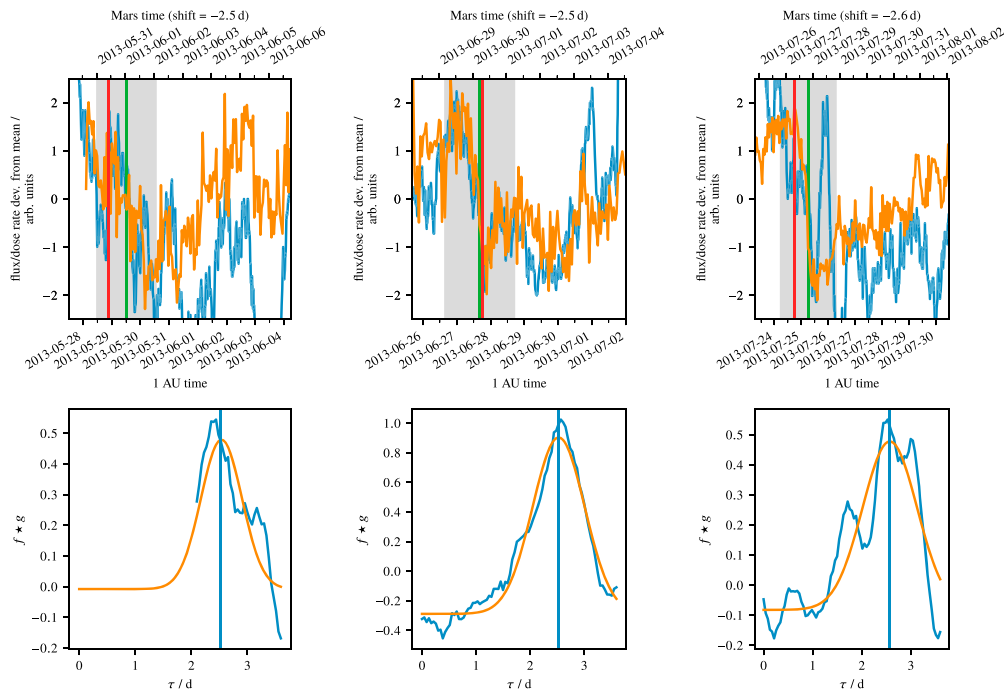


Figure A3. Plots showing the application of the cross-correlation method to every single ICME in the study. These are Events 7 to 9 (all observed at STEREO A and Mars). The legend for the plots is in Figure 2.

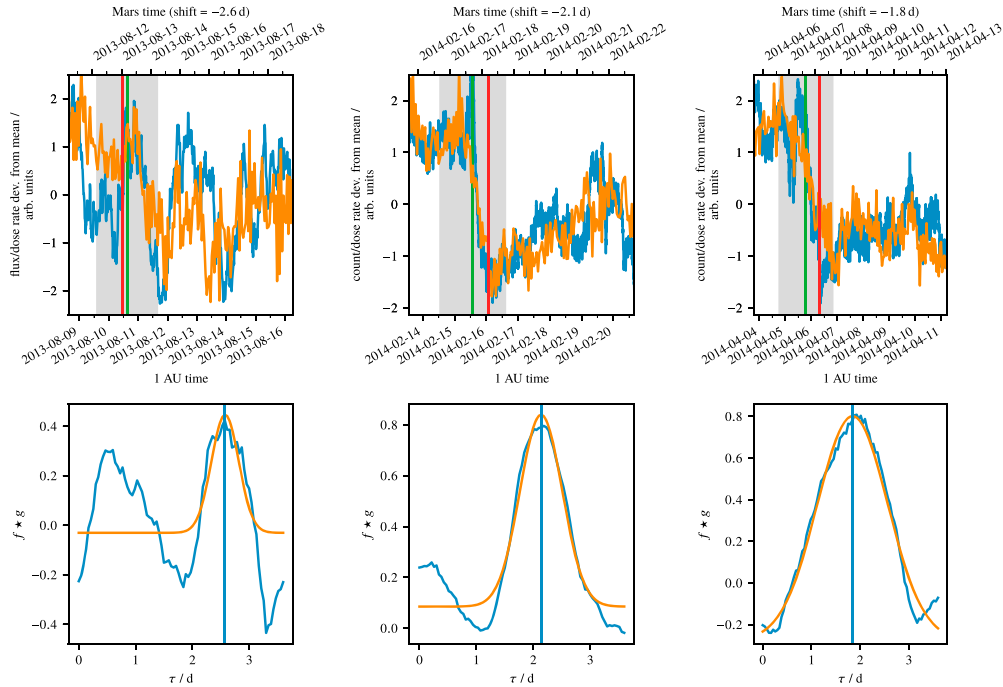


Figure A4. Plots showing the application of the cross-correlation method to every single ICME in the study. These are Events 10 (observed at STEREO A and Mars), 11, and 12 (observed at Earth and Mars).

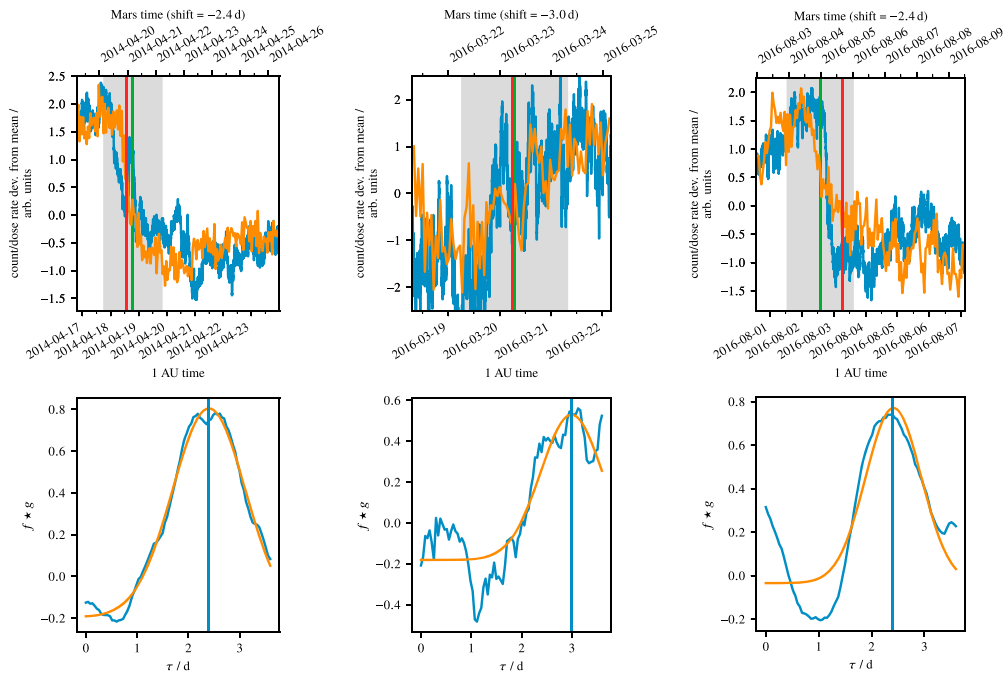


Figure A5. Plots showing the application of the cross-correlation method to every single ICME in the study. These are Events 13 to 15 (all observed at Earth and Mars). The legend for the plots is in Figure 2.

Acknowledgments

RAD is supported by NASA (HEOMD) under JPL subcontract 1273039 to Southwest Research Institute and in Germany by DLR and DLR's Space Administration grants 50QM0501, 50QM1201, and 50QM1701 to the Christian Albrechts University, Kiel. Jingnan Guo and Robert Wimmer-Schweingruber acknowledge stimulating discussions with the ISSI team "Radiation Interactions at Planetary Bodies" and thank ISSI for its hospitality. The research leading to these results has received funding from the European Union's Horizon 2020 research and innovation programme under the Marie Skłodowska-Curie grant agreement 745782. Lan K. Jian is supported by NSF grants AGS 1259549 and 1321493. Bojan Vršnak, Jaša Čalogović and Mateja Dumbović acknowledge financial support by the Croatian Science Foundation under project 6212 "Solar and Stellar Variability". We acknowledge the NMDB database (www.nmdb.eu), funded under the European Union's FP7 Programme (contract 213007), for providing data. The data from South Pole neutron monitor is provided by the University of Delaware with support from the U.S. National Science Foundation under grant ANT-0838839. Simulation results have been provided by the Community Coordinated Modeling Center at Goddard Space Flight Center through their archive of real-time simulations (<http://ccmc.gsfc.nasa.gov/missionsupport>). The CCMC is a multiagency partnership between NASA, AFMC, AFOSR, AFRL, AFWA, NOAA, NSF, and ONR. ENLIL with Cone Model was developed by D. Odstrčil at George Mason University. We thank the ACE SWEPAM instrument team and the ACE Science Center for providing the ACE data. We acknowledge the STEREO IMPACT and PLASTIC teams (NASA contracts NASS5-00132 and NASS5-00133) for the use of the solar wind plasma and magnetic field data.

References

- Burlaga, L. F., McDonald, F. B., Goldstein, M. L., & Lazarus, A. J. (1985). Cosmic ray modulation and turbulent interaction regions near 11 AU. *Journal of Geophysical Research*, *90*, 12,027–12,039. <https://doi.org/10.1029/JA090iA12p12027>
- Cane, H. V. (2000). Coronal mass ejections and Forbush decreases. *Space Science Reviews*, *93*(1), 55–77. <https://doi.org/10.1023/A:1026532125747>
- Ehresmann, B., Zeitlin, C., Hassler, D. M., Wimmer-Schweingruber, R. F., Böhm, E., & Böttcher, S. (2014). Charged particle spectra obtained with the Mars Science Laboratory Radiation Assessment Detector (MSL/RAD) on the surface of Mars. *Journal of Geophysical Research: Planets*, *119*, 468–479. <https://doi.org/10.1002/2013JE004547>
- Forbush, S. E. (1937). On the effects in cosmic-ray intensity observed during the recent magnetic storm. *Physical Review*, *51*, 1108–1109. <https://doi.org/10.1103/PhysRev.51.1108.3>
- Galvin, A. B., Kistler, L. M., Popecki, M. A., Farrugia, C. J., Simunac, K. D. C., Ellis, L., ... Steinfeld, D. (2008). The Plasma and Suprathermal Ion Composition (PLASTIC) investigation on the STEREO observatories. *Space Science Reviews*, *136*(1), 437–486. <https://doi.org/10.1007/s11214-007-9296-x>
- Gopalswamy, N., Lara, A., Yashiro, S., Kaiser, M. L., & Howard, R. A. (2001). Predicting the 1-AU arrival times of coronal mass ejections. *Journal of Geophysical Research*, *106*(A12), 29,207–29,217. <https://doi.org/10.1029/2001JA000177>
- Grotzinger, J. P., Crisp, J., Vasavada, A. R., Anderson, R. C., Baker, C. J., Barry, R., ... Wiens, R. C. (2012). Mars Science Laboratory mission and science investigation. *Space Science Reviews*, *170*(1), 5–56. <https://doi.org/10.1007/s11214-012-9892-2>
- Guo, J., Zeitlin, C., Wimmer-Schweingruber, R. F., Rafkin, S., Hassler, D. M., & Posner, A. (2015). Modeling the variations of dose rate measured by RAD during the first MSL Martian year: 2012–2014. *The Astrophysical Journal*, *810*(1), 24.
- Guo, J., Lillis, R., Wimmer-Schweingruber, R. F., Zeitlin, C., Simonson, P., Rahmati, A., ... Böttcher, S. (2017). Measurements of Forbush decreases at Mars: Both by MSL on ground and by MAVEN in orbit. *Astronomy and Astrophysics*, 1–15. <https://doi.org/10.1051/0004-6361/201732087>
- Guo, J., Slaba, T. C., Zeitlin, C., Wimmer-Schweingruber, R. F., Badavi, F. F., Böhm, E., ... Rafkin, S. (2017). Dependence of the Martian radiation environment on atmospheric depth: Modeling and measurement. *Journal of Geophysical Research: Planets*, *122*, 329–341. <https://doi.org/10.1002/2016JE005206>
- Hassler, D. M., Zeitlin, C., Wimmer-Schweingruber, R. F., Böttcher, S., Martin, C., Andrews, J., ... Cucinotta, F. A. (2012). The radiation assessment detector (RAD) investigation. *Space Science Reviews*, *170*(1), 503–558. <https://doi.org/10.1007/s11214-012-9913-1>
- Hassler, D. M., Zeitlin, C., Wimmer-Schweingruber, R. F., Ehresmann, B., Rafkin, S., & Eigenbrode, J. L. (2014). Mars' surface radiation environment measured with the Mars Science Laboratory's Curiosity rover. *Science*, *343*(6169), 1244797.
- Hess, V. F., & Demmelair, A. (1937). World-wide effect in cosmic ray intensity, as observed during a recent magnetic storm. *Nature*, *140*, 316–317. <https://doi.org/10.1038/140316a0>
- Jian, L. K., Russell, C. T., Luhmann, J. G., Skoug, R. M., & Steinberg, J. T. (2008). Stream interactions and interplanetary coronal mass ejections at 5.3 AU near the solar ecliptic plane. *Solar Physics*, *250*(2), 375–402. <https://doi.org/10.1007/s11207-008-9204-x>
- Jian, L. K., Russell, C. T., Luhmann, J. G., Galvin, A. B., & Simunac, K. D. C. (2013). Solar wind observations at STEREO: 2007–2011. *AIP Conference Proceedings*, *1539*(1), 191–194. <https://doi.org/10.1063/1.4811020>
- Jordan, A. P., Spence, H. E., Blake, J. B., & Shaul, D. N. A. (2011). Revisiting two-step Forbush decreases. *Journal of Geophysical Research*, *116*, A11103. <https://doi.org/10.1029/2011JA016791>
- Kumar, A., & Badruddin (2014). Interplanetary coronal mass ejections, associated features, and transient modulation of galactic cosmic rays. *Solar Physics*, *289*(6), 2177–2205. <https://doi.org/10.1007/s11207-013-0465-7>
- Köhler, J., Zeitlin, C., Ehresmann, B., Wimmer-Schweingruber, R. F., Hassler, D. M., Reitz, G., ... Kortmann, O. (2014). Measurements of the neutron spectrum on the Martian surface with MSL/RAD. *Journal of Geophysical Research: Planets*, *119*, 594–603. <https://doi.org/10.1002/2013JE004539>
- Liu, Y., Davies, J. A., Luhmann, J. G., Vourlidas, A., Bale, S. D., & Lin, R. P. (2010). Geometric triangulation of imaging observations to track coronal mass ejections continuously out to 1 AU. *The Astrophysical Journal Letters*, *710*(1), L82.
- Liu, Y. D., Richardson, J. D., Wang, C., & Luhmann, J. G. (2014). Propagation of the 2012 March coronal mass ejections from the Sun to heliopause. *The Astrophysical Journal Letters*, *788*(2), L28.
- Lockwood, J. A. (1971). Forbush decreases in the cosmic radiation. *Space Science Reviews*, *12*(5), 658–715. <https://doi.org/10.1007/BF00173346>
- Lugaz, N., Farrugia, C. J., Davies, J. A., Möstl, C., Davis, C. J., Roussev, I. I., & Temmer, M. (2012). The deflection of the two interacting coronal mass ejections of 2010 May 23–24 as revealed by combined in situ measurements and heliospheric imaging. *The Astrophysical Journal*, *759*(1), 68.
- Maričić, D., Vršnak, B., Dumbović, M., Žic, T., Roš, D., Hržina, D., ... Mujić, N. (2014). Kinematics of interacting ICMEs and related Forbush decrease: Case study. *Solar Physics*, *289*(1), 351–368. <https://doi.org/10.1007/s11207-013-0314-8>
- Masias-Meza, J. J., Dasso, S., Démoulin, P., Rodríguez, L., & Janvier, M. (2016). Superposed epoch study of ICME sub-structures near Earth and their effects on galactic cosmic rays. *Astronomy and Astrophysics*, *592*, A118. <https://doi.org/10.1051/0004-6361/201628571>
- McComas, D., Bame, S., Barker, P., Feldman, W., Phillips, J., Riley, P., & Griffee, J. (1998). Solar wind electron proton alpha monitor (SWEPAM) for the Advanced Composition Explorer. *Space Science Reviews*, *86*(1), 563–612. <https://doi.org/10.1023/A:1005040232597>
- Möstl, C., Amla, K., Hall, J. R., Liewer, P. C., Jong, E. M. D., Colaninno, R. C., ... Galvin, A. B. (2014). Connecting speeds, directions and arrival times of 22 coronal mass ejections from the Sun to 1 AU. *The Astrophysical Journal*, *787*(2), 119.
- Odstrčil, D., Riley, P., & Zhao, X. P. (2004). Numerical simulation of the 12 May 1997 interplanetary CME event. *Journal of Geophysical Research*, *109*, A02116. <https://doi.org/10.1029/2003JA010135>
- Parks, T. W., & Burrus, C. S. (1987). *Digital filter design*. New York: Wiley-Interscience.
- Prise, A. J., Harra, L. K., Matthews, S. A., Arridge, C. S., & Achilleos, N. (2015). Analysis of a coronal mass ejection and corotating interaction region as they travel from the Sun passing Venus, Earth, Mars, and Saturn. *Journal of Geophysical Research: Space Physics*, *120*, 1566–1588. <https://doi.org/10.1002/2014JA020256>
- Rafkin, S. C. R., Zeitlin, C., Ehresmann, B., Hassler, D., Guo, J., Köhler, J., ... The MSL Science Team (2014). Diurnal variations of energetic particle radiation at the surface of Mars as observed by the Mars Science Laboratory Radiation Assessment Detector. *Journal of Geophysical Research: Planets*, *119*, 1345–1358. <https://doi.org/10.1002/2013JE004525>
- Richardson, I. G. (2014). Identification of interplanetary coronal mass ejections at Ulysses using multiple solar wind signatures. *Solar Physics*, *289*(10), 3843–3894. <https://doi.org/10.1007/s11207-014-0540-8>
- Richardson, I. G., & Cane, H. V. (1995). Regions of anomalously low proton temperature in the solar wind (1965–1991) and their association with ejecta. *Journal of Geophysical Research*, *100*(A12), 23,397–23,412. <https://doi.org/10.1029/95JA02684>

- Richardson, I. G., & Cane, H. V. (2010). Near-Earth interplanetary coronal mass ejections during solar cycle 23 (1996–2009): Catalog and summary of properties. *Solar Physics*, 264, 189–237. <https://doi.org/10.1007/s11207-010-9568-6>
- Stone, E., Frandsen, A., Mewaldt, R., Christian, E., Margolies, D., Ormes, J., & Snow, F. (1998). The Advanced Composition Explorer. *Space Science Reviews*, 86(1), 1–22. <https://doi.org/10.1023/A:1005082526237>
- Temmer, M., Rollett, T., Möstl, C., Veronig, A. M., Vršnak, B., & Odstrčil, D. (2011). Influence of the ambient solar wind flow on the propagation behavior of interplanetary coronal mass ejections. *The Astrophysical Journal*, 743(2), 101.
- von Rosenvinge, T. T., Reames, D. V., Baker, R., Hawk, J., Nolan, J. T., Ryan, L., ... Wiedenbeck, M. E. (2008). The high energy telescope for STEREO. *Space Science Reviews*, 136(1), 391–435. <https://doi.org/10.1007/s11214-007-9300-5>
- Vršnak, B., Ruždjak, D., Sudar, D., & Gopalswamy, N. (2004). Kinematics of coronal mass ejections between 2 and 30 solar radii—What can be learned about forces governing the eruption? *Astronomy and Astrophysics*, 423(2), 717–728.
- Vršnak, B., Žic, T., Vrbanc, D., Temmer, M., Rollett, T., Möstl, C., ... Shanmugaraju, A. (2013). Propagation of interplanetary coronal mass ejections: The drag-based model. *Solar Physics*, 285(1), 295–315. <https://doi.org/10.1007/s11207-012-0035-4>
- Vršnak, B., Temmer, M., Žic, T., Taktakishvili, A., Dumbović, M., Möstl, C., ... Odstrčil, D. (2014). Heliospheric propagation of coronal mass ejections: Comparison of numerical WSA-ENLIL+Cone model and analytical drag-based model. *The Astrophysical Journal Supplement Series*, 213(2), 21.
- Vršnak, B., & Žic, T. (2007). Transit times of interplanetary coronal mass ejections and the solar wind speed. *Astronomy and Astrophysics*, 472(3), 937–943. <https://doi.org/10.1051/0004-6361/20077499>
- Wang, C., Du, D., & Richardson, J. D. (2005). Characteristics of the interplanetary coronal mass ejections in the heliosphere between 0.3 and 5.4 AU. *Journal of Geophysical Research*, 110, A10107. <https://doi.org/10.1029/2005JA011198>
- Wimmer-Schweingruber, R. F., Crooker, N. U., Balogh, A., Bothmer, V., Forsyth, R. J., Gazis, P., ... Zurbuchen, T. H. (2006). Understanding interplanetary coronal mass ejection signatures. *Space Science Reviews*, 123(1), 177–216. <https://doi.org/10.1007/s11214-006-9017-x>
- Wimmer-Schweingruber, R. F., Köhler, J., Hassler, D. M., Guo, J., Appel, J.-K., Zeitlin, C., ... Cucinotta, F. (2015). On determining the zenith angle dependence of the Martian radiation environment at Gale crater altitudes. *Geophysical Research Letters*, 42, 10,557–10,564. <https://doi.org/10.1002/2015GL066664>
- Winslow, R. M., Lugaz, N., Philpott, L. C., Schwadron, N. A., Farrugia, C. J., Anderson, B. J., & Smith, C. W. (2015). Interplanetary coronal mass ejections from MESSENGER orbital observations at Mercury. *Journal of Geophysical Research: Space Physics*, 120, 6101–6118. <https://doi.org/10.1002/2015JA021200>
- Winslow, R. M., Lugaz, N., Schwadron, N. A., Farrugia, C. J., Yu, W., Raines, J. M., ... Zurbuchen, T. H. (2016). Longitudinal conjunction between MESSENGER and STEREO A: Development of ICME complexity through stream interactions. *Journal of Geophysical Research: Space Physics*, 121, 6092–6106. <https://doi.org/10.1002/2015JA022307>
- Witasse, O., Sánchez-Cano, B., Mays, M. L., Kajdič, P., Opgenoorth, H., Elliott, H. A., ... Altobelli, N. (2017). Interplanetary coronal mass ejection observed at STEREO-A, Mars, comet 67P/Churyumov-Gerasimenko, Saturn, and New Horizons en route to Pluto: Comparison of its Forbush decreases at 1.4, 3.1, and 9.9 AU. *Journal of Geophysical Research: Space Physics*, 122, 7865–7890. <https://doi.org/10.1002/2017JA023884>
- Wood, B. E., Wu, C.-C., Lepping, R. P., Nieves-Chinchilla, T., Howard, R. A., Linton, M. G., & Socker, D. G. (2017). A STEREO survey of magnetic cloud coronal mass ejections observed at Earth in 2008–2012. *The Astrophysical Journal Supplement Series*, 229(2), 29.
- Yashiro, S., Gopalswamy, N., Michalek, G., St. Cyr, O. C., Plunkett, S. P., Rich, N. B., & Howard, R. A. (2004). A catalog of white light coronal mass ejections observed by the SOHO spacecraft. *Journal of Geophysical Research*, 109, A07105. <https://doi.org/10.1029/2003JA010282>
- Zhao, L.-L., & Zhang, H. (2016). Transient galactic cosmic-ray modulation during solar cycle 24: A comparative study of two prominent Forbush decrease events. *The Astrophysical Journal*, 827(1), 13.
- Žic, T., Vršnak, B., & Temmer, M. (2015). Heliospheric propagation of coronal mass ejections: Drag-based model fitting. *The Astrophysical Journal Supplement Series*, 218(2), 32.

In the following study, we investigate a separate sample of ICMEs that were detected by the STEREO heliospheric imagers (HIs) and propagated towards Mars, validating their arrival times using the FDs detected at MSL/RAD. A similar study has been performed by Möstl et al. (2017) with in situ measurements at different locations in the inner heliosphere, but this is the first validation of Mars arrival times calculated with the STEREO-HI data. The study also includes some ICMEs that hit the MSL spacecraft during its cruise phase. For the analysis of the HI data, three different single-spacecraft geometric reconstruction methods will be described (fixed ϕ , harmonic mean, and self-similar expansion), and applied to the J-maps. For an introduction into these methods, see Section 2.4 and references therein.

The results show that the performance of the single-spacecraft fitting methods applied to HI data for predicting ICMEs arrivals (see also Section 2.4) is not flawless, as especially the reconstructed propagation longitude has a large uncertainty: Only (39 ± 6) % of the events predicted to hit Mars (or MSL) were actually observed with a clear FD. This may in part also be due to weak ICMEs or flank encounters, which may not cause a strong FD. Still, this value is consistent with the performance scores calculated by Möstl et al. (2017) for the arrival at other locations closer to the Sun.

At the time of this study, we used version 5 of the HELCATS CME kinematics catalog (HIGeoCat), which was updated until the end of September 2017. We have made the arrival time calculations ourselves based on the data available in the HI-GeoCat as the arrival time catalog (ARRCAT) had only been updated until September 2014. After the publication of this study, some updates to the catalog have been released¹, with the latest version from October 8, 2020 containing 82 additional ICMEs (1541 events compared to 1459), which were all observed by STEREO-A HI as there is still no new data available from STEREO-B (see Section 2.4). According to the arrival time catalog (ARRCAT), which is calculated from these data and has been updated until the end of August 2020 on the *Helio4Cast* website², 13 additional ICMEs detected in the recent years have also been determined to hit Mars based on the HI data (5 in 2018, 1 in 2019, and 7 in 2020). The presence of corresponding MSL/RAD FD signatures for these events should be reviewed in future studies.

The following article is reproduced from Freiherr von Forstner et al. (2019) with permission from Space Weather, ©American Geophysical Union:

TRACKING AND VALIDATING ICMEs PROPAGATING TOWARD MARS USING STEREO HELIOSPHERIC IMAGERS COMBINED WITH FORBUSH DECREASES DETECTED BY MSL/RAD

Freiherr von Forstner, J. L., J. Guo, R. F. Wimmer-Schweingruber, M. Temmer, M. Dumbović, A. Veronig, C. Möstl, D. M. Hassler, C. J. Zeitlin, and B. Ehresmann, *Space Weather*, 17, 4, pages 586–598 (2019), DOI: 10.1029/2018SW002138

Own contribution: 90%

¹ https://www.helcats-fp7.eu/catalogues/wp3_cat.html

² <https://helioforecast.space/arrcat>

Space Weather

RESEARCH ARTICLE

10.1029/2018SW002138

Key Points:

- One hundred forty-nine ICMEs propagating toward Mars are studied, combining data from STEREO Heliospheric Imagers with Forbush decreases at MSL/RAD
- Forty-five ICMEs can be clearly associated with a Forbush decrease at MSL/RAD; many others are uncertain due to, for example, CME-CME interaction
- Arrival times predicted from HI data agree with RAD data with a standard deviation of ~17 to 19 hr

Correspondence to:

J. Guo,
jnguo@ustc.edu.cn

Citation:

Freiherr von Forstner, J. L., Guo, J., Wimmer-Schweingruber, R. F., Temmer, M., Dumbović, M., Veronig, A., et al. (2019). Tracking and validating ICMEs propagating toward Mars using STEREO Heliospheric Imagers combined with Forbush decreases detected by MSL/RAD. *Space Weather*, 17, 586–598. <https://doi.org/10.1029/2018SW002138>

Received 7 DEC 2018

Accepted 20 MAR 2019

Accepted article online 1 APR 2019




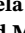





Published online 12 APR 2019

Corrected 24 APR 2019

This article was corrected on 24 APR 2019. See the end of the full text for details.

©2019. American Geophysical Union. All Rights Reserved.

Tracking and Validating ICMEs Propagating Toward Mars Using STEREO Heliospheric Imagers Combined With Forbush Decreases Detected by MSL/RAD

Johan L. Freiherr von Forstner¹ , Jingnan Guo^{1,2} , Robert F. Wimmer-Schweingruber¹ , Manuela Temmer³ , Mateja Dumbović³ , Astrid Veronig³ , Christian Möstl⁴ , Donald M. Hassler⁵ , Cary J. Zeitlin⁶ , and Bent Ehresmann⁵ 

¹Institute of Experimental and Applied Physics, University of Kiel, Kiel, Germany, ²School of Earth and Space Sciences, University of Science and Technology of China, Hefei, China, ³Institute of Physics, University of Graz, Graz, Austria, ⁴Space Research Institute, Austrian Academy of Sciences, Graz, Austria, ⁵Southwest Research Institute, Boulder, CO, USA, ⁶Leidos, Houston, TX, USA

Abstract The Radiation Assessment Detector (RAD) instrument onboard the Mars Science Laboratory (MSL) mission's Curiosity rover has been measuring galactic cosmic rays (GCR) as well as solar energetic particles (SEP) on the surface of Mars for more than 6 years since its landing in August 2012. The observations include a large number of Forbush decreases (FD) caused by interplanetary coronal mass ejections (ICMEs) and/or their associated shocks shielding away part of the GCR particles with their turbulent and enhanced magnetic fields while passing Mars. This study combines MSL/RAD FD measurements and remote tracking of ICMEs using the Solar TERrestrial Relations Observatory (STEREO) Heliospheric Imager (HI) telescopes in a statistical study for the first time. The large data set collected by HI makes it possible to analyze 149 ICMEs propagating toward MSL both during its 8-month cruise phase and after its landing on Mars. We link 45 of the events observed at STEREO-HI to their corresponding FDs at MSL/RAD and study the accuracy of the ICME arrival time at Mars predicted from HI data using different methods. The mean differences between the predicted arrival times and those observed using FDs range from –11–5 hr for the different methods, with standard deviations between 17 and 20 hr. These values for predictions at Mars are very similar compared to other locations closer to the Sun and also comparable to the precision of some other modeling approaches.

1. Introduction

Coronal mass ejections (CMEs), clouds of magnetized plasma expelled from the Sun, often at high speeds, are one of the main concerns of space weather research. The passage of CMEs at Earth can cause geomagnetic storms (e.g., Cane et al., 2000), which are severe disruptions of the terrestrial magnetic field that can in some cases have serious impact on infrastructure on the surface of Earth, such as damaging electricity grids (Boteler et al., 1998; Oughton et al., 2017). Additionally, shocks driven by fast CMEs are believed to be one of the phenomena responsible for the acceleration of solar energetic particles (SEPs, see, e.g., Reames, 2013), which may cause radiation damage to spacecraft, aircraft, and astronauts. Consequently, the observation, modeling, and, eventually, forecasting of CMEs and their interplanetary counterparts (ICMEs) as well as their impacts on Earth have been important topics in the space weather community in the last decades.

CMEs are usually detected remotely using coronagraph instruments, while their interplanetary counterparts can be observed in situ by their signatures in the interplanetary magnetic field, as well as plasma parameters such as the solar wind speed, density, and temperature (cf. Zurbuchen & Richardson, 2006). Additionally, ICMEs impact the galactic cosmic ray (GCR) flux in the form of short-term decreases, first observed by Forbush (1937) and Hess and Demmelmair (1937), and later named Forbush decreases (FDs). Since then, numerous authors have studied these effects, which are caused by the magnetic field structure of the ICME and/or its preceding shock shielding parts of the incoming GCR away from the measurement location. The decrease usually takes less than a day while the recovery period of the GCR flux back to its previous level

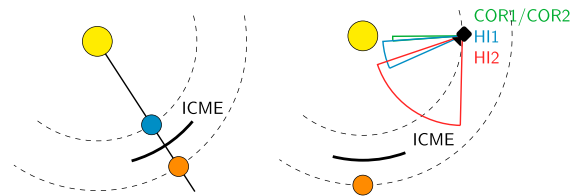


Figure 1. Cartoon comparison of the opposition phase constellation to the observation of interplanetary coronal mass ejections (ICMEs) with the STEREO SECCHI instruments. Observations of the same ICME at Earth and Mars are only possible within a small longitudinal separation between the two planets (left, see Freiherr von Forstner et al., 2018), while the STEREO-HI telescopes allow a continuous remote tracking of ICMEs in a wider range of directions (right, this study). STEREO = Solar TERrestrial Relations Observatory; SECCHI = Sun Earth Connection Coronal and Heliospheric Investigation; HI = Heliospheric Imager.

can be much longer (about 1 week). In the case where both a shock/sheath and the ICME ejecta pass the measurement location, the FD can show a two-step structure, as described by, for example, Cane (2000). FD measurements are suitable for the detection of the arrival time of ICMEs as their onset time usually matches very closely to the corresponding solar wind structure (Cane et al., 1996; Dumbović et al., 2011), and multiple researchers have previously used FDs for this purpose in cases where solar wind and magnetic field measurements are not available (e.g., Lefèvre et al., 2016; Möstl et al., 2015; Vennerstrøm et al., 2016), as was the case at Mars until the MAVEN mission arrived in September 2014—and even MAVEN does not continuously measure the upstream solar wind due to its elliptic orbit that regularly enters Mars’s magnetosphere. Witasse et al. (2017) have also used Forbush decreases to observe the same ICME at multiple locations in the heliosphere out to 9.9 AU.

Similar decreases in the GCR flux can also be caused by stream interaction regions (SIRs), which are the regions where fast and slow solar wind

interact. SIRs often repeat for several solar rotations when the coronal hole structures at the solar surface producing these high speed streams are long-lived (see, e.g., Heinemann et al., 2018). These recurrent GCR decreases are also called FDs by some authors, but in this work, we focus on ICME-caused FDs, as we are using them to investigate the propagation of ICMEs.

Considering the increased interest in the exploration of Mars in the recent times, with multiple ongoing robotic missions and plans for human missions in the future, it becomes important to study the effects of radiation and space weather on Mars as well. In our previous work (Freiherr von Forstner et al., 2018), we presented the first statistical studies of ICMEs arriving at Mars, using data from the *Mars Science Laboratory* (MSL) mission’s *Radiation Assessment Detector* (RAD) instrument, which can detect FDs caused by ICMEs passing Mars. The study was based on in situ observations of the same ICMEs, first at Earth or one of the Solar TERrestrial Relations Observatory (STEREO) spacecraft (i.e., at a radial distance of about 1 AU from the Sun), and then at Mars (which has a radial distance of about 1.5 AU) yielding the result that most ICMEs in our sample continued to decelerate slightly beyond 1 AU, dragged by the slower surrounding solar wind. The amount of deceleration and the ICME speed relative to the ambient solar wind were also found to have a tendency to correlate, but the statistical significance was limited due to the small number of 15 events that could be studied during close alignment of Mars and Earth or STEREO (cf. Figure 1, left).

To enable a more complete observation-based study of ICMEs propagating toward Mars, we turn to remote observations in the current study, in particular those made possible by the Heliospheric Imager (HI) telescopes on the STEREO spacecraft. They facilitate tracking of ICMEs all the way from the Sun to approximately 1 AU in a wide range of directions, thus making the study less dependent on a certain constellation of planets and spacecraft (Figure 1, right).

In this study, we will combine data from the STEREO-HI instruments with MSL/RAD observations to investigate ICMEs and FDs at Mars in more detail as well as to validate the accuracy of determining the ICME arrival at MSL using STEREO-HI data.

2. Data and Methods

2.1. The MSL/RAD Instrument

Since the *Curiosity* rover of NASA’s MSL mission (Grotzinger et al., 2012) landed on Mars on 6 August 2012, its RAD (Hassler et al., 2012) instrument, built in a cooperation between Kiel University, German Aerospace Center (DLR) and Southwest Research Institute (SwRI), has been continuously measuring the particle radiation environment on the surface of Mars. RAD can detect neutral and charged particles using a setup of six detectors, named A through F. For two of the detectors (B and E), the dose rate contributed from all particles observed in the detector is also measured.

The radiation measured on the surface of Mars consists of primary GCRs and SEPs as well as secondary particles created when the primary radiation interacts with the Martian atmosphere (e.g., Guo et al., 2018). The daily variation of atmospheric pressure causes a diurnal pattern in the dose rate measured at MSL/RAD

(Rafkin et al., 2014). Similar to neutron monitors on Earth and other cosmic ray detectors in deep space, RAD can be used for detecting FDs in the GCR. Due to the larger geometric factor, the dose rate in the E detector, a plastic scintillator, is best used for this purpose. To simplify the detection of FDs in the RAD data, the dose rate measurements are processed using a spectral notch filter described by Guo et al. (2018) to compensate for the diurnal variations.

RAD was also active during most of the time of the MSL rover's flight from Earth to Mars from December 2011 to July 2012 (the so-called *cruise phase*). Without the Martian atmosphere around it, part of the RAD view cone was only very lightly shielded during this period (Zeitlin et al., 2013) and thus observed a different range of energies in the primary GCR spectrum and a higher number of SEP events. Besides, FDs were also detected during the cruise phase (Guo et al., 2015).

2.2. The STEREO Heliospheric Imagers

The STEREO mission (Russell, 2008) was launched in 2006. Its two spacecraft, STEREO A (*Ahead*) and STEREO B (*Behind*) enabled a stereoscopic view of the Sun and inner heliosphere for the first time, with one of the main objectives being the study of CMEs and their impact on Earth. The Sun Earth Connection Coronal and Heliospheric Investigation instrument suite (SECCHI, Howard et al., 2008) on STEREO consists of multiple telescopes observing the Sun and heliosphere with different fields of view and wavelengths. The Heliospheric Imagers HI1 and HI2 are white-light telescopes and have the largest field of view—combined ranging from 4 to 88.7° on one side of the Sun. This provides an excellent opportunity to observe ICMEs traveling from the Sun outward to 1 AU and beyond.

Connection to the STEREO B spacecraft was lost on 1 October 2014, a few months before its solar conjunction. So after this date, data are only available from STEREO A.

2.3. Reconstruction of ICME Kinematics From STEREO-HI Data

As ICME propagation is a three-dimensional phenomenon, it is not trivial to derive the trajectory from just one (or, for ICMEs seen by both STEREO spacecraft, two) series of 2-D images from STEREO-HI. The analysis of HI images is therefore typically based on the identification of ICMEs in J-Map (time-elongation map) diagrams, developed by Sheeley et al. (1999) for the analysis of coronagraph images and applied to STEREO-HI by Rouillard et al. (2008) and Davies et al. (2009), combined with a number of different single-spacecraft fitting or multispacecraft triangulation methods to reconstruct the ICME kinematics.

The time-elongation profile identified in J-Maps is converted to the ICME's radial distance $r(t)$ from the Sun based on assumptions about the shape of the ICME and its appearance in the HI images. Different approaches for this conversion can be separated into two types: Single-spacecraft reconstruction methods are based on images from just one of the STEREO spacecraft, while multispacecraft approaches use data from both spacecraft to further constrain the parameters of the ICME trajectory (e.g., Liu, Davies, et al., 2010; Liu, Thernisien, et al., 2010; Lugaz et al., 2010a).

These multispacecraft triangulation methods have been used to study many ICMEs propagating toward Earth, and they make it possible to relax some of the assumptions that need to be made when using only single-spacecraft methods. This allows for a detailed study of the ICME's speed profile within the HI field of view (e.g., Liu et al., 2013, 2016). However, the orbits of the STEREO spacecraft are optimized for observing Earth-directed structures and thus multispacecraft HI observations are often not possible for ICMEs propagating toward Mars. Also, our study includes some events after 2014, where only STEREO A is available. Therefore, we will focus on the most common single-spacecraft methods here, which are shown in Figure 2.

One of the simplest single-spacecraft reconstruction methods is the Point-P method (PP; Howard et al., 2006), where the ICME is regarded as an expanding circular front centered around the Sun. On the contrary, the Fixed- ϕ model (FP; Kahler & Webb, 2007; Sheeley et al., 1999) reduces the shape of the ICME to a single point moving away from the Sun radially with a fixed longitudinal separation ϕ from the observer. The Harmonic Mean method (HM; Lugaz et al., 2009) is a middle ground between these two extremes, where the circular ICME has one edge fixed at the Sun instead of being centered around it, which is equivalent to calculating the harmonic mean of the PP and FP results. Appendix B of Liu, Thernisien, et al. (2010) contains a more detailed description of these three methods.

Finally, the more recent self-similar-expansion method (SSE; Davies et al., 2012; Lugaz et al., 2010b) introduces a second parameter λ for the half-width of the ICME, which can be seamlessly adjusted between the two edge cases for $\lambda = 90^\circ$ (\Rightarrow HM) and $\lambda = 0^\circ$ (\Rightarrow FP).

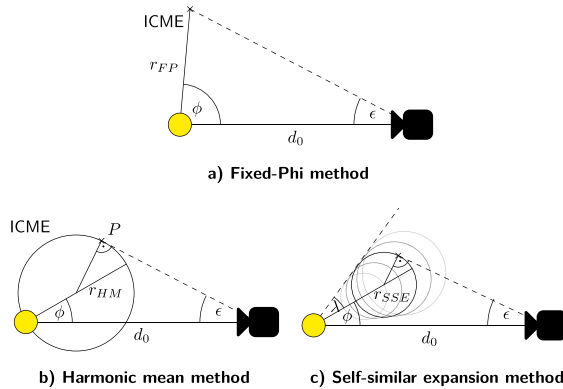


Figure 2. Single-spacecraft reconstruction methods for Heliospheric Imaging observations: (a) Fixed ϕ (Kahler & Webb, 2007), (b) Harmonic mean (Lugaz et al., 2009), and (c) self-similar expansion (Davies et al., 2012; Lugaz et al., 2010b).

The FP, HM, and SSE methods are usually combined with fitting algorithms (FPF, HMF, and SSEF) to determine parameters such as the longitudinal propagation direction of the CME under the assumption of a constant speed. As the leading edge of the visible structure is marked in the J-Map, $r(t)$ and the resulting speed v are believed to most likely correspond to the shock front, if present, and otherwise the front of the ICME ejecta.

2.4. The HELCATS Catalogs

On its website at <https://www.helcats-fp7.eu>, the *Heliospheric Cataloguing, Analysis and Techniques Service* EU project (HELCASTS; Helcats et al., 2018) has collected a large number of ICMEs observed with the STEREO-HI instruments. Their *HIGeoCat* CME kinematics catalog (version 5) contains 1459 ICMEs, each one supplemented with the associated J-Map and a time-elongation profile extracted from it by manual selection. Results for ICME speeds and propagation directions derived using the FPF, HMF, and SSEF methods are also provided (under the assumption of a constant speed v , longitude ϕ , and in the SSE case, a fixed half-width of $\lambda = 30^\circ$).

The *ARRCAT* arrival catalog contains a list of predicted in situ arrival times of ICMEs at different planets and spacecraft including MSL, based on the events in the *HIGeoCat* and currently (version 01) updated until the end of September 2014, where STEREO B data ends. As described by Möstl et al. (2017), the arrival time predictions were calculated based on the SSEF30 method results from *HIGeoCat*, extrapolating the trajectory up to the respective location based on the constant speed v . The calculation also includes the correction described by Möstl and Davies (2013) to account for the SSE geometry at locations that are not directly hit by the ICME apex.

Möstl et al. (2017) also compared the *ARRCAT* data for multiple locations in the inner heliosphere with in situ plasma and magnetic field data to check the accuracy of the predicted arrival times. However, their study does not include MSL or other spacecraft at Mars.

3. Results and Discussion

3.1. ICMEs Observed by STEREO-HI and Their Arrival Times at MSL/RAD

To analyze ICMEs that arrived at MSL, we first select candidate events from the HELCATS *HIGeoCat* by requiring the propagation direction (heliospheric longitude, determined using the SSEF30 method) to be within $\pm 30^\circ$ of MSL's longitude at that time. Although the longitude depends considerably on the geometry used for fitting the HI data (Liu et al., 2013, 2016; Lugaz et al., 2009), we use the modeled direction from SSE as it is the most advanced of the three methods available in the *HIGeoCat*. Also, this selection criterion is equivalent to the one used for the HELCATS *ARRCAT* catalog and the corresponding paper by Möstl et al. (2017), making it possible to compare to their results afterward (see section 3.2). The selection yields 149 ICME events between the beginning of MSL's cruise phase in November 2011 and the current end of the *HIGeoCat* catalog (version 5) in November 2017. Thirty-one of these events were observed with both STEREO spacecraft according to the HELCATS *HIJoinCat* catalog, the remaining 118 ICMEs were only detected by one of them. For events where observations from both spacecraft were available, we use the spacecraft data which predict an arrival at MSL based on the SSEF30 fitting. If both STEREO observations predict the ICME to arrive at MSL, we use STEREO A data as a preference.

A plot showing the time distribution of the 149 events is displayed in Figure 3. It can easily be seen that the ICMEs are not evenly distributed, but rather concentrated into three discrete periods. The reason for this is that in contrast to the coronagraph instruments, the heliospheric imagers' fields of view are limited to one side of the Sun, and the STEREO spacecraft are always pointed in a way that the side of the Sun at which HI is

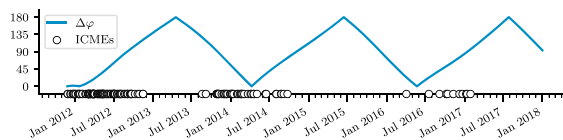


Figure 3. Time distribution of the 149 ICMEs propagating toward MSL $\pm 30^\circ$ from the HELCATS catalog, plotted together with the longitudinal separation $\Delta\phi$ between Earth and MSL. During periods with large $\Delta\phi$, STEREO-HI cannot see ICMEs propagating toward MSL, as it is only looking at one side of the Sun. ICMEs = interplanetary coronal mass ejections; MSL = Mars Science Laboratory; HELCATS = Heliospheric Cataloguing, Analysis and Techniques Service; STEREO-HI = Solar Terrestrial Relations Observatory Heliospheric Imager.

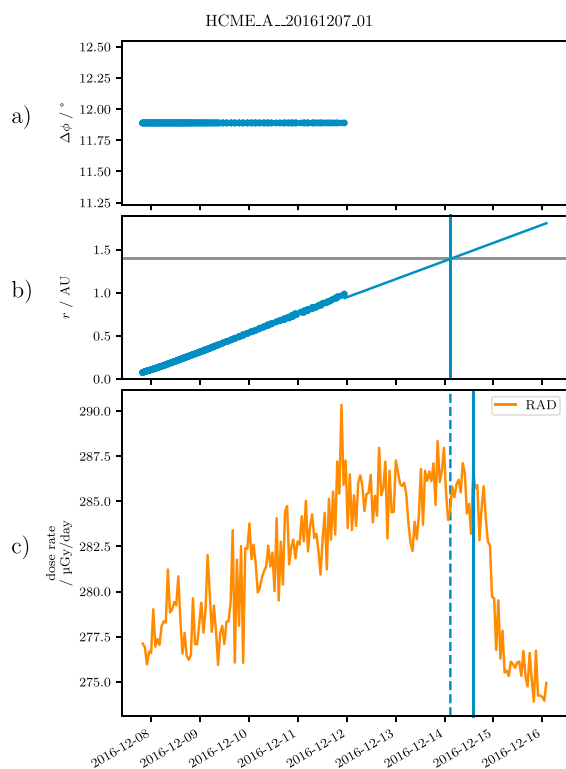


Figure 4. An example of the type of plot used to compare the ICME arrival times at Mars that were predicted using STEREO-HI observations and the onset time of the corresponding Forbush decreases detected at MSL/RAD. This plot is for the “HCME_A_20161207_01” event from the HELCATS catalog. Panel (c) shows the MSL/RAD dose rate measurements where the FD onset is marked with a solid blue line. In panel (b), the trajectory of the ICME in the direction of MSL (radial distance from the Sun over time) is plotted, which was calculated from the time-elongation data using the SSEF30 method and then extrapolated assuming the launch time and the constant speed that result from the SSEF30 fitting procedure. The blue vertical line in this panel marks the time where the extrapolation intersects Mars’s radial distance from the Sun, that is, the predicted arrival time at Mars, and this line was extended into panel (c) as a dashed line. Panel (a) shows the longitudinal separation between Mars and the ICME apex (in this case constant, because it is determined from the SSEF30 fit). ICME = interplanetary coronal mass ejection; STEREO = Solar TErrestrial RElations Observatory; HI = Heliospheric Imager; MSL/RAD = Mars Science Laboratory/Radiation Assessment Detector; HELCATS = Heliospheric Cataloguing, Analysis and Techniques Service.

looking is the one where Earth is located. So when, for example, Earth is on the right side of the Sun as seen from one of the STEREO spacecraft while Mars is on the left side, ICMEs propagating toward Mars cannot be seen using the HI instruments on this spacecraft. The last period in 2016–2017 has fewer events, which is related to the solar cycle approaching its minimum as well as the loss of STEREO B data since 2014.

For each of the 149 events, a plot similar to Figure 4 was constructed, showing time series of the ICME’s radial distance from the Sun, which were derived using the SSE geometry and the longitude derived from the SSEF30 method results (Figure 4b), the longitudinal separation between the CME apex and MSL’s location (Figure 4a) and the MSL/RAD dose rate processed using the notch filter described in section 2.1 (Figure 4c). The time-distance plot was corrected based on the longitudinal separation between the ICME apex and MSL using the equation from Möstl and Davies (2013) so that it shows the radial distance of the part of the ICME in the SSE geometry that hits MSL, therefore resulting in a slightly lower speed. The predicted ICME arrival time at MSL could then be calculated based on the $r(t)$ trajectory and was marked with a vertical line in both the $r(t)$ and RAD dose rate panels.

It needs to be stated that these “predictions” were done on the basis of postevent analysis using science data and not real-time beacon data. However, as ICMEs are usually only visible in HI images up to about 1 AU or less, the predictions at Mars are probably comparable to what could have been done with real-time data in most cases—in contrast to the ARRCAT predictions at locations closer to the Sun (Möstl et al., 2017), which are partly based on observations that would only have been available after the ICME arrival. A study using real-time STEREO-HI data was conducted by Tucker-Hood et al. (2015).

Based on the predicted arrival time at MSL/RAD, a corresponding FD in the MSL/RAD data was searched for. In general, we used a time window of at most ± 2.5 days around the predicted arrival time to make sure that the FD onset time was not too far off and thus maybe related to a completely different event. We also took care that series of events predicted to arrive in a certain order were matched to the FDs in the correct sequence if no interaction between the ICMEs is predicted, and that for CMEs also seen at Earth close to oppositions of MSL and Earth, the arrival at Mars is not earlier than the one at Earth. Although the time window might seem quite small for slow CMEs, a larger window would have caused more ambiguous cases with multiple candidate FDs.

The FD onset was marked to be the point in time where the GCR intensity reaches its maximum at the beginning of the FD. This makes the onset time a more well-defined quantity compared to just marking it “by eye,” and was implemented by searching for the maximum within a ± 4 -hr window around the onset time that was first manually selected.

In the process of marking the FD onset times, the 149 ICMEs were sorted into five categories, by looking at the RAD data as well as the ICME trajectories calculated from HI data and their extrapolations:

1. Events with a clearly identifiable FD at MSL—40 ICMEs
2. ICMEs that might have interacted with others on their way to MSL, but still have a clear correspondence to a FD at Mars (either completely separate or multiple steps)—five ICMEs
3. ICMEs that probably interacted with others on their way to MSL, so that their FDs cannot be matched unambiguously (e.g., because there is only one merged FD or none at all) at MSL—53 ICMEs

Table 1
Table of All 45 Events Where An Arrival Time at Mars Could be Determined (Categories 1 and 2 From Section 3.1)

HCME_A_...	HCME_B_...	SC	ϕ_{SSE} (°)	$\Delta\phi_{STEREO}$ (°)	v_{SSE} (km/s)	$\Delta\phi_{MSL}$ (°)	t_{MSL}	T_{MSL} (day)	$\Delta\phi_{Earth}$ (°)	t_{Earth}
20111211_01	20111211_01	A	3	-27	452	-28.7	2011-12-17 01	5.8	-27	
20111222_01		A	221	-24	320	-25.3	2011-12-28 08	6.1	-24	
	20111226_01	B	206	15	686	13.7	2011-12-30 01	3.7	15	
20120123_01	20120123_01	A	207	20	1,052	20.4	2012-1-24 21	1.9	20	
	20120224_01	B	100	-25	885	-17.6	2012-2-27 08	3.2	-25	2012-2-26 23
20120310_01	20120310_01	A	266	-14	1,447	-1.9	2012-3-12 21	2.3	-14	2012-3-12 02
20120322_01	20120322_01	A	127	-3	469	13.1	2012-3-28 11	6.5	-3	2012-3-26 20
20120415_01	20120415_02	B	133	-39	316	-13.4	2012-4-21 02	5.9	-39	
	20120512_01	B	159	-19	869	17.9	2012-5-15 12	3.6	-19	2012-5-15 00
20120530_01		A	261	-30	686	15.5	2012-6-3 04	3.6	-30	2012-6-2 07
	20120702_01	B	163	-55	697	6.2	2012-7-6 07	4	-55	
20120702_01	20120702_02	B	173	-44	398	17.4	2012-7-9 10	7	-44	
	20120915_01	B	223	-85	441	11	2012-9-21 17	6.5	-85	
	20120918_01	B	193	-84	412	13.1	2012-9-23 14	6.1	-84	
	20120920_01	B	141	-99	528	-1.6	2012-9-25 09	5.2	-99	
	20120922_01	B	111	-111	562	-13	2012-9-27 01	5.5	-111	
	20120923_01	B	121	-78	620	21.5	2012-9-28 10	5	-78	
	20121022_01	B	92	-95	427	16.3	2012-10-27 08	5.7	-95	
	20121029_01	B	357	-89	342	24.6	2012-11-5 16	7.5	-89	
	20121115_01	B	127	-110	349	10.3	2012-11-20 19	6.7	-110	
	20121116_01	B	108	-105	534	15.5	2012-11-20 06	4.4	-105	
20130820_01	20130820_01	A	263	105	701	-22.5	2013-8-24 22	5.1	105	
20131119_01		A	87	55	577	-24.4	2013-11-25 01	5.8	55	
20140101_01		A	249	58	311	2.4	2014-1-10 11	9.7	58	
20140114_01		A	65	46	655	-1.3	2014-1-18 09	4.5	46	
20140130_01		A	197	37	451	-0.6	2014-2-6 18	7.2	37	2014-2-5 18
20140204_01		A	111	9	832	-26.1	2014-2-8 14	4.7	9	2014-2-7 20
20140213_01	20140213_01	A	42	58	661	28	2014-2-17 06	4.4	58	2014-2-15 13
20140220_01		A	298	50	763	24.1	2014-2-24 04	4	50	2014-2-23 14
20140225_01		A	198	13	661	-10.2	2014-3-1 10	4.5	13	2014-2-28 02
20140322_01		A	244	34	798	24.9	2014-3-26 22	4.6	34	
20140404_01		A	54	9	895	6.6	2014-4-6 16	2.8	9	2014-4-5 11
	20140407_01	B	335	-26	535	-26.5	2014-4-14 04	7	-26	2014-4-11 16
20140418_01		A	218	-3	1,265	1.8	2014-4-20 16	2.8	-3	2014-4-20 09
20140418_02		A	235	22	1,092	27.1	2014-4-22 02	3.7	22	2014-4-20 17
20140504_01		A	15	4	866	16.9	2014-5-7 02	3.4	4	
	20140801_01	B	237	-24	754	29.2	2014-8-4 23	3.3	-24	
	20140803_01	B	218	-26	790	27.7	2014-8-6 20	3.9	-26	

4. Other events that do not show a clear FD at Mars (either the FD is too weak or the ICME missed MSL completely)—19 ICMEs
5. Events where the analysis could not be applied due to a data gap or an SEP event at MSL/RAD coinciding with the FD or poor visibility in the STEREO-HI image leading to a high uncertainty of the predicted arrival time—32 ICMEs

This categorization shows that for all 117 events where the HI and RAD data quality is sufficient (excluding category 5), 45 are clearly identifiable. So, based on the results for our sample, there is a $(39 \pm 6)\%$ chance

Table 1 (continued)

HCME_A_...	HCME_B_...	SC	ϕ_{SSE} (°)	$\Delta\phi_{STEREO}$ (°)	v_{SSE} (km/s)	$\Delta\phi_{MSL}$ (°)	t_{MSL}	T_{MSL} (day)	$\Delta\phi_{Earth}$ (°)	t_{Earth}
	20140923_02	B	178	-102	754	-28	2014-9-28 09	4.7	-102	
20160403_01		A	132	0	751	-23.2	2016-4-6 05	3.4	0	
20161007_01		A	112	-56	478	-3.5	2016-10-12 14	4.9	-56	
20161013_01		A	32	-64	345	-9.3	2016-10-19 15	6.5	-64	
20161109_01		A	15	-90	314	-26.7	2016-11-17 17	9.1	-90	
20161207_01		A	23	-63	381	12	2016-12-14 14	7.1	-63	
20161222_01		A	187	-67	330	12.9	2016-12-29 12	7.5	-67	

Note. The first two columns show the IDs of the ICMEs in the HELCATS catalog for STEREO A and B observations, which also correspond to the date where the ICME was first observed in HI images, and the third column shows the STEREO spacecraft that was used for applying the fitting methods. The fourth and sixth columns show the longitude ϕ and the speed v of the ICME as determined by the HELCATS project using the SSEF30 method. Additional columns show the differences between ϕ and the heliospheric longitudes of the respective STEREO spacecraft (column 5) or MSL (column 7) at that time as well as the in situ arrival time (Forbush decrease onset) at MSL and the transit time T_{MSL} between the launch at the Sun and arrival at MSL. The arrival time and longitudinal separation are also given for the arrival at Earth, if applicable. Dates are formatted as year-month-day. ICMEs = interplanetary coronal mass ejections; HELCATS = Heliospheric Cataloguing, Analysis and Techniques Service; STEREO = Solar TERrestrial Relations Observatory; SSE = self-similar-expansion method; MSL = Mars Science Laboratory.

that an ICME observed in STEREO-HI and predicted to arrive at MSL by the SSEF30 method data is actually observed through a FD at MSL/RAD that is clearly related to the ICME. This is consistent with the performances between 12% and 44% for different locations in the inner heliosphere found by Möstl et al., 2017 (2017, see their Table 1).

In $(50 \pm 8)\%$ of the cases, multiple ICMEs interacted and possibly merged, making it impossible to unambiguously match the FD to a single ICME (Category 3). When only considering the 59 individual ICMEs with no others occurring in quick succession and similar direction (Categories 1 and 4), the chance that a clearly related FD is observed at Mars grows to $(68 \pm 14)\%$. The uncertainties of the percentages given here were calculated assuming Poisson statistics ($\sigma = \sqrt{N}$).

Only the events in categories 1 and 2 will be used in the following studies, as these are the only ones where an arrival time at MSL could be defined. A list of these events with the relevant SSE fit results and FD onset times can be found in Table 1.

Fourteen of these 45 ICMEs were close to oppositions of Earth and Mars (cf. Figure 1, left) and thus were also seen at Earth. In these cases, we also included the arrival times at Earth, which were derived in a similar fashion based on FD in data from the South Pole neutron monitor. We have also done a basic comparison of arrival times at Earth with visible shock and/or ICME structures in solar wind and magnetic field measurements from ACE, and found that the Forbush decrease onsets agree reasonably well (usually within $\sim \pm 2$ hr) with these data.

3.2. Comparison of FD Results With STEREO-HI Predictions

For the 45 events where a clear FD at Mars was found (see Table 1), we compared the measured FD onset times to the predicted arrival times using the three single-spacecraft fitting methods used in the HELCATS catalog. Figure 5 shows histograms of the time difference $\Delta t = t_{\text{calculated}} - t_{\text{observed}}$ for each of the three methods with two approaches.

First, Figures 5a–5c show the results from the original techniques (summarized by Möstl et al., 2014), which assume a constant speed and direction to calculate the CME arrival times at Mars. They are based on the CME speed and launch times in the HELCATS HIGeoCAT catalog and we take into account the appropriate correction equations for the circular CME front shapes in the HM and SSE geometries (see Möstl & Davies, 2013; Möstl et al., 2011). This is similar to the aforementioned ARRCAT for SSEF, but here we also include the FPF and HMF methods.

Secondly, in Figures 5d–5f, results on the differences between calculated and observed arrival times are presented, which were generated with an extrapolation method. Here, we do not assume a constant CME speed over the whole HI field of view, but instead only for an interval over the last 10 available HI data points, allowing an acceleration or deceleration before this time. The physical reason behind this assumption is that

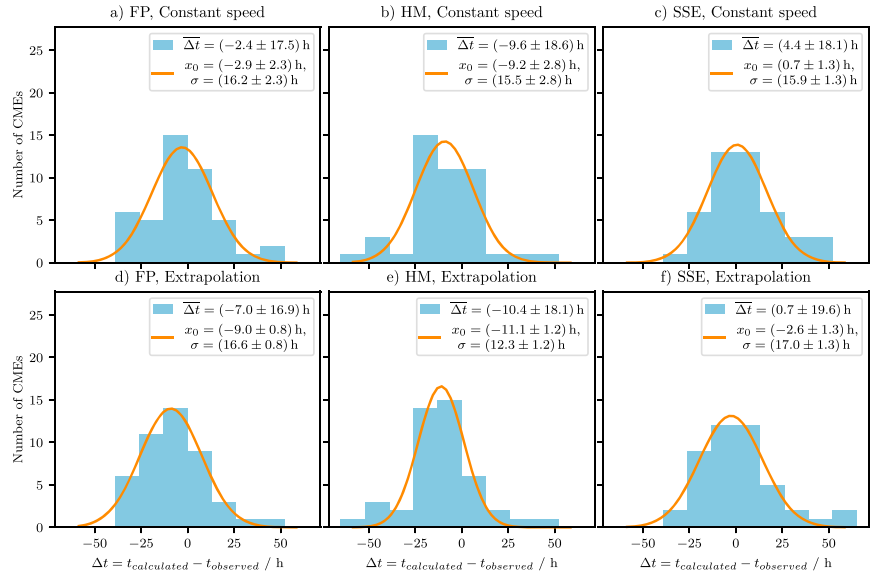


Figure 5. Comparison of arrival times predicted using STEREO-HI tracking with the FP, HM, and SSE methods to actual FD onset times measured at MSL/RAD. $\Delta t < 0$ or $\Delta t > 0$ corresponds to an earlier/later predicted arrival compared to the FD onset. Panels (a)–(c) use the fitting results assuming a constant speed throughout the HI field of view, panels (d)–(f) extrapolate the results using a line fitted to the last 10 points of the $r(t)$ trajectory. All panels have the same x and y axes scaling as well as the same histogram bins. Additionally, a Gaussian distribution fitted to the histograms is displayed. The legends show both the results for the mean and standard deviation of Δt calculated directly from the distribution as well as the parameters x_0 and σ obtained from the Gaussian fit. STEREO = Solar TERrestrial Relations Observatory; HI = Heliospheric Imager; FP = Fixed- ϕ method; HM = Harmonic Mean method; SSE = self-similar-expansion method; MSL/RAD = Mars Science Laboratory/Radiation Assessment Detector; FD = Forbush decreases.

CMEs decelerate or accelerate closer to the Sun and eventually reach an equilibrium with the background solar wind (e.g., Liu et al., 2013). For the larger heliocentric distances of Mars compared to the inner planets, an assumption of constant speed over the full HI field of view may lead to systematic shifts in the predicted arrival times. To this end, for each event an $r(t)$ kinematic is created by the FP, HM, and SSE conversion methods for elongation to distance, including the correction formulas for HMF and SSEF, and a linear fit was applied to the 10 points farthest from the Sun. The arrival time of the CME is then taken as the time where the linear fit intersects the current radial distance of Mars from the Sun.

Note that this second method is not fully self-consistent. In order to derive $r(t)$ we need a CME direction, and the direction from single-spacecraft fitting was determined with the assumption of constant speed. Also, the uncertainty in the elongation value of the last 10 points may be larger due to the CME appearing more faint in the HI images as it expands. This extrapolation method should thus be seen as a first step toward allowing a variation of the CME speed with HI fitting methods (elaborated by Amerstorfer et al., 2018; Rollett et al., 2016; Tucker-Hood et al., 2015) but needs to be taken with a grain of salt due to the abovementioned issues.

Comparing the Fixed- ϕ , Harmonic Mean, and SSE methods as shown in Figure 5, all perform similarly well in predicting the arrival times, with FPF and HMF (panels a and b) giving a slightly earlier arrival ($\Delta t < 0$) and SSEF (panel c) a slightly later arrival ($\Delta t > 0$) on average. The standard deviations are also similar for all three methods, they all fall into the 17-hr range. The extrapolation method in panels (d)–(f) also leads to almost similar results as the original fitting techniques.

Our result for SSE with the assumption of a constant speed ($\Delta t = 4.4 \pm 18.1$ hr, panel c) is also very similar to the values obtained by Möstl et al., 2017 (2017, their Table 1) for arrival time predictions at other locations in the heliosphere: Their results lie between -2.1 hr and 8.0 hr for the average Δt and between 12.9 hr and 23.4 hr for its standard deviation. It is interesting that there seems to be no clear dependence of the prediction accuracy (neither for the average value nor its standard deviation) on the distance from the Sun,

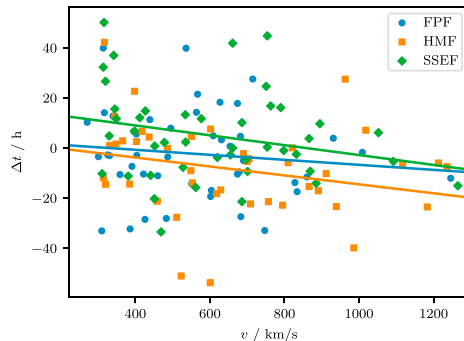


Figure 6. Plot of the dependence of the difference Δt between the predicted and observed arrival times on the speed of the ICME for the three fitting methods FPF, HMF, and SSEF. $\Delta t < 0$ or $\Delta t > 0$ corresponds to an earlier/later predicted arrival compared to the FD onset. Each of the three sets of points is supplemented with a linear regression to show the general trend. The slopes of the three lines are $(-0.010 \pm 0.013) \text{ hr}\cdot\text{km}^{-1}\cdot\text{s}$ (FPF), $(-0.018 \pm 0.008) \text{ hr}\cdot\text{km}^{-1}\cdot\text{s}$ (HMF), $(-0.020 \pm 0.010) \text{ hr}\cdot\text{km}^{-1}\cdot\text{s}$ (SEEF). If we fit all three sets of points together with one line to reduce the uncertainty, we obtain a slope of $(-0.019 \pm 0.005) \text{ hr}\cdot\text{km}^{-1}\cdot\text{s}$. ICME = interplanetary coronal mass ejection; FPF = Fixed- ϕ fitting method; HMF = Harmonic Mean fitting method; SSEF = self-similar-expansion fitting method; FD = Forbush decreases.

even though one would intuitively think that the uncertainty should increase with greater distance as errors in the model accumulate. However, at least up to Mars (~ 1.5 AU), this dependence is probably not significant compared to the inherent uncertainty coming from the strong geometric and kinematic assumptions of the method. This might change with new models such as the ElEvoHI method (Rolle et al., 2016), which relaxes the assumption of a constant speed and also allows the ICME front to have an elliptical shape instead of being necessarily circular. The inclusion of a drag-based model (Vršnak et al., 2013) for the speed evolution is especially important—the assumption of a constant speed in most previous models is very often not true due to the interaction of ICMEs with the surrounding solar wind (as shown by many previous studies, including Freiherr von Forstner et al., 2018; Vršnak & Žic, 2007; Witasse et al., 2017) as well as other heliospheric structures such as stream interaction regions and other ICMEs, with which the ICME can collide (Guo et al., 2018; Shen et al., 2012; Temmer & Nitta, 2015; Temmer et al., 2012). The ElEvoHI implementation is currently still under development and has not yet been applied automatically to large data sets such as the HELCATS catalog. Amerstorfer et al. (2018) have applied ElEvoHI ensemble modeling to a case study of one event and were able to constrain the uncertainties to less than ± 2 hr, which is a very promising result.

To find out to what extent the differences in average values as well as standard deviations for Δt between the different models are significant, we estimated the statistical error of the mean and standard deviation by

fitting a Gaussian profile to the histogram results from Figure 5, which can also be seen in the same figure. The standard deviations for both parameters σ and x_0 , calculated as the square root of the covariance matrix's diagonal, lie in the 0.8- to 2.3-hr range—so in fact, one could argue that at least with respect to the standard deviation of Δt , all single-spacecraft methods perform almost equally well on average, only the systematic offset (Δt) changes depending on the method, similar to what was previously found by Möstl et al. (2014) for ICMEs arriving at 1 AU.

Another way to look at the predicted and observed arrival times is shown in Figure 6, where Δt is plotted against the speed of the ICME. The plot suggests that there is a trend to predicting an earlier arrival for fast ICMEs ($\Delta t < 0$) and a later arrival for slow ICMEs ($\Delta t > 0$), that is, the speed of fast ICMEs is overestimated and the speed of slow ICMEs is underestimated. This is supported by the linear fits shown in the figure, which have a negative slope. Intuitively, this can be explained as being related to the assumption of a constant speed in the three fitting methods—A fast ICME usually decelerates due to the slower surrounding solar wind, but when a constant speed is assumed, the predicted arrival will be earlier. This trend may be slightly less pronounced for FPF than for the other two methods, but in all three cases, the scatter of the data points is significant.

The accuracy of the three different geometric methods can also depend on the longitudinal separation $\Delta\phi$ of the ICME and the observing STEREO spacecraft (which is also shown in Table 1). For example, when applying the FP method to an event with a large longitudinal separation, the geometry can lead to a perceived acceleration of an ICME at larger radial distances, which is often not physical (Liu et al., 2013, 2016). However, this does not directly apply to the FPF, HMS, and SSEF fitting methods, as in this case, $\Delta\phi$ is not predefined, but rather a result of the fitting method and therefore differs between the three methods. For this reason, we have not found a clear trend for the dependence of the prediction accuracy on the longitudinal separation.

The predicted arrival time uncertainties found here with a standard deviation of 17 to 20 hr for the three geometric models are similar to those obtained via some other approaches of modeling ICME propagation, such as the magnetohydrodynamic WSA-ENLIL+Cone model (Odstrcil et al., 2004) as well as the analytical Drag-Based Model (Vršnak et al., 2013). For example, Vršnak et al. (2014), who applied both models to a sample of 50 ICMEs arriving at Earth, found a standard deviation of 16.9 hr for ENLIL and 18.3 to 19.1 hr for DBM. A more recent study by Dumbović et al. (2018) using a different sample of 25 events and the ensemble

modeling versions of ENLIL and DBM found the standard deviations to be slightly lower at 14.4 hr for ENLIL and 16.7 hr for DBM. For arrivals at Mars, these standard deviations are expected to increase slightly more, as the uncertainties of the models accumulate because no measurements further away from the Sun are used to constrain the simulation. Freiherr von Forstner et al. (2018) only found a standard deviation of 11 hr between ENLIL results and measurements, but the set of events was much smaller and carefully chosen, and the simulation input parameters were additionally validated using the measurement at 1 AU, so this is not directly comparable. Dumbovič et al. (2018) also found the prediction accuracy of DBEM to be dependent on the CME speed, where fast CMEs are predicted to arrive earlier than observed—similarly to our STEREO-HI results.

This implies that the forecasting accuracy is very similar for the different fitting methods based on STEREO-HI data and simulations using DBM or ENLIL. Specifically speaking, DBM and ENLIL contain a more sophisticated description of the ICME kinematics and its interaction with the solar wind, but their initial parameters are only based on observations close to the Sun. STEREO-HI, on the other hand, is a direct observation much further out into the heliosphere, but the simple reconstruction methods based on single-spacecraft observations need to make strong assumptions on the ICME geometry and kinematics.

In Freiherr von Forstner et al. (2018), we also applied a different method of forecasting the arrival time at Mars by using the in situ measurement at 1 AU as the inner boundary condition for the DBM model, yielding a higher accuracy. However, this method is only applicable when in situ measurements are available at multiple locations preferentially radially aligned. Such observations are unfortunately rather limited and often taken from planetary missions which are not optimized for studying heliospheric physics (Winslow et al., 2018; Wang et al., 2018; Witasse et al., 2017). In the future, with more data from Parker Solar Probe and Solar Orbiter, we hope to have improved space weather forecasts based on modeling of CME propagations constrained by in situ measurements.

4. Conclusions and Outlook

In this work, we studied 149 ICMEs propagating toward Mars (between August 2012 and February 2017) as well as toward the MSL spacecraft during its flight to Mars (between December 2011 and July 2012). These events were observed remotely with the Heliospheric Imagers onboard the STEREO spacecraft as well as in situ at their arrival through FDs measured with MSL/RAD. Links were established between the remote and in situ observations, with a $(39 \pm 6)\%$ chance that an ICME that is headed for MSL $pm30^\circ$ according to the SSE model corresponds to a clear FD observed at RAD. This can be seen as a measure of the SSE model's performance for predictions of ICME arrivals at MSL's location using FDs as the method of identification of the arrival. In $(50 \pm 8)\%$ of cases, there was likely interaction between multiple ICMEs—when excluding these, the chance of a clear and distinguishable FD grows to $(68 \pm 14)\%$.

For the 45 remaining ICMEs, where a clear FD could be observed at MSL/RAD, we could also measure the accuracy for predicting the arrival time of the ICME using the SSE, Fixed- ϕ and harmonic mean geometries. The average Δt varies between -10.4 and 4.4 hr, while the standard deviations are all very similar between 16.9 and 19.6 hr. The results for the SSE method— $\Delta t = (4.4 \pm 18.1)$ hr—are very comparable to the values that Möstl et al. (2017) found for arrivals at different locations in the inner heliosphere.

These standard deviations are also similar to the performance of most other current ICME modeling approaches, such as the WSA-ENLIL+Cone model and the Drag-Based Model. In the future, better results can probably be obtained with more physical and realistic geometric models applied to heliospheric imager data, such as the ElEvoHI method (Rollett et al., 2016) as well as new state-of-the-art MHD simulations such as the recently developed EUHFORIA model (Pomoell & Poedts, 2018). Certainly, more multipoint HI observations would also be helpful, which are currently not possible as data from STEREO B is not available. Future missions carrying heliospheric imagers include NASA's recently launched Parker Solar Probe (Fox et al., 2016) with its WISPR instrument (Vourlidas et al., 2016), ESA's Solar Orbiter mission (Müller et al., 2013) currently scheduled to launch in 2020 with its SoloHI (Howard et al., 2013), as well as a possible future mission to the L5 Lagrange point (proposed by, e.g., Gopalswamy et al., 2011; Kraft et al., 2017; Lavraud et al., 2016; Vourlidas, 2015).

In a future study, we plan to use the catalog of ICMEs at Mars built in this work to investigate the properties of the FD, such as their magnitude and steepness, in more detail. For the 14 events seen at both Earth and

Mars, we will also directly compare these data at the two planets for better understanding their properties and interplanetary propagations. For up to about six events from this catalog, the ICME and FD properties can be better studied by also taking into account in situ measurements of solar wind and magnetic field from the MAVEN spacecraft that arrived at Mars in late 2014. However, MAVEN can only measure the upstream solar wind intermittently due to the spacecraft orbit (as discussed in section 1), resulting in frequent gaps in the data.

Nevertheless, our current results are important for the understanding of space weather, but of course also for the development of future deep space missions and human spaceflight to Mars, where accurate predictions of ICMEs, their associated shocks and accompanying SEP events, and their impact are essential.

Sources of Data and Supplementary Material

This section includes references to all the data used in this work.

The *HELcats* catalogs are available from the HELcats website, <https://www.helcats-fp7.eu>: HIGeoCat: <https://doi.org/10.6084/m9.figshare.5803176.v1> HJJoinCat: https://www.helcats-fp7.eu/catalogues/wp2_joincat.html ARRCAT: <https://doi.org/10.6084/m9.figshare.4588324>

RAD data are archived in the NASA planetary data systems planetary plasma interactions node (<http://ppi.pds.nasa.gov/>). Other file formats can be provided by the authors on request.

South Pole neutron monitor data can be retrieved from the Neutron Monitor Database at <http://nmdb.eu>.

A text file version of Table 1 in this work can be found on FigShare at <https://doi.org/10.6084/m9.figshare.7440245>.

References

Acknowledgments

J. v. F. thanks Joana Wanger, who helped with the task of marking FD onset times in the MSL/RAD data during her internship in the Extraterrestrial Physics group at Kiel University. C. M. thanks the Austrian Science Fund (FWF): [P26174-N27]. M. T. acknowledges the support by the FFG/ASAP Programme under grant 859729 (SWAMI). M. D. acknowledges funding from the EU H2020 MSCA grant agreement 745782 (project ForbMod). J. G. is partly supported by the Key Research Program of the Chinese Academy of Sciences under grant XDPB11. RAD is supported by NASA (HEOMD) under JPL subcontract 1273039 to Southwest Research Institute and in Germany by DLR and DLR's Space Administration grants 50QM0501, 50QM1201, and 50QM1701 to the Christian Albrechts University, Kiel. We acknowledge the NMDB database (www.nmdb.eu), funded under the European Union's FP7 Programme (contract 213007), for providing data. The data from South Pole neutron monitor is provided by the University of Delaware with support from the U.S. National Science Foundation under grant ANT0838839.

- Amerstorfer, T., Möstl, C., Hess, P., Temmer, M., Mays, M. L., Reiss, M. A., et al. (2018). Ensemble prediction of a halo coronal mass ejection using heliospheric imagers. *Space Weather*, 16, 784–801. <https://doi.org/10.1029/2017SW001786>
- Boteler, D., Pirjola, R., & Nevanlinna, H. (1998). The effects of geomagnetic disturbances on electrical systems at the earth's surface. *Advances in Space Research*, 22(1), 17–27. (Solar-Terrestrial Relations: Predicting the Effects on the Near-Earth Environment) [https://doi.org/10.1016/S0273-1177\(97\)01096-X](https://doi.org/10.1016/S0273-1177(97)01096-X)
- Cane, H. V. (2000). Coronal mass ejections and Forbush decreases. *Space Science Reviews*, 93(1), 55–77. <https://doi.org/10.1023/A:1026532125747>
- Cane, H. V., Richardson, I. G., & St. Cyr, O. C. (2000). Coronal mass ejections, interplanetary ejecta and geomagnetic storms. *Geophysical Research Letters*, 27(21), 3591–3594. <https://doi.org/10.1029/2000GL000111>
- Cane, H. V., Richardson, I. G., & von Rosenvinge, T. T. (1996). Cosmic ray decreases: 1964–1994. *Journal of Geophysical Research*, 101, 21,561–21,572. <https://doi.org/10.1029/96JA01964>
- Davies, J. A., Harrison, R. A., Perry, C. H., Möstl, C., Lugaz, N., Rollett, T., et al. (2012). A self-similar expansion model for use in solar wind transient propagation studies. *The Astrophysical Journal*, 750(1), 12.
- Davies, J. A., Harrison, R. A., Rouillard, A. P., Sheeley Jr. N. R., Perry, C. H., Bewsher, D., et al. (2009). A synoptic view of solar transient evolution in the inner heliosphere using the heliospheric imagers on stereo. *Geophysical Research Letters*, 36, L02102. <https://doi.org/10.1029/2008GL036182>
- Dumbović, M., algović, J., Vrnak, B., Temmer, M., Mays, M. L., Veronig, A., & Piantisch, I. (2018). The drag-based ensemble model (DBEM) for coronal mass ejection propagation. *The Astrophysical Journal*, 854(2), 180.
- Dumbović, M., Vršnak, B., Čalogović, J., & Karlića, M. (2011). Cosmic ray modulation by solar wind disturbances. *Astronomy & Astrophysics*, 531(A91), 17. <https://doi.org/10.1051/0004-6361/201016006>
- Forbush, S. E. (1937). On the effects in cosmic-ray intensity observed during the recent magnetic storm. *Physical Review*, 51, 1108–1109. <https://doi.org/10.1103/PhysRev.51.1108.3>
- Fox, N. J., Velli, M. C., Bale, S. D., Decker, R., Driesman, A., Howard, R. A., et al. (2016). The solar probe plus mission: Humanity's first visit to our star. *Space Science Reviews*, 204(1), 7–48. <https://doi.org/10.1007/s11214-015-0211-6>
- Freiherr von Forstner, J. L., Guo, J., Wimmer-Schweingruber, R. F., Hassler, D. M., Temmer, M., Dumbović, M., et al. (2018). Using forbush decreases to derive the transit time of ICMEs propagating from 1 AU to Mars. *Journal of Geophysical Research: Space Physics*, 123, 39–56. <https://doi.org/10.1002/2017JA024700>
- Gopalswamy, N., Davila, J., Cyr, O. S., Sittler, E., Auchère, F., Duvall, T. Jr., et al. (2011). Earth-affecting solar causes observatory (EASCO): A potential international living with a star mission from Sun-Earth 15. *Journal of Atmospheric and Solar-Terrestrial Physics*, 73(5–6), 658–663.
- Grotzinger, J. P., Crisp, J., Vasavada, A. R., Anderson, R. C., Baker, C. J., Barry, R., et al. (2012). Mars Science Laboratory mission and science investigation. *Space Science Reviews*, 170(1), 5–56. <https://doi.org/10.1007/s11214-012-9892-2>
- Guo, J., Dumbović, M., Wimmer-Schweingruber, R. F., Temmer, M., Lohf, H., Wang, Y., et al. (2018). Modeling the evolution and propagation of 10 September 2017 CMES and SEPS arriving at Mars constrained by remote sensing and in situ measurement. *Space Weather*, 16, 1156–1169. <https://doi.org/10.1029/2018SW001973>
- Guo, J., Lillis, R., Wimmer-Schweingruber, R. F., Zeitlin, C., Simonson, P., Rahmati, A., et al. (2018). Measurements of Forbush decreases at Mars: Both by MSL on ground and by MAVEN in orbit. *Astronomy & Astrophysics*, 611(A79), 14. <https://doi.org/10.1051/0004-6361/201732087>

- Guo, J., Zeitlin, C., Wimmer-Schweingruber, R. F., Hassler, D. M., Posner, A., Heber, B., et al. (2015). Variations of dose rate observed by MSL/RAD in transit to Mars. *Astronomy & Astrophysics*, 577(A58), 6. <https://doi.org/10.1051/0004-6361/201525680>
- Guo, J., Zeitlin, C., Wimmer-Schweingruber, R. F., McDole, T., Khl, P., Appel, J. C., et al. (2018). A generalized approach to model the spectra and radiation dose rate of solar particle events on the surface of Mars. *The Astrophysical Journal*, 155(1), 49.
- Hassler, D. M., Zeitlin, C., Wimmer-Schweingruber, R. F., Böttcher, S., Martin, C., Andrews, J., et al. (2012). The radiation assessment detector (rad) investigation. *Space Science Reviews*, 170(1), 503–558. <https://doi.org/10.1007/s11214-012-9913-1>
- Heinemann, S. G., Temmer, M., Hofmeister, S. J., Veronig, A. M., & Vennerström, S. (2018). Three-phase evolution of a coronal hole. I. 360° remote sensing and in situ observations. *The Astrophysical Journal*, 861, 151. <https://doi.org/10.3847/1538-4357/aac897>
- Helcats, E., Barnes, D., Davies, J., & Harrison, R. (2018). Helcats WP3 CME kinematics catalogue. Figshare. Retrieved from https://figshare.com/articles/HELcats_WP3_CME_KINEMATICS_CATALOGUE/5803176/1 <https://doi.org/10.6084/m9.figshare.5803176.v1>
- Hess, V. F., & Demmelmair, A. (1937). World-wide effect in cosmic ray intensity, as observed during a recent magnetic storm. *Nature*, 140, 316–317. <https://doi.org/10.1038/140316a0>
- Howard, R. A., Moses, J. D., Vourlidas, A., Newmark, J. S., Socker, D. G., Plunkett, S. P., et al. (2008). Sun Earth connection coronal and heliospheric investigation (SECCHI). *Space Science Reviews*, 136(1), 67–115. <https://doi.org/10.1007/s11214-008-9341-4>
- Howard, R. A., Vourlidas, A., Korendyke, C. M., Plunkett, S. P., Carter, M. T., Wang, D., et al. (2013). The solar and heliospheric imager (SOLOHI) instrument for the solar orbiter mission. *Proceedings of the SPIE*, 8862, 13. <https://doi.org/10.1117/12.2027657>
- Howard, T. A., Webb, D. F., Tappin, S. J., Mizuno, D. R., & Johnston, J. C. (2006). Tracking halo coronal mass ejections from 01 AU and space weather forecasting using the solar mass ejection imager (SMEI). *Journal of Geophysical Research*, 111, A04105. <https://doi.org/10.1029/2005JA011349>
- Kahler, S. W., & Webb, D. F. (2007). V arc interplanetary coronal mass ejections observed with the solar mass ejection imager. *Journal of Geophysical Research*, 112, A09103. <https://doi.org/10.1029/2007JA012358>
- Kraft, S., Puschmann, K. G., & Luntama, J. P. (2017). Remote sensing optical instrumentation for enhanced space weather monitoring from the L1 and L5 Lagrange points. *Proceedings of the SPIE*, 10562(10562), 9. <https://doi.org/10.1117/12.2296100>
- Lavraud, B., Liu, Y. D., Segura, K., He, J., Qin, G., Temmer, M., et al. (2016). A small mission concept to the Sun Earth Lagrangian L5 point for innovative solar, heliospheric and space weather science. *Journal of Atmospheric and Solar-Terrestrial Physics*, 146, 171–185. <https://doi.org/10.1016/j.jastp.2016.06.004>
- Lefèvre, L., Vennerström, S., Dumbović, M., Vršnak, B., Sudar, D., Arlt, R., et al. (2016). Detailed analysis of solar data related to historical extreme geomagnetic storms: 1868–2010. *Solar Physics*, 291, 1483–1531. <https://doi.org/10.1007/s11207-016-0892-3>
- Liu, Y. D., Davies, J. A., Luhmann, J. G., Vourlidas, A., Bale, S. D., & Lin, R. P. (2010). Geometric triangulation of imaging observations to track coronal mass ejections continuously out to 1 AU. *The Astrophysical Journal Letters*, 710(1), L82–L87.
- Liu, Y. D., Hu, H., Wang, C., Luhmann, J. G., Richardson, J. D., Yang, Z., & Wang, R. (2016). On sun-to-earth propagation of coronal mass ejections: II. Slow events and comparison with others. *The Astrophysical Journal Supplement Series*, 222(2), 23.
- Liu, Y. D., Luhmann, J. G., Lugaz, N., Möstl, C., Davies, J. A., Bale, S. D., & Lin, R. P. (2013). On sun-to-earth propagation of coronal mass ejections. *The Astrophysical Journal*, 769(1), 45.
- Liu, Y. D., Thernisien, A., Luhmann, J. G., Vourlidas, A., Davies, J. A., Lin, R. P., & Bale, S. D. (2010). Reconstructing coronal mass ejections with coordinated imaging and in situ observations: Global structure, kinematics, and implications for space weather forecasting. *The Astrophysical Journal*, 722(2), 1762.
- Lugaz, N., Hernandez-Charpak, J. N., Roussev, I. I., Davis, C. J., Vourlidas, A., & Davies, J. A. (2010a). Determining the azimuthal properties of coronal mass ejections from multi-spacecraft remote-sensing observations with STEREO SECCHI. *The Astrophysical Journal*, 715(1), 493.
- Lugaz, N., Hernandez-Charpak, J. N., Roussev, I. I., Davis, C. J., Vourlidas, A., & Davies, J. A. (2010b). Determining the azimuthal properties of coronal mass ejections from multi-spacecraft remote-sensing observations with STEREO SECCHI. *The Astrophysical Journal*, 715(1), 493.
- Lugaz, N., Vourlidas, A., & Roussev, I. I. (2009). Deriving the radial distances of wide coronal mass ejections from elongation measurements in the heliosphere—Application to CME-CME interaction. *Annales Geophysicae*, 27(9), 3479–3488. <https://doi.org/10.5194/angeo-27-3479-2009>
- Lugaz, N., Vourlidas, A., Roussev, I. I., & Morgan, H. (2009). Solar-terrestrial simulation in the STEREO era: The 24–25 January 2007 eruptions. *Solar Physics*, 256(1), 269–284. <https://doi.org/10.1007/s11207-009-9339-4>
- Möstl, C., Amla, K., Hall, J. R., Liewer, P. C., Jong, E. M. D., Colaninno, R. C., et al. (2014). Connecting speeds, directions and arrival times of 22 coronal mass ejections from the Sun to 1 AU. *The Astrophysical Journal*, 787(2), 119.
- Möstl, C., & Davies, J. A. (2013). Speeds and arrival times of solar transients approximated by self-similar expanding circular fronts. *Solar Physics*, 285(1), 411–423. <https://doi.org/10.1007/s11207-012-9978-8>
- Möstl, C., Isavnin, A., Boakes, P. D., Kilpua, E. K. J., Davies, J. A., Harrison, R. A., et al. (2017). Modeling observations of solar coronal mass ejections with heliospheric imagers verified with the heliophysics system observatory. *Space Weather*, 15, 955–970. <https://doi.org/10.1002/2017SW001614>
- Möstl, C., Rollett, T., Frahm, R. A., Liu, Y. D., Long, D. M., Colaninno, R. C., et al. (2015). Strong coronal channelling and interplanetary evolution of a solar storm up to Earth and Mars. *Nature Communications*, 6, 7135. <https://doi.org/10.1038/ncomms8135>
- Möstl, C., Rollett, T., Lugaz, N., Farrugia, C. J., Davies, J. A., Temmer, M., et al. (2011). Arrival time calculation for interplanetary coronal mass ejections with circular fronts and application to STEREO observations of the 2009 February 13 eruption. *The Astrophysical Journal*, 741(1), 34.
- Müller, D., Marsden, R. G., St. Cyr, O. C., Gilbert, H. R., & The Solar Orbiter Team (2013). Solar orbiter. *Solar Physics*, 285(1), 25–70. <https://doi.org/10.1007/s11207-012-0085-7>
- Odstrcil, D., Riley, P., & Zhao, X. P. (2004). Numerical simulation of the 12 May 1997 interplanetary CME event. *Journal of Geophysical Research*, 109, A02116. <https://doi.org/10.1029/2003JA010135>
- Oughton, E. J., Skelton, A., Horne, R. B., Thomson, A. W. P., & Gaunt, C. T. (2017). Quantifying the daily economic impact of extreme space weather due to failure in electricity transmission infrastructure. *Space Weather*, 15, 65–83. <https://doi.org/10.1002/2016SW001491>
- Pomoell, J., & Poedts, S. (2018). EUHFORIA: European heliospheric forecasting information asset. *Journal of Space Weather and Space Climate*, 8(A35), 14. <https://doi.org/10.1051/swsc/2018020>
- Rafkin, S. C. R., Zeitlin, C., Ehresmann, B., Hassler, D., Guo, J., Köhler, J., et al. (2014). Diurnal variations of energetic particle radiation at the surface of Mars as observed by the Mars Science Laboratory radiation assessment detector. *Journal of Geophysical Research: Planets*, 119, 1345–1358. <https://doi.org/10.1002/2013JE004525>
- Reames, D. V. (2013). The two sources of solar energetic particles. *Space Science Reviews*, 175(1), 53–92. <https://doi.org/10.1007/s11214-013-9958-9>

- Rollett, T., Möstl, C., Isavnin, A., Davies, J. A., Kubicka, M., Amerstorfer, U. V., & Harrison, R. A. (2016). ElEvoHI: A novel CME prediction tool for heliospheric imaging combining an elliptical front with drag-based model fitting. *The Astrophysical Journal*, *824*(2), 131.
- Rouillard, A. P., Davies, J. A., Forsyth, R. J., Rees, A., Davis, C. J., Harrison, R. A., et al. (2008). First imaging of corotating interaction regions using the stereo spacecraft. *Geophysical Research Letters*, *35*, L10110. <https://doi.org/10.1029/2008GL033767>
- Russell, C. T. (Ed.) (2008). *The STEREO Mission Edited by Russell, C. T.* New York: Springer. <https://doi.org/10.1007/978-0-387-09649-0>
- Sheeley, N. R., Walters, J. H., Wang, Y.-M., & Howard, R. A. (1999). Continuous tracking of coronal outflows: Two kinds of coronal mass ejections. *Journal of Geophysical Research*, *104*(A11), 24,739–24,767. <https://doi.org/10.1029/1999JA900308>
- Shen, C., Wang, Y., Wang, S., Liu, Y., Liu, R., Vourlidas, A., et al. (2012). Super-elastic collision of large-scale magnetized plasmoids in the heliosphere. *Nature Physics*, *8*, 923–928. <https://doi.org/10.1038/nphys2440>
- Temmer, M., & Nitta, N. V. (2015). Interplanetary propagation behavior of the fast coronal mass ejection on 23 July 2012. *Solar Physics*, *290*(3), 919–932. <https://doi.org/10.1007/s11207-014-0642-3>
- Temmer, M., Vršnak, B., Rollett, T., Bein, B., de Koning, C. A., Liu, Y., et al. (2012). Characteristics of kinematics of a coronal mass ejection during the 2010 August 1 CME-CME interaction event. *The Astrophysical Journal*, *749*(1), 11. <https://doi.org/10.1088/0004-637x/749/1/57>
- Tucker-Hood, K., Scott, C., Owens, M., Jackson, D., Barnard, L., Davies, J. A., et al. (2015). Validation of a priori CME arrival predictions made using real-time heliospheric imager observations. *Space Weather*, *13*, 35–48. <https://doi.org/10.1002/2014SW001106>
- Vennerstrom, S., Lefevre, L., Dumbović, M., Crosby, N., Malandraki, O., Patsou, I., et al. (2016). Extreme Geomagnetic Storms—1868–2010. *Solar Physics*, *291*, 1447–1481. <https://doi.org/10.1007/s11207-016-0897-y>
- Vourlidas, A. (2015). Mission to the Sun-Earth L5 Lagrangian point: An optimal platform for space weather research. *Space Weather*, *13*, 197–201. <https://doi.org/10.1002/2015SW001173>
- Vourlidas, A., Howard, R. A., Plunkett, S. P., Korendyke, C. M., Thernisien, A. F. R., Wang, D., et al. (2016). The wide-field imager for solar probe plus (WISPR). *Space Science Reviews*, *204*(1), 83–130. <https://doi.org/10.1007/s11214-014-0114-y>
- Vršnak, B., Temmer, M., Žic, T., Taktakishvili, A., Dumbović, M., Möstl, C., et al. (2014). Heliospheric propagation of coronal mass ejections: Comparison of numerical wsa-enlil+cone model and analytical drag-based model. *The Astrophysical Journal Supplement Series*, *213*(2), 9.
- Vršnak, B., & Žic, T. (2007). Transit times of interplanetary coronal mass ejections and the solar wind speed. *Astronomy & Astrophysics*, *472*(3), 937–943. <https://doi.org/10.1051/0004-6361:20077499>
- Vršnak, B., Žic, T., Vrbanec, D., Temmer, M., Rollett, T., Möstl, C., et al. (2013). Propagation of interplanetary coronal mass ejections: The drag-based model. *Solar Physics*, *285*(1), 295–315. <https://doi.org/10.1007/s11207-012-0035-4>
- Wang, Y., Shen, C., Liu, R., Liu, J., Guo, J., Li, X., et al. (2018). Understanding the twist distribution inside magnetic flux ropes by anatomizing an interplanetary magnetic cloud. *Journal of Geophysical Research: Space Physics*, *123*, 3238–3261. <https://doi.org/10.1002/2017JA024971>
- Winslow, R. M., Schwadron, N. A., Lugaz, N., Guo, J., Joyce, C. J., Jordan, A. P., et al. (2018). Opening a window on ICME-driven GCR modulation in the inner solar system. *The Astrophysical Journal*, *856*(2), 139. <https://doi.org/10.3847/1538-4357/aab098>
- Witasse, O., Sanchez-Cano, B., Mays, M. L., Kajdi, P., Opgenoorth, H., Elliott, H. A., et al. (2017). Interplanetary coronal mass ejection observed at STEREO-A, Mars, comet 67p/Churyumov-Gerasimenko, Saturn, and new horizons en route to Pluto: Comparison of its Forbush decreases at 1.4, 3.1, and 9.9 AU. *Journal of Geophysical Research: Space Physics*, *122*, 7865–7890. <https://doi.org/10.1002/2017JA023884>
- Zeitlin, C., Hassler, D. M., Cucinotta, F. A., Ehresmann, B., Wimmer-Schweingruber, R. F., Brinza, D. E., et al. (2013). Measurements of energetic particle radiation in transit to Mars on the Mars Science Laboratory. *Science*, *340*(6136), 1080–1084. <https://doi.org/10.1126/science.1235989>
- Zurbuchen, T. H., & Richardson, I. G. (2006). In-situ solar wind and magnetic field signatures of interplanetary coronal mass ejections, *Coronal mass ejections* (pp. 31–43). New York: Springer. <https://doi.org/10.1007/978-0-387-45088-93>

Erratum

In the originally published version of this manuscript, Dumbović was erroneously published as Dumbovi. These errors and all affected text have since been corrected, and this version may be considered the authoritative version of record.

COMPARING FORBUSH DECREASE PROPERTIES AT EARTH AND MARS

While in [Chapter 3](#) Forbush decreases (FDs) have mainly been used to determine the arrival time of interplanetary coronal mass ejections (ICMEs) at 1 AU and Mars, other properties of FDs have been neglected in these studies. However, some empirical relations between different properties of a FD at Earth as well as between the FD and properties of the associated ICME are known, as shown e.g. by [Belov \(2008\)](#) and [Abunin et al. \(2012\)](#). For example, there is a clear correlation between the relative FD amplitude or the maximum decrease rate (“steepness”) with the product of the maximum solar wind speed and maximum magnetic field. This parameter $v_{\max} \cdot B_{\max}$ can be used to describe the intensity of the disturbance in the solar wind. The correlation is shown in [Figure 8 of Belov \(2008\)](#) and [Figure 7 of Abunin et al. \(2012\)](#). However, solar wind plasma and magnetic field measurements at Mars are only available from the Mars Atmosphere and Volatile Evolution (MAVEN) spacecraft since 2014, and as explained in [Section 1.5](#), it does not observe the upstream solar wind continuously. Consequently, the determination of maximum values for B and v , which would be necessary for the validation of this relation at Mars, may be complicated for many events.

Instead, in this study, we focus on the correlation of two parameters of the FDs themselves: the relative amplitude and the maximum decrease rate. These parameters are already known to be correlated at Earth, as seen in [Figure 7 of Belov \(2008\)](#) and [Figure 5 of Abunin et al. \(2012\)](#). We use our catalog of FDs from [Freiherr von Forstner et al. \(2019\)](#), as well as the larger catalog by [Papaioannou et al. \(2019\)](#) to reproduce this relation at Mars. Consulting the analytical FD models, [PDB](#) and [ForbMod](#), which were introduced in [Section 1.4](#), it becomes possible to interpret the difference between the two observed relations as a result of the expansion of the interplanetary structures.

The following article is reproduced from [Freiherr von Forstner et al. \(2020\)](#) from *Journal of Geophysical Research: Space Physics*, ©American Geophysical Union, under the Creative Commons CC-BY ([CC](#)[BY](#)) license:

COMPARING THE PROPERTIES OF ICME-INDUCED FORBUSH DECREASES AT EARTH AND MARS

Freiherr von Forstner, J. L., J. Guo, R. F. Wimmer-Schweingruber, M. Dumbović, M. Janvier, P. Démoulin, A. Veronig, M. Temmer, A. Papaioannou, S. Dasso, D. M. Hassler, and C. J. Zeitlin, *Journal of Geophysical Research: Space Physics*, 125, 5, e2019JA027662 (2020), DOI: [10.1029/2019JA027662](#) Own contribution: 80%



RESEARCH ARTICLE

10.1029/2019JA027662

Comparing the Properties of ICME-Induced Forbush Decreases at Earth and Mars

Key Points:

- We examine a large number of Forbush decreases (FDs) at Mars observed by MSL/RAD, comparing their properties with those observed at Earth
- The maximum hourly decrease of the FDs is correlated with their amplitude, but with different linear regression slopes at Earth and Mars
- This effect may be due to the broadening of the coronal mass ejection's sheath region, which we motivate with theoretical calculations

Correspondence to:

J. L. Freiherr von Forstner and Jingnan Guo, forstner@physik.uni-kiel.de; jnguo@ustc.edu.cn

Citation:

Freiherr von Forstner, J. L., Guo, J., Wimmer-Schweingruber, R. F., Dumbović, M., Janvier, M., Démoulin, P. et al. (2020). Comparing the properties of ICME-induced Forbush decreases at Earth and Mars. *Journal of Geophysical Research: Space Physics*, 125, e2019JA027662. <https://doi.org/10.1029/2019JA027662>

Received 20 NOV 2019

Accepted 25 FEB 2020

Accepted article online 10 MAR 2020

Johan L. Freiherr von Forstner¹ , Jingnan Guo^{1,2,3} , Robert F. Wimmer-Schweingruber¹ , Mateja Dumbović^{4,5}, Miho Janvier⁶, Pascal Démoulin⁷ , Astrid Veronig^{5,8} , Manuela Temmer⁵ , Athanasios Papaioannou⁹, Sergio Dasso^{10,11}, Donald M. Hassler¹² , and Cary J. Zeitlin¹³

¹Institute of Experimental and Applied Physics, University of Kiel, Kiel, Germany, ²School of Earth and Space Sciences, University of Science and Technology of China, Hefei, China, ³CAS Center for Excellence in Comparative Planetology, Hefei, China, ⁴Hvar Observatory, Faculty of Geodesy, University of Zagreb, Zagreb, Croatia, ⁵Institute of Physics, University of Graz, Graz, Austria, ⁶Institut d'Astrophysique Spatiale, CNRS, Université Paris-Sud, Université Paris-Saclay, Orsay, France, ⁷LESIA, Observatoire de Paris, Université PSL, CNRS, Sorbonne Université, Université Paris Diderot, Sorbonne Paris Cité, Meudon, France, ⁸Kanzelhöhe Observatory for Solar and Environmental Research, University of Graz, Graz, Austria, ⁹Institute for Astronomy, Astrophysics, Space Applications and Remote Sensing (IAASARS), National Observatory of Athens, Athens, Greece, ¹⁰Facultad de Ciencias Exactas y Naturales, Departamento de Ciencias de la Atmósfera y los Océanos-Departamento de Física, Universidad de Buenos Aires, Buenos Aires, Argentina, ¹¹Instituto de Astronomía y Física del Espacio (IAFE), CONICET-Universidad de Buenos Aires, Buenos Aires, Argentina, ¹²Southwest Research Institute, Boulder, CO, USA, ¹³Leidos, Houston, TX, USA

Abstract Forbush decreases (FDs), which are short-term drops in the flux of galactic cosmic rays, are caused by the shielding from strong and/or turbulent magnetic structures in the solar wind, especially interplanetary coronal mass ejections (ICMEs) and their associated shocks, as well as corotating interaction regions. Such events can be observed at Earth, for example, using neutron monitors, and also at many other locations in the solar system, such as on the surface of Mars with the Radiation Assessment Detector instrument onboard Mars Science Laboratory. They are often used as a proxy for detecting the arrival of ICMEs or corotating interaction regions, especially when sufficient in situ solar wind measurements are not available. We compare the properties of FDs observed at Earth and Mars, focusing on events produced by ICMEs. We find that FDs at both locations show a correlation between their total amplitude and the maximum hourly decrease, but with different proportionality factors. We explain this difference using theoretical modeling approaches and suggest that it is related to the size increase of ICMEs, and in particular their sheath regions, en route from Earth to Mars. From the FD data, we can derive the sheath broadening factor to be between about 1.5 and 1.9, agreeing with our theoretical considerations. This factor is also in line with previous measurements of the sheath evolution closer to the Sun.

Plain Language Summary When eruptions from the Sun propagate through the interplanetary space, their strong and turbulent magnetic field deflects background cosmic ray particles nearby. This causes a temporary decrease of the flux of cosmic rays observed at locations that were passed by the eruption, a so-called Forbush decrease. These decreases can be measured on Earth, and also by space missions around the solar system, and are often used to detect the arrival of solar eruptions, especially when no other direct measurements are available. We look at catalogs of Forbush decreases observed at Earth and Mars, which is 50% farther away from the Sun than Earth, and compare their properties to investigate whether, in addition to the arrival time, it is possible to derive more information about the eruptions from the observed Forbush decreases. We find that the relation of characteristic parameters describing the Forbush decrease changes between the two planets and that this can be explained by the broadening of the interplanetary structure erupted from the Sun during its propagation. The magnitude of this broadening derived from our data agrees with theoretical expectations and is in line with previous measurements of the evolution of solar eruptions at locations closer to the Sun.

©2020. The Authors.

This is an open access article under the terms of the Creative Commons Attribution License, which permits use, distribution and reproduction in any medium, provided the original work is properly cited.

1. Introduction

Forbush decreases (FDs) are temporary decreases in the flux of galactic cosmic rays (GCRs). They are caused by strong and/or turbulent magnetic structures in the solar wind associated with interplanetary coronal

mass ejections (ICMEs) and the discontinuities driven by them or by corotating interaction regions (CIRs). They were first observed by Forbush (1937) and Hess and Demmelair (1937) and later named after Forbush. In the case of ICMEs, the GCR decrease is often caused by the close succession of two separate effects: the turbulent sheath region, which is preceded by the interplanetary discontinuity, and the magnetic ICME ejecta itself. Sometimes, these two effects can even be clearly separated into a two-step decrease, as described by, for example, Cane (2000). However, in recent times, it has been debated whether this is always the case (e.g., Jordan et al., 2011), and it can be challenging to clearly separate the two steps with limited data resolution. Following the sudden decrease phase, which usually takes less than 1 day, the GCR intensity recovers to its previous level within about 1 week (up to several weeks for some very strong events).

Nowadays, GCRs and FDs are routinely measured not only on the surface of the Earth, for example, using neutron monitors, but also on various spacecraft near Earth as well as in deep space, and even on the surface of other solar system bodies such as at Mars with the Radiation Assessment Detector (RAD, Hassler et al., 2012) instrument on the Mars Science Laboratory (MSL) mission (Guo et al., 2018), and, since January 2019, on the Moon with the Lunar Lander Neutrons and Dosimetry experiment (Wimmer-Schweingruber et al., 2020) on the Chinese Chang'E 4 mission. As the FD onset time matches very well with the arrival of the corresponding solar wind structure (see, e.g., Cane et al., 1996; Dumbović et al., 2011), FDs can be used as a proxy to determine the arrival time of ICMEs or CIRs, which is particularly useful in cases where no plasma or magnetic field measurements are available (e.g., Lefèvre et al., 2016; Möstl et al., 2015; Vennerstrøm et al., 2016; Witasse et al., 2017). This approach was also used in our previous studies investigating the travel time of ICMEs between 1 AU and Mars (Freiherr von Forstner et al., 2018) and validating the accuracy of geometric models to calculate the arrival time at Mars based on heliospheric imager data from the Solar Terrestrial Relations Observatory (STEREO) mission (Freiherr von Forstner et al., 2019).

While the accurate prediction of ICME arrival times is still a complex task in space weather research, the exact description of the ICMEs' geometric and magnetic structure and its evolution over time, which is also important for their impact on Earth and other planets, is even more challenging. For the further development and improvement of models, it is important to exploit many sources of data, so we are investigating how FDs can be included into the portfolio of available space weather data. As all methods to detect ICMEs, FDs have certain limitations in how much information they can give us about the ICME. But with sufficient understanding of the FD physics (using recent modeling approaches such as given in Dumbović et al., 2018), there can be more information that can be obtained from the FD data than just the ICME arrival time. Some investigations in this direction were done by Liu et al. (2006) and Masías-Meza et al. (2016), who linked averaged FD profiles with the corresponding magnetic field and solar wind observations using a superposed epoch method, finding, for example, an increase of the FD amplitude and recovery time for the category of fast ICMEs compared to slower events.

In this paper, we combine FDs at Mars identified by MSL/RAD with catalogs of FDs at Earth for a statistical study of their properties. Section 2 contains information about the different sources of data in use. Section 3 describes the FD properties we are investigating and gives an introduction to a modeling approach that we use for FDs. The main part of our study is in section 4, where we derive a relation of the FD's amplitude to the maximum decrease rate, and compare this relation between Earth and Mars. We interpret this effect using idealized models as well as the more sophisticated approaches described in section 3.2 and continue with further discussions. Section 5 then concludes this work with a summary and outlook.

2. Data Sources and Catalogs

2.1. MSL/RAD and FDs at Mars

Since the landing of the MSL mission's Curiosity rover on 6 August 2012, its RAD instrument has been continuously measuring the radiation environment on the Martian surface, including both charged and neutral particles. Among other data products, RAD provides measurements of the total ionizing dose rate, which results from the incident GCR, and is enhanced during solar energetic particle (SEP) event periods. Radiation dose is defined as the energy (measured in J) deposited by radiation in a detector of mass m per unit mass and is thus measured in units of J/kg (or Gy). Dose is measured in two of the six RAD detectors, B, a silicon solid-state detector, and E, a tissue-equivalent plastic scintillator (Hassler et al., 2012).

Similar to neutron monitors on Earth and other cosmic ray detectors in deep space, RAD can be used for detecting FDs in the GCR. Although the unit of dose rate is different from count rate measured at neutron

monitors on Earth, the relative change in the GCR fluxes, which corresponds to the magnitude of FDs, is unitless and can be well observed in dose measurements. Due to the larger geometric factor therefore and higher possible cadence (up to one observation per minute), the dose rate in the E detector is best suited for this purpose (Guo et al., 2018). In situ solar wind and interplanetary magnetic field data at Mars are available from the Mars Atmosphere and Volatile Evolution (MAVEN) spacecraft (Jakosky et al., 2015), which arrived at Mars in late 2014, more than 2 years later than MSL. MAVEN data are, however, not always optimal for studying solar wind phenomena at Mars, as MAVEN's orbit often takes the spacecraft within Mars's bow shock and thus out of the undisturbed upstream solar wind. These periods need to be excluded from the data for solar wind analysis, so the remaining coverage of the interplanetary medium at Mars is significantly reduced. On the other hand, RAD measures surface GCR flux uninterruptedly since August 2012 and detects many FDs, which have been used successfully to detect the arrival of ICMEs at Mars, such as by Witasse et al. (2017), Freiherr von Forstner et al. (2018), Guo, Dumbović, et al. (2018), Guo, Lillis, et al. (2018), Winslow et al. (2018), Freiherr von Forstner et al. (2019), Papaioannou et al. (2019), and Dumbović et al. (2019).

The radiation environment on the surface of Mars differs considerably from that in deep space. The primary GCR particles arriving at Mars, as well as SEPs, are modulated by the Martian atmosphere and also influenced by the surface of Mars. Thus, the radiation measured by RAD is a mix of the primary GCR/SEP particles and secondary particles produced in the atmosphere and soil (Guo et al., 2017, 2018). To model the response of a detector on the surface to a certain incoming GCR spectrum above the atmosphere, it is necessary to construct a response function (yield function) that computes the resulting spectrum at the surface for different particle species and then calculates a prediction for the quantity measured by the instrument (e.g., dose rate or count rate) from this surface spectrum. For the case of Mars and the RAD instrument, such functions were modeled by Guo et al. (2019), showing that the Martian atmosphere shields the surface of Mars from GCR protons below an energy of 140 to 190 MeV, depending on the surface atmospheric depth, which changes seasonally. The largest contribution from the primary GCR spectrum to the Martian surface dose rate comes from primary GCR protons in the ~1- to 3-GeV energy range, which is easily calculated by folding the atmospheric response functions provided by Guo et al. (2019) with typical primary GCR spectra. Similar effects occur for Earth-based cosmic ray measurements, such as using neutron monitors, though the composition, density, and depth of atmosphere are of course different and the terrestrial magnetic field also plays an important role in modulating the GCR measured at different latitudes. The construction of yield functions for neutron monitors on Earth, taking into account the atmospheric and magnetic effects as well as the neutron detection efficiency, was described by Clem and Dorman (2000). Due to the thicker atmosphere of the Earth, the atmospheric cutoff energy is significantly higher than on Mars—it has been determined to be around 450 MeV for protons. The effect of the magnetosphere, which is largely missing at Mars, increases the cutoff energy at lower latitudes and is a consequence of the local magnetic cutoff rigidity at the measurement location. At the poles, the influence of the magnetosphere decreases to zero (see, e.g., Smart & Shea, 2008), for example, to a cutoff rigidity 0.1 GV at the location of the South Pole neutron monitor. This corresponds to a proton kinetic energy of about 100 MeV, so the atmospheric effect is dominant in these polar regions. The difference in the observed GCR energy range is a limitation for studies comparing FDs measured with different instruments and will be taken into account using modeling approaches.

The daily variation of atmospheric pressure primarily due to thermal tide at Mars causes a significant diurnal pattern in the dose rate measured at MSL/RAD (Rafkin et al., 2014), stronger than what is usually seen at Earth. To facilitate the detection of FDs in the RAD data, the dose rate measurements are processed using a spectral notch filter described by Guo et al. (2018) to compensate for the diurnal variations while keeping other fluctuations that do not have a diurnal periodicity. We note that this technique may also remove the diurnal signal due to GCR anisotropy, if exists, during a FD (e.g., Tortermun et al., 2018). As there are no other GCR measurements on the Martian surface, preferentially on the opposite side of the planet, the FD anisotropy at Mars cannot yet be studied and separated from the diurnal atmospheric effects.

2.2. Catalogs of FDs at Earth and Mars

In this section, we describe the different catalogs of FDs that we use in this study. The catalogs and the results later obtained using these data are also summarized in Table 1.

Catalog I: In our previous work (Freiherr von Forstner et al., 2019), we assembled a catalog of ICMEs propagating toward Mars that were observed remotely with the Heliospheric Imagers (HI, Eyles et al., 2009)

Table 1
Results for the Sheath Broadening Factor E Estimated in Different Parts of This Study, and Summary of How They Were Obtained

Result no.	(a)	(b)	(c)	(d)
FD catalog	Catalog I	Catalogs II and III		Theoretical estimation
FD data @ Mars	MSL/RAD (~1- to 3-GeV/nuc GCRs)	MSL/RAD (~1- to 3-GeV/nuc GCRs)		N/A
FD data @ Earth	South Pole NM (≥ 0.1 -GV GCRs)	Global survey method (=10-GV GCRs)		N/A
Catalog description	FDs at Mars associated with ICMs observed with STEREO-HI <ul style="list-style-type: none"> •Complex CME-CME interaction events excluded •Subset of Mars events also seen at Earth during close alignment 	FDs at Earth/Mars <ul style="list-style-type: none"> •Semi-automatic detection in GCR data •Association with CMEs based on SOHO/LASCO observations 		First-order approximation, two effects taken into account: <ul style="list-style-type: none"> •Pileup of solar wind in front •Internal sheath velocity profile
Threshold condition	None	$f = 1$	$g = 0.3$	Calculation based on typical speeds from superposed epoch analyses
Reference	Section 4.1	Section 4.1	Section 4.2.2	N/A
Sheath broadening factor E	1.9 ± 0.4	1.5 ± 0.2	1.5 ± 0.4	Section 4.2.4 1.2 to 1.8

Note. The different catalogs referenced in the table are explained in section 2.2. For the each catalog, we also give the instruments that were used to obtain the FD measurements, and the energy/rigidity ranges of primary GCR (above the atmosphere/magnetosphere) that their data are mainly influenced by.

onboard the STEREO spacecraft (Russell, 2008) and caused a FD at MSL/RAD. The STEREO-HI observations were taken from the HIGeoCat catalog assembled by the HELCATS project (Barnes et al., 2019; Helcats et al., 2018). This allowed us to study the accuracy of various methods for predicting the arrival time at Mars using the STEREO-HI data. The catalog can also be found on FigShare at <https://doi.org/10.6084/m9.figshare.7440245> and contains the ICME data from HIGeoCat as well as arrival times at MSL based on our FD observations. The catalog contains 45 FDs and serves as one of the data sources for this study, with the FD properties discussed in section 3.1 derived from the RAD observations. Of the 45 events, 14 were also clearly observed at Earth during close radial alignments of the two planets. In these cases, we have also identified the arrival time at Earth and derived the terrestrial FD properties using data from the South Pole neutron monitor (*SOPO* in the NMDB database at <http://www.nmdb.eu/>).

As known, complex and interacting ICME events can occur often, especially during solar maximum (e.g., Burlaga et al., 2002; Gopalswamy et al., 2001; Lugaz et al., 2005; Liu et al., 2012). A recent study (Dumbović et al., 2019) has analyzed in detail the interaction of two ICMEs and with the ambient solar wind, which adds up to the complex substructures of an FD observed at Mars. During such complex events, FD profiles cannot be used to study the propagation and evolution a single ICME. During the assembly of Catalog I, we have excluded events, which could not be clearly linked from the HI observations to a single FD in the RAD data and therefore minimized the possibility of including complex cases with interactions of multiple successive ICMEs.

Catalog II: The comparison of the derived FD properties between Earth and Mars based on Catalog I (as will be discussed later in section 4) shows some prominent characteristics, with, however, rather low statistics. Therefore, to extend the study to a larger set of events, we also use data from the catalog of FDs at Mars compiled by Papaioannou et al. (2019), where FDs were detected in the in situ GCR measurement using an automated method. Following the automatic detection, each event was manually inspected by Papaioannou et al., 2019 and, if possible, associated with a corresponding ICME based on the SOHO/LASCO coronal mass ejection (CME) catalog (https://cdaw.gsfc.nasa.gov/CME_list/) and WSA-ENLIL heliospheric magnetohydrodynamic simulations with a cone CME model (Odstrčil et al., 2004). Events where no corresponding CME is listed may have been caused by CIRs or complex cases with CME-CME or CME-CIR interaction, or they were in fact caused by a CME that was not seen in the SOHO/LASCO coronagraph. Of the 424 thus identified events, 96 were marked as being caused by an ICME in the catalog. This catalog also contains a quality index $q \in [1..5]$ for each event, giving an estimation of the reliability of the FD identification and determination of its parameters. We restricted ourselves to the events with a high-quality index ($q \geq 4$), meaning that during the selection of the FD and determination of its amplitude, the authors faced no or only minor problems due to data gaps, insufficient suppression of the diurnal variations or other difficulties. This restriction results in 310 FDs in total, of which 83 are marked as being ICME induced.

Catalog III: Finally, for a comparison of Martian FDs from Catalog II with terrestrial FDs, we employ the extensive catalog of FDs observed using neutron monitor data provided by the Space Weather Prediction Center of the Russian Institute of Terrestrial Magnetism, Ionosphere, and Radio Wave Propagation (IZMIRAN). This catalog is available online at <http://spaceweather.izmiran.ru/eng/dbs.html> and was described by Belov (2008). The FD properties in this database are not derived from a single neutron monitor measurement, but rather using the global survey method (GSM; Belov et al., 2005, 2018) data, which calculates the GCR flux at a fixed rigidity of 10 GV based on measurements from the global network of neutron monitors. These data, in comparison to single neutron monitor measurements, avoid potential issues arising from different atmospheric and magnetic influences on monitors at different geographic locations, as they take into account the different yield functions of each neutron monitor station. We use the latest version of the online database, which was last updated on 27 June 2018. The data are subject to revisions due to possible corrections in the neutron monitor data used for the GSM calculation, but the results are not expected to change drastically. The rigidity of 10 GV corresponds to a proton kinetic energy of 9.1 GeV, much higher than the main contribution to dose at Mars with proton kinetic energies of 1 to 3 GeV (see section 2.1). As GCRs with these lower energies are modulated more easily (Guo et al., 2018), this is what causes FDs observed by RAD at Mars to have a larger amplitude on average than those in the GSM data (Figure 7; Papaioannou et al., 2019).

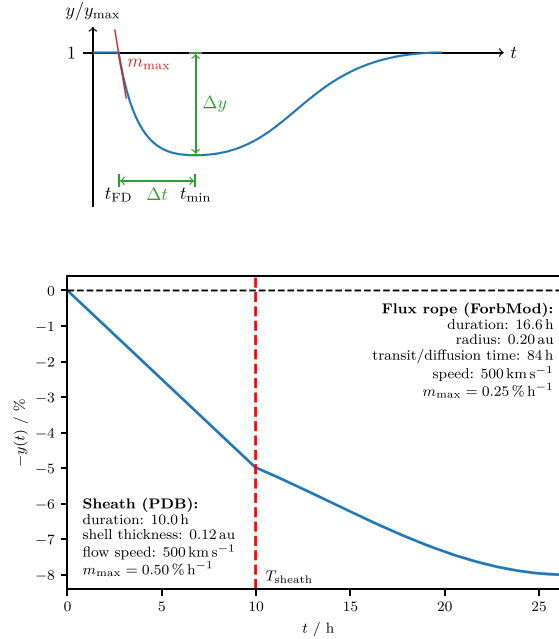


Figure 1. (upper panel) Idealized schematic picture of a Forbush decrease, showing the different properties that we are investigating. The blue curve represents the measured GCR intensity, normalized to the pre-FD level (y_{\max}). The FD magnitude Δy (percentage drop) and decrease duration Δt are defined based on the onset and minimum of the FD. (lower panel) Example of the application of the analytical PDB and ForbMod models to describe the profile of a Forbush decrease caused by an ICME consisting of a sheath and the following flux rope. The model plotted here is described in equation (10). The red dashed line marks the boundary between the sheath and the ejecta; that is, it corresponds to the duration T_{sheath} of the sheath. The model parameters were chosen as specified in the insets, and the values of the diffusion parameters in both models were also chosen within their typical ranges.

3. Definitions and Methodology

3.1. Properties of FDs

Figure 1 (upper panel) shows an idealized schematic profile of a FD, which consists of the decrease phase and a longer recovery period. Based on this, we define the various FD parameters investigated in this study.

The FD onset time is named t_{FD} , and the time where the GCR intensity reaches its minimum is called t_{min} , so the duration of the decrease phase can be calculated as $\Delta t = t_{\text{min}} - t_{\text{FD}}$. To define the FD amplitude as a percentage, the values $y(t)$ of the GCR intensity are normalized to the value y_{\max} at the onset time. The FD percentage drop is then defined as

$$\Delta y = \frac{y_{\max} - y_{\min}}{y_{\max}} = \frac{y(t_{\text{FD}}) - y(t_{\text{min}})}{y(t_{\text{FD}})} \cdot 100\% \quad (1)$$

and the average slope is

$$\bar{m} := \frac{\Delta y}{\Delta t} = \frac{\Delta y}{t_{\text{min}} - t_{\text{FD}}} \quad (2)$$

The maximum decrease rate m_{\max} is another often-used parameter, which was studied, for example, by Belov (2008) and Abunin et al. (2012) as well as at Mars by Papaioannou et al. (2019). In practice, this is usually not calculated directly from the derivative of the original high time resolution GCR data, as it can be quite noisy due to low counting statistics. Instead, m_{\max} is calculated as the maximum hourly decrease by evaluating the same $\Delta y/\Delta t$ difference quotient for each time step in the GCR data when averaged into hourly bins t_i :

$$m_{\max} = \frac{\delta y}{\delta t} = \max_{i \in \{0,1, \dots, N\}} \left(\frac{y(t_{i-1}) - y(t_i)}{(y(t_{\text{FD}}))(t_i - t_{i-1})} \right) \cdot 100\%, \quad (3)$$

where $t_i - t_{i-1} = 1h$ for all i . As for \bar{m} , the units of m_{\max} are %/hr. Abunin et al. (2012) have found that the time of the maximum hourly decrease ($t(m_{\max})$) usually occurs immediately after the time of the maximum interplanetary magnetic field strength ($t(B_{\max})$). We will investigate the distribution of $t(m_{\max})$ within the FD further in section 4.2 and Figure A1.

Note that despite being properties of a GCR decrease, we have defined Δy , \bar{m} and m_{\max} to be positive quantities.

3.2. Modeling of FDs

To be able to obtain more ICME information from our FD observations, we also perform some basic calculations using a theoretical model of the FD profile. Our approach combines two analytical models to describe the FD and thus accounts for both the sheath and the ejecta effect. The sheath is described by the propagating diffusive barrier (PDB) model (Wibberenz et al., 1998), while the magnetic ejecta is represented by ForbMod (Dumbović et al., 2018). Figure 1 (lower panel) shows an example of this combination of the two models. Values of all parameters were chosen in a typical range just for illustration purposes, not to resemble a specific event. Both models are used here in a one-dimensional fashion; that is, we assume the sheath and ejecta as well as the observer to lie in the ecliptic plane. The GCR drop is then described based on the one-dimensional location of the observer within the ICME substructures. The calculation will be explained in detail below.

In the PDB model, the sheath is represented by a shell of thickness S where the flow speed is increased and the diffusion coefficient decreased. Both values are assumed to be constant across the shell. The resulting GCR density drop $y_s(x_s)$ in the sheath (normalized to the onset value), where the index s stands for sheath, can be defined as

$$y_s(x_s) = \frac{y_{\max} - y(x_s)}{y_{\max}}, \quad (4)$$

where, as before, y_{\max} is the undisturbed GCR density and $y_s(x_s)$ is the GCR density at a distance x_s from the outer border of the shell, where we define the antisunward border of the shell as the outward one. In the PDB model, $y_s(x_s)$ is a linear function of the distance x_s :

$$y_s(x_s) = \frac{v_{\text{sheath}}}{K'} x_s. \quad (5)$$

Here, the flow speed in the shell is named v_{sheath} and the radial diffusion coefficient within the shell is K' . Our equation (5) corresponds to equation (4) of Wibberenz et al. (1998) under the assumption that the radial gradient G_r of the ambient GCRs is small.

The ForbMod model (Dumbović et al., 2018) describes the ICME ejecta as a cylindrical structure (flux rope) of radius a , which is assumed to initially contain no GCRs when it is launched from the Sun. As it propagates outward, the flux rope expands (e.g., at a larger rate than the typical solar wind, Bothmer & Schwenn, 1997; Gulisano et al., 2010; Liu et al., 2005) and GCRs gradually diffuse into it at a rate slower than they would in the ambient solar wind. As a result, after some time, the flux rope will be only partially filled with GCRs compared to the ambient solar wind and therefore will appear as a decrease in the GCR flux. The decrease of the GCR phase space density in the flux rope (normalized as before in equation (4)) is described using the Bessel function of first kind and order zero ($J_0(x)$):

$$y_e(r_e, t_E) = J_0\left(\alpha_1 \frac{r_e}{a}\right) e^{-\alpha_1^2 f(t_E)}, \quad (6)$$

where $\alpha_1 \approx 2.40$ is the first positive root of the Bessel function J_0 , r_e is the radial distance of the observer from the flux rope's central axis, and $f(t_E)$ is a function that is monotonically increasing with the expansion time t_E and does not depend on r_e . Note that the index e (as in y_e, r_e) stands for ejecta and E (as in t_E) for expansion. Equation (6) states that in the ForbMod model, the GCR suppression due to the flux rope is 0 at its border ($r_e = a, y_e \propto J_0(\alpha_1) = 0$); that is, the flux rope has no GCR shielding effect outside of its bounds. The maximum depression is reached on the flux rope axis at $r_e = 0$ ($\rightarrow J_0(0) = 1$). For details on the derivation of equation (6) and the functional form of $f(t_E)$, we refer to Dumbović et al. (2018).

To combine the two models and convert $y_s(x_s)$ and $y_e(r_e)$ into a $y(t)$ profile, we apply the following scheme: We define the time where the outer boundary of the sheath reaches the position of the observer ($x_s = 0$) as $t = 0$. Within the sheath region, the GCR drop is only driven by the sheath and described by equation

(5). The sheath is moving with respect to the observer with a speed v_{sheath} , which is assumed to be constant within the passage duration, so

$$x_s(t) = v_{\text{sheath}} t. \quad (7)$$

At the end of the sheath region (time $t = T_{\text{sheath}}$, calculated with $x_s(T_{\text{sheath}}) = S$), we then continue with the ForbMod model given by equation (6). In this case, we first define the trajectory of the observer as before, but with the propagation speed v_{ICME} of the ejecta:

$$x_e(t) = S + v_{\text{ICME}}(t - T_{\text{sheath}}) \quad (8)$$

The distance r_e to the center of the flux rope, which is needed for equation (6), can then be calculated using the radius a of the flux rope:

$$r_e(t) = S + a - x_e(t) = a - v_{\text{ICME}}(t - T_{\text{sheath}}). \quad (9)$$

Note that this equation is only valid up to the point where the flux rope axis reaches the observer, which is the point of maximal GCR suppression. We do not consider the following recovery phase, as explained below. So in summary, our model combination, as it is plotted in Figure 1 (lower panel), can be written as follows:

$$y(t) = \begin{cases} y_s(v_{\text{sheath}} t), & t \leq T_{\text{sheath}} \\ y_s(S) + y_e(a - (t - T_{\text{sheath}})v_{\text{ICME}}, t_E), & t \geq T_{\text{sheath}} \end{cases} \quad (10)$$

where the various quantities have been defined above.

The combination of these two models in this way is of course a simplification, as any interplay between sheath and ejecta is not really taken into account. In particular, the GCR suppression at the end of the sheath ($y_s(S)$) is added as a constant value to the following additional suppression by the ejecta without accounting for the recovery from the sheath FD, which is not modeled by PDB. Also, the recovery phase after the ejecta is not modeled. A more complicated model combining the two structures would be needed for including these effects, but that is not necessary for the purposes of this study because we only focus on the GCR minimum, Δy and the steepest slope, m_{max} .

4. Results and Discussions

4.1. Observations

When plotting the maximum hourly decrease m_{max} versus the FD amplitude Δy (as defined in section 3.1) for the 45 events in the STEREO-HI catalog, which were also observed by RAD at Mars, as seen in Figure 2 (orange points), a striking correlation appears with a Pearson correlation coefficient of $r = 0.77$. The probability p that this distribution is caused by an uncorrelated system is below $10^{-4}\%$. We also plotted the FDs at Earth (measured at the South Pole neutron monitor) from the subset of ICMEs that were seen at both Earth and Mars (blue points in Figure 2). To make clear which of the events at Mars were also seen at Earth, the corresponding orange points in the figure were marked with blue outlines, and as expected, they follow a similar distribution as the rest of the 45 events at Mars.

The same correlation was already found at Earth by Abunin et al., 2012 (2012, Figure 5) and Belov (2008, Figure 7), with corresponding correlation coefficients between 0.57 and 0.87 for different samples of FDs. This correlation coefficient can vary depending on the specifics of the FDs, such as what type of structures they are caused by. In particular, Belov (2008) found a higher correlation coefficient for FDs related to ICMEs that drive a shock than for other ICMEs. To further evaluate the m_{max} versus Δy correlation, we applied a linear regression to calculate the parameters for the equation:

$$\Delta y = A m_{\text{max}} + B, \quad (11)$$

where A is expressed in hours and B in %. B corresponds to the amplitude of a “FD” with a maximum hourly decrease of 0, so it is expected to be 0. Considering the uncertainties in the measurement of the FD magnitudes and maximum hourly decreases, we therefore constrained B to be within the bounds of $[-0.5\%, +0.5\%]$ for the fitting procedure, instead of forcing it to be 0. The uncertainties of the linear regression results

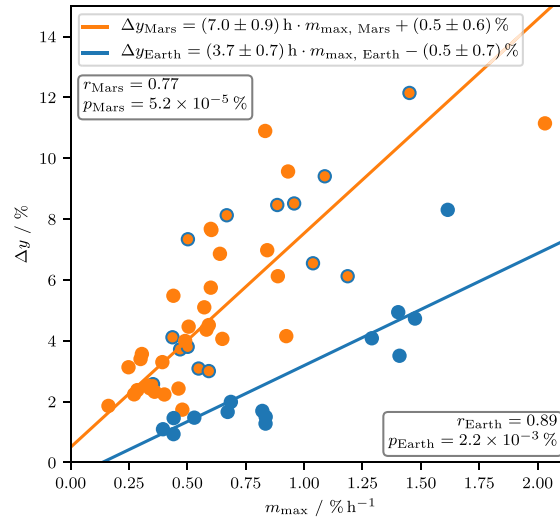


Figure 2. Comparison of the correlations between the FD amplitude Δy and the maximum hourly decrease m_{\max} at Earth (blue) and Mars (orange), based on the ICME and FD catalog from Freiherr von Forstner et al. (2019). The orange dots with a blue outline correspond to the Mars events that were also seen at Earth as FDs in the South Pole neutron monitor during close alignments of the two planets. The blue points show the properties of the terrestrial FDs for these events. The Pearson correlation coefficients r as well as the probabilities p that such a distribution was produced by an uncorrelated system are given in the plot, as well as the results of a linear regression for the two data sets.

are given as the standard deviation estimated by calculating the square root of the diagonal elements of the covariance matrix.

The linear regressions by Abunin et al. (2012) and Belov (2008) yielded values of A between 2.9 and 3.5 hr at Earth, and this roughly agrees with our result of 3.7 ± 0.7 hr obtained for the subset of events from our catalog that were also seen at Earth (14 events). However, the linear regression for MSL/RAD measurements at Mars in Figure 2 results in a slope of $A = 7.0 \pm 0.9$ hr; that is, the ratio between FD amplitudes and their respective maximum slopes increases by a factor of $\sim 1.9 \pm 0.4$ at MSL/RAD compared to the South Pole neutron monitor.

On the other hand, Papaioannou et al. (2019), who studied a much larger catalog of FDs at Mars using MSL/RAD data, found about the same value for A for Earth and Mars FDs in their Figure 6, with A values of (3.64 ± 0.32) hr for Mars and (3.69 ± 0.16) hr for Earth. Considering this discrepancy, we now take a closer look at the FD data from this catalog. As stated in section 2.2, this catalog includes both FDs caused by ICMEs as well as other heliospheric transients, such as CIRs.

In order to separate the FDs caused by different heliospheric dynamic structures, we used the Papaioannou et al. (2019) catalog of FDs at Mars and the IZMIRAN database of FDs at Earth to produce separate plots in Figure 3. All FDs at Earth (left) and Mars (right) were plotted together in the two topmost panels, followed by the subset of FDs that were marked as being caused by an ICME in the respective catalogs (middle panels) and the remaining FDs, which were probably caused by CIRs or combinations of CIRs and ICMEs (lower panels). The linear regression was then applied separately for each panel of the Figure. For the purpose of comparability, the events from the IZMIRAN catalog were restricted to the same time range as the Papaioannou et al. (2019) catalog (August 2012 to December 2016). As before for Figure 2, we restricted the y intercept of the linear regression to be within $\pm 0.5\%$. Additionally, we introduced a threshold condition specifying the minimum amplitude (percentage drop Δy) a FD needs to have to be included in the calculation of the linear regression. This is done to exclude FDs with very low amplitudes where the values of Δy and m_{\max} may have larger uncertainties, limited by the observational resolution. The threshold condition was defined as follows:

$$\Delta y \geq f \cdot \text{median}(\Delta y), \quad (12)$$

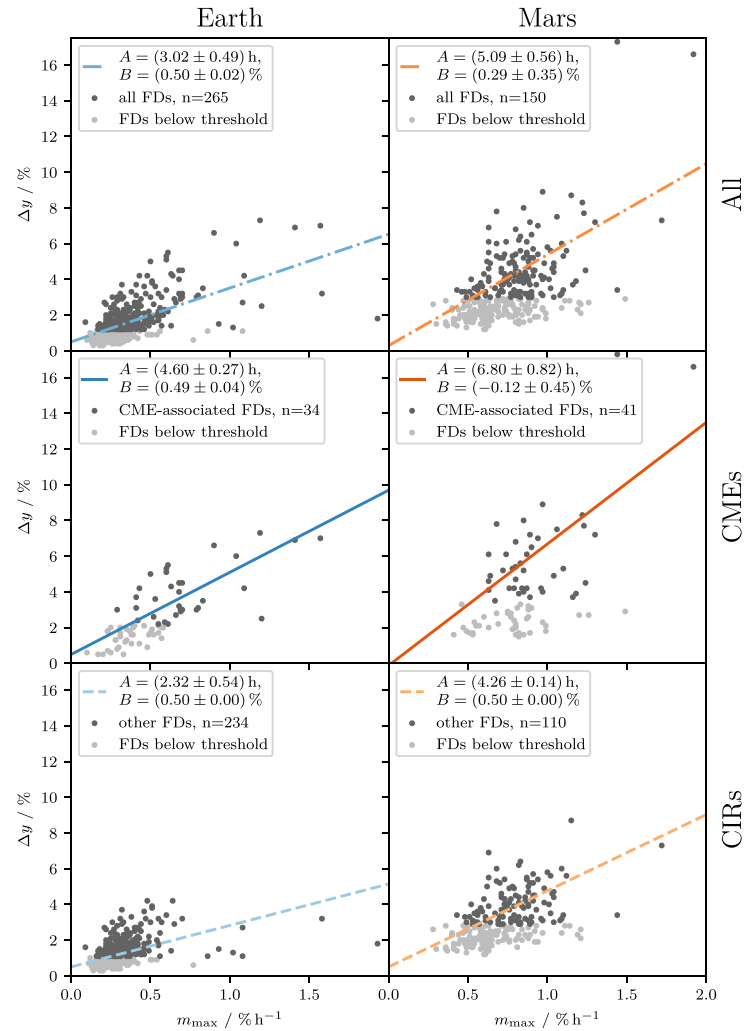


Figure 3. Scatter plot of the FD parameters m_{\max} (maximum hourly decrease) and Δy (drop ratio). The left panels are based on the IZMIRAN FD catalog at Earth, while the right column shows data from the catalog of FDs at Mars by Papaioannou et al. (2019). Each column contains separate panels for one plot with all events (top row), one with just FDs related to ICMEs (middle row), and one with all other FDs, most of which were probably caused by CIRs (bottom row). The blue and orange lines show linear regressions to the data, where the light gray points denote events that were excluded from the fit because they lie below the $f = 1$ threshold (as defined in equation (12)).

where the dimensionless value f can be adjusted as needed and was initially chosen as 1 for the plots in Figure 3 to remove all FDs with an amplitude below the median. To more accurately estimate the uncertainties of the fitting parameters with this larger set of events, a bootstrap method was applied by taking 10,000 different random samples of the points to be fitted and then applying the fit separately to each of the samples. From the resulting distribution of fit parameters, the mean and standard deviation of A and B were then calculated and displayed in the insets of Figure 3.

The results we obtained for all FDs (upper panel) seem to be different from those by Papaioannou et al. (2019)—we find a larger A value at Mars than at Earth, while their analysis showed almost the same value at both planets. This is both due to the threshold condition used here as well as a different fitting algorithm used by Papaioannou et al. (2019): They did not directly apply a linear regression to the data but first binned the data on the m_{\max} axis, calculated average values and standard deviations of Δy for each bin, and then

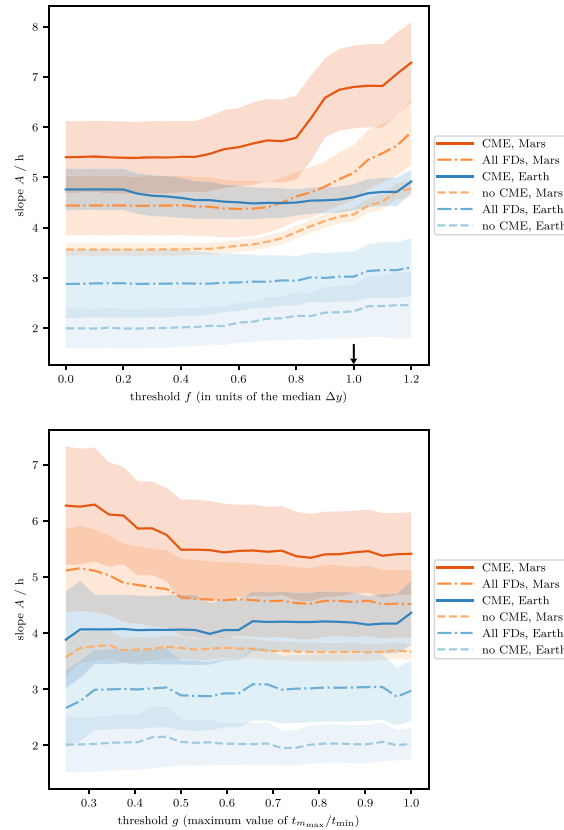


Figure 4. Dependence of the linear regression slope A on the chosen threshold parameters f and g . Solid blue and orange lines show results for ICME-induced FDs at Earth and Mars, while dashed and dotted lines denote the values for non-CME events and all events, respectively. The shaded areas correspond to the 1σ uncertainty of the linear regression obtained from the bootstrap method. The upper panel shows the results for the f parameter for the condition in equation (12), while the lower panel gives the corresponding results for the g parameter for the condition in equation (13) explained in Appendix A. The arrow in the upper panel marks the value $f = 1$ which was used for the plot in Figure 3.

used these values as the input for the linear fit. This approach means that data about the single events are not available to the fitting procedure anymore, which can be a drawback especially when the number of events is reduced in the case where; for example, we only look at ICME-caused FDs. Also, the result can significantly change depending on the choice of bin locations and sizes and whether bins containing a low number of events are excluded from the fit or not.

For the above reasons, we decided to alternatively apply a simple linear regression to all the data without prebinning them. However, we do note that there are a few outlier events that may have been weighted much less by Papaioannou et al.'s (2019) fitting algorithm than by ours. Nevertheless, we are mainly interested in the two panels in the middle row, which show the FDs associated with CMEs at Earth and Mars. In agreement with Figure 2, we also find a larger A value at Mars than at Earth (factor 1.5 ± 0.2) here.

We will now check how our result depends on the choice of the threshold parameter f for values different than 1. The upper panel of Figure 4 shows values of f between 0 (i.e., no threshold condition) and 1.2 and the resulting A values. The uncertainties calculated using the bootstrap method are shown as shaded areas in this plot. While the results for CME-induced FDs at Earth as well as non-CME FDs at both planets change rather slowly with a rising threshold, there is quite a steep increase in the A values for CME events at Mars above $f = 0.8$. This might be an effect of outlier events—completely removing three events at the bottom right of the “CMEs at Mars” panel results in a smoother increase of A with increasing f . But the trend of

increasing A with f is still present, and this suggests a change of physical FD and/or ICME properties for FDs with larger magnitudes. We will discuss this hypothesis further in the next section.

4.2. Interpretation

4.2.1. Cartoon Illustration of the Effect

There are two factors that might be important for the difference between the A values found at Earth and Mars: The evolution of the ICME structure between 1 and 1.5 AU, as well as the different observed GCR energies (protons mainly between $E_{\text{kin}} \sim 1$ to 3 GeV at Mars versus $E_{\text{kin}} = 9.1$ GeV at Earth in the GSM data; see section 2.1). We will first discuss the influences of these two effects on our result under the simple assumption that the GCR energy affects only the amplitude of the FD, while an increase of the size or thickness of the ICME can increase the passage duration and thus the duration of the FD decrease phase. In the following section 4.2.3, we will then justify these assumptions with modeling results.

In Figure 5a, we show idealized schematic profiles of three FDs at Earth with different amplitudes but similar duration of their decrease phase. The recovery phase is faded out to indicate that it is not relevant for our study and can be different for each event. The FD profiles are just plotted for illustration purposes here and do not represent profiles calculated from the models described in section 3.2, which we will go into later. We also do not yet separate the shock/sheath and ejecta effects here. In the right panel, the three FDs are plotted in the familiar Δy versus m_{max} scheme—as we saw in the measurements, m_{max} is proportional to Δy in this case. When the ICME travels from Earth to Mars and increases its size during this time, the duration of the FD increases (panel b), and thus, m_{max} is decreased for the same FD amplitude; that is, the slope A of the linear relationship between Δy and m_{max} increases. When also taking into account the effect of the lower observed GCR energy in panel (c), Δy and m_{max} increase proportionally, so A stays at the same value. Of course, in reality, the two effects cannot be observed separately, because there is no direct GCR measurement at Mars (or somewhere else at 1.5-AU solar distance) with exactly the same energy response as at Earth. For example, the 9.1-GeV primary GCR protons considered in the GSM data could not be easily isolated in RAD measurements, and secondaries produced by those particles in the Martian atmosphere would also need to be taken into account.

This simple model described in Figure 5 explains the observations presented in Figures 2 and 3 very nicely, but it has a few aspects that need some closer inspection: First, it is also possible that the ICME broadening already causes a change of the FD amplitude independent of the GCR energy effect. This could, for example, be due to a decrease of the magnetic field strength within the ICME that is associated to its expansion. This is not accounted for in the figure, but as the change in amplitude only shifts the points in the Δy versus m_{max} plot along the same linear regression, this would not have any effect on the result for A . Second, the illustration might suggest that all FDs have the same duration at Earth. This is obviously not true, as the FD duration depends on the ICME speed and size as well as turbulent and magnetic properties, which contributes to the dispersion of the points in Figure 3. Also, the ICME structure as a whole does not grow linearly; rather, the evolutions of the sheath and ejecta regions are governed by different physical processes and thus can behave differently between Earth and Mars. We will further investigate the distribution of m_{max} in the following section and also apply the FD models introduced in section 3.2 to get a better understanding of how this effect is related to the different substructures of the ICME.

4.2.2. Distribution of m_{max} Within the ICME Substructures

Based on a separate statistical study we have performed (see Appendix A), we estimate that at Earth, m_{max} occurs in the sheath about twice as often as in the ejecta. Therefore, we expect the main influence on the observed difference of the linear regression slope A at Earth and Mars to be the evolution of the sheath region. This should mean that the difference is more clearly visible if we exclude events where m_{max} is not in the sheath, which is what we try to reproduce in this section.

In the lower panel of Figure 4, we have defined a new threshold condition to filter the FDs in our catalog and plotted the result in the same fashion as for the previous threshold parameter f (upper panel, see section 4.1). The threshold condition is defined as

$$t_{m_{\text{max}}} \leq g \cdot \Delta t, \quad (13)$$

where Δt is the duration of the FD decrease phase as defined in Figure 1 (upper panel). For example, for a threshold of $g = 0.5$, the time where the maximum hourly decrease occurred needs to be within the first half of the FD's decrease phase. A low g value does not necessarily mean that m_{max} is within the sheath (as the

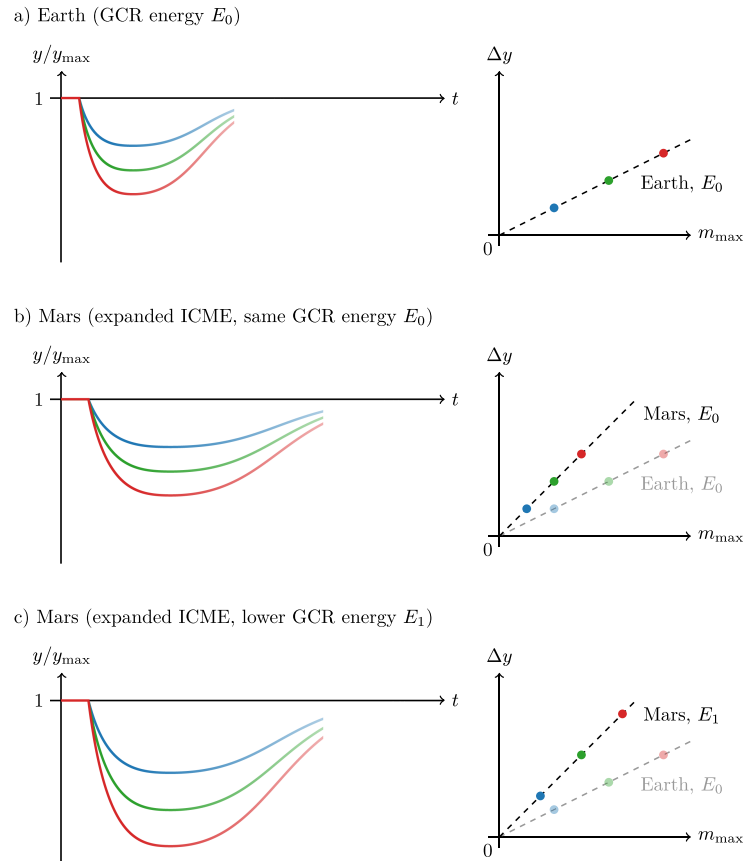


Figure 5. Illustration of the Δy versus m_{\max} correlation for Earth and Mars. Panel (a) shows three different examples of FDs at Earth with different amplitudes, where m_{\max} is linearly correlated with Δy . When the ICME's size increases during the propagation from Earth to Mars, the FD duration increases (panel b), thus decreasing m_{\max} . Due to the lower observed GCR energies, FDs observed at Mars using RAD also have a larger amplitude than their terrestrial counterparts (panel c). However, this effect does not change the slope of the linear regression. Panel (b) is a theoretical case which cannot be observed in reality, because there is no GCR measurement at Mars that has exactly the same energy response as an Earth-based measurement.

sheath could be very short or not seen by the observer at all), but the likelihood that m_{\max} is in the sheath definitely increases with decreasing g . The previous threshold condition from equation (12) is not applied anymore in this case.

While the error bars, again showing the standard deviation obtained from the bootstrap method, become slightly larger than those in the case of the upper panel, it can still be seen in the lower panel that the linear regression slope A increases with lower values of g for CME-related FDs at Mars. At a value of $g = 0.3$, the ratio between CME-caused FDs at Earth and Mars has increased to 1.5 ± 0.4 , comparable to the ratio obtained in the upper panel for the $f > 0.8$ cases. Based on these results, we suspect that there are two populations of CME-caused FDs seen at Mars: FDs with m_{\max} observed in the sheath result in a larger slope A and FDs where m_{\max} is caused by the ejecta have a lower value of A . Such a trend can be seen in both panels of Figure 4.

4.2.3. Analytical Modeling of the Effect

To give a more sophisticated theoretical description of the FDs than the qualitative illustration in Figure 5, we now employ the analytical FD models introduced in section 3.2.

In the sheath region (again denoted with the index s), the FD is described by the PDB model as a linear function (equation (5)), so we can easily calculate the decrease rate (which is constant and therefore equivalent to m_{\max}) and the FD amplitude, and give the ratio of the two:

$$m_{\max,s} = \frac{dy_s}{dt} = \frac{\partial y_s}{\partial x_s} \frac{dx_s}{dt} = \frac{v_{\text{sheath}}}{K'} v_{\text{sheath}} \quad (14)$$

$$\Delta y_s = y_s(S) = \frac{v_{\text{sheath}}}{K'} S \quad (15)$$

$$\Rightarrow \frac{\Delta y_s}{m_{\max,s}} = \frac{S}{v_{\text{sheath}}} = T_{\text{sheath}} \quad (16)$$

As expected, m_{\max} is proportional to Δy and the proportionality factor is S/v_{sheath} , that is, the length of the sheath region divided by its speed, which is equal to its passage duration T_{sheath} .

For the magnetic ejecta described by ForbMod (index e), the decrease rate is not constant, as can be seen in equation (6). Assuming that the flux rope expansion while it passes by the observer is negligible (as the passage duration is small compared to the transit time from the Sun to the observer), we can ignore the time dependence of $f(t_E)$ and estimate that the speed of the flux rope passing by the observer is constant and equal to the propagation speed of the flux rope, $dr_e/dt \approx v_{\text{ICME}}$. With these simplifications, we can again derive an equation for m_{\max} :

$$\frac{\partial y_e}{\partial r_e} = \frac{\alpha_1}{a} J_1 \left(\alpha_1 \frac{r_e}{a} \right) e^{-\alpha_1^2 f(t_E)} \quad (17)$$

$$m_{\max,e} = \max \left(\frac{dy_e}{dt} \right) \quad (18)$$

$$= \max \left(\frac{\partial y_e}{\partial x_e} \frac{dx_e}{dt} + \frac{\partial y_e}{\partial t_E} \frac{dt_E}{dt} \right) \quad (19)$$

$$\approx \max \left(\frac{\partial y_e}{\partial x_e} \frac{dx_e}{dt} \right) \quad (20)$$

$$= \max \left(\frac{\alpha_1}{a} J_1 \left(\alpha_1 \frac{r_e}{a} \right) e^{-\alpha_1^2 f(t_E)} \right) v_{\text{ICME}} \quad (21)$$

$$= \frac{\alpha_1}{a} v_{\text{ICME}} \xi_1 e^{-\alpha_1^2 f(t_E)}, \quad (22)$$

where we used the simplification $t_E = \text{const.}$, as the expansion time, which is equal to the transit time, is large compared to the passage duration at the observer, and the result $dr_e/dx_e = -1$, which follows from equation (9). Additionally, the relation for the derivative of the zeroth-order Bessel function $dJ_0(x)/dx = -J_1(x)$ was used, and $\xi_1 \approx 0.58$ is the global maximum of the first-order Bessel function $J_1(x)$. For Δy , we evaluate equation (6) on the axis of the flux rope ($r_e = 0$) to obtain the following equation:

$$\Delta y_e = y_e(r_e = 0, t) = J_0(0) e^{-\alpha_1^2 f(t_E)} = e^{-\alpha_1^2 f(t_E)}, \quad (23)$$

where the property of the Bessel function $J_0(0) = 1$ was used. The ratio of Δy and m_{\max} is then again just dependent on the passage duration of the ejecta T_{ICME} :

$$\Rightarrow \frac{\Delta y_e}{m_{\max,e}} = \frac{a}{v_{\text{ICME}}} \frac{1}{\alpha_1 \xi_1} \approx \frac{1}{2} T_{\text{ICME}} \cdot 0.71 = 0.36 \cdot T_{\text{ICME}} \quad (24)$$

As a corresponds to the flux rope radius and not its total thickness, the passage duration T_{ICME} is $2a/v_{\text{ICME}}$, and 0.71 is the approximate numerical value of $1/\alpha_1 \xi_1$.

A few main conclusions can be drawn from these calculations:

First, we find the expected proportionality of Δy_s or Δy_e versus m_{\max} in the sheath or in the ejecta region. We note that there is no dependence of the proportionality factor on the GCR energy. Any such dependence would need to be induced by a variation of the diffusion coefficients (K' for the sheath, and quantities within $f(t_E)$ for the ejecta) for different GCR energies, but these cancel out in the calculation of the ratio (equations (16) and (24)). Thus, a change in this value can only be due to evolutionary changes in the extent of the respective region (sheath or ejecta).

Second, m_{\max} in the ejecta part is expected to decrease exponentially over time (equation (22)), while m_{\max} of the sheath can change in different ways depending on the evolution of the sheath speed and the magnetic field (which affects the diffusion coefficient K). This means that due to these two competing effects, it could happen that close to the Sun, m_{\max} occurs in the ejecta, but moves to the sheath at a later time. As for the majority of events at Earth, m_{\max} is already in the sheath (see section 4.1 and Figure A1), we expect this fraction to be similar or even higher at Mars.

There is one more point that we have to account for in this calculation: From the analytical solutions, we can only derive ratios $\Delta y_s/m_{\max,s}$ and $\Delta y_e/m_{\max,e}$. However, from GCR observations alone, one could only obtain Δy , that is, the total amplitude of the FD caused by both ICME regions together. The proportionality factor $A = \Delta y/m_{\max}$ would have to be calculated like this:

$$A = \frac{\Delta y}{m_{\max}} = \begin{cases} \frac{\Delta y_s + \Delta y_e}{m_{\max,s}}, & m_{\max,s} \geq m_{\max,e} \\ \frac{\Delta y_s + \Delta y_e}{m_{\max,e}}, & m_{\max,s} \leq m_{\max,e} \end{cases} \quad (25)$$

If we do not see a clear two-step FD, which is most often the case (especially with limited data resolution), there is no trivial way to measure Δy_s or Δy_e directly without additional data (e.g., solar wind plasma or magnetic field measurements) that allows for an exact definition of the separation between sheath and ejecta (if either part exists). Therefore, to explain the observed linear relationship, it needs to be assumed that there is always a dominant part which drives the FD; that is, $\Delta y \approx \Delta y_s$ or $\Delta y \approx \Delta y_e$. As we have found in Appendix A and Figure A1, m_{\max} is more likely to appear in the sheath at Earth and Mars. Besides, Masías-Meza et al. (2016) have shown in their Figure 6 that the amplitude of the FD in the ejecta, Δy_e , is usually much smaller than the one driven by the sheath, Δy_s , so the first assumption, $\Delta y \approx \Delta y_s$ is probably valid for most ICMEs.

4.2.4. Quantification of the Sheath Broadening Processes

The evolution of the sheath during the propagation of an ICME is governed by five main physical processes, as explained by Janvier et al. (2019) and discussed in more detail by Manchester et al. (2005) and Siscoe and Odstrcil (2008): (1) the pileup of solar wind in front, (2) reconnection with the following ejecta, (3) compression of the sheath by the following ejecta, (4) expansion or contraction associated to the radial velocity profile of the sheath, and (5) lateral transport of plasma orthogonal to the ejecta motion, that is, away from the ICME apex. We will go through each of these effects to estimate their importance for the evolution of the sheath between 1 and 1.5 AU and, if possible, give a first-order approximation of their magnitude. As the observed difference in $\Delta y/m_{\max}$ ratios in FDs is expected to be mainly caused by the sheath evolution (see the previous two sections), we will not do a similar estimation for the evolution of the ICME ejecta here, and we refer to previous studies such as Bothmer and Schwenn (1997) and Liu et al. (2005). For the following calculations, we will call the sheath thickness S and the radial distance of the sheath from the Sun r . We also define $\Delta v_{\text{shock}} = v_{\text{shock}} - v_{\text{sw}}$ to be the speed of the shock relative to the ambient solar wind, $\langle v_{\text{sheath}} \rangle$ the mean speed within the sheath and $\Delta v_{\text{sheath}} = v_{\text{S,front}} - v_{\text{S,rear}}$ the velocity difference between the front and rear end of the sheath.

1. The sheath thickness gained through the pileup of solar wind in front can be estimated to be proportional to the speed of the shock relative to the surrounding solar wind; that is, $\Delta S_{\text{pileup}} = (v_{\text{shock}} - v_{\text{sw}})\Delta t/f_c$, where f_c is the factor by which the plasma added to the sheath is then compressed. Some rearranging yields

$$\Delta S_{\text{pileup}} = \frac{1}{f_c}(v_{\text{shock}} - v_{\text{sw}})\Delta t = \frac{1}{f_c}(v_{\text{shock}} - v_{\text{sw}})\frac{\Delta r}{v_{\text{shock}}} = \frac{1}{f_c}\frac{\Delta v_{\text{shock}}}{v_{\text{shock}}}\Delta r \quad (26)$$

The factor f_c is expected to be close to the density ratio between the sheath and the ambient solar wind in front. This is typically around 2.5 at 1 AU (see, e.g., Janvier et al., 2014, Figure 5b) and is expected to decrease on the way to Mars.

2. We assume reconnection with the following ejecta to be negligible at these distances from the Sun. This effect, which is responsible for an erosion of the ejecta, can be significant close to the Sun, but as Lavraud et al. (2014) have shown, it becomes less important at larger distances due to the dropping Alfvén speed v_A . They found that the reconnection rate at 1 AU is already up to 10 times smaller than the average value between the Sun and 1 AU required for the erosion seen at Earth.

3. Compression of the sheath by the following ejecta is also expected to be small for most events, because by the time an ICME arrives at 1 AU, it has usually already reached a state where the velocities of the rear end of the sheath and the front of the ejecta are very similar. This can be seen, for example, in the superposed epoch analysis results by Masias-Meza et al., 2016 (2016, Figures 2 and 4).

These three effects correspond to outer influences on the sheath region. There are two more effects related to the motion of plasma within the sheath:

4. The expansion (or, possibly, contraction), which corresponds to the radial velocity profile within the sheath, can be calculated based on the front and rear velocities of the sheath region:

$$\Delta S_{\text{exp}} = (v_{S,\text{front}} - v_{S,\text{rear}})\Delta t = \frac{\Delta v_{\text{sheath}}}{\langle v_{\text{sheath}} \rangle} \Delta r \quad (27)$$

This velocity profile can be the result of previous external influences on the sheath (1–3) during the propagation from the Sun to 1 AU, so these are not neglected in our simple model.

5. The decrease of sheath thickness due to lateral plasma motion away from the ICME apex is not as simple to estimate as the previous effects. With plasma data at multiple radially aligned spacecraft, it might be possible to measure the magnitude of this effect, such as was done by Nakwacki et al. (2011) for the ejecta (magnetic cloud), but this would be difficult at Mars due to the scarcity of plasma data and the rare occurrence of radial alignments with Earth as well as the turbulent nature of the sheath. An alternative would be to employ numerical simulations, but this is also beyond the scope of this paper.

In summary, we can say that, unless the lateral deflection (5) is the dominant process, the sheath thickness is expected to increase proportionally to the solar distance. This is only true if the velocities of the ICME substructures evolve slowly between Earth and Mars, but this is probably a valid assumption as the overall propagation velocity usually does not change much beyond 1 AU (Liu et al., 2013; Freiherr von Forstner et al., 2018; Zhao et al., 2019). If lateral deflection is significant, the sheath thickness would increase more slowly, so our following calculations are a kind of upper limit approximation.

The estimations we have made for the different processes influencing the sheath size are likely to be valid between 1 and 1.5 AU, but not necessarily closer to the Sun. This means we cannot calculate ΔS all the way from the Sun to Mars based on our equations above but instead have to start with the sheath thickness S_{Earth} at Earth and add ΔS between Earth and Mars to it. Thus, we calculate the broadening factor E between Earth and Mars, which is the ratio of the sheath thicknesses S at the two planets, in the following way:

$$E = \frac{S_{\text{Mars}}}{S_{\text{Earth}}} = \frac{S_{\text{Earth}} + \Delta S}{S_{\text{Earth}}}. \quad (28)$$

Inserting the terms from above to substitute ΔS with quantities that can be measured at Earth, we get

$$E = 1 + \frac{1}{S_{\text{Earth}}} \left(\frac{\Delta v_{\text{shock}}}{v_{\text{shock}} f_c} + \frac{\Delta v_{\text{sheath}}}{\langle v_{\text{sheath}} \rangle} \right) \Delta r \quad (29)$$

So to calculate the broadening factor between Earth and Mars, typical values of the shock and sheath speeds as well as the sheath thickness at Earth S_{Earth} are needed. Based on the solar wind speeds from the superposed epoch analysis shown in Figure 4 of Masias-Meza et al. (2016) (or similar results by Liu et al., 2006) and the expected value of $f_c \lesssim 2.5$, we can estimate the term $\Delta v_{\text{shock}}/(v_{\text{shock}} f_c) + \Delta v_{\text{sheath}}/\langle v_{\text{sheath}} \rangle$ to be between about 0.07 and 0.26. According to Janvier et al. (2019), the median duration of the sheath at 1 AU is approximately half a day, and with a typical sheath speed of 560 km/s (similar to the value given in Table 1 of Masias-Meza et al., 2016), we can then calculate $S_{\text{Earth}} \approx 0.17$ AU. This is also in agreement with Kilpua et al. (2017), who find a duration of 11.1 hr and a thickness of 0.13 AU for their sample of ICMEs at Earth.

The parameters estimated above can be inserted into equation (29) together with the radial distance $\Delta r \approx 0.5$ AU between Earth and Mars, resulting in values of E between 1.2 and 1.8. As we have shown in section 4.2.3, the broadening factor

$$E = \frac{S_{\text{Mars}}}{S_{\text{Earth}}} \approx \frac{T_{\text{sheath, Mars}}}{T_{\text{sheath, Earth}}} \quad (30)$$

should be equivalent to the ratio of the slopes $A_{\text{Mars}}/A_{\text{Earth}}$ in the relation of the FD parameters. And in fact, the values of $A_{\text{Mars}}/A_{\text{Earth}}$ that we have calculated from FD measurements in sections 4.1 and 4.2.2 to be between 1.5 and 1.9 are comparable to our theoretical estimations of E .

Comparing with results of Janvier et al. (2019) in their Table 1, we see that the broadening of the sheath slows down as the ICME propagates outward. This is expected, especially because the pileup of solar wind in front (Process (1)) decreases rapidly when the shock decelerates and approaches the speed of the ambient solar wind. Between Mercury (~ 0.4 AU) and Venus (~ 0.72 AU), the sheath duration increases by a factor of 3 over a distance of just 0.32 AU, and from Venus to Earth (1 AU), a distance of 0.28 AU, it grows by a factor of 1.7. Our result with a broadening factor of 1.2 to 1.8 between Earth and Mars (0.5 AU distance) extends these results to beyond 1 AU.

5. Conclusions and Outlook

In this work, we analyzed the properties of FDs measured at Mars by MSL/RAD compared to those measured at Earth. Our study focused on the correlation of the maximum hourly decrease m_{max} and the FD amplitude Δy and how this differs between FDs at Earth and Mars. We first investigated this effect using our own catalog of 45 ICMEs observed by the STEREO Heliospheric Imagers that caused FDs at Mars (Freiherr von Forstner et al., 2019) and later expanded the study to larger catalogs of FDs at Mars (Papaioannou et al., 2019) and Earth (IZMIRAN catalog). The correlation between m_{max} and Δy is also seen in these two catalogs. We applied further filtering to the catalog to only consider FDs caused by ICMEs. Also, with two different threshold conditions, we filtered out FDs with small amplitudes whose properties may be associated with larger uncertainties or the smaller population of FDs where the maximum hourly decrease does not occur close to the beginning of the ICME sheath region. With these conditions applied, we found that the slope of the linear regression is steeper at Mars than at Earth by a factor of about 1.5 to 1.9 with an error of ± 0.2 to 0.4.

In a simple approximation of the physical processes involved in the evolution of the ICME sheath region, we found that the sheath broadens by a factor $1.2 \lesssim E \lesssim 1.8$ between Earth and Mars, very similar to the factor obtained for the relation of the FD parameters. Additionally, with analytical models of the FD profile, we could show that the broadening of the sheath can indeed lead to an increase of the $\Delta y/m_{\text{max}}$ ratio, while the different observed GCR energy range at the two locations should have no effect on this quantity.

We have summarized the results for the sheath broadening factor E obtained both from the FD observations in different parts of this study as well as from the theoretical estimation in Table 1. The sheath broadening factor between Earth and Mars that we derived extends previous observations of the evolution closer to the Sun by Janvier et al. (2019). Their results showed that the speed at which the broadening happens decreases further away from the Sun, and our result for the evolution beyond 1 AU agrees with this trend.

Our results show that it is possible to obtain more information about ICMEs from FD measurements than just their arrival time by incorporating different characteristics of the FD and consulting theoretical FD models to find out how they depend on the ICME properties. If statistics allow for this, a future study might be able to verify our findings by measuring the ICME sheath duration directly using in situ solar wind data at Earth and Mars. Also, as FDs can be observed at many locations in the solar system, this approach could be applied to other missions closer to (e.g., Helios, Parker Solar Probe, and Solar Orbiter) and further away from the Sun (e.g., Ulysses) to investigate the ICME evolution in these regions.

Appendix A: Location of m_{max} Within the ICME Substructures

In Figure A1, we plot a histogram of the time where the maximum hourly decrease occurs within the different parts the ICME. This plot combines data from the IZMIRAN FD catalog, where we find the time of the occurrence of m_{max} , with the Richardson and Cane (2010) catalog of ICMEs observed near Earth (available online at <http://www.srl.caltech.edu/ACE/ASC/DATA/level3/icmetable2.htm>), where the shock and ejecta arrival times are listed. Note that in this case, we use the whole time range from 1996 to 2017 that is covered by both catalogs, so this plot is based on a different, larger data set than the rest of the study. The reason for this is that we need the data set to be as large as possible for this study to get a significant overlap between the two catalogs of FD and ICME observations. In both catalogs, many events are associated with CMEs observed by SOHO/LASCO, and we used this column for quickly matching the events in the two catalogs—that is, if a FD in the IZMIRAN catalog is marked as being related to one particular SOHO/LASCO

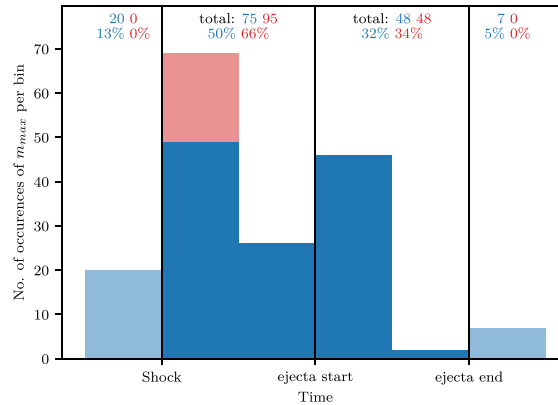


Figure A1. Distribution of the time where m_{\max} occurs between the different parts of the ICME. The sheath and ejecta regions are divided into two equidistant bins each, and two overflow bins show the unphysical cases where m_{\max} occurs after the end of the ejecta or before the shock. The blue numbers and percentages at the top indicate the total number of events within the respective ICME structure (sheath or ejecta) and in the overflow bins. The red bar indicates a version of the histogram where the left overflow bin has been included into the sheath and the right overflow bin dropped from the analysis, as explained in the text—indicated by the light blue color. The updated numbers and percentages for this case are indicated in red.

CME and an ICME in the Richardson and Cane list is associated to the same SOHO/LASCO event, we regard the FD to be caused by this ICME. A manual inspection of each FD-ICME pair might increase the accuracy of this FD-ICME assignment, but this simple approach is sufficient for the purpose of this plot. Then, for each ICME/FD pair, the sheath and ejecta phases were each divided into two equidistant time bins, and the FD onset time was sorted into the respective time bin. The duration of the bins is adjusted for each event depending on its shock, ejecta onset, and ejecta end time from the Richardson and Cane list, so the FD profile duration is normalized into these two bins. This approach is similar to the superposed epoch analysis technique also employed by, for example, Liu et al. (2006), Masias-Meza et al. (2016), and Janvier et al. (2019). If the FD onset time happened at any time before the shock arrival listed by Richardson and Cane, or after the end of the ICME ejecta, it was sorted into a corresponding overflow bin on the left or right side of the plot.

It can be clearly seen that m_{\max} usually occurs either right after the shock or near the beginning of the ejecta phase. In the case of the ejecta, the number of events in the following bin drops off even more than in the sheath, which is reasonable due to the more turbulent nature of the sheath region (see, e.g., Masias-Meza et al., 2016). Nevertheless, in total, m_{\max} occurs more frequently in the sheath than in the ejecta (50% vs. 32% of cases). As there is an uncertainty associated with the determination of shock, ICME and FD onset times, some of the events in the first overflow bin might still belong into the “sheath” category (for most of them, the FD starts just 1–2 hr before the shock arrival time). This could also be a physical effect where the GCRs start to be shielded by the ICME already slightly before its arrival time. On the other hand, the cases in the overflow bin at the end are almost certainly due to an incorrect assignment of the FD to this ICME or the influence of another ICME or CIR structure following the event. Such cases with ICMEs followed by CIRs were also found, for example, by Rodriguez et al. (2016). As per these considerations, we then include the first overflow bin into the sheath and exclude the second overflow bin and find that m_{\max} occurs in the sheath about twice as often as in the ejecta (66% vs. 34%).

To check that the use of a larger time range spanning almost two solar cycles does not distort our results, we have also done this analysis for just the events between August 2012 and December 2016 (same as Catalog II in our main study). The total number of events in the histogram is obviously decreased in this case, but we still obtained very similar results for the distribution between sheath and ejecta.

Acronyms

CIR	Corotating interaction region
CME	Coronal mass ejection

FD	Forbush decrease
ForbMod	Forbush decrease model for flux rope ICMEs (Dumbović et al., 2018)
GCR	Galactic cosmic radiation
GSM	Global survey method (Belov et al., 2005; Belov et al., 2018)
ICME	Interplanetary coronal mass ejection
LASCO	Large Angle and Spectrometric Coronagraph
MAVEN	Mars Atmosphere and Volatile Evolution
MHD	Magnetohydrodynamics
MSL	Mars Science Laboratory
PDB	Propagating diffusive barrier model for Forbush decreases (Wibberenz et al., 1998)
RAD	Radiation Assessment Detector
SEP	Solar energetic particles
STEREO	Solar Terrestrial Relations Observatory
STEREO-HI	Solar Terrestrial Relations Observatory Heliospheric Imagers
SOHO	Solar and Heliospheric Observatory

Acknowledgments

RAD is supported by NASA (HEOMD) under JPL Subcontract 1273039 to Southwest Research Institute and in Germany by DLR and DLR's Space Administration Grants 50QM0501, 50QM1201, and 50QM1701 to the Christian Albrechts University, Kiel. We acknowledge the NMDB database (www.nmdb.eu), funded under the European Union's FP7 Programme (Contract 213007), for providing data. The data from South Pole neutron monitor are provided by the University of Delaware with support from the U.S. National Science Foundation under Grant ANT-0838839. J. G. is supported by the Strategic Priority Program of the Chinese Academy of Sciences (Grants XDB41000000 and XDA15017300), the Key Research Program of the Chinese Academy of Sciences (Grant QYZDB-SSW-DQC015), and the CNSA preresearch Project on Civil Aerospace Technologies (Grant D020104). The visit of J. G. to Paris was funded by the LabEx Plas@Par, which is driven by Sorbonne Université and LabEx P2iO and by researcher scheme "Emilie du Châtelet" to Université Paris-Saclay. M. D. acknowledges partial funding from the EU H2020 MSCA Grant Agreements 745782 (ForbMod) and 824135 (SOLARNET) and support by the Croatian Science Foundation under the Project 7549 (MSOC). A. P. would like to acknowledge the TRACER project funded by the National Observatory of Athens (NOA) (Project ID: 5063).

References

- Abunin, A. A., Abunina, M. A., Belov, A. V., Eroshenko, E. A., Oleneva, V. A., & Yanke, V. G. (2012). Forbush effects with a sudden and gradual onset. *Geomagnetism and Aeronomy*, *52*(3), 292–299. <https://doi.org/10.1134/S0016793212030024>
- Barnes, D., Davies, J. A., Harrison, R. A., Byrne, J. P., Perry, C. H., Bothmer, V., & Odstrčil, D. (2019). CMEs in the heliosphere: II. A statistical analysis of the kinematic properties derived from single-spacecraft geometrical modelling techniques applied to CMEs detected in the heliosphere from 2007 to 2017 by STEREO/HI-1. *Solar Physics*, *294*(5), 57. <https://doi.org/10.1007/s11207-019-1444-4>
- Belov, A. V. (2008). Forbush effects and their connection with solar, interplanetary and geomagnetic phenomena. *Proceedings of the International Astronomical Union*, *4*(S257), 439–450. <https://doi.org/10.1017/S1743921309029676>
- Belov, A. V., Baisultanova, L., Eroshenko, E., Mavromichalaki, H., Yanke, V., Pchelkin, V., & Mariatos, G. (2005). Magnetospheric effects in cosmic rays during the unique magnetic storm on November 2003. *Journal of Geophysical Research*, *110*, A09S20. <https://doi.org/10.1029/2005JA011067>
- Belov, A. V., Eroshenko, E., Yanke, V., Oleneva, V., Abunin, A., Abunina, M., & Mavromichalaki, H. (2018). The global survey method applied to ground-level cosmic ray measurements. *Solar Physics*, *293*(4), 68. <https://doi.org/10.1007/s11207-018-1277-6>
- Bothmer, V., & Schwenn, R. (1997). The structure and origin of magnetic clouds in the solar wind. *Annales Geophysicae*, *16*(1), 1–24. <https://doi.org/10.1007/PL00021390>
- Burlaga, L. F., Plunkett, S. P., & St. Cyr, O. C. (2002). Successive CMEs and complex ejecta. *Journal of Geophysical Research*, *107*(A10), 1266. <https://doi.org/10.1029/2001JA000255>
- Cane, H. V. (2000). Coronal mass ejections and Forbush decreases. *Space Science Reviews*, *93*(1), 55–77. <https://doi.org/10.1023/A:1026532125747>
- Cane, H. V., Richardson, I. G., & von Roseninge, T. T. (1996). Cosmic ray decreases: 1964–1994. *Journal of Geophysical Research*, *101*, 21,561–21,572. <https://doi.org/10.1029/96JA01964>
- Clem, J. M., & Dorman, L. I. (2000). Neutron monitor response functions. *Space Science Reviews*, *93*(1), 335–359. <https://doi.org/10.1023/A:1026508915269>
- Dumbović, M., Heber, B., Vršnak, B., Temmer, M., & Kirin, A. (2018). An analytical diffusion–expansion model for Forbush decreases caused by flux ropes. *The Astrophysical Journal*, *860*(1), 71. <https://doi.org/10.3847/1538-4357/aac2de>
- Dumbović, M., Guo, J., Temmer, M., Mays, M. L., Veronig, A., Heinemann, S. G., et al. (2019). Unusual plasma and particle signatures at Mars and STEREO-A related to CMCEME interaction. *The Astrophysical Journal*, *880*(1), 18. <https://doi.org/10.3847/1538-4357/ab27ca>
- Dumbović, M., Vršnak, B., Čalogović, J., & Karlića, M. (2011). Cosmic ray modulation by solar wind disturbances. *Astronomy & Astrophysics*, *531*, A91. <https://doi.org/10.1051/0004-6361/201016006>
- Eyles, C. J., Harrison, R. A., Davis, C. J., Waltham, N. R., Shaughnessy, B. M., Mapson-Menard, H. C. A., & Rochus, P. (2009). The Heliospheric Imagers onboard the STEREO mission. *Solar Physics*, *254*(2), 387–445. <https://doi.org/10.1007/s11207-008-9299-0>
- Forbush, S. E. (1937). On the effects in cosmic-ray intensity observed during the recent magnetic storm. *Physical Review*, *51*, 1108–1109. <https://doi.org/10.1103/PhysRev.51.1108.3>
- Freiherr von Forstner, J. L., Guo, J., Wimmer-Schweingruber, R. F., Hassler, D. M., Temmer, M., Dumbović, M., & Zeitlin, C. J. (2018). Using Forbush decreases to derive the transit time of ICMEs propagating from 1 AU to Mars. *Journal of Geophysical Research: Space Physics*, *123*, 39–56. <https://doi.org/10.1002/2017JA024700>
- Freiherr von Forstner, J. L., Guo, J., Wimmer-Schweingruber, R. F., Temmer, M., Dumbović, M., Veronig, A., & Ehresmann, B. (2019). Tracking and validating ICMEs propagating toward Mars using STEREO Heliospheric Imagers combined with Forbush decreases detected by MSL/RAD. *Space Weather*, *17*, 586–598. <https://doi.org/10.1029/2018SW002138>
- Gopalswamy, N., Yashiro, S., Kaiser, M. L., Howard, R. A., & Bougeret, J. L. (2001). Radio signatures of coronal mass ejection interaction: Coronal mass ejection cannibalism? *The Astrophysical Journal*, *548*(1), L91–L94. <https://doi.org/10.1086/318939>
- Gulisano, A. M., Démoulin, P., Dasso, S., Ruiz, M. E., & Marsch, E. (2010). Global and local expansion of magnetic clouds in the inner heliosphere. *Astronomy and Astrophysics*, *509*, A39. <https://doi.org/10.1051/0004-6361/200912375>
- Guo, J., Dumbović, M., Wimmer-Schweingruber, R. F., Temmer, M., Lohf, H., Wang, Y., & Posner, A. (2018). Modeling the evolution and propagation of 10 September 2017 CMEs and SEPs arriving at Mars constrained by remote sensing and in situ measurement. *Space Weather*, *16*(8), 1156–1169. <https://doi.org/10.1029/2018SW001973>
- Guo, J., Lillis, R., Wimmer-Schweingruber, R. F., Zeitlin, C., Simonson, P., Rahmati, A., & Böttcher, S. (2018). Measurements of Forbush decreases at Mars: Both by MSL on ground and by MAVEN in orbit. *Astronomy & Astrophysics*, *611*, A79. <https://doi.org/10.1051/0004-6361/201732087>

- Guo, J., Slaba, T. C., Zeitlin, C., Wimmer-Schweingruber, R. F., Badavi, F. F., Böhm, E., & Rafkin, S. (2017). Dependence of the Martian radiation environment on atmospheric depth: Modeling and measurement. *Journal of Geophysical Research: Planets*, *122*, 329–341. <https://doi.org/10.1002/2016JE005206>
- Guo, J., Wimmer-Schweingruber, R. F., Grande, M., Lee-Payne, Z. H., & Matthia, D. (2019). Ready functions for calculating the Martian radiation environment. *Journal of Space Weather and Space Climate*, *9*, A7. <https://doi.org/10.1051/swsc/2019004>
- Guo, J., Zeitlin, C., Wimmer-Schweingruber, R. F., McDole, T., Kühl, P., Appel, J. C., & Köhler, J. (2018). A generalized approach to model the spectra and radiation dose rate of solar particle events on the surface of Mars. *The Astronomical Journal*, *155*(1), 49. Retrieved from <http://stacks.iop.org/1538-3881/155/i=1/a=49>.
- Hassler, D. M., Zeitlin, C., Wimmer-Schweingruber, R. F., Böttcher, S., Martin, C., Andrews, J., & Cucinotta, F. A. (2012). The Radiation Assessment Detector (RAD) investigation. *Space Science Reviews*, *170*(1), 503–558. <https://doi.org/10.1007/s11214-012-9913-1>
- Helcats, E., Barnes, D., Davies, J., & Harrison, R. (2018). HELCATS WP3 CME kinematics catalogue. figshare. Retrieved from <https://figshare.com/articles/HELCATSWP3CMEKINEMATICSCATALOGUE/5803176/1> doi: 10.6084/m9.figshare.5803176.v1.
- Hess, V. F., & Demmelmair, A. (1937). World-wide effect in cosmic ray intensity, as observed during a recent magnetic storm. *Nature*, *140*, 316–317. <https://doi.org/10.1038/140316a0>
- Jakosky, B. M., Lin, R. P., Grebowsky, J. M., Luhmann, J. G., Mitchell, D. F., Beutelschies, G., & Zurek, R. (2015). The Mars Atmosphere and Volatile Evolution (MAVEN) mission. *Space Science Reviews*, *195*(1), 3–48. <https://doi.org/10.1007/s11214-015-0139-x>
- Janvier, M., Démoulin, P., & Dasso, S. (2014). Mean shape of interplanetary shocks deduced from in situ observations and its relation with interplanetary CMEs. *Astronomy and Astrophysics*, *565*, A99. <https://doi.org/10.1051/0004-6361/201423450>
- Janvier, M., Winslow, R. M., Good, S., Bonhomme, E., Démoulin, P., Dasso, S., & Boakes, P. D. (2019). Generic magnetic field intensity profiles of interplanetary coronal mass ejections at Mercury, Venus, and Earth from superposed epoch analyses. *Journal of Geophysical Research: Space Physics*, *124*, 812–836. <https://doi.org/10.1029/2018JA025949>
- Jordan, A. P., Spence, H. E., Blake, J. B., & Shaul, D. N. A. (2011). Revisiting two-step Forbush decreases. *Journal of Geophysical Research*, *116*, A11103. <https://doi.org/10.1029/2011JA016791>
- Kilpua, E., Koskinen, H. E. J., & Pulkkinen, T. I. (2017). Coronal mass ejections and their sheath regions in interplanetary space. *Living Reviews in Solar Physics*, *14*(1), 5. <https://doi.org/10.1007/s41116-017-0009-6>
- Lavraud, B., Ruffenach, A., Rouillard, A. P., Kajdic, P., Manchester, W. B., & Lugaz, N. (2014). Geo-effectiveness and radial dependence of magnetic cloud erosion by magnetic reconnection. *Journal of Geophysical Research: Space Physics*, *119*, 26–35. <https://doi.org/10.1002/2013JA019154>
- Lefèvre, L., Vennerström, S., Dumbović, M., Vršnak, B., Sudar, D., Arlt, R., & Crosby, N. (2016). Detailed analysis of solar data related to historical extreme geomagnetic storms: 1868–2010. *Solar Physics*, *291*, 1483–1531. <https://doi.org/10.1007/s11207-016-0892-3>
- Liu, Y. D., Luhmann, J. G., Lugaz, N., Möstl, C., Davies, J. A., Bale, S. D., & Lin, R. P. (2013). On Sun-to-Earth propagation of coronal mass ejections on Sun-to-Earth propagation of coronal mass ejections. *The Astrophysical Journal*, *769*(1), 45. <https://doi.org/10.1088/0004-637x/769/1/45>
- Liu, Y. D., Luhmann, J. G., Möstl, C., Martínez-Oliveros, J. C., Bale, S. D., Lin, R. P., & Odstreil, D. (2012). Interactions between coronal mass ejections viewed in coordinated imaging and in situ observations. *The Astrophysical Journal*, *746*(2), L15. <https://doi.org/10.1088/2041-8205/746/2/L15>
- Liu, Y. D., Richardson, J., & Belcher, J. (2005). A statistical study of the properties of interplanetary coronal mass ejections from 0.3 to 5.4 AU. *Planetary and Space Science*, *53*(1), 3–17. <https://doi.org/10.1016/j.pss.2004.09.023>
- Liu, Y. D., Richardson, J. D., Belcher, J. W., Kasper, J. C., & Skoug, R. M. (2006). Plasma depletion and mirror waves ahead of interplanetary coronal mass ejections. *Journal of Geophysical Research*, *111*, A09108. <https://doi.org/10.1029/2006JA011723>
- Lugaz, N., Manchester, W. B. IV, & Gombosi, T. I. (2005). Numerical simulation of the interaction of two coronal mass ejections from Sun to Earth. *The Astrophysical Journal*, *634*(1), 651–662. <https://doi.org/10.1086/491782>
- Manchester, W. B., Gombosi, T. I., Zeeuw, D. L. D., Sokolov, I. V., Roussev, I. I., Powell, K. G., & Zurbuchen, T. H. (2005). Coronal mass ejection shock and sheath structures relevant to particle acceleration. *The Astrophysical Journal*, *622*(2), 1225–1239. <https://doi.org/10.1086/427768>
- Masias-Meza, J. J., Dasso, S., Démoulin, P., Rodriguez, L., & Janvier, M. (2016). Superposed epoch study of ICME sub-structures near Earth and their effects on galactic cosmic rays. *Astronomy & Astrophysics*, *592*, A118. <https://doi.org/10.1051/0004-6361/201628571>
- Möstl, C., Rollett, T., Frahm, R. A., Liu, Y. D., Long, D. M., Colaninno, R. C., & Vršnak, B. (2015). Strong coronal channelling and interplanetary evolution of a solar storm up to Earth and Mars. *Nature Communications*, *6*, 7135. <https://doi.org/10.1038/ncomms8135>
- Nakwacki, M. S., Dasso, S., Démoulin, P., Mandrini, C. H., & Gulisano, A. M. (2011). Dynamical evolution of a magnetic cloud from the Sun to AU. *Astronomy & Astrophysics*, *535*, A52. <https://doi.org/10.1051/0004-6361/201015853>
- Odstreil, D., Riley, P., & Zhao, X. P. (2004). Numerical simulation of the 12 May 1997 interplanetary CME event. *Journal of Geophysical Research*, *109*, A02116. <https://doi.org/10.1029/2003JA010135>
- Papaloannou, A., Belov, A. V., Abunina, M., Guo, J., Anastasiadis, A., Wimmer-Schweingruber, R. F., & Steigies, C. T. (2019). A catalogue of Forbush decreases recorded on the surface of Mars from 2012 until 2016: Comparison with terrestrial FDs. *Solar Physics*, *294*(6), 66. <https://doi.org/10.1007/s11207-019-1454-2>
- Rafkin, S. C. R., Zeitlin, C., Ehresmann, B., Hassler, D., Guo, J., Köhler, J., & the MSL Science Team (2014). Diurnal variations of energetic particle radiation at the surface of Mars as observed by the Mars Science Laboratory Radiation Assessment Detector. *Journal of Geophysical Research: Planets*, *119*, 1345–1358. <https://doi.org/10.1002/2013JE004525>
- Richardson, I. G., & Cane, H. V. (2010). Near-Earth interplanetary coronal mass ejections during solar cycle 23 (1996–2009): Catalog and summary of properties. *Solar Physics*, *264*, 189–237. <https://doi.org/10.1007/s11207-010-9568-6>
- Rodriguez, L., Masias-Meza, J. J., Dasso, S., Démoulin, P., Zhukov, A. N., Gulisano, A. M., & Janvier, M. (2016). Typical profiles and distributions of plasma and magnetic field parameters in magnetic clouds at 1 AU. *Solar Physics*, *291*(7), 2145–2163. <https://doi.org/10.1007/s11207-016-0955-5>
- Russell, C. T. (2008). *The STEREO mission*. New York: Springer. <https://doi.org/10.1007/978-0-387-09649-0>
- Siscoe, G., & Odstreil, D. (2008). Ways in which ICME sheaths differ from magnetosheaths. *Journal of Geophysical Research*, *113*, A9. <https://doi.org/10.1029/2008JA013142>
- Smart, D., & Shea, M. (2008). World grid of calculated cosmic ray vertical cutoff rigidities for epoch 2000.0. *Proceedings of the 30th International Cosmic Ray Conference*, *1*, 737–740.
- Tortermun, U., Ruffolo, D., & Bieber, J. W. (2018). Galactic cosmic-ray anisotropy during the Forbush decrease starting 2013 April 13. *The Astrophysical Journal*, *852*(2), L26. <https://doi.org/10.3847/2041-8213/aaa407>
- Vennerström, S., Lefèvre, L., Dumbović, M., Crosby, N., Malandraki, O., Patsou, I., & Moretto, T. (2016). Extreme geomagnetic storms—1868–2010. *Solar Physics*, *291*, 1447–1481. <https://doi.org/10.1007/s11207-016-0897-y>

- Wibberenz, G., le Roux, J., Potgieter, M., & Bieber, J. (1998). Transient effects and disturbed conditions. *Space Science Reviews*, 83(1), 309–348. <https://doi.org/10.1023/A:1005083109827>
- Wimmer-Schweingruber, R. F., Yu, J., Böttcher, S. I., Zhang, S., Burmeister, S., Lohf, H., & Fu, Q. (2020). The Lunar Lander Neutron and Dosimetry (LND) experiment on Chang'E 4. Retrieved from <https://arxiv.org/abs/2001.11028>
- Winslow, R. M., Schwadron, N. A., Lugaz, N., Guo, J., Joyce, C. J., Jordan, A. P., & Mays, M. L. (2018). Opening a window on ICME-driven GCR modulation in the inner solar system. *The Astrophysical Journal*, 856(2), 139. <https://doi.org/10.3847/1538-4357/aab098>
- Witasse, O., Sánchez-Cano, B., Mays, M. L., Kajdič, P., Opgenoorth, H., Elliott, H. A., & Altobelli, N. (2017). Interplanetary coronal mass ejection observed at STEREO-A, Mars, comet 67P/Churyumov-Gerasimenko, Saturn, and New Horizons en route to Pluto: Comparison of its Forbush decreases at 1.4, 3.1, and 9.9 AU. *Journal of Geophysical Research: Space Physics*, 122, 7865–7890. <https://doi.org/10.1002/2017JA023884>
- Zhao, X., Liu, Y. D., Hu, H., & Wang, R. (2019). Quantifying the propagation of fast coronal mass ejections from the Sun to interplanetary space by combining remote sensing and multi-point in situ observations. *The Astrophysical Journal*, 882(2), 122. <https://doi.org/10.3847/1538-4357/ab379b>

MAJOR SPACE WEATHER EVENTS: THE EVENTS OF SEPTEMBER 2017

Between September 4 and 10, 2017, there was a sudden increase in solar activity when an active region (number 12673, as assigned by the National Oceanic and Atmospheric Administration, NOAA) produced four X-class flares, including the two strongest flares of Solar Cycle 24 (X9.3 on September 6 and X8.2 on September 10). These solar events, associated with the release of solar energetic particles (SEPs) as well as the eruption of multiple fast coronal mass ejections (CMEs), caused a ground level enhancement (GLE) of energetic particles seen with neutron monitors on the surface of the Earth (GLE # 72 in the GLE database at the University of Oulu¹) as well as with the Mars Science Laboratory (MSL) Radiation Assessment Detector (RAD) on Mars. This makes it the first GLE observed simultaneously on the surface of two different planets. The SEP event was very widespread (Earth and Mars had a longitudinal separation of $\sim 155^\circ$ at that time) and the largest GLE seen on the surface of Mars with MSL/RAD so far. At Earth, the disturbances associated with the solar events caused, for example, a suppression of critical high frequency (HF) radio communications systems (Frissell et al., 2019; Bland et al., 2018) as well as of navigation satellite systems such as GPS (Berdermann et al., 2018; Sato et al., 2019). These major events have been studied in great detail, and many of the articles concerning these events can be found in the special issues of *Space Weather* (2018) as well as *Geophysical Research Letters* (2018), where the latter is focusing on its impact on Mars.

While the September 6 flare had the stronger X-ray emission, the SEP event associated with the later September 10 flare is the one that caused the GLE which was seen at Earth and Mars due to the better magnetic connection. Three CMEs also erupted on September 9 and 10 from the same active region in similar directions ($\sim 115^\circ$ in Heliocentric Earth Ecliptic (HEE) coordinates), the last one with an extremely high speed of more than 2600 km/s. This fast and wide CME quickly merged with the two previous ones and formed an intense interplanetary shock. The merged eruption propagated outward quickly and was observed in situ at both Earth and Mars on September 12 and 13, respectively. While the SEP event at Mars was still in its declining phase, the shock arrival caused a strong Forbush decrease (FD) at Mars with an amplitude of 15 %, the largest FD seen by RAD to date. This decrease below the pre-SEP levels was sustained over 5 days and then gradually recovered over the course of several weeks.

The following two articles (Zeitlin et al., 2018 and Guo et al., 2018) study the effects of the September 10 events on Mars as measured by MSL/RAD and explain these observations by modeling the SEP event and the three CMEs. Zeitlin et al. (2018) report on the dosimetric quantities measured on the Martian surface, emphasizing that the increased dose and dose equivalent rates during the GLE on

¹ <https://gle.oulu.fi/>

Mars are almost canceled out by the long-lasting **FD** following it. Thus, in the case of a long-stay mission scenario, the increased radiation exposure due to the September event would have been insignificant for astronauts on Mars despite the 2- to 3-fold increase during the peak of the **SEP** event. However, as Mars was not particularly well connected to the active region, the impact of the **SEP** event could have been much larger, so this conclusion should not be generalized to all major solar events at Mars.

In Guo et al. (2018), the propagation of the 3 **CMEs** towards Earth and Mars is studied in more detail. The initial parameters of the **CMEs** close to the Sun are reconstructed using graduated cylindrical shell (**GCS**) fitting (see also **Appendix B**), and then the kinematics of the propagation are calculated using the drag-based model (**DBM**) (see **Section 1.3**). This is one of the first instances where **DBM** is used in a **CME-CME**-interaction scenario, with one previous example being the study of Temmer et al. (2012). In this case, we assume a simple conservation of momentum for modeling the interaction process. The values of the drag parameter γ were then chosen appropriately to reproduce the observed arrival times at Earth and Mars. These results are also compared to more sophisticated magnetohydrodynamic (**MHD**) simulations performed for the same event.

The following article is reproduced from Zeitlin et al. (2018) with permission from Geophysical Research Letters, ©American Geophysical Union:

ANALYSIS OF THE RADIATION HAZARD OBSERVED BY RAD ON THE SURFACE OF MARS DURING THE SEPTEMBER 2017 SOLAR PARTICLE EVENT

Zeitlin, C., D. M. Hassler, J. Guo, B. Ehresmann, R. F. Wimmer-Schweingruber, S. C. R. Rafkin, **J. L. Freiherr von Forstner**, H. Lohf, T. Berger, D. Matthiä, and G. Reitz, *Geophysical Research Letters*, 45, 12, pages 5845–5851 (2018), DOI: [10.1029/2018GL077760](https://doi.org/10.1029/2018GL077760) Own contribution: 10%



Geophysical Research Letters

RESEARCH LETTER

10.1029/2018GL077760

Special Section:

Impact of the Sept. 10, 2017,
solar event on Mars

Key Points:

- Protons accelerated during the large solar particle event of September 2017 reached the surface of Mars and were observed by MSL-RAD
- Dose rates were seen to increase by factors of 2 to 3 above the background level of the galactic cosmic rays
- Doses integrated over a 30-day interval that included the event remained well below NASA radiation exposure limits for astronauts

Correspondence to:

C. Zeitlin,
cary.j.zeitlin@nasa.gov

Citation:

Zeitlin, C., Hassler, D. M., Guo, J., Ehresmann, B., Wimmer-Schweingruber, R. F., Rafkin, S. C. R., et al. (2018). Analysis of the radiation hazard observed by RAD on the surface of Mars during the September 2017 solar particle event. *Geophysical Research Letters*, 45, 5845–5851. <https://doi.org/10.1029/2018GL077760>

Received 2 MAR 2018

Accepted 9 MAY 2018

Accepted article online 18 MAY 2018

Published online 29 JUN 2018

Analysis of the Radiation Hazard Observed by RAD on the Surface of Mars During the September 2017 Solar Particle Event

C. Zeitlin¹ , D. M. Hassler², J. Guo³ , B. Ehresmann² , R. F. Wimmer-Schweingruber³ , S. C. R. Rafkin², J. L. Freiherr von Forstner³ , H. Lohf³, T. Berger⁴ , D. Matthiae⁴ , and G. Reitz⁴ 

¹Leidos Innovations Corporation, Houston, TX, USA, ²Southwest Research Institute, Boulder, CO, USA, ³Department of Physics, Christian Albrechts University, Kiel, Germany, ⁴German Aerospace Center, Cologne, Germany

Abstract We report dosimetric quantities measured by the Mars Science Laboratory Radiation Assessment Detector (RAD) on the surface of Mars during the 10–12 September 2017 solar particle event. Despite 23 g/cm² of CO₂ shielding provided by the atmosphere above RAD, dose rates rose above background galactic cosmic ray levels by factors of 2 to 3 over the course of several hours and leveled off at sustained peak rates for about 12 hr before declining over the following 36 hr. As the solar particle event flux was gradually declining, a shock front reached Mars and caused a sudden drop of about 15% in instantaneous dose rates. No solar particles followed the shock arrival, and the magnetic shielding of galactic cosmic rays by the shock reduced their intensity to levels below those seen before the start of the event. This event is the largest seen to date by RAD on Mars.

Plain Language Summary We report the radiation dose rate on the surface of Mars measured by the Radiation Assessment Detector (RAD) aboard the Curiosity rover before, during, and after the solar energetic particle (SEP) event of 10–12 September 2017. Future astronauts exploring Mars will be at risk from SEP events, which occur sporadically and often with little warning, as well as from galactic cosmic rays, which are a continuous source of radiation dose and which generally have higher energies than SEPs. The event described here was the largest so far observed by RAD in more than five years on Mars. Although the atmosphere of Mars is only about 1–2% as thick as Earth's, it provides a measure of shielding against solar particles, most of which are protons with energies insufficient to penetrate Mars' atmosphere and reach the surface. But in this event, RAD saw a clear increase in dose rates; the peak dose rate was nearly three times above galactic cosmic ray levels measured prior to the event. Though the increase was rapid and lasted for three days, it was too small to represent a risk to the health of an astronaut receiving it. Much larger SEP events are possible and could cause problematic doses.

1. Introduction

Solar activity became surprisingly intense in September 2017, due to Active Region 2673, which produced four X-class flares between 4 and 10 September. Enhancements were seen in various GOES proton channels (Onsager et al., 1996); prior to 10 September, enhancements were seen only in channels that measure protons with kinetic energies below 100 MeV, with the exception of a small, brief rise in the >100 MeV channel on 6 September. However, following the 10 September flare, GOES observed a large, rapidly rising spike in the >100 MeV proton flux. This channel is important when considering shielded environments such as the interior of a spacecraft in interplanetary space and the Martian surface, because such energetic protons can penetrate modest depths of shielding and can potentially impart dangerous doses to astronauts. When Earth and Mars are widely separated in terms of heliospheric longitude, as was the case in September 2017 (approximately 155° separation), an event seen at one planet might not be seen at the other. This event was seen on both planets, and by several instruments aboard the International Space Station. Kinematics and modeling of the coronal mass ejections that produced the particle event are described elsewhere (Guo et al., 2018).

2. Triggering and Data Acquisition

The Radiation Assessment Detector aboard the Mars Science Laboratory (MSL-RAD) has been described in the literature (Hassler et al., 2012; Zeitlin et al., 2016). Dosimetric results (Guo et al., 2015; Hassler et al., 2014; Zeitlin et al., 2013) have also been reported. Figure 1 shows a schematic diagram of the detectors

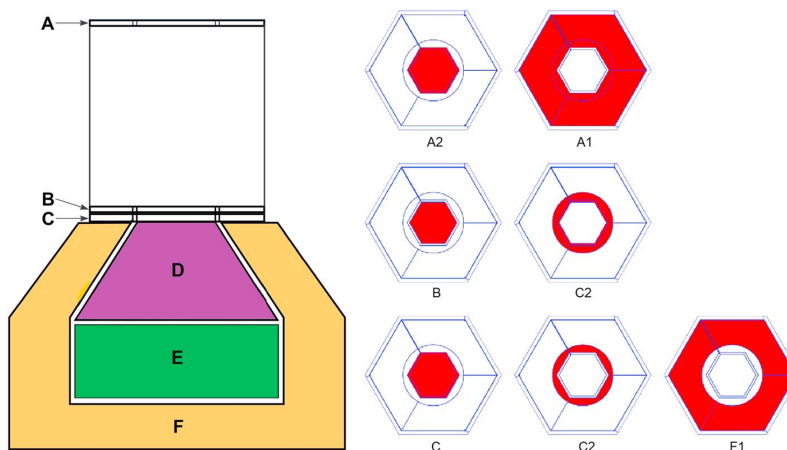


Figure 1. Schematic drawing of the RAD sensor head, left, showing the stack consisting of three silicon detectors (A, B, and C) and three scintillators (D, E, and F). The scintillators enable measurements of neutral particle spectra and are also useful for charged particle measurements. The segmentation of the silicon diodes is as indicated on the right; light from the F scintillator is collected in the outermost segments of the C detector diode.

contained in the sensor head. The A silicon detector is roughly level with the rover's deck, and the detector generally points within a few degrees of vertical. RAD records dose rate information in real time in its onboard data processing using the B (silicon) and E (plastic) detectors. The dosimetry triggers (one for B, one for E) accept any energy deposition above threshold in either detector; running sums are kept onboard for telemetry to Earth. Because each of these triggers depends only on a single detector, there are no restrictions on the direction of incidence of incoming particles; that is, these triggers enable dose measurements with omnidirectional detector responses. RAD also has triggers for incident energetic charged particles, which require coincidences of the A and B silicon detectors, which are the topmost two detectors in the stack. The A detector consists of outer (A1) and inner (A2) segments. Unlike the omnidirectional responses of the dosimetry triggers, these viewing cones are restricted: A2*B coincidences occur when charged particles arrive at angles less than about 18° from the vertical, and A1*B coincidences occur for incident angles from about 18° to 30°. When either trigger fires, all hit detectors are read out, and the complete event record is stored, provided storage space is available. If storage is unavailable, the event is counted, enabling needed corrections in subsequent data analysis.

RAD also has counters that group triggered events into broad categories. Of interest here are the counters for vertical penetrating charged particles (defined as simultaneous hits in the A2, B, C, D, E, and F2 detectors) and for vertical charged particles that stop in the D detector (hits in A2, B, C, and D only). Counters are also defined for neutral particles in the D and E detectors.

RAD runs on an autonomous observing cadence, set to 16 min in solar quiet time but switching to 8 min when high count rates are observed during the 10-s sampling period prior to the start of each observation. At the end of each measurement period, data are stored internally for later telemetry to Earth.

In the following, the dose rates recorded by the B silicon detector have been converted, approximately, to dose rates in water, which is the quantity of interest for radiation dosimetry. A constant scaling factor of 1.3 has been applied to the silicon dose rate data. No conversion is applied to the data from the E detector, as plastic is close to water in terms of its response to the energetic charged particles that dominate the radiation environment on Mars.

3. Results

3.1. Event Timeline

Figure 2a shows the dose rates as recorded in the B and E detectors from 12:00 UTC on 9 September through midnight UTC of 15 September. Prior to the onset of the event, dose rates in RAD were entirely due to galactic

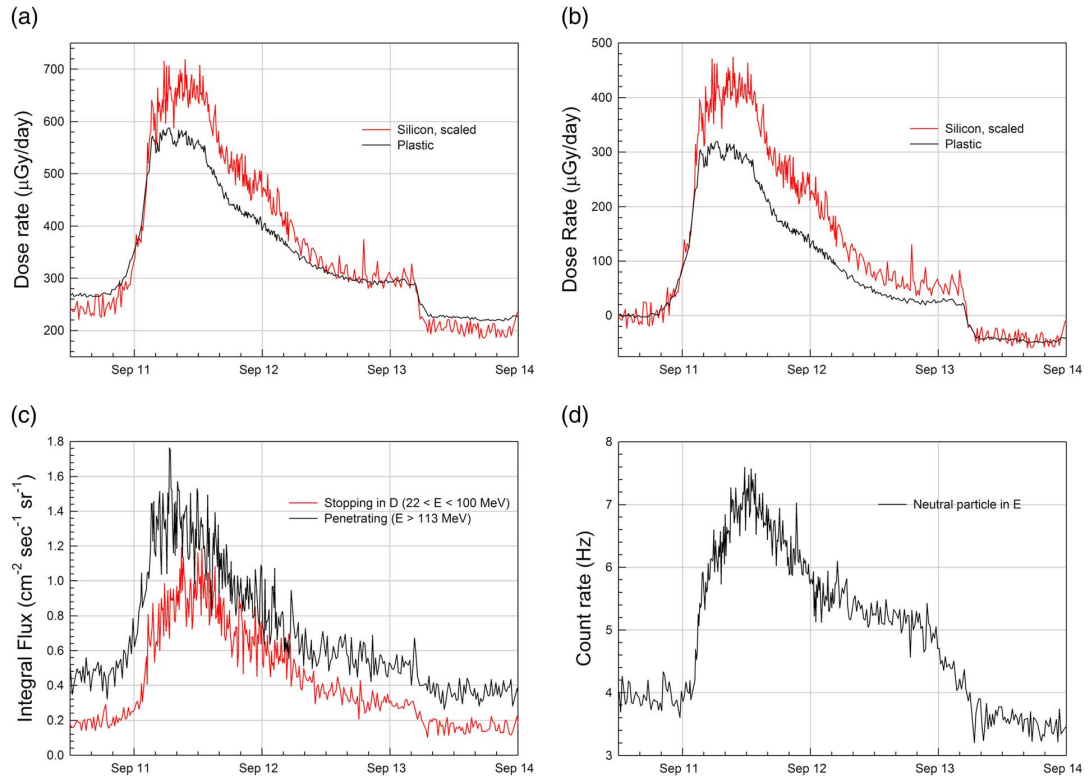


Figure 2. Dose rates as measured on Mars using the “B” silicon detector and “E” plastic scintillator. (a) Dose rates include contributions from galactic cosmic rays. (b) These contributions are subtracted. (c) The integral fluxes of stopping and penetrating particles seen before, during, and after the event. (Quoted energy ranges are for protons.) (d) The count rate of neutral particles hitting the E detector in the same time period.

cosmic rays (GCRs). The B dose rate averaged over 8 and 9 September was 244 $\mu\text{Gy/day}$ in water (after conversion from silicon), and the E dose rate averaged 268 $\mu\text{Gy/day}$ in plastic for the same days. The $\sim 10\%$ difference in dose rates is expected based on the different responses of the detectors to energetic charged particles; there is also a small contribution to the E dose rate from high-energy neutrons ($E > 6 \text{ MeV}$), on the order of a few percent of the total during solar quiet time (Köhler et al., 2014).

Figure 2b shows the same dose rate data as Figure 2a, but with the average pre-SPE GCR dose rates subtracted. During the event, the dose rate in the B detector exceeded that in E because E is shielded by the surrounding detectors, and low-energy solar particles that deposit energy in B stop before they reach E.

A steady, statistically significant increase in the E dose rate started around 19:50 UTC on 10 September. By 03:00 UTC on 11 September, both B and E dose rates had reached about 90% of the eventual peak dose rates, which came a few hours later at about 07:00. There is considerable structure in the dose rates, particularly in the B detector data, though it is noisier statistically than E due to its smaller volume.

The event peaked on 11 September, from about 4:00 to 14:00 UTC. Dose rates then fell gradually until about 05:00 UTC on 13 September, at which point they fell steeply (see Figure 1b). Following the steep fall, associated with the arrival of the shock front of the interplanetary coronal mass ejection at Mars, no evidence of solar particles was observed, and GCR rates dropped to a (highly significant) level 15–20% below the rates prior to the event. Propagation of the shock through interplanetary space is discussed by Guo et al. (2018).

In the declining phase of the SPE, the dose rate in the B detector stayed at higher rates longer than that in the E detector, reflecting the typical softening of SPE spectra seen during prolonged events. Integrating the B and

E dose rates for the period from the start of the event until the arrival of the shock front at Mars, we find that the SPE contributed 544 μGy of dose in water as measured by the B detector, and 369 μGy of dose as measured by E. These are the estimated doses above GCR that are attributable to the SPE.

The fact that the dose rates in both B and E climbed by roughly similar amounts is notable. For particles coming into RAD from above, B is shielded by the atmosphere, which had an average vertical column depth 23.4 g/cm^2 during this period. This stops protons with kinetic energies less than about 175 MeV. The B detector is additionally shielded by two very thin windows and the A detector, but these are negligible for present purposes. The E detector is shielded by the same things, plus the B, C, and—most importantly—D detectors, the latter consisting of 12.54 g/cm^2 of CsI. Vertical protons energetic enough to reach RAD will stop in D (or higher up in the stack) if their remaining energy is less than 100 MeV. Thus, any proton—or ^4He ion—that reaches E and deposits energy there must have had a kinetic energy of at least 275 MeV/nuc at the top of the Martian atmosphere, whereas the corresponding minimum energy to deposit energy in B is 175 MeV/nuc. This difference in minimum energy explains the higher dose rate observed in B during the SPE. It is also clear that the event had a hard spectrum, a conclusion further supported by the spectral analysis presented elsewhere in this issue and by the fact that a ground-level enhancement was also seen at Earth starting at about 16:15 UTC on 10 September. (Neutron-monitor data for ground-level enhancements, including this one—number 72—can be found at <http://www.nmdb.edu>.)

The coincidence count rates for vertical charged particles that either stop in D or penetrate the entire detector stack are also of interest. Protons in the former category have kinetic energies in the range from 24 to 100 MeV when they enter RAD, and protons in the latter category must have at least 113 MeV when they enter RAD. (Incident protons with energies below 24 MeV either do not reach D or do not deposit sufficient energy to fire the D discriminator; protons with energies from 100 to 113 MeV stop in E.) Figure 2c shows the fluxes derived from these two count rates. It is important to note that the stopping flux shown here includes a large contribution from secondary electrons with energies in the 8 to 85 MeV range, which account for about 75% of the total. The flux of penetrating particles started increasing before the stopping flux did, reflecting the earlier arrival times of more energetic ions. The penetrating flux eventually rose by a factor of 3 compared to the period just before the SPE. The stopping flux increased by about a factor of 5 compared to quiet time, but more detailed analysis that excludes the electron contribution shows that the flux of stopping protons increased by about a factor of 30 compared to quiet time.

The increased flux of charged particles also produced an increased flux of neutral particles. Figure 2d shows the corrected count rate of hits in the E detector with no simultaneous hits in the other detectors that comprise the anticoincidence system. The E detector is sensitive to neutrons with energies above about 8 MeV, and, to a lesser extent, γ rays. The increase in flux relative to solar quiet time is less than a factor of 2. The increase of the neutral count rate appears to have been delayed by several hours relative to the arrival of charged particles. The cause of the delay is not obvious and is the subject of ongoing investigation.

The onset time of the event is an important consideration for future human explorers who would likely perform expeditions in which they drive considerable distances from their habitat. The event as seen on Mars was unambiguously underway by about 21:00 UTC on 10 September, and dose rates doubled within about 7 hr. If one were relying only on monitors on the surface of Mars or in orbit, this could be problematic for long drives, particularly in the case of a more intense solar event. However, for this event, the exposure incurred by being away from shelter for the duration would have been comparable to adding about two days of GCR exposure. In the context of a long-stay mission scenario, with a surface mission on the order of hundreds of days, this is insignificant. The Forbush decrease (FD) that followed the event mitigated even this small increase.

3.2. Deposited Energy Spectra and Radiation Quality Factors for Vertical Ions

It has long been known that the biological damage caused by radiation does not depend simply on physical dose, which is the energy deposited per unit mass (Rossi, 1964). This fact has motivated the use of radiation quality factors, which are particularly important in the context of human spaceflight. This is because the GCRs include high-energy heavy ions, the biological effects of which are known to be—for some biological endpoints—very large per unit dose compared to more common radiation types such as γ rays or X-rays (Blakely & Kronenberg, 1998).

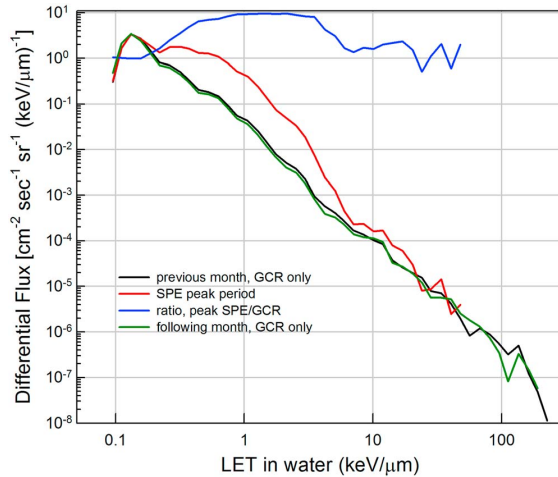


Figure 3. Differential LET spectra measured by MSL-RAD on Mars for 30 days prior to the event (black curve), 30 days after the event (green curve), and during the SPE peak (red curve). Spectra in water are obtained by scaling spectra measured in the B silicon detector. Measured particles are incident vertically on RAD. Also shown (blue curve) is the ratio of the event-peak flux to the quiet time GCR flux, showing that the flux increase was greatest below 10 keV/μm.

Here we use the quality factor defined by International Commission on Radiation Protection (ICRP) Report 60 (International Commission on Radiation Protection, 1991). Calculation of the dose equivalent, written as H , depends on knowledge of the dose and linear energy transfer (LET) spectrum in water. RAD measures LET in silicon for particles in either of the A*B coincidence cones (i.e., for incident angles $<30^\circ$ from the vertical). We perform an approximate conversion from the measured dE/dx in silicon to LET in using a simple scaling factor. The conversion factor is, in principle, energy-dependent, and for thin detectors such as the silicon detectors in RAD, should take account of losses due to escaping “knock-on” electrons. A reasonable estimate of the factor is 1.79; that is, LET in silicon is divided by this factor to obtain the approximate corresponding LET in water (which yields the dose conversion factor of 1.30 used in the preceding). The ICRP 60 report defines $Q(LET)$, or $Q(L)$, as a piecewise function with a value of 1.0 for LETs below 10 keV/μm, the range populated by the large majority of the observed SEPs.

Although GCR dose rates dropped by 15–20% immediately after the end of the event at Mars, there is no indication of GCR suppression during the event; we therefore use data taken prior to the onset of the event to estimate the GCR spectrum during the event. High-LET events are rare, so a comparatively lengthy period of 30 days was chosen, and similarly for the period after the event. Even with 30-day integration

times, statistics at high LET are meager. The spectrum for the period before the event is shown as the black curve in Figure 3, the spectrum obtained during the peak of the event is shown in red, and the ratio of the two is shown in blue. The spectrum obtained from the 30 days following the event is shown in green; it is nearly indistinguishable from the preevent spectrum.

The peak of the SPE was (somewhat arbitrarily) defined as the time period during which the dose rate in E exceeded 100 μGy/day after subtracting the GCR background. This period runs from 1:23 UTC on 11 September until 3:16 UTC on 12 September, during which the flux of minimum-ionizing singly charged particles was virtually unchanged compared to the GCR spectrum for the prior month. This peak appears at LET of about 0.14 keV/μm, consistent with the calculated most probable energy deposit for minimum-ionizing protons in 300 μm of silicon (Bichsel, 1988) when our factor for scaling to water is applied. This value of LET is not the same as the mean LET in water (0.20 keV/μm) from the Bethe formula (Patrignani & Particle Data Group, 2016) for minimum-ionizing protons; the difference is due to straggling.

At LET values above about 0.18 keV/μm—corresponding to most probable energy depositions of protons with energies below about 800 MeV—the flux during the event was enhanced compared to quiet time levels. The enhancement reached a factor of nearly 10 in the LET range from about 1.5 keV/μm to 2.1 keV/μm. In this range, there may be a contribution from energetic helium ions, but if so, it is not distinguishable on the basis of LET alone. Between about 6 and 20 keV/μm, the flux enhancement is modest—the ratio averages less than 2 in this region. Above 20 keV/μm, the spectrum during the event is consistent, within statistics, with being purely GCRs. In this brief interval of maximum flux intensity, no events were seen with LET above 50 keV/μm.

The LET spectra have been integrated against the ICRP 60 $Q(L)$ to obtain average radiation quality factor $\langle Q \rangle$ and dose equivalent for each period. Events in the A2*B field of view were used to obtain the $\langle Q \rangle$ values. For the most intense portion of the SPE, $\langle Q \rangle$ was 1.17, compared to values of 2.3 found for GCR-only periods before and after the event. The GCR $\langle Q \rangle$ of 2.3 is less than our previously reported value of 3.0 from early in the mission (Hassler et al., 2014), owing primarily to seasonal variations in the atmospheric column depth.

Table 1 shows rates for both the B and E detectors using the omnidirectional dose data as described above. The B dose rates have been converted to water using the 1.30 factor mentioned above. The dose equivalent rate in B is also shown (obtained by multiplying the dose rate by the appropriate $\langle Q \rangle$ for the time period). Despite the significant dose rate increase during the event, the peak dose equivalent rate in the B detector—which can be considered to be something like a skin exposure—was only about 50% greater than the GCR

Table 1
Dose and Dose Equivalent Rates and Totals

	Average rates 5-day pre-SPE	Peak rates during SPE	Average rates during SPE	Average rates 5-day post-SPE	Totals, 30 days before SPE	Totals, 30 days starting 11/9/17
B, omnidirectional	240 $\mu\text{Gy}/\text{day}$	718 $\mu\text{Gy}/\text{day}$	464 $\mu\text{Gy}/\text{day}$	208 $\mu\text{Gy}/\text{day}$	7.3 mGy	7.7 mGy
E, omnidirectional	265 $\mu\text{Gy}/\text{day}$	588 $\mu\text{Gy}/\text{day}$	417 $\mu\text{Gy}/\text{day}$	232 $\mu\text{Gy}/\text{day}$	8.1 mGy	8.2 mGy
Dose equivalent using B	543 $\mu\text{Sv}/\text{day}$	841 $\mu\text{Sv}/\text{day}$	543 $\mu\text{Sv}/\text{day}$	480 $\mu\text{Sv}/\text{day}$	16.5 mSv	16.6 mSv

dose equivalent rates before and after the event, and the average dose equivalent rate during the event was nearly identical to GCR rates before. The FD that immediately followed the event caused GCR dose rates in both B and E to drop by 12% in the 5-day period after the event. GCR rates then recovered gradually, and by mid-October had returned to the levels seen before the event.

We have investigated the effect of the event on the integrated dose and dose equivalent the 30 days prior to the start of the event, and for the 30-day period that starts with the onset of the event as seen on Mars. Results are shown in the two right-most columns of Table 1. The FD that followed the arrival of the interplanetary coronal mass ejection shock at Mars caused GCR dose rates to drop by about 5% when averaged over this longer period (compared to the $\sim 12\%$ decreases in the five days immediately afterward). Considered over these two 30-day periods, the effect of the FD almost exactly offset the dose and dose equivalent contributions of the SPE in both B and E detector data. Note that the effective $\langle Q \rangle$ for the 30-day period including the event is 2.15, slightly less than the GCR $\langle Q \rangle$ due to dilution by the predominantly low-LET particles in the SPE. For all practical purposes, there is no difference in the accumulated exposures in the two periods.

One cannot generalize from this event to other SPE scenarios. Mars was not magnetically connected to the acceleration site until a later phase (Guo et al., 2018); had the active region been better connected to Mars, the dose rate increases would likely have been much larger. Also, the atmospheric shielding above RAD—23 g/cm^2 during the event—is greater than at higher elevations on Mars. At the mean Martian elevation, the vertical column depth of atmosphere is 16 g/cm^2 , and—depending on the energy spectrum of the SEPs—there can be considerably larger exposures at this (and higher) elevation.

In the assessment of deterministic (noncancer) effects of radiation, the unit of gray equivalent (Gy-Eq) is used to account for the enhanced biological effectiveness of protons compared to photons. A relative biological effectiveness factor of 1.5 is assigned to protons in National Council on Radiation Protection and Measurements Report 142 (National Council on Radiation Protection and Measurements, 2002). National Council on Radiation Protection and Measurements has also defined 30-day exposure limits for astronauts (National Council on Radiation Protection and Measurements, 1989). Multiplying the SPE doses quoted above (544 μGy in B and 369 μGy in the more-shielded E detector) by the proton relative biological effectiveness of 1.5 yields exposures far below even the smallest of the 30-day exposure limits, which is 250 mGy-Eq for the heart and blood-forming organs. Even if the event had been an order of magnitude more intense, there would have been a large safety margin.

4. Conclusions

The SPE of September 2017 accelerated particles to energies high enough to easily penetrate the Martian atmosphere, even in Gale Crater, more than 4 km below the mean elevation on Mars. MSL-RAD observed roughly factor-of-two increases in dose rates, both in the lightly shielded B detector and in the more-shielded E detector. The count rate of neutral particles in the E detector, dominantly low-energy neutrons, rose by a factor of about 2 during the event, while the counts of penetrating ($E_{\text{proton}} > 113 \text{ MeV}$) and stopping particles rose by factors of 3 and 5, respectively. Folding the LET spectrum of vertical-going particles with the ICRP 60 quality factor yields an average quality factor $\langle Q \rangle$ of 1.17 during the peak of the event, compared to values of about 2.3 found for GCR-only spectra before and after the event. For purposes of calculating dose equivalent, the decrease in $\langle Q \rangle$ tends to offset the increase in dose rates, so that the dose equivalent rate was only slightly greater than during the preceding solar quiet time in the B detector and was actually slightly below the quiet time rate in the E detector. The FD following the event reduced GCR dose rates, yielding integrated doses and dose equivalents for the 30-day period including the event that are only slightly greater than for

the 30-day period prior to the event. These exposures are well below National Aeronautics and Space Administration's 30-day limits. However, it is not possible to generalize from one medium-size event to other SPE scenarios. Mars was not magnetically connected to the active region on the Sun at the time of the 10 September flare; a well-connected event with the same hard spectrum would certainly produce much larger dose rates on the Martian surface and would likely produce a stronger FD following the SPE.

Acknowledgments

This work was supported by the NASA Johnson Space Center through NASA Human Health and Performance Contract NNJ15HK11B. The MSL-RAD project is supported in the United States by the National Aeronautics and Space Administration's Human Exploration and Operations Mission Directorate, under Jet Propulsion Laboratory sub-contract 1273039 to Southwest Research Institute, and in Germany by the German Aerospace Center (DLR) and DLR's Space Administration grants 50QM0501, 50QM1201, and 50QM1701 to the Christian Albrechts University, Kiel. The data used in this article are available through the NASA Planetary Data System archive, at the Planetary Plasma Interactions node hosted by UCLA, <http://pds-ppi.igpp.ucla.edu>.

References

Bichsel, H. (1988). Straggling in thin silicon detectors. *Reviews of Modern Physics*, 60(3), 663–699. <https://doi.org/10.1103/RevModPhys.60.663>

Blakely, E. A., & Kronenberg, A. (1998). Heavy-ion radiobiology: New approaches to delineate mechanisms underlying enhanced biological effectiveness. *Radiation Research*, 150(5), S126–S145. <https://doi.org/10.2307/3579815>

Guo, J., Dumbovic, M., Wimmer-Schweingruber, R. F., Temmer, M., Lohf, H., Wang, Y., et al. (2018). Modeling the evolution and propagation of the 2017 September 9th and 10th CMEs and SEPs arriving at Mars constrained by remote-sensing and in-situ measurement, arXiv:1803.00461v3 [physics.space-ph].

Guo, J., Zeitlin, C., Wimmer-Schweingruber, R. F., Rafkin, S., Hassler, D. M., Posner, A., et al. (2015). Modeling the variations of dose rate measured by RAD during the first MSL Martian year: 2012–2014. *The Astrophysical Journal*, 810(1), 24–33. <https://doi.org/10.1088/0004-637X/810/1/24>

Hassler, D. M., Zeitlin, C., Wimmer-Schweingruber, R. F., Boettcher, S., Martin, C., Andrews, J., et al. (2012). The Radiation Assessment Detector (RAD) investigation. *Space Science Reviews*, 170(1–4), 503–558. <https://doi.org/10.1007/s11214-012-9913-1>

Hassler, D. M., Zeitlin, C., Wimmer-Schweingruber, R. F., Ehresmann, B., Rafkin, S., Eigenbrode, J. L., et al. (2014). Mars' surface radiation environment measured with the Mars Science Laboratory's Curiosity rover. *Science*, 343(6169), 1244797. <https://doi.org/10.1126/science.1244797>

International Commission on Radiation Protection (1991). Publication 60, *Ann. ICRP*, 21 (1–3). Elsevier, Amsterdam.

Köhler, J., Zeitlin, C., Ehresmann, B., Wimmer-Schweingruber, R. F., Hassler, D. M., Reitz, G., et al. (2014). Measurements of the neutron spectrum on the Martian surface with MSL/RAD. *Journal of Geophysical Research: Planets*, 119, 594–603. <https://doi.org/10.1002/2013JE004539>

National Council on Radiation Protection and Measurements (1989). Report no. 98, *Guidance on Radiation Received in Space Activities*. Bethesda, Md.

National Council on Radiation Protection and Measurements (2002). Report no. 142, *Operational Radiation Safety Program for Astronauts in Low-Earth Orbit: A Basic Framework*. Bethesda, Md.

Onsager, T., Grubb, R., Kunches, J., Matheson, L., Speich, D., Zwickl, R. W., & Sauer, H. (1996). Operational uses of the GOES energetic particle detectors, Proc. SPIE 2812, *GOES-8 and Beyond*. <https://doi.org/10.1117/12.254075>

Patrignani, C., & Particle Data Group (2016). Review of particle physics. *Chinese Physics C*, 40(10), 100,001. <https://doi.org/10.1088/1674-1137/40/10/100001>

Rossi, H. H. (1964). Correlation of radiation quality and biological effect. *Annals of the New York Academy of Sciences*, 114(1), 4–15. <https://doi.org/10.1111/j.1749-6632.1964.tb53559.x>

Zeitlin, C., Hassler, D. M., Cucinotta, F. A., Ehresmann, B., Wimmer-Schweingruber, R. F., Brinza, D. E., et al. (2013). Measurements of energetic particle radiation in transit to Mars on the Mars Science Laboratory. *Science*, 340(6136), 1080–1084. <https://doi.org/10.1126/science.1235989>

Zeitlin, C., Hassler, D. M., Wimmer-Schweingruber, R. F., Ehresmann, B., Appel, J., Berger, T., et al. (2016). Calibration and characterization of the radiation assessment detector (rad) on curiosity. *Space Science Reviews*, 201(1–4), 201–233. <https://doi.org/10.1007/s11214-016-0303-y>

The following article is reproduced from Guo et al. (2018) with permission from Space Weather, ©American Geophysical Union:

MODELING THE EVOLUTION AND PROPAGATION OF 10 SEPTEMBER 2017 CMEs AND SEPs
ARRIVING AT MARS CONSTRAINED BY REMOTE SENSING AND IN SITU MEASUREMENT

Guo, J., M. Dumbović, R. F. Wimmer-Schweingruber, M. Temmer, H. Lohf, Y. Wang, A. Veronig, D. M. Hassler, L. M. Mays, C. Zeitlin, B. Ehresmann, O. Witasse, **J. L. Freiherr von Forstner**, B. Heber, M. Holmström, and A. Posner, *Space Weather*, 16, 8, pages 1156–1169 (2018), doi: [10.1029/2018SW001973](https://doi.org/10.1029/2018SW001973) Own contribution: 10%



Space Weather

RESEARCH ARTICLE

10.1029/2018SW001973

Special Section:

Space Weather Events of 4–10
September 2017

Key Points:

- The 10 September 2017 SEP event was the first GLE observed on the surface of two different planets: Earth and Mars
- The SEP and ICME impact on Mars is helping us better understand extreme space weather conditions at Mars
- Synergistic modeling of the ICME and SEP propagation advances our understanding of such complex events for improved space weather forecasts

Correspondence to:

J. Guo,
guo@physik.uni-kiel.de

Citation:

Guo, J., Dumbović, M., Wimmer-Schweingruber, R. F., Temmer, M., Lohf, H., Wang, Y., et al. (2018). Modeling the evolution and propagation of September 2017 CMEs and SEPs arriving at Mars constrained by remote sensing and in situ measurement. *Space Weather*, 16, 1156–1169. <https://doi.org/10.1029/2018SW001973>

Received 12 JUN 2018

Accepted 19 JUL 2018

Accepted article online 27 JUL 2018

Published online 30 AUG 2018

©2018. American Geophysical Union.
All Rights Reserved.

Modeling the Evolution and Propagation of 10 September 2017 CMEs and SEPs Arriving at Mars Constrained by Remote Sensing and In Situ Measurement

Jingnan Guo¹, Mateja Dumbović², Robert F. Wimmer-Schweingruber¹, Manuela Temmer², Henning Lohf¹, Yuming Wang³, Astrid Veronig², Donald M. Hassler⁴, Leila M. Mays⁵, Cary Zeitlin⁶, Bent Ehresmann⁴, Olivier Witasse⁷, Johan L. Freiherr von Forstner¹, Bernd Heber¹, Mats Holmström⁸, and Arik Posner⁹

¹Institut fuer Experimentelle und Angewandte Physik, University of Kiel, Kiel, Germany, ²Institute of Physics, University of Graz, Graz, Austria, ³School of Earth and Space Sciences, University of Science and Technology of China, Hefei, China, ⁴Southwest Research Institute, Boulder, CO, USA, ⁵NASA Goddard Space Flight Center, Greenbelt, MD, USA, ⁶Leidos, Houston, TX, USA, ⁷ESTEC-Science Support Office, European Space Agency, Noordwijk, The Netherlands, ⁸Swedish Institute of Space Physics, Kiruna, Sweden, ⁹Science Mission Directorate, NASA Headquarters, Washington, DC, USA

Abstract On 10 September 2017, solar energetic particles originating from the active region 12673 produced a ground level enhancement at Earth. The ground level enhancement on the surface of Mars, 160 longitudinally east of Earth, observed by the Radiation Assessment Detector (RAD) was the largest since the landing of the Curiosity rover in August 2012. Based on multipoint coronagraph images and the Graduated Cylindrical Shell model, we identify the initial 3-D kinematics of an extremely fast coronal mass ejection (CME) and its shock front, as well as another two CMEs launched hours earlier with moderate speeds. The three CMEs interacted as they propagated outward into the heliosphere and merged into a complex interplanetary CME (ICME). The arrival of the shock and ICME at Mars caused a very significant Forbush decrease seen by RAD only a few hours later than that at Earth, which was about 0.5 AU closer to the Sun. We investigate the propagation of the three CMEs and the merged ICME together with the shock, using the drag-based model and the WSA-ENLIL plus cone model constrained by the in situ observations. The synergistic study of the ICME and solar energetic particle arrivals at Earth and Mars suggests that to better predict potentially hazardous space weather impacts at Earth and other heliospheric locations for human exploration missions, it is essential to analyze (1) the eruption of the flare and CME at the Sun, (2) the CME kinematics, especially during their interactions, and (3) the spatially and temporally varying heliospheric conditions, such as the evolution and propagation of the stream interaction regions.

Plain Language Summary From 4 to 6 September 2017, heliospheric activity suddenly and drastically increased starting from a simple sunspot which transformed into a complex region with four X-class flares accompanied by several Earth-directed magnetic clouds and shocks driven by them. Only a few days later, on 10 September 2017 starting at about 15:53, the same region launched another extremely fast magnetic cloud accompanied by an intense shock, which spread rapidly across the entire solar surface. Ten to 20 min later, particles accelerated at the Sun arrived at Earth, some of them with enough energy to reach Earth's surface and caused a ground level enhancement of radiation. A few hours later and shortly before 20:00, the Radiation Assessment Detector observed the biggest event since the landing of the Curiosity rover in August 2012 on the surface of Mars which was about 160 degrees east from Earth in the heliosphere. This was the first solar energetic particle event seen at ground level on the surface of two planets. Some particles were also transported across magnetic field lines throughout the heliosphere and were detected at the back side of the Sun where the eruption was centered. Meantime, the intense and wide shock also propagated into the interplanetary space, reached Earth on its west edge ~50.5hr after launch and hit Mars on its east flank ~59hr after launch, causing the biggest depression of the galactic cosmic ray flux measured by Radiation Assessment Detector on Mars. We analyzed this event starting from the flare and particle acceleration at the solar surface. Constrained by in situ observations at both planets, we observed and modeled the eruptions, solar energetic particles, magnetic clouds, and their shock fronts from the Sun into interplanetary space and all the way to Mars and Earth.

1. The Flare, CMEs, and GLE 72: Close to the Sun

During the declining phase of solar cycle 24, from the 6 to 10 September 2018 heliospheric activity suddenly and drastically increased when the complex Active Region (AR) 12673 located at the western solar hemisphere, produced four X-class flares and several Earth-directed coronal mass ejections (CMEs; Redmon et al., 2018). The X9.3 flare on 6 September 2017 at S09W34 started at 11:53 UT and impulsively reached its peak in the Geostationary Operational Environmental Satellite (GOES) soft X-ray flux at 12:02 UT. It was registered as the largest flare of solar cycle no. 24.

1.1. The 10 September Flare, Flux Rope, and Initial Acceleration of Particles

On 10 September 2017, the same AR produced an X8.2 flare at S08W88 (being the second largest one of Cycle 24) starting around 15:35 UT and peaking at 16:06 UT (Jiang et al., 2018; Li et al., 2018; Long et al., 2018; Seaton & Darnel, 2018; Warren et al., 2018). The flare was located on and slightly behind the west limb of the Sun as seen from Earth. Remote sensing observations of the solar corona in Figures 1a and 1b show that a magnetic flux rope (MFR) associated with the energetic flare started emerging at about 15:50, rose rapidly and triggered a fast eruption starting from about 15:53. It was later observed as a CME in the white light coronagraph images of both the Solar Terrestrial relations observatory Ahead (STA; Howard et al., 2008) and the Solar and Heliospheric Observatory (SOHO; Brueckner et al., 1995) as shown in Figure 1e. References and descriptions of all the measurements and databases employed in this study are given in Appendix A.

Since the initial emergence of the MFR, the formation of a linear bright current sheet between the flare loop and the filament, shown in Figure 1a, was clearly observed by the EUV Imaging Spectrometer/Hinode (Warren et al., 2018), the Atmospheric Imaging Assembly (Lemen et al., 2011)/Solar Dynamics Observatory (Li et al., 2018) and also by the Solar Ultraviolet Imager (SUVI) on the GOES16 spacecraft (Seaton & Darnel, 2018). The high-resolution imaging and spectroscopic observations show that the current sheet had a very high temperature (>10 MK) and very large nonthermal velocities (>150 km/s). It also exhibited turbulent features associated with cascading magnetic reconnection process (Li et al., 2018), which were likely responsible for the initial stage of the acceleration of particles. Highly energetic particles have also caused hard X-ray emissions in the flare (via bremsstrahlung radiation) observed up to at least 300 keV by the Reuven Ramaty High-Energy Solar Spectroscopic Imager (Lin et al., 2002) and the Fermi Gamma-ray space telescope, with two broad X-ray bursts centered at 15:57 and 16:10 UT on 10 September 2017.

The launch of the extremely fast erupting MFR and CME likely drove a global shock ahead of it indicated by the extreme ultraviolet (EUV) waves (or EIT waves, Dere et al., 1997) in SUVI's 195 Å passband (Figure 1b and better shown in a movie in the online version of Seaton & Darnel, 2018). This strong EUV wave had a speed of at least 1,000 km/s and even up to 2,000 km/s, which places it among the fastest EUV waves observed (Long et al., 2018; Liu et al., 2018). It propagated across the entire solar disk within half an hour starting from the eruption at 15:53 (Seaton & Darnel, 2018). This could indicate a global shock propagation within this short time period (Long et al., 2017). In fact, a signature of shock-related type II-like radio emission (detected by the Greenland radio monitor) started at around 15:53. Almost simultaneously, type III radio emission (related to kiloelectron volt nonthermal electrons propagating outward along magnetic field lines) was detected by the STA WAVES instrument (the WIND spacecraft at Earth did not have observations at this time period) suggesting the initial release of accelerated particles.

Starting from 16:15 UT on 10 September 2017, solar energetic particles (SEPs) arriving at Earth were registered as a ground level enhancement (GLE) seen by multiple neutron monitors (NMs) with cutoff rigidities up to about 3 GV (corresponding to 2 GeV protons) as shown in Figure 2b. Different energy channels in GOES (panel a) clearly show an intense, sudden, and long-lasting enhancement of the accelerated protons with energies larger than hundreds of MeV. From the clear onset time of relativistic particles, a release time around 16:00 UT can be inferred for 1 GeV protons. This timing matches reasonably well with the final eruption of the flux rope and the X-ray bursts. However, the timing of the initial signature of the shock and the reconnection process was very close (both starting around 15:53) and it is difficult to tell whether the shock or magnetic reconnection (flare) contributed more to the initial acceleration of particles. It is likely due to the combination of both as often observed in such eruptive and complex events (e.g., Aschwanden, 2002).

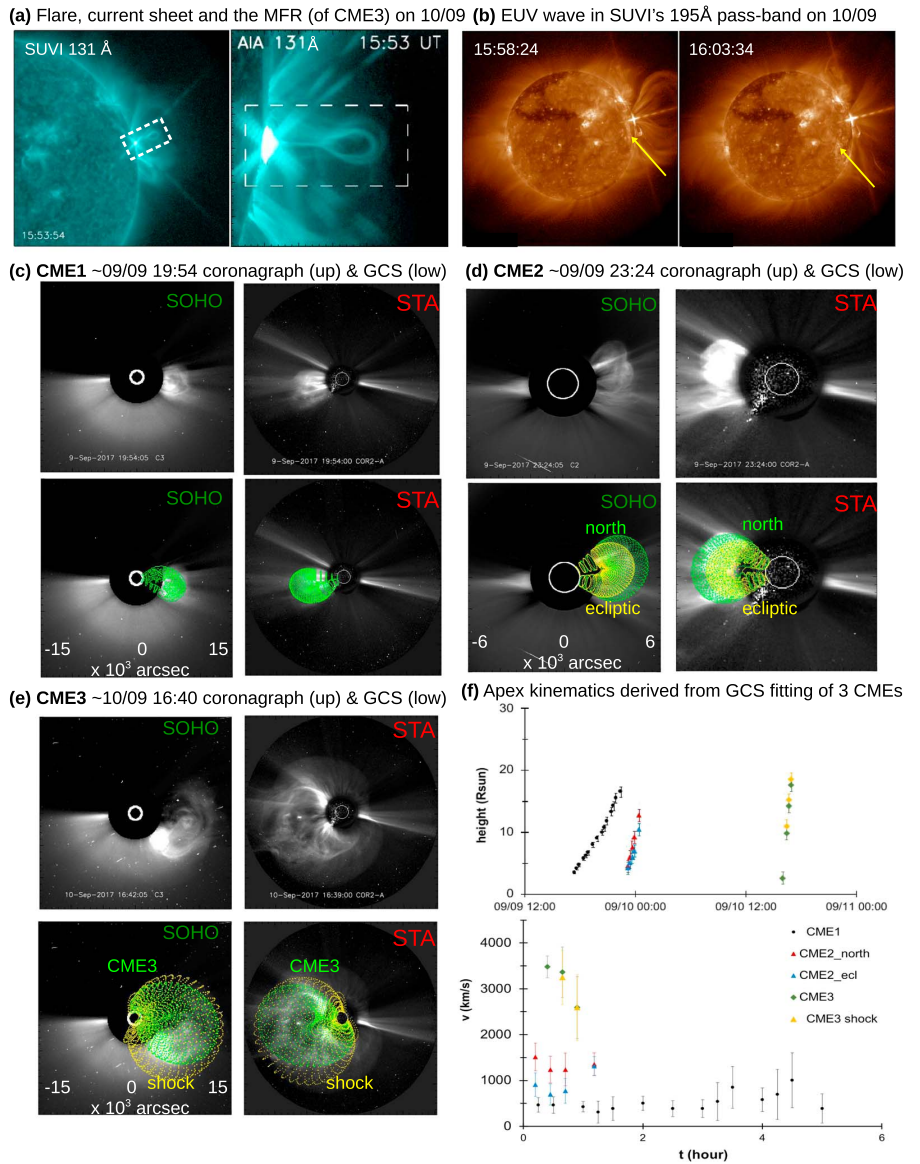


Figure 1. Remote sensing observations of the 10 September 2017 flare and three coronal mass ejections (CMEs) launched in the same Active Region from 9 to 10 September 2017. (a) The GOES16/SUVI 131 Å (adapted from Seaton & Darnel, 2018) and SDO/AIA 131 Å (adapted from Li et al., 2018) observations of the flare and initial eruption of the magnetic flux rope (MFR; associated with CME3) with the white dashed box marking the flare, current sheet, and MFR. (b) The posteruption phase of the MFR and fast propagation of the extreme ultraviolet wave away from the onset location with the yellow arrow pointing at the wave front. (c–e; top panels) The stereoscopic coronagraph white light images (equal ranges in x and y axes) of CME1, CME2, and CME3 at selected times. The bottom panels illustrate graduated cylindrical shell (GCS) reconstruction of the CME geometry. The northern and ecliptic components of CME2 have been fitted respectively, and the CME and shock components of CME3 seen from SOHO (left) and STA (right) have also been modeled separately. (f) CME and shock apex kinematics evolution in time derived from GCS modeling. The upper panel shows the height (in solar radii) versus time, and the lower panel is the velocity-time plot where time is normalized to the start of each CME.

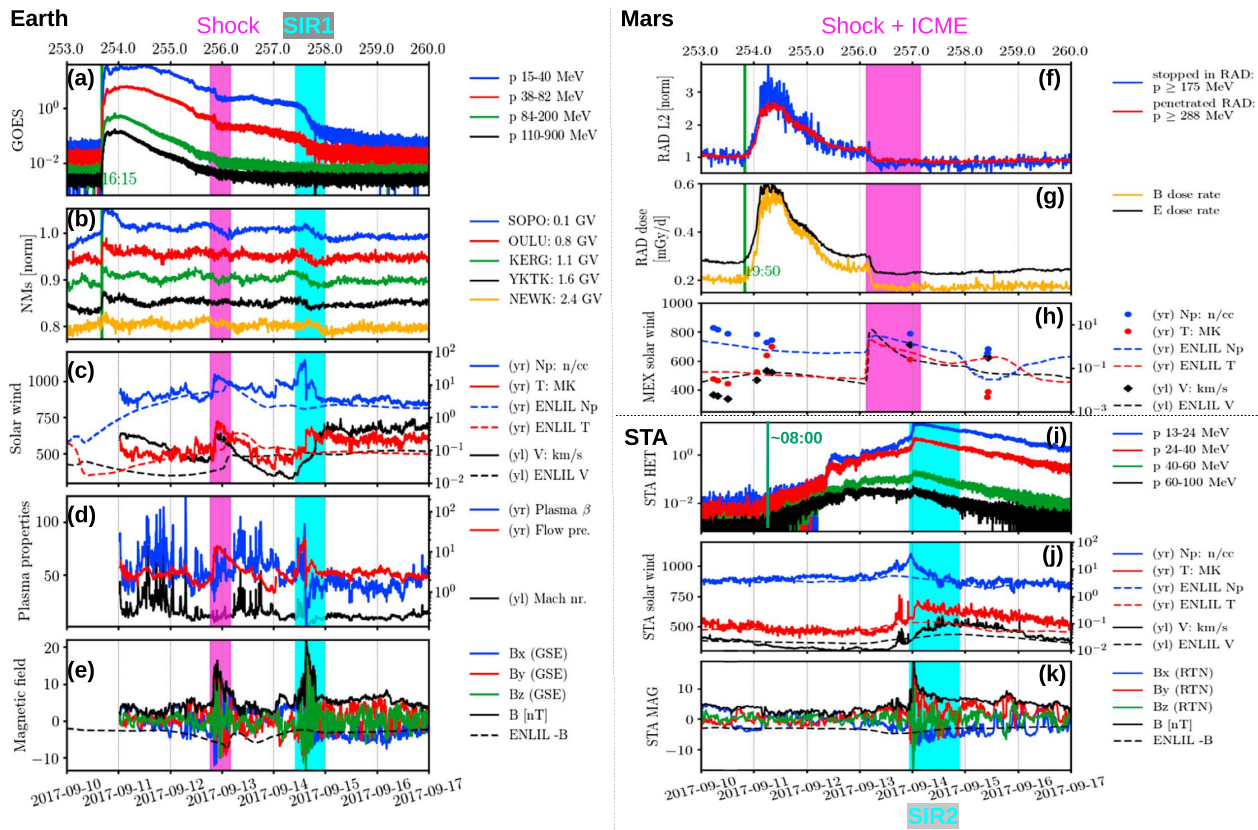


Figure 2. In situ observations of the 10 September 2017 events at Earth (a–e), Mars (f–h), and STA (i–k). (a/i) The energy-dependent particle flux (counts/cm²/sr/MeV/s) measured by GOES and STA. Panel (b) includes count rate of several ground-based neutron monitors with different cutoff rigidities (each neutron monitor data set is normalized to the average value of the selected time range and shifted apart in y axis). Panels (c), (h), and (j) present the solar wind speed (black, left y axis (y)), proton density (blue, right y axis, (yr)), and temperature (red, yr) for Earth (OMNI), Mars (Mars-EXpress, MEX), and STA, respectively. The ENLIL-modeled results at three locations are also plotted as dashed lines. Panel (d) plots the Alfvén Mach number (black, y), plasma β (blue, yr), and flow pressure (red, yr) estimated at Earth. (e/k) displays the vector magnetic fields at Earth/STA in Geocentric Solar Ecliptic or spacecraft Radial-Tangential-Normal coordinate and negative ENLIL modeled magnetic field strength (dashed line). (f) contains the normalized count rate for downward particles stopping in RAD and penetrating RAD with the former/late approximating protons with energies larger than 175/288 MeV arriving at Mars. Panel (g) shows the dose rate recorded in RAD B (silicon) and E (plastic) detectors. Magenta highlighted areas are the ICME and/or its associated shock passage at Earth and Mars. Cyan highlighted areas are high-speed streams (of two different ones) passing Earth and STA during this period. Vertical solid lines in (a)-(b)/(f)-(g)/(i) indicate the particle onset time at Earth/Mars/STA.

1.2. The Early Kinematics of Three CMEs Launched From 9 to 10 September

To further track the erupted MFR and CME propagation into the interplanetary space, it is important to understand the contextual solar and heliospheric conditions prior to this event. Starting from 9 September 2017, two CMEs were seen in the STA and the SOHO coronagraph images as shown in Figures 1c and 1d. The two CMEs (named CME1 and CME2 in the order of their launch sequence) were launched before the aforementioned CME on 10 September 2017 (named CME3) from the same AR with similar directions.

We utilized the graduated cylindrical shell (GCS) model (Thernisien, 2011; Thernisien et al., 2009) based on stereoscopic coronagraph observations of STA and SOHO to reconstruct the initial 3-D geometry and kinematics of the CMEs. The GCS fits of CME1, CME2, and CME3 are shown in Figures 1c–1e, respectively. The northern and ecliptic components of CME2 have been reconstructed separately as the idealized single GCS reconstruction is not sufficient to describe the asymmetrical structure of CME2. However, only the component in the ecliptic plane was used as input for the later kinematics and propagation of CME2 in the interplanetary space (Table 1) as modeled by the 2-D drag-based model (DBM; section 2). In the coronagraph images of

Table 1

The Mass and GCS Reconstructed Initial Kinematics of Three CMEs and CME3-driven Shock as Well as the Launch Information (Direction, Location [Distance From the Sun], Time, and Speed), and Drag-Parameter γ for DBM

	Long. HEE	1/2 width (degree)	Mass (10^{15} g)	DBM launch direction/location	Time dd/mm hh:min	Speed (km/s)	γ (10^{-7} km^{-1})
CME1	119	35	3.4	apex/ $20 R_{\odot}$	09/09 23:46	500	0.1
CME2	116	19	3.5	apex/ $20 R_{\odot}$	10/09 02:16	1,000	0.05
CME3	110	67	9.1	apex/ $17.6 R_{\odot}$	10/09 16:54	2,600	0.01
CME1+2	119	35	$2M_0^a$	to Mars/ $24 R_{\odot}$	10/09 04:50	750	0.05
CME1+2+3	110	67	$5M_0^a$	to Mars/ $68 R_{\odot}$	10/09 21:00	1,800	0.052
Shock	110	110–122 ^b	NA	to Mars/ $18.1 R_{\odot}$	10/09 16:54	2,500	0.15
				to Earth/ $11.6 R_{\odot}$	10/09 16:54	1,600	0.4

Note. CME = coronal mass ejection; GCS = graduated cylindrical shell; DBM = drag-based model; HEE = Heliocentric Earth Ecliptic.

^aThe mass of CME1, CME2, and CME3 was approximated as M_0 , M_0 , and $3M_0$, where $M_0 \approx 3 \times 10^{15}$ g as only their mass ratio matters for the interaction kinematics treated in DBM (Temmer et al., 2012).

^bThe half-width of the shock in the interplanetary space is given in a range constrained by in situ observations (see section 3).

CME3, the flux rope is distinguished as a bright and structured component while the associated shock front is identified as a fainter quasi-spherical feature ahead of it.

Multiple GCS fits over different time steps were used to derive the CME kinematic evolution. Height-time and velocity-time profiles of the CME apex are given in Figure 1f, which show that CME1 and CME2 had moderate and roughly constant launch speeds while CME3 erupted extremely rapidly ($>2,600$ km/s at the apex) and was subsequently decelerated. This is consistent with the trajectory and velocity of the flux rope of CME3 below 2 solar radii (R_{\odot}) derived by Seaton and Darnel 2018 where its velocity was approximately $2,000$ km/s at $1.5 R_{\odot}$, which suggests that the CME continued to accelerate up to a few R_{\odot} (our GCS fitting started from $\approx 3 R_{\odot}$).

CME3 drove a globally propagating shock wave, observed in the low corona as an EUV wave as discussed in section 1.1. We reconstructed the CME3 shock kinematics focusing on its initial velocity using the GCS model. The shock was modeled as a sphere-like structure with one pole attached to the solar surface (Figure 1e). Although this assumption does not match well the observations which quickly extended into a global structure, the front part of the shock in the ecliptic plane can be fitted well with GCS, from which we derived the initial shock speed as also shown in Figure 1e together with the velocities of three CMEs. We assume the direction of the shock to be the same as that of CME3 and, as will be shown later, we fine-tune its geometric extent based on available in situ plasma observations. The longitudinal direction of the central portion of each CME/shock in the Heliocentric Earth Ecliptic (HEE) coordinate, its longitudinal half-width, and launch speed derived using GCS reconstruction are listed in Table 1 and also illustrated in Figures 3a and 3b. The plane-of-sky mass of each CME was estimated based on SOHO/Large Angle and Spectrometric Coronagraph C2 images (Colaninno & Vourlidas, 2009), and their approximate values are also listed in the table.

2. The Interplanetary Trajectory and Interaction of Three CMEs Modeled by the DBM

Assuming that the main force that governs the propagation behavior of a CME in interplanetary space is the magnetohydrodynamical drag force, we simulated the kinematic profile of the CMEs via the DBM (Vršnak & Žic, 2007; Vršnak et al., 2013). We used the 2-D DBM with the leading edge of the CME considered to be a semicircle (diameter is the CME full angular width) such that although the apex initially propagates faster compared to the flanks, the variation of speed along the CME front decreases in time and the front gradually flattens during the propagation (Dumbović et al., 2018; Žic et al., 2015).

Within 1 day the three CMEs erupted in a similar direction, each with a higher speed than the preceding one; hence, we expect that CME2 catches up and interacts with CME1 and later on CME3 catches up and interacts with the previous two CMEs. We assume that their mass merged as an entity and the two colliding bodies continued their propagation further with the momentum conserved before and after the interaction (Temmer et al., 2012). This assumption is supported by Shen et al. 2012 who also suggested that the influence

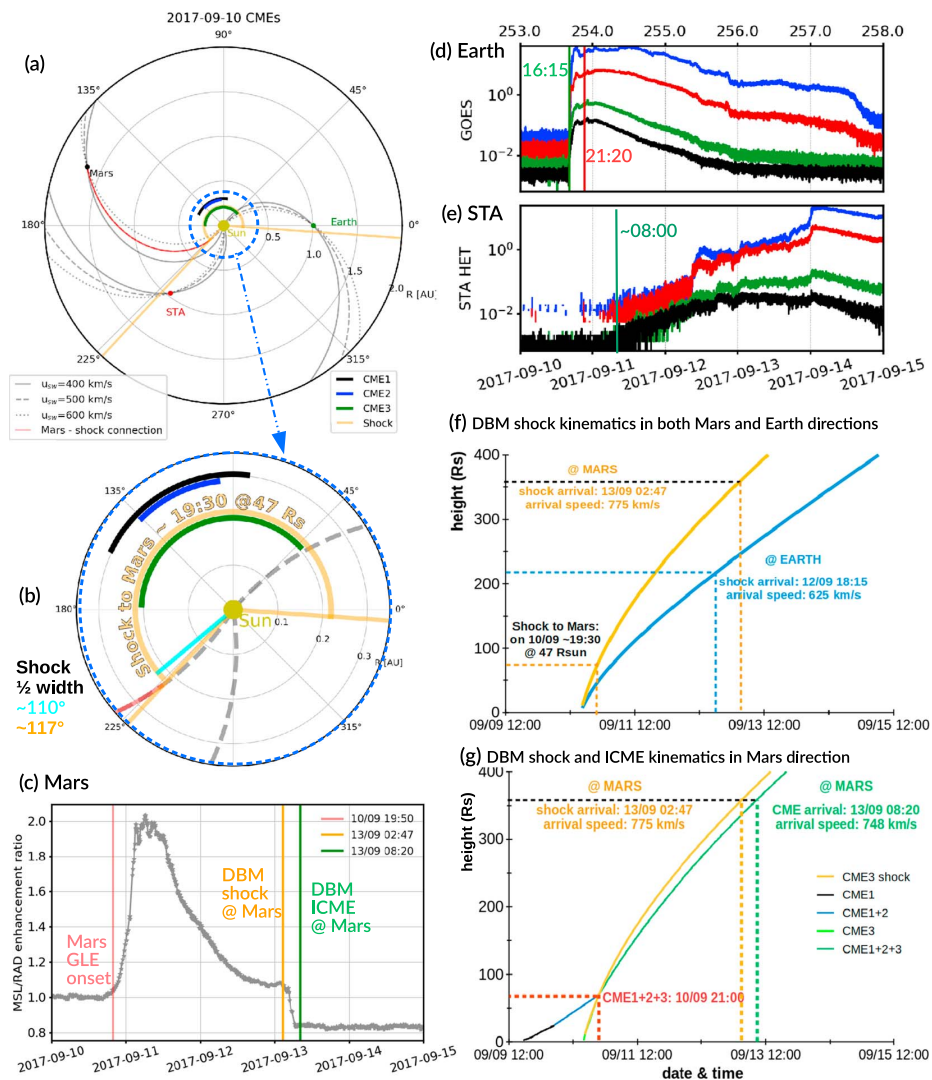


Figure 3. Panel (a) shows heliospheric locations of the Earth, Mars, and STA in HEE coordinates. Longitudinal extents of three CMEs and the interplanetary shock driven by CME3 are approximated by circular contours (their geometries are not modeled as sun-centered circles). Nominal IMFs passing three observers under different solar wind conditions are plotted. At ~19:30 on 9 September 2017 the shock (yellow contour) is at a distance of 47 R_s . Yellow cone boundaries show the extent of the shock with a half-width of 117°, which could connect to the 500 km/s solar wind IMF toward Mars upon the SEP onset. Panel (b) is a zoom-in of (a) within 0.35 AU and also shows the left edge of the shock with a half-width of 110° not connecting to the 500 km/s Parker spiral. Panel (c) plots the enhancement rate (to the background value) representing SEPs \geq about 275 MeV reaching Mars. Panels (d) and (e) show the energy-dependent particle flux measured by GOES at Earth and STA (units and legends are the same as in Figure 2). Panels (f) and (g) are the best fitting DBM results of the shock and ICME kinematics in Mars and Earth directions with more descriptions and discussions in sections 2–4.

of CME kinematics by solar wind is much smaller compared to that due to collisions. After each CME-CME interaction in DBM we relaunched the merged CME from the merging location with reevaluated drag parameters γ until the next interaction.

We used the solar wind speed of 500 km/s, which was the average in situ measurement before the ICME/shock arrival at Mars/Earth (shown in Figure 2) and was also constrained by the shock propagation discussed later in section 3. The drag parameter γ used in the DBM for each CME before and after the interactions is shown in Table 1. Since γ depends on the CME mass and cross-sectional area, it was recalculated after each interaction (Temmer et al., 2012). The initial γ of the three CMEs were empirically set to decrease after one another since earlier CMEs have been observed to be able to efficiently *sweep the way* and decrease the drag force for successive CMEs (Temmer & Nitta, 2015). The choice of γ and solar wind speed has been fine-tuned, through a forward modeling process using different input parameters, to best match the in situ arrival of the merged ICME at Mars marked by the magenta bar in Figures 2f–2h (the ICME ejecta did not reach operational spacecraft at Earth and other locations).

As shown in Figure 3g and Table 1 of the results from DBM, given the differences of their launch speeds, CME2 caught up with CME1 at about $24 R_s$ at 04:50 UT on 10 September 2017. The merged CME (named CME1+2) had a cross section combining the two CMEs, which is equal to CME1 as it is wider than CME2 on both edges. CME1+2 had a speed of 750 km/s based on momentum conservation before and after the collision. The entity was later caught up by CME3 at about $68 R_s$ at 21:00 UT on 10 September 2017 and the merged CME1+2+3 had a width of CME3 and a speed of $\approx 1,800$ km/s. It arrived at Mars at about 08:20 UT on 13 September 2017 (Figures 3f and 3g) with an arrival speed of about 748 km/s. This is comparable to the Mars-EXpress (MEX) measurement by the Analyzer of Space Plasmas and Energetic Atoms 3 instrument (Barabash et al., 2006) in the solar wind, which is, however, very scarce (black squares in Figure 2h). We will discuss about the modeled ICME and its shock arrival in comparison with in situ observations in section 4.

3. Shock Kinematics and Propagation Toward Earth and Mars: Data-Constrained DBM

The fast and global propagation of the EUV wave discussed in section 1 indicates a wide extent of the shock reaching the direction of Earth. In situ measurements at Earth clearly reveal the shock arrival as shown in Figures 2c–2e with the 5-min resolution OMNI data. The magenta bars in (a)–(e) mark the shock arrival at Earth characterized by enhancements of the magnetic fields, solar wind velocity, density, temperature, and plasma flow pressure as well as the Forbush decrease (FD) in various NMs and GOES high-energy particle fluxes. FDs are identified as temporary and rapid depressions in the galactic cosmic rays (GCRs) intensity caused by interplanetary disturbances and magnetic shielding against charged particles during the passage of shocks and/or magnetic clouds (e.g., Cane, 2000).

Toward Mars, the left flank of the ICME shock and ejecta are expected to hit the planet. Unfortunately, in situ solar wind and magnetic field observations at Mars upon the ICME shock arrival are very limited as shown in Figure 2h. A clear signature indicating the shock arrival is the FD at $\sim 02:50$ UT on 13 September 2017 detected by the Radiation Assessment Detector (RAD; Hassler et al., 2012) onboard the Mars Science Laboratory (MSL) rover Curiosity on the surface of Mars. Compared to previous FD observations at Mars (Guo, Lillis, et al., 2018), this event has a magnitude up to $\sim 23\%$ in the RAD dose rate which makes it the largest FD observed by RAD since the landing of MSL in August 2012. Witasse et al. 2017 have studied one of the largest FD event seen by RAD with a $\sim 19\%$ magnitude of decrease observed on 17 October 2014. This event is similar to the 2017 September event studied here that Mars were located at the east flank of both CMEs. But the launch speed of the 17 October 2014 CME was much smaller $\sim 1,015$ km/s, while the September 2017 event studied here had a launch speed of about 2,600 km/s (Table 1). Consequently, the transit time of the September CME from the Sun to Mars is only about 58.5 hr, which is ~ 10 hr shorter than the 17 October 2014 event.

We constrained the longitudinal extent of the shock based on (1) the assumption that the shock is symmetric around the direction of CME3 (110° in HEE coordinate), (2) the in situ OMNI data showing that the right edge of the shock passed Earth, and (3) STA plasma and magnetic field measurements suggesting that the left edge of the shock should not reach STA at 232° (Figures 2i–2k). This constrained half-width of the shock is between 110° and 122° as given in Table 1 and Figure 3b.

Because Earth and Mars were $\sim 160^\circ$ apart, different interplanetary conditions should be considered for the shock propagation in each direction. Various solar wind speeds and drag parameters γ were tested for multiple runs and for each run, we compared the modeled results with in situ observational constraints including:

1. Shock arrival time at Mars should be around 02:50 UT on 13 September 2017, which corresponds to the onset of the FD seen by MSL/RAD on the surface of Mars as shown in Figures 2f and 2g.
2. The shock arrival speed at Mars should match the in situ solar wind speed, which is about 650–800 km/s indicated by the scarce but precious solar wind data measured by MEX (Figure 2h).
3. Shock arrival time at Earth should be around 18:30 UT on 12 September 2017, which is suggested by magnetic field and solar wind measurement at Earth (Figures 2a–2e, magenta bars).
4. The shock arrival speed at Earth should match the in situ solar wind speed, which is about 600 km/s shown in Figure 2c.
5. The solar wind speed prior to the shock arrival at Earth/Mars varied between 400 and 600 km/s as shown in Figures 2c/2h. Different DBM runs with 400, 500, and 600 km/s were performed and compared.

The optimized fitting result from these DBM runs is shown in Figure 3f where the shock was launched with different speeds toward Earth and Mars as derived from GCS fits (Table 1). The best derived γ values are 0.15 and $0.4 \times 10^{-7}/\text{km}$ in the direction of Mars and Earth respectively while the best-matching solar wind speed is 500 km/s in both directions. We note that in order to match the shock arrival time at Earth and Mars, we had to use rather large γ values compared to those for the associated ICME. We justify the increased drag by the assumption that the shock caused by CME3 is only weakly driven over certain distance ranges. In the Mars direction, this happens beyond the distance of $68 R_\odot$ due the sudden deceleration of CME3 as it interacts with the previous CMEs. Toward Earth, the shock is even less strongly driven as the main propagation direction of the magnetic structure is directed toward Mars, and, hence, experiences a larger drag.

4. The Shock and ICME Arrival at Mars and Earth: Modeled Results and In Situ Observations

In situ observations at Mars of the ICME structure are very limited (Figure 2h) and the magenta highlighted bars in (f)–(h) mark the possible passage of the shock and ICME at Mars indicated by MEX measurement in the solar wind overplotted with the WSA-ENLIL (Mays et al., 2015, and references therein) modeling results. The current run of the WSA-ENLIL plus cone model (run ID 'Leila_Mays_120817_SH_9' on the CCMC server) has included the launch and propagation of the aforementioned three CMEs and is explained in better details in Luhmann et al. 2018. Note that similar to DBM, input parameters for the ENLIL modeling were tweaked in order to best match the observations. Unlike the decoupled structures in DBM, CMEs in ENLIL could drive the shock front in a more physical manner. The ENLIL-modeled ICME shock arrived at Mars at about 04:00 UT on 13 September 2017, which is very close to the onset time of the FD at Mars (Figure 2g) and the solar wind speed and density peaked at around 820 km/s and $3.2 \text{ protons}/\text{cm}^3$, which are consistent with the MEX measurement during the ICME passage (Figure 2h).

Given the direction and the longitudinal extent of the three CMEs derived from the GCS model (Table 1 and Figures 3a and 3b) and the in situ observation at Earth (Figures 2c–2e), no ICME ejecta but only the right flank of the shock arrived at Earth. The ENLIL modeled shock arrived at Earth at $\sim 00:00$ UT on 13 September 2017, which is about 5.5 hr later than the in situ detection of the shock arrival (Figures 2c–2e). The modeled peak magnetic field strength and solar wind speed are also slightly smaller than the measured values. Considering the complexity of the events, the shock/ICME arrival at both Earth and Mars modeled by ENLIL matches reasonably well with observations within the limit of statistical uncertainties. The mean absolute arrival time prediction error was about 12 hr as studied by Mays et al. 2015 of 17 CMEs which were predicted to arrive at Earth.

The DBM modeled results of the shock arrivals at Earth and Mars are illustrated in Figure 3f. The launch speed of the shock in the direction of Earth was slightly smaller than that toward Mars as derived from GCS fits (Table 1). The drag parameter is also larger for the shock propagating toward Earth as it was not really driven by the ICME magnetic structure in this direction. The DBM predicted shock arrival at Earth is at about 18:15 UT on 12 September 2017 with an arrival speed of ~ 625 km/s, which are very close to the observational arrival time of 18:30 and speed of ~ 630 km/s (which is expected as DBM is tuned to match the observation). The modeled shock arrived at Mars with a speed of 775 km/s at around 02:47 UT on 13 September 2017, which is perfectly matching the onset time of the RAD seen FD at 02:50 as shown in Figure 3c.

As modeled by the DBM and described in section 2, three CMEs were launched in similar directions and interacted with one another as they propagated toward the direction of Mars. The merged entity arrived at Mars at about 08:20 UT on 13 September 2017 (Figure 3g) with an arrival speed of about 748 km/s, which agrees with the MEX solar wind speed of 714 km/s measured hours later at 22:57 UT. Unfortunately, in situ interplanetary magnetic field (IMF) or solar wind data are rather limited for identifying the arrival and the structure of the magnetic ejecta (Lee et al., 2018).

Upon the ICME's arrival at Mars, the FD measured by RAD on the surface of Mars had a decrease in the high-energy count rate up to $\sim 23\%$ (Figure 3c) and is the biggest FD detected by RAD to date. A classical picture of FDs (Cane, 2000) suggests that an ICME with a shock front passing by an observation point could result in a two-step structure, that is, with the first decrease corresponding to the shock arrival and the turbulent sheath region and the second step indicating passage of the magnetic ejecta. However, recent studies suggest that the ejecta may not always be associated with a decrease, especially at distances further away from the Sun (Winslow et al., 2018). As shown in Figures 3c and 3f, the modeled shock arrival time at Mars agrees nicely with the initial FD onset while the ICME (merged ejecta) arrival might correspond to a rather weak second decrease. However, due to the scarce in situ magnetic and plasma measurement in the solar wind, we cannot confirm the two-step FD profile and its corresponding ICME structure.

5. SEPs Arriving at Earth, Mars, and STA and the Indication of the Shock and Stream Interaction Region Propagation

As discussed in section 1.1, the onset of relativistic particles at Earth was about 10–15 min after the flare onset indicating a good magnetic connection between the particle injection site and Earth. As shown in Figure 2j, high energetic protons started slowly arriving at STA at around $\sim 08:00$ UT on 11 September 2017, which was ~ 16 hr later than the flare onset. The arrival of these SEPs is probably attributed to cross-field diffusion in the solar wind (e.g., Dröge et al., 2010). This is supported by Figure 3a, which shows that STA was connected to the back side of the Sun where the flare erupted. At Mars, the earliest possible onset of > 100 MeV protons is at 19:50 UT, ~ 215 min later than that at Earth. Considering the Mars IMF footpoint separation from the flare longitude is about 135° , this onset delay is within the statistical uncertainties of high-energy proton onset delay studied by Richardson et al. (2014, Figure 16). However, it is unclear whether the SEP onset at Mars is due to cross-field diffusion or a later magnetic connection to the acceleration/injection site or both.

First, we consider the model with continuous particle injection at the shock as it propagates outward (due to reacceleration of particles by the interplanetary shock) and establishes magnetic connection to the observer (e.g., Lario et al., 2013, 2017). Given the proton onset at 19:50 seen by the highest energy channels of MSL/RAD, this model requires that the shock started connecting to the Parker spiral toward Mars under a solar wind speed of 500 km/s at $\sim 19:30$ UT to allow for parallel and efficient particle transport to Mars. As modeled by DBM (Figure 3f), at $\sim 19:30$, the shock front in the direction of Mars has a propagation distance of $47 R_s$ and the magnetic establishment would require the shock to have a half-width of about 117° (cone boundaries shown as yellow lines in Figures 3a and 3b), which is in-between the constrained range (section 3 and Table 1). The path of particles along the 500 km/s Parker spiral from the shock front to Mars is highlighted in red. We note that the solar wind speed of 500 km/s is an approximation of the observation and a fitted parameter from DBM. With a slightly faster solar wind speed (e.g., the 600-km/s IMF plotted as dotted lines in Figure 3a/3b), the magnetic establishment at $\sim 19:30$ requires a smaller shock width. Alternatively, if the solar wind speed is about 400 km/s (solid curves in the plots), it has to be considerably wider to establish the magnetic connection upon the SEP onset under the condition of undisturbed IMF. However, this wider shock, while propagating radially outward, should also reach STA which is however not supported by the STA in situ observations (Figure 2i–2k).

In the scenario of continuous particle injection at the shock front, the preceding two CMEs may provide a *seed* population for the catching-up shock (Gopalswamy et al., 2002, 2004). In fact, a small jump in the GOES data at around 21:20 UT as indicated by the vertical red line in Figure 3d may indicate the injection of more particles at the shock through merging of CME3 with CME1+2 at around 21:00 UT predicted by DBM (Table 1 and Figure 3g). Alternatively, as the Earth connection point along the shock front changes, the discontinuity or evolution of the shock parameters may also contribute to the second peak as observed in situ at around 21:20.

Nevertheless, particle scattering and transport across the IMF could have also played a role during the event. As STA was not magnetically connected to the flare or the shock (Figure 3a) from the beginning, early SEPs detected at STA (gradual time profile of the flux) should have been transported there across IMF lines. Toward the direction of Mars, with a smaller width of 110° (left edge of the shock is marked in cyan in Figure 2b), which is the lower limit of the constrained shock width, the DBM modeled shock could not be connected to the 500-km/s Parker spiral toward Mars upon the SEP onset. In this case, SEPs first arriving at Mars are likely due to particle transport across IMF from the injection site which could be the shock front and/or the flare reconnection region.

We have compared the in situ observations with the results from the WSA-ENLIL predictions at Mars, Earth, and STA in Figure 2 (ENLIL results are plotted as dashed lines) as discussed in section 4. From ENLIL simulations, the shock information and propagation along the IMF passing certain observers could be extracted for each CME (Bain et al., 2016; Luhmann et al., 2017). Extracted shock information in the current run indicates that the shock started connecting to the IMF toward Mars at about 06:00 UT on 11 September, a few hours later than the SEP onset at Mars. In such a case, cross-field transport, presumably close to the Sun, must have dominated over establishment of a direct magnetic connection to the shock. However, a detailed investigation would require careful studies of the particle transport modeling, taking into account effects such as adiabatic cooling, focusing, turbulent scattering, pitch angle scattering, and cross-field diffusion (e.g., Hu et al., 2017; Zhang et al., 2009).

At a later phase of the SEP event, particles were widely distributed across heliospheric longitudes $\geq 232^\circ$ (or even wider as this is constrained by three observational locations), the interaction of SEPs with large-scale heliospheric structures is particularly interesting. Stream interaction regions (SIR, ; Burlaga, 1974) are interaction regions between the fast and slow solar wind characterized by sudden changes in the flow density, temperature, and significant increase of solar wind as well as compressed magnetic field. Stable SIR structures may corotate with the Sun which has a rotation period of ~ 27 days in the solar equatorial plane. In Figure 2, we identified two SIRs passing Earth and STA, respectively (named SIR1 for the one passing Earth and SIR2 for the one across STA) as highlighted in cyan areas.

As shown in Figures 2i–2k, SIR2 arrived at STA at about 22:48 UT on 13 September 2017 and the high-energy proton flux (up to 100 MeV) has a small enhancement which suggests SEPs may have leaked into, get trapped and/or reaccelerated in the SIR structure. Considering the SIR rotates with the Sun, we time-shift the SIR2 structure observed at STA back to 10 September 2017 at 19:30 UT (approximately shortly before the SEP event at Mars). As illustrated in Figure 4a, SIR2 arrived at Mars at almost this time. In fact, in situ solar wind and magnetic field observations were available during this period and an SIR was identified to have impacted Mars at 23:30 UT (Lee et al., 2018), which perfectly agrees with the time-shifted SIR2 from STA to Mars. Figure 2h also shows the evolution of proton temperature, density, and solar wind speed (from ~ 300 to ~ 500 km/s) at Mars during the SIR2 passage which is consistent with the solar wind changes when SIR2 passed STA.

Upon the SEP onset at Mars (Figure 4a), SIR2 was connected even closer to the central part of the shock/flare than Mars. Therefore, SEPs were likely also injected into the SIR structure, preferentially along the IMF direction directly from the shock front as particles cannot easily penetrate through an SIR structure. Such a scenario may have also contributed to the SEPs first arriving at Mars even if Mars were not directly connected to the injection site. These high-energy particles were trapped in (or perhaps even reaccelerated therein) and corotated with SIR2 and caused a remarkable enhancement of the SEP flux when SIR2 arrived at STA (Figure 2i) at 22:48 UT on 13 September 2017. Since these SEPs were accelerated by the flare/shock closer to the Sun, they have a higher energy component (up to 100 MeV).

On the other hand, SIR1 (cyan area in Figures 2a–2e) had a more significant enhancement of the solar wind speed (Figure 2c) with a more compressed shock structure causing substantial FDs in the NM count rates. It passed Earth starting around 10:15 UT on 14 September 2017. Time-shift analysis shows that shortly after the flare and SEP onset, SIR1 was about 50° west of Earth and was barely magnetically connected to the right edge of the shock as shown in Figure 4a, thus making particle injection into SIR1 rather unlikely. It is evident in Figure 2a that high energy particle fluxes observed at Earth had a rather gradual declining time profile especially after the shock passed Earth. In particular, between the shock structure (which passed Earth at 04:00 UT on 13 September 2017, magenta area) and SIR1 arrival at Earth, there is a plateau in the GOES high-energy flux. This may be caused by energetic particles being trapped between the shock and SIR1, which act as two

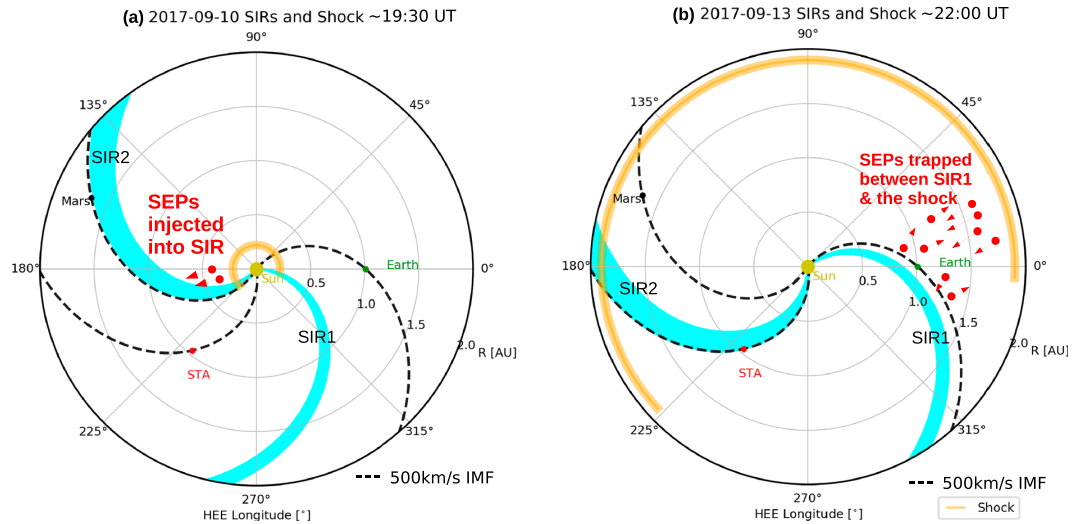


Figure 4. Illustration of the two SIRs detected at Earth (SIR1) and STA (SIR2) as highlighted in Figure 2. Both SIRs are time shifted to 10 September 2017 at around 19:30 UT shown in (a) and to 13 September 2017 at around 22:00 UT shown in (b). The widths of SIR1 and SIR2 are derived from their in situ passages at Earth and STA, respectively. Nominal IMFs passing Earth, Mars, and STA under a solar wind speed of ~ 500 km/s are plotted in dashed lines. SEP = solar energetic particle; SIR = stream interaction region; IMF = interplanetary magnetic field; STA = Solar Terrestrial relations observatory Ahead.

barriers for these SEPs, as illustrated in Figure 4b. This is supported by Strauss et al. (2016) who suggested that perpendicular diffusion could be strongly damped at magnetic discontinuities, which may be responsible for the large particle gradients associated with these structures such as an SIR. When SIR1 shock passed Earth, this reservoir of SEPs also passed Earth causing a sudden decrease of the GOES flux at energies below ~ 80 MeV. This decrease is deferent from a normal FD in the GCR flux as seen by NMs on ground.

6. Summary and Conclusion

We investigated and modeled the geometry, kinematics, propagation, and interaction of three CMEs launched around 10 September 2017 from their solar origin to their arrivals at Mars and Earth. The modeled results are constrained by and compared with in situ measurements at Earth, Mars, and STA. Observation-based modeling of the ICME and the interplanetary shock reveals the complexity of the event and the advantage of more measurements for advancing space weather predictions. The optimized modeling for the ICME arrival at both Earth and Mars suggests that in order to better predict the ICME arrival and its potential space weather impact at different heliospheric locations, it is important to consider (1) the eruption of the flare and CME at the Sun, (2) the evolution of the ICME kinematics, especially during interactions of different CMEs, and (3) the dynamic heliospheric conditions at different locations in the heliosphere.

The SEP event associated with the flare and the eruption of the last CME has been detected, for the first time, at the surface of two planets, registered as GLE72 at Earth and the biggest GLE seen by MSL/RAD on Mars. Relativistic particles first arriving at Earth and causing GLE72 were mainly accelerated by the flare and the initial shock. The particle onset at Mars is ~ 3.5 hr later than that at Earth, and this was caused by either a later magnetic connection of Mars to the shock front which serves as an injection source for SEPs and/or cross-field diffusion of SEPs from the acceleration and injection site. Particles started arriving at STA ~ 16 hr later with a gradual rising profile indicating perpendicular diffusion across IMF was mostly responsible at this phase. Numerical modeling of particle propagation in the heliosphere taking into account of the dynamic acceleration and injection process would also be helpful for understanding the interplanetary journey of these highly energetic particles arriving at three locations $> 230^\circ$ longitudinally apart.

Two SIRs have been detected in situ at Earth and STA. We shifted SIR2 (detected at STA) back in time and found that its arrival time at Mars is coincident with the SEP onset time at Mars, and it had a magnetic connection even closer to the central part of the shock. This may have favored particles injected into the SIR which were later observed as an enhancement in the SEP flux when it passed STA. On the other hand, SIR1 arrived at Earth

~ 1.5 days after the CME shock passed Earth and SEPs were trapped between these two structures causing a plateau profile in the GOES SEP flux.

Appendix A: References of the Measurements and Databases Employed in This Study

In this appendix, we provide descriptions and references of all the data from various spacecraft, instruments, and databases employed in this study.

1. High energetic proton data from the Energetic Proton Electron and Alpha Detector of the GOES15 have been plotted in Figures 2a and 3d. The data are documented at www.ngdc.noaa.gov/stp/satellite/goes/ and are publicly available at <https://satdat.ngdc.noaa.gov/>.
2. Earth ground-based NMs measure the secondary particles generated in the atmosphere by primary cosmic energetic charged particles including GCRs and SEPs. The NM data plotted in Figure 2b are obtained from the NM Data Base (www.nmdb.eu/nest/).
3. The Space Physics Data Facility OMNIWeb database (<https://omniweb.gsfc.nasa.gov/>) provides the solar wind data combined from different measurements of available spacecraft including the Advanced Composition Explorer (Stone et al., 1998), WIND (Lin et al., 1995), and the International Monitoring Platform 8. Data plotted in Figures 2c–2e are in 5-min resolution, and the magnetic fields are in the Geocentric Solar Ecliptic coordinate.
4. The RAD (Hassler et al., 2012) measures GCRs and SEPs and their secondaries generated in the Martian atmosphere and regolith at Gale Crater on the surface of Mars since the landing of the Curiosity rover in August 2012. Figure 2f plots the normalized (data divided by the background value) RAD level 2 count rate with the blue curve for particles stopping inside the detector and red curve for particles penetrating through the whole instruments. The average vertical column depth of the atmosphere on top of RAD was about 23.4 g/cm^2 during the period of the event. This would only allow protons with kinetic energies larger than about 175 MeV to reach the surface (Guo, Zeitlin, et al., 2018) which translates into the minimum primary energy for protons (SEP on top of the atmosphere) stopping in RAD. For protons to penetrate through the entire detector stack, a minimum energy of 113 MeV is required and this adds to about 288 MeV of primary SEP energy. Note that this approximation is under the assumption that the majority of particles reaching Mars surface are protons which is valid during the SEP events. Figure 2g plots the RAD dose rate (mGray/day) recorded in B (silicon) and E (plastic) detectors. Dose rate is a measure of the energy (10^{-3} Joule) deposited by all detected particles per detector mass (kg) per time unit (day). A zoomed-in plot (to emphasize the onset of the SEP) of the enhancement ratio of the dose rate (normalized to the background value) in the plastic detector is shown in Figure 3c. For downward directed particles during the solar event, they need ~ 100 MeV kinetic energy to reach the E detector. This corresponds to a primary SEP energy \geq about 275 MeV arriving at Mars. Both the count rate and dose rate data are generally in cadence of 17 min as RAD runs on an autonomous observing cycle with 16 min per observation plus 1 min of sleep mode.
5. The Analyzer of Space Plasmas and Energetic Atoms 3 (Barabash et al., 2006) experiment of the MEX mission has been used to derive the solar wind properties (Ramstad et al., 2015) plotted in Figure 2h, including the proton density, temperature and solar wind speed.
6. The High Energy Telescope (Von Rosenvinge et al., 2008) on the STA spacecraft provides proton flux rate in various energy ranges which are combined into four different channels and plotted in Figure 2i. The STA Plasma and Suprathermal Ion Composition (Galvin et al., 2008) measurement of the solar wind properties (proton density, temperature, and solar wind speed) is shown in Figure 2j. The In situ Measurements of Particles And CME Transients data of the magnetic field experiment (Acuña et al., 2008) on STA are plotted in Figure 2k in the spacecraft Radial-Tangential-Normal coordinate.
7. Remote sensing coronagraph images of the Sun at two different heliospheric locations have been obtained from (a) the Large Angle and Spectrometric Coronagraph (Brueckner et al., 1995) instrument onboard the SOHO at Earth and (b) the coronagraph (COR) data from the Sun Earth Connection Coronal and Heliospheric Investigation (Howard et al., 2008) at STA.
8. Observations of EUV phenomena in the solar corona are shown in Figures 1a and 1b. They are from the SUVI on the GOES16 spacecraft and the Atmospheric Imaging Assembly (Lemen et al., 2011) on board the Solar Dynamics Observatory spacecraft.

Acknowledgments

We acknowledge use of NASA/SPDF OMNIWeb service and OMNI data, EU NMDB database (www.nmdb.eu), STEREO data (<https://stereo-ssc.nascom.nasa.gov/>), and NOAA GOES data (<https://satdat.ngdc.noaa.gov/>). ENLIL with Cone Model was developed by D. Odstrcil at George Mason University. MSL RAD is supported by NASA (HEOMD) under JPL subcontract 1273039 to SWRI, and in Germany by DLR (under German Space Agency grants 50QM0501, 50QM1201, and 50QM1701) to the Christian-Albrechts-University of Kiel. RAD data are archived in the NASA planetary data systems' planetary plasma interactions node (<http://ppi.pds.nasa.gov/>). The Swedish contribution to the ASPERA-3 experiment is supported by the Swedish National Space Board. ASPERA-3 data are public at the ESA Planetary Science Archive. M. D. acknowledges funding from the EU H2020 MSCA grant agreement (745782). M. T. acknowledges the support by the FFG/ASAP program under grant 859729 (SWAMI). Y. W. is supported by the grants from NSFC (41574165 and 41774178). A. M. V. acknowledges support from the Austrian Science Fund (FWF): P27292-N20. J. G. thanks Christina Lee, Andreas Klassen, Fernando Carcaboso, Nina Dresing, and Andreas Taut for helpful advices and discussions. J. G. and R. F. W. S. acknowledge discussions during various ISSI team meetings.

References

- Acuña, M., Curtis, D., Scheifele, J., Russell, C., Schroeder, P., Szabo, A., & Luhmann, J. (2008). The STEREO/IMPACT magnetic field experiment. *Space Science Reviews*, *136*(1–4), 203–226.
- Aschwanden, M. J. (2002). Particle acceleration and kinematics in solar flares, *Particle acceleration and kinematics in solar flares* (pp. 1–227). Dordrecht: Springer.
- Bain, H., Mays, M., Luhmann, J., Li, Y., Jian, L., & Odstrcil, D. (2016). Shock connectivity in the 2010 August and 2012 July solar energetic particle events inferred from observations and ENLIL modeling. *The Astrophysical Journal*, *825*(1), 1.
- Barabash, S., Lundin, R., Andersson, H., Brinkfeldt, K., Grigoriev, A., Gunell, H., et al. (2006). The Analyzer of Space Plasmas and Energetic Atoms (ASPERA-3) for the Mars Express mission. *Space Science Reviews*, *126*(1–4), 113–164.
- Brueckner, G. E., Howard, R. A., Koomen, M. J., Korendyke, C. M., Michels, D. J., Moses, J. D., et al. (1995). The Large Angle Spectroscopic Coronagraph (LASCO). *Solar Physics*, *162*, 357–402.
- Burlaga, L. F. (1974). Interplanetary stream interfaces. *Journal of Geophysical Research*, *79*, 3717–3725. <https://doi.org/10.1029/JA079i025p03717>
- Cane, H. V. (2000). Coronal mass ejections and Forbush decreases. *Space Science Reviews*, *93*(1–2), 55–77.
- Colaninno, R. C., & Vourlidas, A. (2009). First determination of the true mass of coronal mass ejections: A novel approach to using the two stereo viewpoints. *The Astrophysical Journal*, *698*(1), 852–858.
- Dere, K. P., Brueckner, G. E., Howard, R. A., Koomen, M. J., Korendyke, C. M., Kreplin, R. W., et al. (1997). EIT and LASCO observations of the initiation of a coronal mass ejection. *Solar Physics*, *175*, 601–612. <https://doi.org/10.1023/A:1004907307376>
- Dröge, W., Kartavykh, Y. Y., Klecker, B., & Kovaltsov, G. A. (2010). Anisotropic three-dimensional focused transport of solar energetic particles in the inner heliosphere. *The Astrophysical Journal*, *709*, 912–919. <https://doi.org/10.1088/0004-637X/709/2/912>
- Dumbović, M., Čalogović, J., Vršnak, B., Temmer, M., Mays, M. L., Veronig, A., & Piantischtsch, I. (2018). The drag-based ensemble model (DBEM) for coronal mass ejection propagation. *The Astrophysical Journal*, *854*(2), 180.
- Galvin, A. B., Kistler, L. M., Popecki, M. A., Farrugia, C. J., Simunac, K. D. C., Ellis, L., et al. (2008). The plasma and suprathermal ion composition (PLASTIC) investigation on the STEREO observatories. *The STEREO Mission*, 437–486. <https://doi.org/10.1007/s11214-007-9296-x>
- Gopalswamy, N., Yashiro, S., Krucker, S., Stenborg, G., & Howard, R. A. (2004). Intensity variation of large solar energetic particle events associated with coronal mass ejections. *Journal of Geophysical Research*, *109*, A12105. <https://doi.org/10.1029/2004JA010602>
- Gopalswamy, N., Yashiro, S., Michalek, G., Kaiser, M. L., Howard, R. A., Reames, D. V., et al. (2002). Interacting coronal mass ejections and solar energetic particles. *The Astrophysical Letters*, *572*, L103–L107. <https://doi.org/10.1086/341601>
- Guo, J., Lillis, R., Wimmer-Schweingruber, R. F., Zeitlin, C., Simonson, P., Rahmati, A., et al. (2018). Measurements of Forbush decreases at Mars: Both by MSL on ground and by MAVEN in orbit. *Astronomy & Astrophysics*, *611*, A79.
- Guo, J., Zeitlin, C., Wimmer-Schweingruber, R. F., McDole, T., Kühl, P., Appel, J. C., et al. (2018). A generalized approach to model the spectra and radiation dose rate of solar particle events on the surface of Mars. *The Astronomical Journal*, *155*(1), 49.
- Hassler, D., Zeitlin, C., Wimmer-Schweingruber, R., Böttcher, S., Martin, C., Andrews, J., et al. (2012). The radiation assessment detector (RAD) investigation. *Space Science Reviews*, *170*(1–4), 503–558.
- Howard, R. A., Moses, J. D., Vourlidas, A., Newmark, J. S., Socker, D. G., Plunkett, S. P., et al. (2008). Sun Earth Connection Coronal and Heliospheric Investigation (SECCHI). *Space Science Reviews*, *136*, 67–115. <https://doi.org/10.1007/s11214-008-9341-4>
- Hu, J., Li, G., Ao, X., Zank, G. P., & Verkhoglyadova, O. (2017). Modeling particle acceleration and transport at a 2-D CME-driven shock. *Journal of Geophysical Research: Space Physics*, *122*, 10,938–10,963. <https://doi.org/10.1002/2017JA024077>
- Jiang, C., Zou, P., Feng, X., Hu, Q., Duan, A., Zuo, P., et al. (2018). Decipher the three-dimensional magnetic topology of a great solar flare, arXiv preprint arXiv:1802.02759.
- Lario, D., Aran, A., Gómez-Herrero, R., Dresing, N., Heber, B., Ho, G., et al. (2013). Longitudinal and radial dependence of solar energetic particle peak intensities: STEREO, ACE, SOHO, GOES, and MESSENGER observations. *The Astrophysical Journal*, *767*(1), 41.
- Lario, D., Kwon, R.-Y., Richardson, I. G., Raouafi, N. E., Thompson, B., Von Rosenvinge, T. T., et al. (2017). The solar energetic particle event of 2010 August 14: Connectivity with the solar source inferred from multiple spacecraft observations and modeling. *The Astrophysical Journal*, *838*(1), 51.
- Lee, C., Jakosky, B., Luhmann, J., Brain, D., Mays, M., Hassler, D., et al. (2018). MAVEN observations of the solar cycle 24 space weather conditions at Mars. *Geophysical Research Letters*, *122*, 2768–2794. <https://doi.org/10.1002/2016JA023495>
- Lemen, J. R., Akin, D. J., Boerner, P. F., Chou, C., Drake, J. F., Duncan, D. W., et al. (2011). The Atmospheric Imaging Assembly (AIA) on the Solar Dynamics Observatory (SDO). *Solar Physics*, *275*(1–2), 17–40.
- Li, Y., Xue, J., Ding, M., Cheng, X., Su, Y., Feng, L., et al. (2018). Spectroscopic observations of a current sheet in a solar flare, arXiv preprint arXiv:1801.03631.
- Lin, R., Anderson, K., Ashford, S., Carlson, C., Curtis, D., Ergun, R., et al. (1995). A three-dimensional plasma and energetic particle investigation for the wind spacecraft. *Space Science Reviews*, *71*(1–4), 125–153.
- Lin, R. P., Dennis, B. R., Hurford, G., Smith, D., Zehnder, A., Harvey, P., et al. (2002). The Reuven Ramaty High-Energy Solar Spectroscopic Imager (RHESSI). *Solar Physics*, *210*(1–2), 3–32.
- Liu, W., Jin, M., Downs, C., Ofman, L., Cheung, M., Nitta, N. V. (2018). A Truly Global EUV Wave From the SOL2017-09-10 X8.2 Solar Flare-CME Eruption. *The Astrophysical Journal Letter*, accepted.
- Long, D. M., Bloomfield, D. S., Chen, P.-F., Downs, C., Gallagher, P. T., Kwon, R.-Y., et al. (2017). Understanding the physical nature of coronal “EIT waves”. *Solar physics*, *292*(1), 7.
- Long, D. M., Harra, L. K., Matthews, S. A., Warren, H. P., Lee, K.-S., Doschek, G. A., et al. (2018). Plasma evolution within an erupting coronal cavity. *The Astrophysical Journal*, *855*(2), 74.
- Luhmann, J., Mays, M., Li, Y., Lee, C., Bain, H., Odstrcil, D., et al. (2018). Shock connectivity and the late cycle 24 solar energetic particle events in July and September 2017. *Space Weather*, *16*, 557–568. <https://doi.org/10.1029/2018SW001860>
- Luhmann, J., Mays, M., Odstrcil, D., Li, Y., Bain, H., Lee, C., et al. (2017). Modeling solar energetic particle events using ENLIL heliosphere simulations. *Space Weather*, *15*, 934–954. <https://doi.org/10.1002/2017SW001617>
- Mays, M. L., Taktakishvili, A., Pulkkinen, A., MacNeice, P. J., Rastätter, L., Odstrcil, D., et al. (2015). Ensemble modeling of CMEs using the WSA-ENLIL+Cone model. *Solar Physics*, *290*, 1775–1814. <https://doi.org/10.1007/s11207-015-0692-1>
- Ramstad, R., Barabash, S., Futaana, Y., Nilsson, H., Wang, X.-D., & Holmström, M. (2015). The Martian atmospheric ion escape rate dependence on solar wind and solar EUV conditions: 1. Seven years of Mars Express observations. *Journal of Geophysical Research: Planets*, *120*, 1298–1309. <https://doi.org/10.1002/2015JE004816>
- Redmon, R. J., Seaton, D. B., Steenburgh, R., He, J., & Rodríguez, J. V. (2018). September 2017 geoeffective space weather and impacts to caribbean 2 radio communications during hurricane response. *Space Weather*, *16*. <https://doi.org/10.1029/2018SW001897>

- Richardson, I., von Rosenvinge, T., Cane, H., Christian, E., Cohen, C., & Labrador, A. (2014). > 25 MeV proton events observed by the high energy telescopes on the STEREO A and B spacecraft and/or at earth during the first seven years of the STEREO mission. *Solar Physics*, 289(8), 3059–3107.
- Seaton, D. B., & Darnel, J. M. (2018). Observations of an eruptive solar flare in the extended EUV solar corona. *The Astrophysical Journal Letters*, 852(1), L9.
- Shen, C., Wang, Y., Wang, S., Liu, Y., Liu, R., Vourlidas, A., et al. (2012). Super-elastic collision of large-scale magnetized plasmoids in the heliosphere. *Nature Physics*, 8(12), 923.
- Strauss, R. D., le Roux, J. A., Engelbrecht, N. E., Ruffolo, D., & Dunzlaff, P. (2016). Non-axisymmetric perpendicular diffusion of charged particles and their transport across tangential magnetic discontinuities. *The Astrophysical Journal*, 825(1), 43. <http://stacks.iop.org/0004-637X/825/i=1/a=43>
- Stone, E. C., Frandsen, A., Mewaldt, R., Christian, E., Margolies, D., Ormes, J., & Snow, F. (1998). The advanced composition explorer. *Space Science Reviews*, 86(1–4), 1–22.
- Temmer, M., & Nitta, N. (2015). Interplanetary propagation behavior of the fast coronal mass ejection on 23 July 2012. *Solar Physics*, 290(3), 919–932.
- Temmer, M., Vršnak, B., Rollett, T., Bein, B., de Koning, C. A., Liu, Y., et al. (2012). Characteristics of kinematics of a coronal mass ejection during the 2010 August 1 CME–CME interaction event. *The Astrophysical Journal*, 749(1), 57.
- Thernisien, A. (2011). Implementation of the graduated cylindrical shell model for the three-dimensional reconstruction of coronal mass ejections. *The Astrophysical Journal Supplement Series*, 194(2), 33.
- Thernisien, A., Vourlidas, A., & Howard, R. A. (2009). Forward modeling of coronal mass ejections using STEREO/SECCHI data. *Solar Physics*, 256, 111–130. <https://doi.org/10.1007/s11207-009-9346-5>
- Von Rosenvinge, T., Reames, D., Baker, R., Hawk, J., Nolan, J., Ryan, L., et al. (2008). The high energy telescope for STEREO. *Space Science Reviews*, 136(1–4), 391–435.
- Vršnak, B., & Žic, T. (2007). Transit times of interplanetary coronal mass ejections and the solar wind speed. *Astronomy & Astrophysics*, 472(3), 937–943.
- Vršnak, B., Žic, T., Vrbanc, D., Temmer, M., Rollett, T., Möstl, C., et al. (2013). Propagation of interplanetary coronal mass ejections: The drag-based model. *Solar Physics*, 285(1–2), 295–315.
- Warren, H. P., Brooks, D. H., Ugarte-Urra, I., Reep, J. W., Crump, N. A., & Doschek, G. A. (2018). Spectroscopic observations of current sheet formation and evolution. *The Astrophysical Journal*, 854(2), 122.
- Winslow, R. M., Schwadron, N. A., Lugaz, N., Guo, J., Joyce, C. J., Jordan, A. P., et al. (2018). Opening a window on ICME-driven GCR modulation in the inner solar system. *The Astrophysical Journal*, 856(2), 139.
- Witasse, O., Sánchez-Cano, B., Mays, M., Kajdič, P., Opgenoorth, H., Elliott, H., et al. (2017). Interplanetary coronal mass ejection observed at STEREO-A, Mars, comet 67P/Churyumov-Gerasimenko, Saturn, and New Horizons en-route to Pluto. Comparison of its Forbush decreases at 1.4, 3.1 and 9.9 AU. *Journal of Geophysical Research: Space Physics*, 122, 7865–7890. <https://doi.org/10.1002/2017JA023884>
- Zhang, M., Qin, G., & Rassoul, H. (2009). Propagation of solar energetic particles in three-dimensional interplanetary magnetic fields. *The Astrophysical Journal*, 692, 109–132. <https://doi.org/10.1088/0004-637X/692/1/109>
- Žic, T., Vršnak, B., & Temmer, M. (2015). Heliospheric propagation of coronal mass ejections: Drag-based model fitting. *The Astrophysical Journal Supplement Series*, 218(2), 32.

CASE STUDY: FIRST CME SEEN AT SOLAR ORBITER

Together with the NASA Parker Solar Probe (PSP) launched in August 2018, the ESA Solar Orbiter (SolO) mission ushers in a new era of solar and heliospheric physics. For the first time since the 1970s, these spacecraft will approach the Sun significantly closer than the orbit of Mercury — PSP has already set a new record with less than 0.1 AU solar distance at its most recent perihelion in September 2020. On the other hand, SolO, which was launched in February 2020, will come very close to the Sun as well (~ 0.28 AU), although it will stay far enough away to also allow for imaging observations through holes in its heatshield. In the extended mission phase, it is planned to incline the orbit of SolO to also observe the poles of the Sun directly for the first time.

As part of the Energetic Particle Detector (EPD) suite on SolO (Rodríguez-Pacheco et al., 2020), the High Energy Telescope (HET, Section 2.2) has been successfully commissioned and is providing some first measurements of high-energy charged particles. While a few solar energetic particle (SEP) events in the first 10 months of the mission did extend to the energies covered by HET ($\gtrsim 6$ MeV/nuc ions and > 450 keV electrons), HET spent most of the time observing the galactic cosmic ray (GCR) background, as the solar activity was quite low during this time. As discussed in Section 2.2, HET is also able to resolve short-term variations of GCRs with some of its data products. Consequently, some Forbush decreases (FDs) could be measured, which were caused by coronal mass ejections (CMEs) and corotating interaction regions (CIRs) that passed SolO during its first orbit.

The first CME-induced FD seen at SolO on April 19, 2020 is especially interesting, as it is a multispacecraft event that was also observed near Earth one day later during a close longitudinal alignment and with a radial separation of 0.2 AU. Measurements of the FD near Earth have been taken by neutron monitors as well as the Cosmic Ray Telescope for the Effects of Radiation (CRaTER) onboard the Lunar Reconnaissance Orbiter (LRO). The CME was also seen at the BepiColombo spacecraft that was still close to Earth at this time, and may also have hit Venus, though no observations are available at this location due to the loss of contact with the Venus Express spacecraft since 2014. Furthermore, STEREO-A was in an excellent position to provide a side view of the CME with its remote sensing instruments. In the following publication, which was submitted to *Astronomy & Astrophysics* in November 2020, we describe the capabilities of HET, present the FD observed at SolO and the corresponding observations near Earth, and investigate the radial evolution of the CME by applying ForbMod (see Section 1.4) to this event. Two other studies of the same event, have also been submitted to *A&A*: Davies et al. (2021) focus on the magnetic field observations, while O’Kane et al. (2021) investigate the solar source of the CME. All three papers will be published in the *A&A* “Solar Orbiter First Results” special issue in 2021.

In the process of this study, a new software implementation of the graduated cylindrical shell (GCS) model (Thernisien, 2011) has been developed. Details about this tool can be found in [Appendix B](#).

The following article is reproduced from Freiherr von Forstner et al. (2021) with permission from Astronomy & Astrophysics, ©ESO:

RADIAL EVOLUTION OF THE APRIL 2020 STEALTH CORONAL MASS EJECTION BETWEEN 0.8 AND 1 AU: A COMPARISON OF FORBUSH DECREASES AT SOLAR ORBITER AND EARTH

Freiherr von Forstner, J. L., M. Dumbović, C. Möstl, J. Guo, A. Papaioannou, R. Elftmann, Z. Xu, J. C. Terasa, A. Kollhoff, R. F. Wimmer-Schweingruber, J. Rodríguez-Pacheco, A. J. Weiss, J. Hinterreiter, T. Amerstorfer, M. Bauer, A. V. Belov, M. A. Abunina, T. Horbury, E. E. Davies, H. O'Brien, R. C. Allen, G. B. Andrews, L. Berger, S. Boden, I. Cernuda Cangas, S. Eldrum, F. Espinosa Lara, R. Gómez-Herrero, J. R. Hayes, G. C. Ho, S. R. Kulkarni, W. J. Lees, C. Martín, G. M. Mason, D. Pacheco, M. Prieto Mateo, A. Ravanbakhsh, O. Rodríguez Polo, S. Sánchez Prieto, C. E. Schlemm, H. Seifert, K. Tyagi, and M. Yedla, *A&A* (2021), DOI: [10.1051/0004-6361/202039848](https://doi.org/10.1051/0004-6361/202039848)

Own contribution: 80%

Radial evolution of the April 2020 stealth coronal mass ejection between 0.8 and 1 AU

Comparison of Forbush decreases at Solar Orbiter and near the Earth

Johan L. Freiherr von Forstner¹, Mateja Dumbović², Christian Möstl³, Jingnan Guo^{4,5,1}, Athanasios Papaioannou⁶, Robert Elftmann¹, Zigong Xu¹, Jan Christoph Terasa¹, Alexander Kollhoff¹, Robert F. Wimmer-Schweingruber¹, Javier Rodríguez-Pacheco⁷, Andreas J. Weiss³, Jürgen Hinterreiter³, Tanja Amerstorfer³, Maike Bauer³, Anatoly V. Belov⁸, Maria A. Abunina⁸, Timothy Horbury⁹, Emma E. Davies⁹, Helen O'Brien⁹, Robert C. Allen¹⁰, G. Bruce Andrews¹⁰, Lars Berger¹, Sebastian Boden^{1,11}, Ignacio Cernuda Cangas⁷, Sandra Eldrum¹, Francisco Espinosa Lara⁷, Raúl Gómez Herrero⁷, John R. Hayes¹⁰, George C. Ho¹⁰, Shrinivasrao R. Kulkarni^{1,12}, W. Jeffrey Lees¹⁰, César Martín^{1,13}, Glenn M. Mason¹⁰, Daniel Pacheco¹, Manuel Prieto Mateo⁷, Ali Ravanbakhsh^{1,14}, Oscar Rodríguez Polo⁷, Sebastián Sánchez Prieto⁷, Charles E. Schlemm¹⁰, Helmut Seifert¹⁰, Kush Tyagi¹⁵, and Mahesh Yedla^{1,14}

(Affiliations can be found after the references)

March 4, 2021

ABSTRACT

Aims. We present observations of the first coronal mass ejection (CME) observed by the Solar Orbiter spacecraft on April 19, 2020 and the associated Forbush decrease (FD) measured by the High Energy Telescope (HET). This CME is a multi-spacecraft event that was also seen near Earth the following day.

Methods. We highlight the capabilities of the HET for observing small short-term variations of the galactic cosmic ray count rate using its single detector counters. We applied the analytical ForbMod model to the FD measurements to reproduce the Forbush decrease at both locations. Input parameters for the model were derived from both in situ and remote-sensing observations of the CME.

Results. The very slow (~ 350 km/s) stealth CME caused an FD with an amplitude of 3% in the low-energy cosmic ray measurements at HET and 2% in a comparable channel of the Cosmic Ray Telescope for the Effects of Radiation (CRaTER) on board the Lunar Reconnaissance Orbiter, as well as a 1% decrease in neutron monitor measurements. Significant differences are observed in the expansion behavior of the CME at different locations, which may be related to influence of the following high speed solar wind stream. Under certain assumptions, ForbMod is able to reproduce the observed FDs in low-energy cosmic ray measurements from HET as well as CRaTER, however, with the same input parameters, the results do not agree with the FD amplitudes at higher energies measured by neutron monitors on Earth. We study these discrepancies and provide possible explanations.

Conclusions. This study highlights the notion that the novel measurements of Solar Orbiter can be coordinated with observations from other spacecraft to improve our understanding of space weather in the inner heliosphere. Multi-spacecraft observations combined with data-based modeling are also essential for understanding the propagation and evolution of CMEs, in addition to their space weather impacts.

Key words. Sun: coronal mass ejections (CMEs) - Sun: heliosphere - cosmic rays

1. Introduction

On April 19, 2020, a coronal mass ejection (CME) passed Solar Orbiter (SolO, Müller et al. 2020) spacecraft, making it the first large-scale flux rope CME seen in situ at SolO. At this time, the spacecraft was closely aligned in heliospheric longitude with Earth (less than 4° separation) and it was located at a radial distance of 0.8 AU from the Sun, as shown in Fig. 1. Consequently, the same slow CME ($v < 400$ km/s) was also observed near Earth the next day, causing the first geomagnetic storm of the year with a Dst index of -59 nT and Kp index of 5. During the event, SolO was still in its Near Earth Commissioning Phase (NECP), which ended on June 15, 2020; nevertheless, some of the in situ instruments, including the Energetic Particle Detector suite (EPD, Rodríguez-Pacheco et al. 2020) and the magnetometer (MAG, Horbury et al. 2020) were already taking continuous measurements and were able to observe signatures of the CME. In addition, the STEREO-A spacecraft had a sufficient longitudinal separation of $\sim 75^\circ$ from SolO and the Earth, thus, making it

capable of providing excellent remote sensing observations of the CME propagation from a side view. This event was observed from both SolO and the Earth, providing an excellent example for the coordinated science that is possible with SolO and other heliophysics missions in the Solar System.

Clouds of magnetized plasma ejected from the Sun, known as CMEs, are one of the key phenomena in space weather research, as they can cause severe geomagnetic storms (Kilpua et al. 2017) that disrupt the terrestrial infrastructure. The shocks driven by CMEs are also partly responsible for energetic particles in the heliosphere (Reames 2013), which may pose radiation danger to astronauts and spacecraft. Consequently, two of the four main scientific questions of the Solar Orbiter mission (Müller et al. 2013) are also linked to the goal of attaining a better understanding of CMEs.

Forbush decreases (FDs), first observed by and later named after Scott E. Forbush (1937), are short-term decreases of the galactic cosmic ray (GCR) flux, caused by the passage of mag-

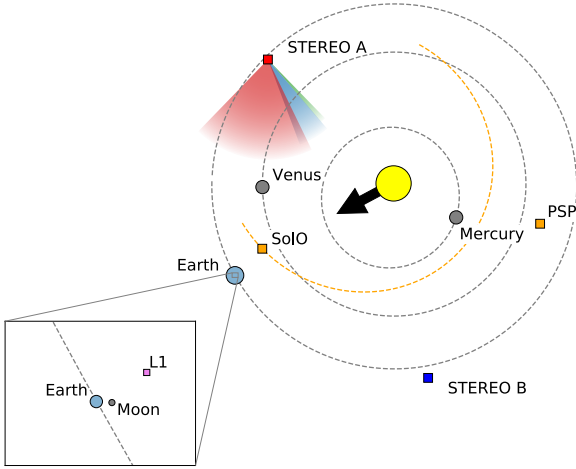


Fig. 1. Locations of planets and spacecraft in the inner solar system on April 20, 2020, the day the CME arrived in the vicinity of Earth. The trajectory of Solar Orbiter (SolO) is shown as an orange dashed line and PSP denotes the location of Parker Solar Probe. The large black arrow indicates the approximate propagation direction of the CME and the colored segments next to STEREO-A show the fields of view of the remote sensing instruments COR1/COR2 (green), HI1 (blue), and HI2 (red). The inset shows a zoomed-in view of the relative positions of Earth, the Moon, and the Lagrange point L1, where the Wind spacecraft is located.

netic field structures in the solar wind, such as CMEs or stream interaction regions (SIRs). Such magnetic structures can act as a barrier for the propagation of GCRs, as, for instance, the GCRs need to diffuse across a strong field, so that the observed flux is temporarily decreased at the locations where these structures pass. The decrease phase usually takes less than one day, followed by an often slower recovery to the previous level (on the order of one week). In the case of CMEs, FDs are driven by both the turbulent shock-sheath region (if present) as well as the following magnetic ejecta; these are two effects that can sometimes be clearly separated when a two-step decrease is observed (e.g., Cane 2000). The amplitude of an FD depends not only on the properties of the heliospheric structure, but also on the energy of the observed GCR particles: lower energy particles are modulated more easily and thus tend to show larger FDs (e.g., Lockwood 1971; Lockwood et al. 1991; Cane 2000; Guo et al. 2020). In the past, the study of FDs was mainly based on data from neutron monitors on the surface of the Earth, but nowadays, GCR measurements suitable for FD studies are also available from many spacecraft in the near-Earth space as well as on other solar system bodies and these have been routinely used for multi-spacecraft studies (e.g., Cane et al. 1994; Lockwood et al. 1991; Freiherr von Forstner et al. 2018, 2019, 2020; Witasse et al. 2017; Winslow et al. 2018). In all cases, it is important to take into account the energy dependence of the FD amplitude, as such instruments may be sensitive to different GCR energies.

In this work, we present the EPD observations of the FD associated with the April 19 CME at SolO, as well as the corresponding observations at Earth. We describe which EPD data products are best suited to make measurements of FDs, and we analyze these data to see how the CME affected the GCR flux at different heliospheric locations and at different particle energies. We also employ the ForbMod model to reproduce the observed

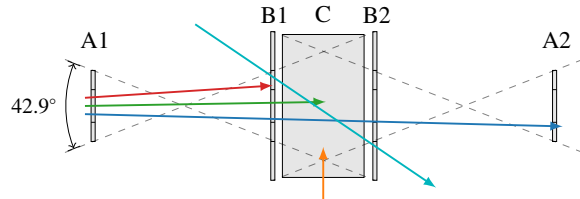


Fig. 2. Schematic diagram of the HET sensor head. Exemplary particle trajectories ending up in different data products are shown by the arrows: **stopping in B**, **stopping in C**, **penetrating**, GCR channel, **C single counter**. A 3D graphic of the sensor head is shown in Rodríguez-Pacheco et al. (2020, Fig. 31).

FD and gain insight into the how the large-scale evolution of the CME structure affected the properties of the FD. One study from Davies et al. (2021) complements this work by investigating the magnetic field measurements at both Solar Orbiter and Earth in more detail. In Sect. 2, we introduce the different instruments used as data sources in this study, followed by an overview of our modeling methods in Sect. 3. The measurement and modeling results are presented in Sect. 4 and then discussed in more detail in Sect. 5.

2. Data sources

2.1. HET on Solar Orbiter

As part of the EPD suite (Rodríguez-Pacheco et al. 2020) on board the Solar Orbiter mission (Müller et al. 2013; Müller et al. 2020), the High Energy Telescope (HET) is a particle telescope covering the high-energy end of the solar energetic particle (SEP) spectrum as well as galactic cosmic rays (GCR). Its two double-ended telescopes each consist of four thin 300 μm silicon solid-state detectors (named the A1, B1, B2, and A2 detectors) and the C detector, a 2 cm thick $\text{Bi}_4\text{Ge}_3\text{O}_{12}$ (BGO) scintillator, in the center. This detector layout is shown in Fig. 2. The C detector is read out using two photodiodes placed on either side, named C1 and C2. HET is designed to measure the fluxes of electrons above 300 keV, protons above 7 MeV, as well as heavier ions, with one telescope (HET1) providing the sunward and anti-sunward viewing directions (parallel to the mean Parker spiral angle); and with the other telescope (HET2) being mounted perpendicular to HET1 in order to measure particles coming from outside the ecliptic plane. The telescopes distinguish between particles stopping in one of the B detectors (B1 or B2, e.g., red arrow in Fig. 2), particles stopping in the C (green arrow) detector, and particles penetrating the whole telescope (blue arrow) to achieve a large energy coverage; in addition, they use the dE/dx - E -method to separate different particle species. This technique has been applied in many earlier space-borne charged particle detectors, including the Interplanetary Monitoring Platform-1 mission in the 1960s (McDonald & Ludwig 1964) as well as more recent instruments, such as the Mars Science Laboratory Radiation Assessment Detector (Hassler et al. 2012) and the Chang'E 4 Lunar Lander Neutrons and Dosimetry experiment (Wimmer-Schweingruber et al. 2020). For more details about the application of the dE/dx - E -method in HET, see Rodríguez-Pacheco et al. (2020, Sect. 7.2.5).

While the nominal data products of HET are optimized for the study of high intensity SEP events by choosing a rather small opening angle to achieve a high energy resolution, these data are not optimal for observing short-term variations of the GCR

background due to their low level of counting statistics. Alternatively, HET provides a separate “GCR channel” that observes penetrating particles with a larger opening angle by omitting the A detectors from the coincidence condition, namely, by counting all particles that penetrate B1, C, and B2 (e.g., teal arrow in Fig. 2). This leads to an almost 20-fold increase in the geometric factor compared to the nominal penetrating particle channel.

For applications requiring even higher counting statistics, it is also possible to use single detector count rates without any coincidence conditions, similar to the technique applied, for instance, by Richardson et al. (1996) for the IMP 8 and Helios E6 instruments and Kühl et al. (2015) for SOHO-EPHIN. In this case, GCR particles are measured from all directions (e.g., orange arrow in Fig. 2), but without any energy resolution or species separation. The HET C detectors are best suited for this purpose due to their large size and nearly isotropic shielding by the aluminum housing. For each HET telescope, four such counters are available, where each of the two photodiodes has a high-gain channel (C1H, C2H), with a deposited energy threshold of $E_{\text{th}} = 4$ MeV, and a low-gain channel (C1L, C2L), with $E_{\text{th}} = 10$ MeV. As these C detector counters provide no directional information, the values from HET 1 and HET 2 and from the two photodiodes in each telescope can be simply summed up to achieve an even higher count rate, that is, approximately 270 counts/s for the high-gain channels (C1H + C2H \times 2 units) or 230 counts/s for the low-gain channels (C1L + C2L \times 2 units). We note that summing up the counts of the two photodiodes does not remove events that were detected in both photodiodes at the same time as such a counter of all valid events in the C detector is not available in the HET data products and could only be approximated using the pulse height analysis data.

To investigate the response of the HET C counters to an isotropic flux of incoming GCR particles, we performed a simulation using Geant4 (Agostinelli et al. 2003), version 10.1.2, with the physics list QGSP_BERT. The simulated geometry included a detailed model of the EPT-HET sensor head and the corresponding electronics box, so that the shielding by the instrument housing and electronics box, as well as the generation of secondary particles, are taken into account. A simplified model of the Solar Orbiter spacecraft was also optionally included in the simulation setup to consider the influence of the spacecraft body on the incoming particle flux. This may be important for the C detector counters, as they are sensitive to particles entering HET from any direction. The spacecraft was modeled as a cuboid with the size of the main body (2.20 m \times 1.81 m \times 1.46 m) and total mass of 1700 kg (which corresponds to the launch mass of Solar Orbiter, excluding its solar panels). Its composition was assumed to be 200 kg of hydrazine fuel, 750 kg of aluminum representing the structural components of the spacecraft, and 750 kg of a printed circuit board (PCB)-like material, as defined by Appel et al. (2018) and Appel (2018, Table 6.2) representing the electronics components of the spacecraft and its payload. The development of a more detailed Geant4 model of the spacecraft body based on CAD models of its components is in progress, but was not possible within the time constraints of this study and is not expected to change the results significantly. Only protons between 5 MeV and 100 GeV were used as input particles to reduce the complexity of the simulation setup, as protons comprise 90 % of primary GCR particles (Simpson 1983).

The proton response function resulting from the simulation is shown in Fig. 3 (upper panel). Four curves are shown, corresponding to the simulation setup with and without the spacecraft model, and for the different threshold energies of the high- and low-gain channels. It becomes clear that the low-energy cutoff

is mainly influenced by the threshold energy: 12 MeV for the high-gain channel and 16 MeV for the low-gain channel. After the cutoff follows a narrow plateau corresponding to particles entering C through the nominal field of view (i.e., through the A and B detectors), followed by an increase related to particles entering from the sides through the HET housing. The spacecraft body provides additional shielding ($\sim 20\%$) for the detector in the lower energy part, but generates additional secondary particles above a primary proton energy of 1 GeV — up to a 2.5-fold increase in the geometric factor for 100 GeV particles. On the other hand, without the spacecraft body, the geometric factor for high energies stays approximately constant above 1 GeV, at $G = (128 \pm 2)$ cm² sr for $E_{\text{th}} = 4$ MeV and $G = (106 \pm 2)$ cm² sr for $E_{\text{th}} = 10$ MeV. As the GCR proton flux typically peaks at or below 1 GeV and decreases again for higher energies, the differences caused by the spacecraft body only exert a minor influence on the observed count rates. By folding the response function for $E_{\text{th}} = 4$ MeV with a typical GCR spectrum at solar minimum ($\Phi = 270$ MV) and integrating over the primary energy, we obtained count rates of 48/s without the spacecraft model and 53/s with the spacecraft model, an increase on the order of 10 %. This is only about 80 % of the typically observed count rate (270/s, divided among four channels), as only protons were simulated. We note that the effect of the spacecraft body may be larger for heavier ions, as they fragment more in the spacecraft and may thus contribute more to the response function with the generated secondaries.

2.2. CRaTER on LRO

The Cosmic Ray Telescope for the Effects of Radiation (CRaTER, Spence et al. 2010) is an instrument on the Lunar Reconnaissance Orbiter (LRO) mission measuring the radiation dose and linear energy transfer (LET) spectra in lunar orbit. CRaTER consists of three pairs of thin (140 μ m) and thick (1000 μ m) silicon detectors, D1 through D6, separated by sections of tissue-equivalent plastic serving as an absorber. The D1 end of the telescope is pointed towards the zenith, while the D6 end points towards the surface of the Moon. Similarly to HET, CRaTER uses multiple coincidence conditions between its detectors to measure particles of different energies. For example, the lowest energy particles are detected using the coincidence of D1 and D2 (the uppermost two detectors), with a minimum energy of 12.7 MeV required for protons to penetrate D1 and reach into D2 according to Spence et al. (2010). This value of 12.7 MeV is also the minimum energy for protons to be detected in any CRaTER detector, as D1 has a higher energy deposit threshold, so that it rejects most protons and many helium ions.

The CRaTER Level 2 secondary science data, available through NASA PDS¹ and on the CRaTER web site², provide single counters for each of the six detectors, similar to the HET counters described in Sect. 2.1, as well as additional counters for “rejected events”, “good events”, and “total events”, where a good event is any valid event where an incoming particle triggered at least one detector.

This means that there are two different counters in the CRaTER data (D2 and good events) measuring protons with energies ≥ 12.7 MeV, while the threshold is higher for all other counters. The good events counter was already used by Sohn et al. (2019b,a) to study Forbush decreases and energetic particle events, and it has the best counting statistics (on the order of

¹ <https://pds-ppi.igpp.ucla.edu/>

² <http://crater-web.sr.unh.edu/>

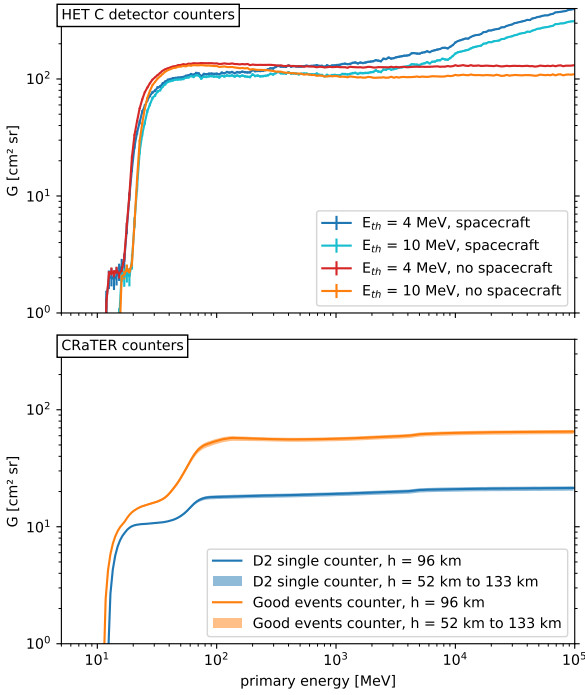


Fig. 3. Response functions (i.e. energy-dependent geometric factors) of the SoLo HET and LRO CRaTER detectors employed to measure FDs in this study. *Upper panel:* HET C detector single counters. The four lines correspond to four different scenarios depending on the threshold applied for the available counters. The derivation of the response function using a Geant4 simulation is described in Sect. 2.1. *Lower panel:* D2 detector single counter (blue) and *good events* counter (orange) of CRaTER. Lines show the response for the mean altitude of CRaTER during the event, while shaded areas mark the range of responses for the maximum and minimum altitudes. These response functions were derived by Looper et al. (2013) and are described in Sect. 2.2.

$\sim 66/\text{s}$ at the time of the event studied here). However, while the threshold is well defined, the response function of the good events counter is slightly more complex, as it includes multiple detectors with different shielding conditions and measures a higher amount of secondary particles coming from the lunar surface (the so-called albedo) than D2 alone. Looper et al. (2013, Appendix A) derived the response functions of the single detector count rates using a Geant4 (Agostinelli et al. 2003) simulation. The response functions of the D2 detector single counter as well as the good events counter are plotted in Fig. 3 (lower panel). Similarly to the HET response function in the upper panel, steps in the response function occur when different parts of the telescope are penetrated by particles.

In addition to the count rate files, we used the ancillary data of the LRO to exclude time periods where the spacecraft is not in its nominal orientation, for instance, due to orbit adjustment maneuvers. Any data where the LRO is more than 1° away from the nominal orientation, with CRaTER’s D2 detector pointing towards the zenith, is excluded to make sure that the measured count rates are not affected by these activities. This exclusion only affects few data points, as the LRO pointing is usually very precise to support its imaging instruments.

As the LRO orbit is elliptical and relatively close to the lunar surface (between 54 km and 132 km above the surface in the

time period studied in this work), the Moon takes up a significant portion of the sky as viewed from CRaTER. Thus, the Moon shields CRaTER from part of the incoming GCR, but also produces albedo particles. This means that the count rate of particles measured using a single-detector counter (i.e., in a 4π solid angle field of view) periodically varies with the current altitude, which is also shown in the altitude-dependent response functions in Fig. 3 (lower panel). The plotted altitudes are slightly different from the actual values (± 2 km) due to the limited altitude resolution of the simulation, but this only makes a small difference. The orbital period of the LRO is about 110 minutes, which determines the frequency of this periodic signal. Multiple methods have been developed to correct for this effect, such as the dose correction factor given by Schwadron et al. (2012) based on geometrical calculation of the covered solid angle, or the Fourier series method introduced by Winslow et al. (2018). In this study, we apply a simple empirical method in which we create a scatter plot of the time-dependent CRaTER count rate $c(t)$ versus the LRO altitude $h(t)$ for the time period of interest, apply a linear regression, and use the obtained slope m to calculate the corrected count rate

$$c_{\text{corrected}}(t) = c(t) - m \cdot (h(t) - \bar{h}), \quad (1)$$

where \bar{h} denotes the mean altitude of the LRO during the time period investigated, which is 93 km for the event studied in this work. In this case, we found this method to work about as well as the Fourier series method in suppressing the periodic signal and better than the simple geometrical calculation, which does not take into account the albedo particles generated by the Moon. However, short- or long-term variations of the GCR spectrum, which influence the ratio between the counts of primary GCR and albedo particles, and thus the necessary correction factor, are not accounted for by any of these methods and can still cause the periodic component to appear in the corrected signal, albeit with a much lower amplitude. Due to these difficulties with the altitude correction, we additionally always plot orbit-averaged values of the CRaTER data.

2.3. Neutron monitor observations and the global survey method

As stated above, neutron monitors have historically been the most important data source for the study of GCR variations in general and FDs in particular. The global network of neutron monitors, whose data are available from the Neutron Monitor Database (NMDB)³, provides continuous measurements from many locations around the globe. In contrast to deep space measurements, neutron monitors have an inherent cutoff energy (often given in terms of rigidity) determined by the Earth’s magnetosphere and atmosphere, which depends on the latitude as well as the altitude of the neutron monitor. At the poles, the influence of the magnetosphere decreases to zero (see e.g., Smart & Shea 2008), leading to a cutoff rigidity of 0.1 GV at the location of the South Pole neutron monitor, which would correspond to a proton energy of ~ 5 MeV. At these locations, the atmospheric cutoff dominates and results in a cutoff energy of about 450 MeV for protons Clem & Dorman (2000), that is, a factor of ~ 20 – 30 larger than in the abovementioned response functions of HET and CRaTER. This causes Forbush decreases observed by neutron monitors to usually be smaller in amplitude than in deep space observations.

³ <http://www.nmdb.eu>

A method that takes into account simultaneous ground-level observations of cosmic rays by neutron monitors at different locations to calculate the main characteristics of cosmic-ray variations outside of the atmosphere and magnetosphere of Earth has long been proposed (see Krymsky 1964; Krymsky et al. 1966; Belov et al. 1973, 1974; Dorman 2009) and is still used nowadays (e.g., Papaioannou et al. 2019, 2020; Abunina et al. 2020). This technique is called the global survey method (GSM). The GSM separates the isotropic part of the variations of cosmic rays from the anisotropic part and uses spherical harmonics to express their respective amplitudes. In the following, A_0 is used for the amplitude of the isotropic variations; A_x , A_y , and A_z are the corresponding amplitudes of the first harmonic (higher orders are not considered). Here, A_x and A_y denote the equatorial components of the anisotropy, with x pointing away from the Sun and y perpendicular to that, while z is the north-south component. However, in order to achieve this, first the atmospheric and instrumental response functions, which couple the primary particles at the top of the atmosphere to the secondaries recorded by neutron monitors on the ground, and a backmapping of cosmic ray particles traveling under the influence of Earth's magnetic field are applied. The historical development, scientific argumentation, and mathematical formulation of the GSM can be found in the recent comprehensive report of Belov et al. (2018). The GSM incorporates a power-law dependence on the rigidity for the isotropic part of the CR variations (i.e., A_0) and thus can provide outputs for a set of fixed rigidities (see e.g., Figure 2 in Belov 2000). However, a fixed rigidity of 10 GV (corresponding to a proton energy of 9.1 GeV) has typically been used for more than 65 years (e.g., Belov 2000; Belov et al. 2015, 2018; Papaioannou et al. 2020; Abunina et al. 2020). This value is more illustrative on the actual GCR modulation and is close to the effective rigidity of NMs to detect GCRs (see e.g., Asvestari et al. 2017; Koldobskiy et al. 2018), implying that a NM is mostly responsive to the variability of mid-rigidity CRs from several GV to several tens of GV in rigidity.

3. ForbMod

ForbMod (Dumbović et al. 2018) is an analytical physics-based model to describe Forbush decreases caused by flux rope CMEs. Its calculations are based on the self-similar expansion of a flux rope, which is modeled as a (locally) cylindrical structure with an initial radius, a_0 , close to the Sun that initially contains no GCRs at its center. While the flux rope propagates away from the Sun, it expands self-similarly: Both the increase in the flux rope radius a and the decrease in the central magnetic field magnitude B_c are assumed to follow power law expressions with the so-called expansion factors n_a and n_B used as power law indices:

$$a(t) = a_0 \left(\frac{R(t)}{R_0} \right)^{n_a}, \quad B_c(t) = B_0 \left(\frac{R(t)}{R_0} \right)^{-n_B}, \quad (2)$$

where $R(t)$ describes the radial distance of the flux rope from the Sun, R_0 the initial distance at time $t = 0$, and B_0 the initial central magnetic field. As stated by Dumbović et al. (2018), previous observational studies (Bothmer & Schwenn 1998; Leitner et al. 2007; Démoulin et al. 2008; Gulisano et al. 2012) constrained the power law indices to $0.45 < n_a < 1.14$ and $0.88 < n_B < 1.89$. During the expansion and radial propagation of the CME, the GCRs gradually diffuse into the flux rope slower than in the surrounding solar wind, so that the GCR phase space density within the flux rope is decreased while it passes by an observer.

ForbMod then describes the GCR phase space density within the flux rope using the following main equations, which are derived in detail by Dumbović et al. (2018):

$$U(r, t) = U_0 \left(1 - J_0 \left(\alpha_1 \frac{r(t)}{a(t)} \right) e^{-\alpha_1^2 f(t)} \right), \quad f(t) = \frac{D_0}{a_0^2} \left(\frac{v}{R_0} \right)^x \frac{t^{x+1}}{x+1}, \quad (3)$$

where U_0 is the GCR phase space density outside the flux rope, J_0 is the Bessel function of the first kind and order zero, α_1 is a constant corresponding to the first positive root of J_0 , r is the radial distance of the observer from the flux rope center (which may be time-dependent, hence $r(t)$), D_0 is the initial diffusion coefficient, and v is the CME propagation speed. The function $f(t)$ describes the GCR diffusion into the flux rope, where the diffusion time is equivalent to the propagation time t since the initial condition ($t = 0$) near the Sun. It is assumed that v is constant and that the diffusion coefficient D is inversely proportional to the central magnetic field, $D \propto 1/B_c$, so that $D(t)$ follows a power law with the index n_B (c.f. Eq. 2). This power law relation was already inserted to obtain the expression for $f(t)$ given in Equation 3. Additionally, the ambient GCR phase space density, U_0 , is assumed to be constant to simplify the calculation; the known radial gradient the GCR flux of about 3%/AU (Webber & Lockwood 1999; Gieseler & Heber 2016; Lawrence et al. 2016) is not taken into account. The expansion type

$$x = n_B - 2n_a \neq -1 \quad (4)$$

describes the expansion behavior of the CME, and in particular its magnetic flux. $x = 0$ corresponds to a conservation of magnetic flux (as the product of the flux rope cross section and the central magnetic field stays constant), while $x > 0$ describes a decrease in the flux with heliospheric distance and $x < 0$ an increasing flux. $x = -1$ is a special case, which requires a different functional form of $f(t)$ in Equation 3 (for details, see Dumbović et al. 2018). The influence of the value of x on the ForbMod result can be understood as the interplay between the expansion and diffusion effects – when the diffusion (which depends on the magnetic field, and thus, n_B) is very efficient, the flux rope is quickly filled with GCR particles, but a fast increase in the flux rope size (large n_a) can counteract this effect by increasing the space that needs to be filled with GCRs.

In addition to its dependence on the magnetic field, the GCR diffusion coefficient D also depends on the particle energy. For instance, higher energy particles diffuse into the flux rope more easily and thus show a shallower FD. While the original model of Dumbović et al. (2018) describes only the FD profile of one specific GCR energy, for which D_0 needs to be provided, Dumbović et al. (2020) extended the model with empirical functions for the energy dependence of the diffusion coefficient, so that the FD profile can be calculated for any GCR energy. By folding the resulting spectrum with the response function of a particle detector, it is then possible to simulate the measurement of the FD by this detector. In this version of ForbMod, the input GCR spectrum and the energy dependence of the diffusion coefficient D are needed as input parameters for the model. As described by Dumbović et al. (2020, Appendix B), the modified force-field approximation described by Gieseler et al. (2017) is used to calculate the GCR spectrum based on the values of the solar modulation potential Φ obtained from neutron monitor data by Usoskin et al. (2011) and from ACE/CRIS data by Gieseler et al. (2017). For our event in April 2020, near the minimum between Solar Cycles 24 and 25, the corresponding measurements of Φ

are not yet available, so we use the values from similar conditions for the previous solar cycle in June 2009. The values from Usoskin et al. (2011) are derived based on data from the Oulu neutron monitor; as its count rates between April 2020 and June 2009 are comparable, this supports our assumption that the solar modulation conditions are very similar. The energy-dependent diffusion coefficient is calculated using the empirical formula given by Potgieter (2013), with parameters derived by Potgieter et al. (2014) for the period 2006–2009 from PAMELA data and by Corti et al. (2019) for the period 2011–2017 from AMS-02 measurements. In this case, data for 2020 are not yet available either, so we use the values from 2009 with comparable solar cycle conditions. More detailed explanations about these parameters are given by Dumbović et al. (2020, Appendix A).

To convert the $U(r, t)$ dependence in Equation 3 into a function that purely depends on the time, t , and can thus directly be compared to in situ GCR measurements, the observer location, r , with respect to the flux rope center, needs to be defined. For this, we can use the in situ measured velocity profile $v_{\text{in situ}}(t)$ of the flux rope, namely, the observer passes through the flux rope at this measured velocity:

$$r(t) = |a(t) - v_{\text{in situ}}(t) \cdot (t - t_{\text{CME}})|, \quad (5)$$

where t_{CME} is the in situ arrival time of the CME. The conversion of $U(r)$ into $U(t)$ introduces some asymmetry into the FD profile, as the in situ measured velocity profile $v_{\text{in situ}}(t)$ is typically not constant. We note that ForbMod only models the GCR modulation due to a flux rope CME, not the additional influence of a shock-sheath region, although it may be combined with other models to take this into account (see e.g., Dumbović et al. 2020; Freiherr von Forstner et al. 2020).

4. Results

4.1. In situ observations

The April 19 CME was observed at Solar Orbiter using its magnetometer, showing a clear signature of a flux rope with a south-east-north field rotation and a maximum field intensity of $B_{\text{max}} = 21.2$ nT, a preceding shock with a jump of about 3 nT in magnetic field intensity, and a turbulent sheath region in between (see the upper panel in Fig. 4, and see Davies et al. (2021) for further discussion of the MAG data). The shock arrival time was 05:06 UTC on April 19, 2020, the flux rope arrived at 08:58 UTC on the same day and ended at 01:11 UTC on April 20. MAG data from April 21 (i.e., one day after the end of the CME flux rope) are not displayed here because spacecraft commissioning activities affected the sensor temperatures on that day. Solar wind plasma measurements from the Solar Wind Analyzer instrument on SolO (SWA, Owen et al. 2020) are not available for this event, as it was not yet fully commissioned. EPD measured the fluxes of suprathermal ions slightly above solar wind energies (5.3 keV to 85 keV, i.e., 1000 km/s to 4000 km/s) using the SupraThermal Electrons and Protons (STEP) instrument. As shown in the second panel of Fig. 4, STEP sees a clear enhancement of suprathermal ions accelerated in the sheath region, and this is also confirmed by EPD's Electron Proton Telescope (EPT, not shown here), which saw enhancements of ions up to 100 keV. No significant enhancements of energetic electrons were observed in EPT or STEP.

The flux rope is followed by a separate structure with enhanced levels of magnetic turbulence. In comparison with the solar wind plasma observations near Earth (see Fig. 5 and its description later in this section), where clear increases in solar wind

speed and temperature are observed, we identified this to be a stream interaction region (SIR), followed by a stream of high-speed solar wind. We determined the onset times of the three SIR structures, the forward shock (F), stream interface (I), and reverse shock (R) at SolO by searching for shock signatures in the magnetic field data that are similar to those seen at Wind, although the identification is less reliable than at Earth due to the missing SWA data. In addition, STEP and EPT see another enhancement of energetic ions close to the stream interface.

However, the main focus of this study is the signature in the high energy particles, where a clear Forbush decrease with a drop amplitude of around 3 % in both the GCR channel as well as the C detector counters is observed (bottom panels of Fig. 4). The C counter is plotted in ten-minute time averages, with an additional curve showing a smoothed version of these data (rolling mean) and the GCR channel is shown in a similar fashion with a one-hour cadence. Due to the higher count rate, the FD is especially well observed in the C counters. The main part of the decrease occurs during the passage of the flux rope — the decrease within the sheath region is well below 1 %. This means that the assumption of the ForbMod model (Sect. 3) that only the flux rope effect is taken into account is fulfilled. A second GCR decrease is observed after the CME, coinciding with the passage of the SIR.

Figure 5 shows the in situ measurements of the CME arrival near Earth, including solar wind magnetic field and plasma data from the Magnetic Field Investigation (MFI, Lepping et al. 1995) and the Solar Wind Experiment (SWE, Ogilvie et al. 1995) on board the Wind spacecraft, as well as GCR measurements from the South Pole neutron monitor (SoPo), the GSM outputs and the CRaTER D2 counter. The measured speed of the CME at Wind is very slow, with a maximum of 370 km/s. The Wind and CRaTER measurements were shifted forward in time taking into account the radial distance to Earth (1 h 7 min for Wind at L1, and 15 min for CRaTER at the Moon; cf. inset in Fig. 1). These time shifts were calculated using the abovementioned maximum speed of 370 km/s, which is seen at the front of the CME flux rope. Considering this time shift, the shock arrival time at Earth is 02:40 UTC on April 20, and the flux rope arrived a few hours later at 09:01 UTC. In comparison to Solar Orbiter, the magnetic field strength of the flux rope has decreased to a maximum of $B_{\text{max}} = 16.2$ nT, while the sheath region still has field intensities similar to the SolO measurement around 6 nT. Apart from the lower intensity, the magnetic field signatures of the flux rope look very similar to those observed at Solar Orbiter, showing the same south-east-north orientation. The large negative out-of-ecliptic component (B_Z , or B_N) seen at the beginning of the flux rope is a feature which is typically associated with high geoeffectiveness (e.g., Gopalswamy 2008). The sheath duration increased by more than two hours (~ 60 %), which is probably related to the accumulation of additional solar wind plasma in front of the CME as well as expansion due to the increasing velocity profile of the sheath region (see e.g., Manchester et al. 2005; Siscoe & Odstrčil 2008; Janvier et al. 2019; Freiherr von Forstner et al. 2020), while the expansion of the flux rope is more moderate at a bit over one hour (~ 8 %). The transit times from Solar Orbiter to L1 correspond to an average transit speed of 363 km/s for the flux rope front, which matches the in situ measured front speed of 370 km/s very well.

As mentioned earlier in this section, the SIR following the CME is clearly seen in the in situ data at Wind, showing signatures such as the increases in temperature and velocity as well as a decrease in density. According to these signatures, the time of the forward shock (F), stream interface (I), and reverse shock

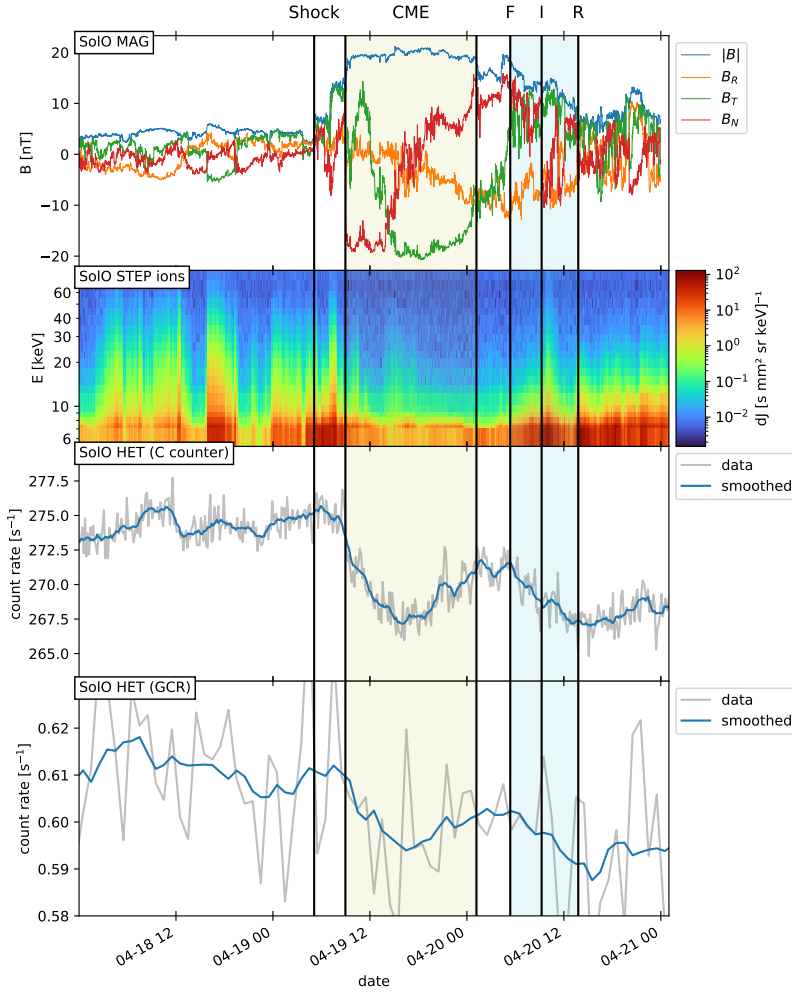


Fig. 4. Measurements from MAG, STEP, and HET on Solar Orbiter, showing the magnetic structure of the CME, suprathermal particle signatures, and the associated FD observations in the GCR channel and the C detector counter of HET. The MAG measurements are displayed in radial (R), tangential (T) and normal (N) coordinates. Black vertical lines and shaded regions mark the time periods corresponding to different events: Shock arrival, CME (flux rope) start and end, as well as forward shock (F), stream interface (I), and reverse shock (R) of the SIR.

(R) were marked in Fig. 5. Even though the solar wind plasma data are not available at Solar Orbiter for this event (as described above), it is clear from the magnetic field measurements that the SIR followed closely behind the CME at both locations, separated by a region of high plasma density (seen in the Wind measurements). Assuming an average solar wind speed within the SIR of approximately 400 km/s, the separation of the Parker spiral footprints of SoLo and Earth is 16.7° , corresponding to an expected SIR delay time of 27.2 hours. The measured delay varies between 24.9 hours for the forward shock, 27.7 hours for the stream interface, and 31.4 hours for the reverse shock, suggesting that the SIR has significantly expanded in both directions. This means that the SIR may have affected the evolution of the CME, for example, by compressing it from behind. We will discuss this further in Sect. 5.

Comparing the GCR measurements at SoPo and CRaTER, as well as the outputs of GSM, when utilizing measurements of ~ 35 neutron monitors, it can be seen that the relative amplitudes of the FD profiles induced by the CME at SoPo and from GSM are quite similar, whereas both are quite different compared to CRaTER. As discussed in Sect. 2.2, CRaTER covers a similar energy range as the HET C counter at SoLo, while neutron monitors have a larger cutoff energy. The South Pole neutron mon-

itor has much higher counting statistics than CRaTER, but the FD there only reaches an amplitude of 1.2%, as higher energy particles are modulated less by the CME's magnetic field. This is also true for the outputs of GSM that reach an amplitude of 1.1%. The minimum of the FD appears to fall within the magnetic cloud (MC), and as at SoLo, the MC seems to be the main driver of the FD in comparison to the shock-sheath structure, during which only a small decrease is observed. On the other hand, the FD at CRaTER has an amplitude of 2.0%. The FD onset at CRaTER appears to be slightly earlier than the arrival of the flux rope, but the difference is only less than one orbital period of CRaTER, so this may also be an artifact of the altitude correction (cf. Sect. 2.2). The slightly enhanced periodic variations of the CRaTER signal seen close to the minimum of the FD are also a sign that the altitude correction is not completely suppressing the periodic signal due to the modulated GCR spectrum.

Figure 6 presents the density variations of cosmic rays at Earth obtained from GSM: A_0 (in %), together with the components of the anisotropy A_{xy} (equatorial components) and A_z (polar component). The characteristics of the cosmic ray anisotropy that signify the effect of a MC on GCRs are summarized as follows: (a) the amplitude of A_{xy} is higher within the MC, reaching

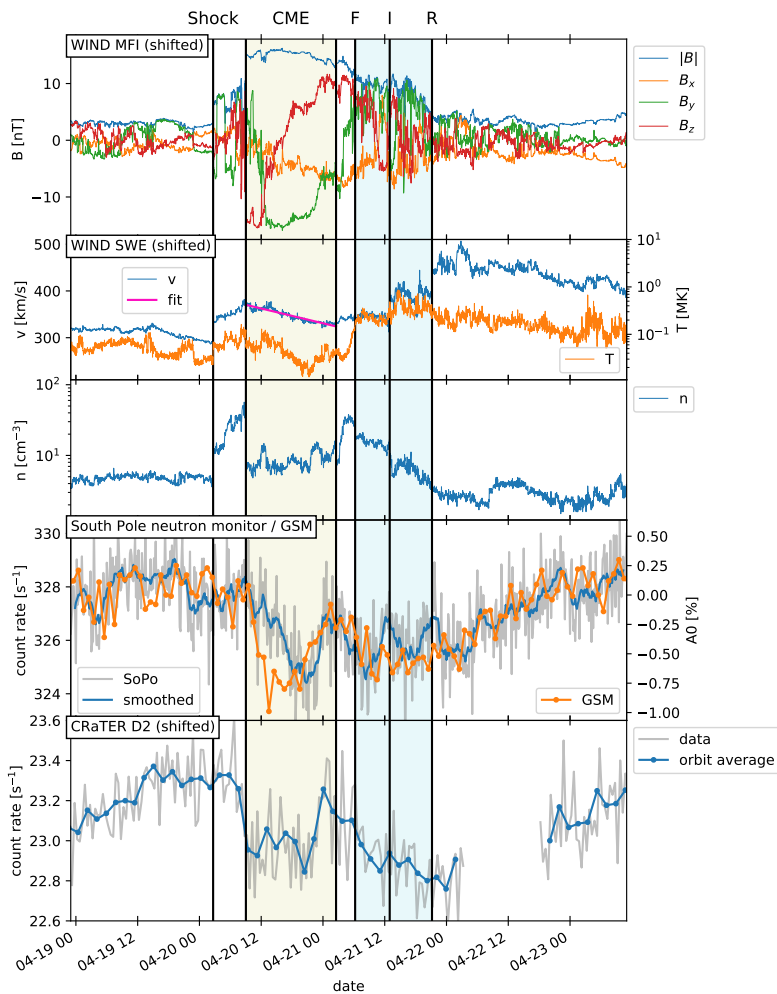


Fig. 5. Measurements near Earth from MFI and SWE on Wind and neutron monitors on Earth as well as the CRaTER D2 counter, showing the in situ signatures of the CME and the associated FD, as well as a high speed stream following afterwards. Wind data were shifted forward in time by 1 hour and 7 minutes to account for the expected transit time between the L1 Lagrange point and Earth, and CRaTER data were shifted by 15 minutes, corresponding to the Moon–Earth radial distance. Black vertical lines and shaded regions mark the time periods corresponding to different events: shock arrival, CME start and end, as well as forward shock (F), stream interface (I), and reverse shock (R) of the SIR. Wind MFI measurements are given in Heliocentric Earth Ecliptic (HEE) coordinates, with X pointing from the Sun to Earth and Z being perpendicular to the ecliptic pointing north, and Y completing the right handed triad. The general orientation of HEE is thus comparable to RTN, which is used for SoLo data in Fig. 4, and the difference to RTN is small. A linear fit to the velocity profile of the flux rope, which is used to determine the expansion speed as explained by Gulisano et al. (2012), is shown in pink. The second panel from the bottom shows both measurements from the south pole neutron monitor (gray, blue) and the GCR density variation at 10 GV (corresponding to 9.1 GeV proton energy) obtained from GSM.

a maximum of $\sim 1\%$ coinciding with the minimum of the FD; (b) the direction of the anisotropy vector (i.e., orange part of the vector diagram) changes abruptly when entering the MC (Belov et al. 2015); (c) there is a rotation of the A_{xy} vector within the MC; and (d) the north-south component A_z changes by 1.1% during the FD, including a reversal of direction during the decay phase of the FD (Abunin et al. 2013; Belov et al. 2015). The CME parameters calculated from the in situ data at Solar Orbiter and near Earth, as well as the onset times of the SIR structures are summarized in Table 1.

Figure 7 (also available as an online animation) shows the results from an application of the semi-empirical 3DCORE model (Möstl et al. 2018; Weiss et al. 2020), based on the SoLo MAG observations of the flux rope. This model provides a global context for the flux rope structure, propagation, and orientation at Solar Orbiter and Wind. Further applications of this model and its results are described in more detail by Davies et al. (2021), whereas here we show a few main results relevant for our study. In order to reconstruct the magnetic field configuration and its 3D structure, the 3DCORE model ensembles were fitted to an interval of the MAG data with a clean magnetic field rotation; here, we have a run that represents a best fit which covers an interval from Apr 19 11:13 UTC to Apr 20 01:59 UTC. This

interval starts about 2 hours later than the start of the flux rope interval stated above at 08:58 UT as the B_T component is positive for a short while after 09:00 UT, which is inconsistent with its unipolar excursion to $B_T < 0$ later. This first feature in B_T cannot be fitted with the 3DCORE flux rope model, and thus we choose to narrow the fitting interval to what Davies et al. (2021) call the “unperturbed” inner part of the flux rope.

The 3DCORE technique consists of a Gold-Hoyle uniform twist magnetic field in an elliptical flux rope cross section placed in a 3D toroidal shape (Weiss et al. 2020). Here, we set the cross section aspect ratio, otherwise a free parameter to be determined from the fitting analysis, to a value of 2.0, which is consistent with the angular width of the CME void in Heliospheric Imager observations (Davies et al. 2021). In Fig. 7a-c, a 3D visualization of the 3DCORE envelope is presented from several viewpoints at the time of the Forbush decrease onset at Earth. Fig. 7d demonstrates the ability of the model to fit the Solar Orbiter observations. In Fig. 7e, we propagated the model to the Wind spacecraft self-similarly, where the power law exponents for the expansion of the diameter and magnetic field (as defined in Equation 2) were set to previously empirically derived values of $n_a = 1.14$ and $n_B = 1.64$, respectively. Those values are based on a power law fit of the mean total magnetic field of a large sample of in

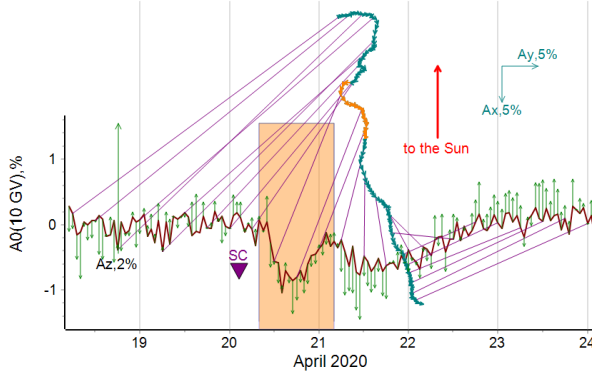


Fig. 6. GCR density variation A_0 at Earth obtained from GSM at a fixed rigidity of 10 GV (brown line, corresponding to 9.1 GeV proton energy), together with the first harmonic of the cosmic ray anisotropy. The equatorial component A_{xy} of the anisotropy is displayed as a vector diagram (teal and orange triangles), which are connected to the corresponding points in time on the A_0 plot with magenta lines. Additionally, the north-south component A_z is shown as green vertical arrows on top of A_0 time profile. The shaded rectangle and the orange part of the vector diagram correspond to the duration of the magnetic cloud (MC). The shock arrival at Earth is indicated by the arrow labeled SC (“sudden storm commencement”), and the direction to the Sun in the vector diagram is indicated with a red arrow. The components of the anisotropy A_x and A_y that define the plane for the calculation of A_{xy} are indicated on the top right corner of the figure. Numbers at each anisotropy component on the figure indicate the scale used for the plotting of the relevant arrows.

situ measured CME flux ropes in the inner heliosphere (Leitner et al. 2007).

The 3DCORE torus propagates according to a drag-based model (see details in Weiss et al. 2020). The results show that the modeled magnetic field components are consistent at Solar Orbiter and Wind at L1, but as seen in Fig. 7e, there is a time shift between the model and the observations of the flux rope magnetic field at Wind (concerning all components and the total field). This points to a slight inconsistency of the Solar Orbiter fit results when they are propagated to L1, which most likely arises from the shape and direction of the 3DCORE torus being determined with data from a single spacecraft, and it is expected that due to the model assumptions this does not exactly reproduce the observations at another spacecraft. This inconsistency can be alleviated with simultaneously fitting 3DCORE to Solar Orbiter and Wind in situ magnetic field data, but this is the subject of future studies.

In Fig. 7, we show a model which uses parameters representative of the best fit, but the fitting algorithm that we use (Weiss et al. 2020) allows us to derive distributions for each of the flux rope parameters. The main results from the Solar Orbiter 3DCORE fit (with the results stated as means \pm standard deviations) are as follows: the CME is directed at $(13 \pm 5)^\circ$ longitude (HEEQ) and $(-5 \pm 5)^\circ$ latitude, which means that it has a close to central impact at Solar Orbiter and Wind and the observations at the two spacecraft are clearly connected. The orientation of the axis is $(11 \pm 13)^\circ$ to the solar equatorial plane, thus, it is a low inclination flux rope. At the heliocentric distance of Wind (0.995 AU), the axial magnetic field strength in the model is (14.3 ± 0.9) nT, and the model flux rope has a diameter of (0.114 ± 0.022) AU. For Solar Orbiter at 0.809 AU, this axial field is (20.1 ± 1.2) nT and the diameter is (0.090 ± 0.017) AU.

Table 1. CME and SIR parameters derived from the in situ measurements at Solar Orbiter and near Earth.

	Solar Orbiter	near Earth
Radial distance		
R [AU]	0.809	0.995 ^a / 1.005 ^b
CME and SIR onset times		
t_{shock} [UTC]	2020-04-19 05:06	2020-04-20 02:40
t_{CME} [UTC]	2020-04-19 08:58	2020-04-20 09:01
$t_{\text{CME end}}$ [UTC]	2020-04-20 01:11	2020-04-21 02:32
$t_{\text{forward shock}}$ [UTC]	2020-04-20 05:22 ^c	2020-04-21 06:15
$t_{\text{stream interface}}$ [UTC]	2020-04-20 09:15 ^c	2020-04-21 12:58
$t_{\text{reverse shock}}$ [UTC]	2020-04-20 13:47 ^c	2020-04-21 21:11
Duration		
Δt_{sheath} [h]	3.9	6.4
Δt_{CME} [h]	16.2	17.5
In situ parameters		
B_{max} [nT]	21.2	16.2
\bar{v}_{CME} [km/s]	—	347
v_{exp} [km/s]	—	46
A_{FD} [%]	2.9	2.0

Notes. Listed Forbush decrease amplitudes A_{FD} correspond to the HET C counter at Solar Orbiter and the CRaTER D2 counter near Earth.

^(a) L1 ^(b) Earth ^(c) Due to the missing plasma data, SIR onset times are less certain at SolO.

As explained by Démoulin & Dasso (2009) and Gulisano et al. (2012), the measured velocity profile of the flux rope can be used to estimate the expansion factor, n_a , which describes the increase in the flux rope radius a with the radial distance from the Sun (see definition in Sect. 3). From a linear fit, we calculate the expansion speed v_{exp} , which is the velocity difference between the front and rear end of the flux rope, to be 46 km/s, and together with the mean speed of $\bar{v}_{\text{CME}} = 347$ km/s, we calculate:

$$n_{a,\text{in situ @ Wind}} = \frac{v_{\text{exp}}}{\Delta t_{\text{CME}}} \frac{R}{\bar{v}_{\text{CME}}^2} = 0.90, \quad (6)$$

where R is the radial distance of Wind at this time (see Eq. 1).

It is also possible to calculate a value of n_a for the propagation between SolO and Wind, using the two in situ measurements:

$$n_{a,\text{SolO-Wind}} = \log \left(\frac{\Delta t_{\text{CME, Wind}}}{\Delta t_{\text{CME, SolO}}} \right) / \log \left(\frac{R_{\text{Wind}}}{R_{\text{SolO}}} \right) = 0.37, \quad (7)$$

and, similarly, we can derive the expansion factor n_B for the magnetic field magnitude between SolO and Wind:

$$n_{B,\text{SolO-Wind}} = -\log \left(\frac{B_{\text{max, Wind}}}{B_{\text{max, SolO}}} \right) / \log \left(\frac{R_{\text{Wind}}}{R_{\text{SolO}}} \right) = 1.30, \quad (8)$$

The values for both $n_{B,\text{SolO-Wind}}$ and $n_{a,\text{in situ @ Wind}}$ are within the typical ranges found in previous observational studies, as described in Sect. 3. The value of $n_{a,\text{SolO-Wind}}$ is unusually low and quite different from the in situ measurement. This could be interpreted as a sudden change in the expansion rate of the CME, but may also be related to the difference of the inherent assumptions in the two methods; for example, the local determination of the expansion factor at Wind (Eq. 6) assumes a quasi-undisturbed

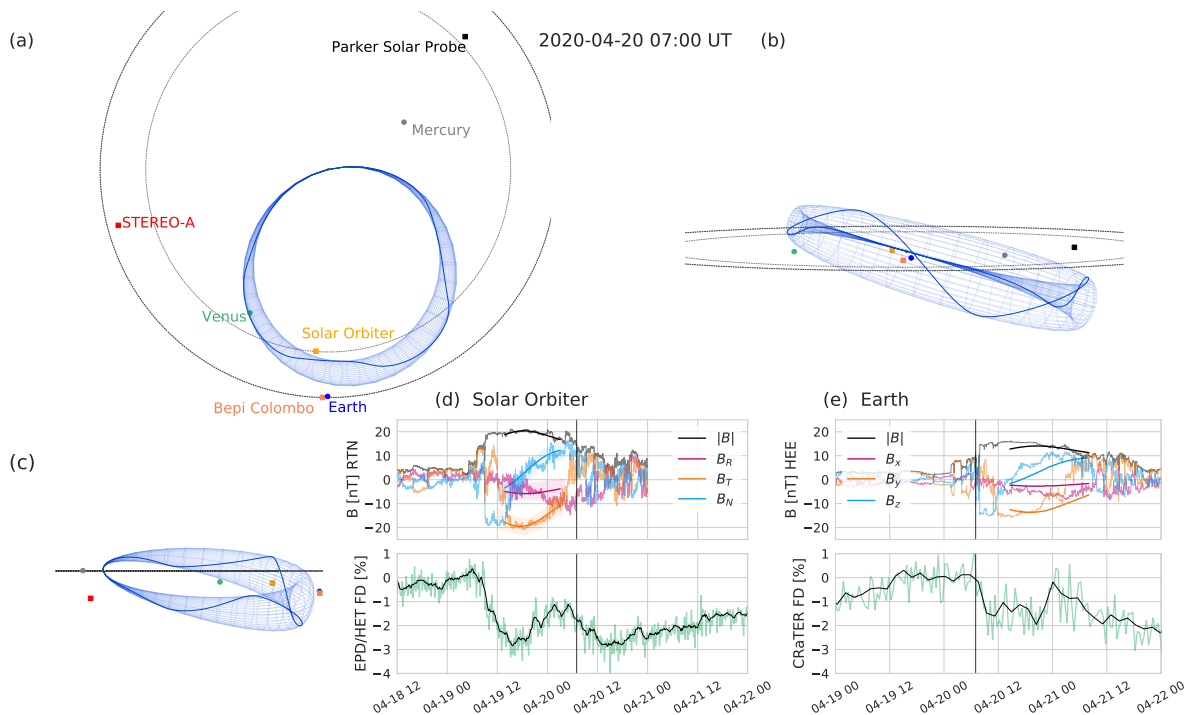


Fig. 7. Visualization of the results of the 3DCORE flux rope model fitted to the Solar Orbiter MAG observations, shown at the time of the onset of the Forbush decrease at Earth. The reconstructed 3D flux rope structure is shown: (a) looking down from the solar north pole onto the solar equatorial plane, (b) in a frontal view along the Sun–Earth line, and (c) in a side view at a 75 degree angle, the longitude of STEREO–A to Earth. A flux rope field line is highlighted as a solid blue line. The panels (d) and (e) show the in situ magnetic field data from Solar Orbiter and Wind at Earth/L1 compared to the GCR variation as a percentage drop in the amplitude measured by EPD/HET and CRATER. The Wind magnetic field components are given here in Heliocentric Earth Ecliptic (HEE) coordinates, as in Fig. 5. The 3DCORE modeled magnetic field is overlaid in panel (d) and propagated to Earth as shown in (e). An animation of this figure is available as an **online movie**.

expansion of the CME following the current velocity profile within the flux rope, while external influences are not taken into account. In contrast, the observation of a SIR that follows closely behind the CME (as described above) suggests that there may have been some interaction between the two structures that may have affected the expansion. This is discussed in more detail in Sects. 4.3 and 5. We also note that the derived values of n_a and n_B are both lower than the fixed values assumed in the 3DCORE model, but this is partly due to the fact that the 3DCORE modeling excludes the first part of the flux rope duration (as explained above). Also, as stated above, a more detailed 3DCORE analysis fitting the CME structure simultaneously at both locations will be explored in future studies.

4.2. Remote sensing observations

Due to its 75° longitudinal separation from Solar Orbiter and Earth at the time (cf. Fig. 1), the STEREO-A spacecraft has provided excellent remote-sensing observations of this CME event. Figure 8 shows observations from the Sun Earth Connection Coronal and Heliospheric Investigation suite on board STEREO-A (SECCHI, Howard et al. 2008), namely, the COR2 white-light coronagraph, as well as from the Heliospheric Imagers (HI). The COR2 image shows two CMEs launched from the Sun in close succession on April 14–15 2020. The CME visible on the right side of the COR2 image, which first appears at approximately 19:30 UTC on April 14 and then slowly moves outward, is the

one that headed towards SoIo and Earth, while the larger CME on the left side is backside from the Earth point of view.

To reconstruct the CME shape near the Sun, we applied the Graduated Cylindrical Shell model (GCS, Thernisien et al. 2006; Thernisien 2011) to the STEREO-A/COR2 and SOHO/LASCO C2, and C3 (Brueckner et al. 1995) coronagraph images, which allows us to derive such parameters as latitude and longitude as well as the flux rope height and radius. In the course of this study, we developed a new implementation of the GCS model in Python⁴ and verified its results against the existing SolarSoft IDL version. During the reconstruction process, it became apparent that the structure seen on the east limb from SOHO/LASCO C3 cannot belong to the Earth-directed CME. To fit the GCS geometry to this structure, it would have been necessary to shift the CME longitude by more than 30° away from Earth or increase the flux rope height significantly, which contradicts the position of the clear flux rope structure observed at STEREO-A/COR2 and the in situ observation at Earth and Solar Orbiter. Considering this, we suspect that this signature is instead caused by the backside CME and we verified this assumption by also approximately fitting the backside CME with the GCS model (as plotted in orange in Fig. 8). The Earth-directed CME is not clearly seen in the LASCO C3 images, but it shows a weak signature in C2 on the northwestern limb. This structure was used in conjunction with the clear observations in the STEREO-A COR2 data to reconstruct the CME (plotted in blue in Fig. 8). The GCS results

⁴ https://github.com/johan12345/gcs_python,
<https://doi.org/10.5281/zenodo.4443203>

show that the two CMEs partly overlap in the SOHO/LASCO observations due to the line of sight effect, which is probably the reason why the Earth-directed CME is only seen from SOHO on the west limb. The fit parameters for both CMEs are listed in Table 2, where the uncertainties were derived by performing the GCS fit for the Earth-directed CME 40 times and then calculating the mean and standard deviation of each parameter. This was not done for the back-sided CME as its parameters are not needed for the further analysis in this study. The GCS fit results for the latitude, longitude, and tilt angle are also approximately consistent with the data derived from the 3DCORE reconstruction based on the in situ data (see Sect. 4.1, although these are, of course, also associated with some uncertainties. We note that the 40 GCS fits of the Earth-directed CME were performed by a single person, which may decrease the uncertainties compared to a result produced using independent reconstructions from different scientists. Still, care was taken to sample a large range of possible values for each parameter and adjust the remaining parameters accordingly to fit the coronagraph images. Additionally, the data were compared to a single independent GCS reconstruction by another researcher and the results agree within the given uncertainty ranges.

There is also no obvious signature of the CME in the low corona (low coronal signatures, LCS), as observed with the SDO/AIA (Lemen et al. 2012) 211 Å extreme ultraviolet (EUV) images, making it a challenge to identify the CME source region. A weak brightening is observed at approximately 2°N 8°E, but this is too far away from the GCS-reconstructed CME longitude of (18 ± 7)°W. Thus, the CME can be considered as a type of “stealth CME” (see e.g., Howard & Harrison 2013, and references therein) both due to the weak LCS and the lack of a clear halo CME in the coronagraphs from the Earth point of view. Stealth CMEs have weak LCS because only a relatively small amount of energy is released from the corona at their onset due to their low speed (typically < 300 km/s according to Ma et al. (2010) and these signatures may be too weak to be detected with the established observational and data processing techniques (e.g., Alzate & Morgan 2017). A more detailed study of the source region of this CME will be performed by O’Kane et al. (2021, in preparation for *A&A*).

As a result of the GCS fit, we derived the initial height of the flux rope $R_0 = (9.64 \pm 0.40) R_\odot$ and the initial radius at the apex $a_0 = (1.93 \pm 0.15) R_\odot$, calculated using the equation from Thernisien (2011). These parameters will be needed for the application of the ForbMod model in Sect. 4.3.

Based on the GCS results, we can make a new calculation for the expansion factor n_a : The calculation in Equation 6 corresponds to the instantaneous expansion of the flux rope near 1 AU, which may not be the same as closer to the Sun. The average expansion factor between the Sun and Earth can be calculated by comparing the initial flux rope size a_0 with the one measured in situ at Wind:

$$n_{a,\text{Sun-Wind}} = \log\left(\frac{a_{\text{Wind}}}{a_0}\right) / \log\left(\frac{R_{\text{Wind}}}{R_0}\right) = 0.70, \quad (9)$$

where R_{Wind} is the radial distance of the Wind spacecraft from the Sun and $a_{\text{Wind}} = \Delta t_{\text{CME}} \cdot \bar{v}_{\text{CME}}/2 = 15.7 R_\odot$ is the flux rope radius calculated from the in situ data (see Table 1). A similar value of $n_a = 0.69$ can be calculated from the SolO measurements, when assuming the CME speed to be the same as at Wind.

STEREO-A HI observations clearly show the CME signature out to elongation angles of approximately 35° (corresponding to a radial distance of ~0.6 AU), as seen in the running dif-

Table 2. Results from the graduated cylindrical shell (GCS) model.

	CME 1 ^a	CME 2 ^b
HEEQ Longitude [°]	18 ± 7	229
HEEQ Latitude [°]	3 ± 3	-1
Tilt angle [°]	18 ± 6	6
Half angle [°]	35 ± 11	15
Height [R_\odot]	9.5 ± 0.8	14.73
Ratio κ	0.23 ± 0.04	0.30
FR radius at apex [R_\odot]	1.8 ± 0.3	3.78

Notes. A GCS fitting was applied in the 2020-04-15 05:39:00 UTC image from STEREO-A COR2 and the 2020-04-15 05:36:07 UTC image from SOHO/LASCO C2. Results are plotted in Fig. 8. Error bars are given only for CME 1, as CME 2 is not further studied here.

^(a) Directed towards SolO and Earth ^(b) Back-sided as seen from SolO/Earth

ference images and the time-elongation map (Fig. 8, bottom panels). This event is cataloged by the HELCATS project⁵ under the ID HCME_A_20200415_01. According to the self-similar expansion fitting (SSEF) result (Davies et al. 2012) given in the HELCATS HIGeoCat catalog (Barnes et al. 2019), the CME direction in Heliocentric Earth Equatorial (HEEQ) coordinates is -6° in longitude and -2° in latitude. The longitude does not match what we determined in our GCS reconstruction (Table 2), but as the SSEF technique only uses data from a single spacecraft and makes certain assumptions about the CME, such as a constant speed and a fixed half-width of 30°, it is known to often produce large uncertainties for the CME longitude (see e.g., Barnes et al. 2019). The SSEF results can also be used to calculate the arrival time at Solar Orbiter and Earth, as described by Möstl et al. (2017). The calculated arrival times available from the ARRCAT v2.0⁶ are 2020-04-19 09:10 ± 3.2 h for SolO and 2020-04-20 09:45 ± 4.0 h for L1, which are both about eight hours later than the in situ shock arrival times. This is well within a usual range of arrival time errors with this method of ±17 hours. (Möstl et al. 2017). The arrival speed at Earth is predicted as (335 ± 11) km/s, which is also consistent with the in situ measured CME speed (mean speed $\bar{v} = 347$ km/s, see Table 1).

4.3. Application of the ForbMod model

In the previous sections (Sects. 4.1 and 4.2), we show how we derived all input parameters necessary for applying the ForbMod model to the Forbush decreases at Solar Orbiter and Earth. For the flux rope radius expansion factor, n_a , multiple values were calculated from measurements at different locations, with quite significant differences: $n_{a,\text{SolO-Wind}} = 0.37$, $n_{a,\text{in situ @ Wind}} = 0.90$, and $n_{a,\text{Sun-Wind}} = 0.70$. Additionally, we derived one value of the magnetic field expansion factor $n_{B,\text{SolO-Wind}} = 1.30$, based on the SolO and Wind in situ measurements of the magnetic field.

While n_B is also used separately to derive the radial dependence of the diffusion coefficient D , the key purpose of the two expansion factors within ForbMod is to calculate the so-called expansion type, a quantity defined as $x = n_B - 2n_a$ (see Eq. 4). Consequently, the model is very sensitive to the values of n_a and n_B . x describes the evolution of the magnetic flux and

⁵ <https://www.helcats-fp7.eu/>

⁶ <https://helioforecast.space/arrcat>,
<https://doi.org/10.6084/m9.figshare.12271292>

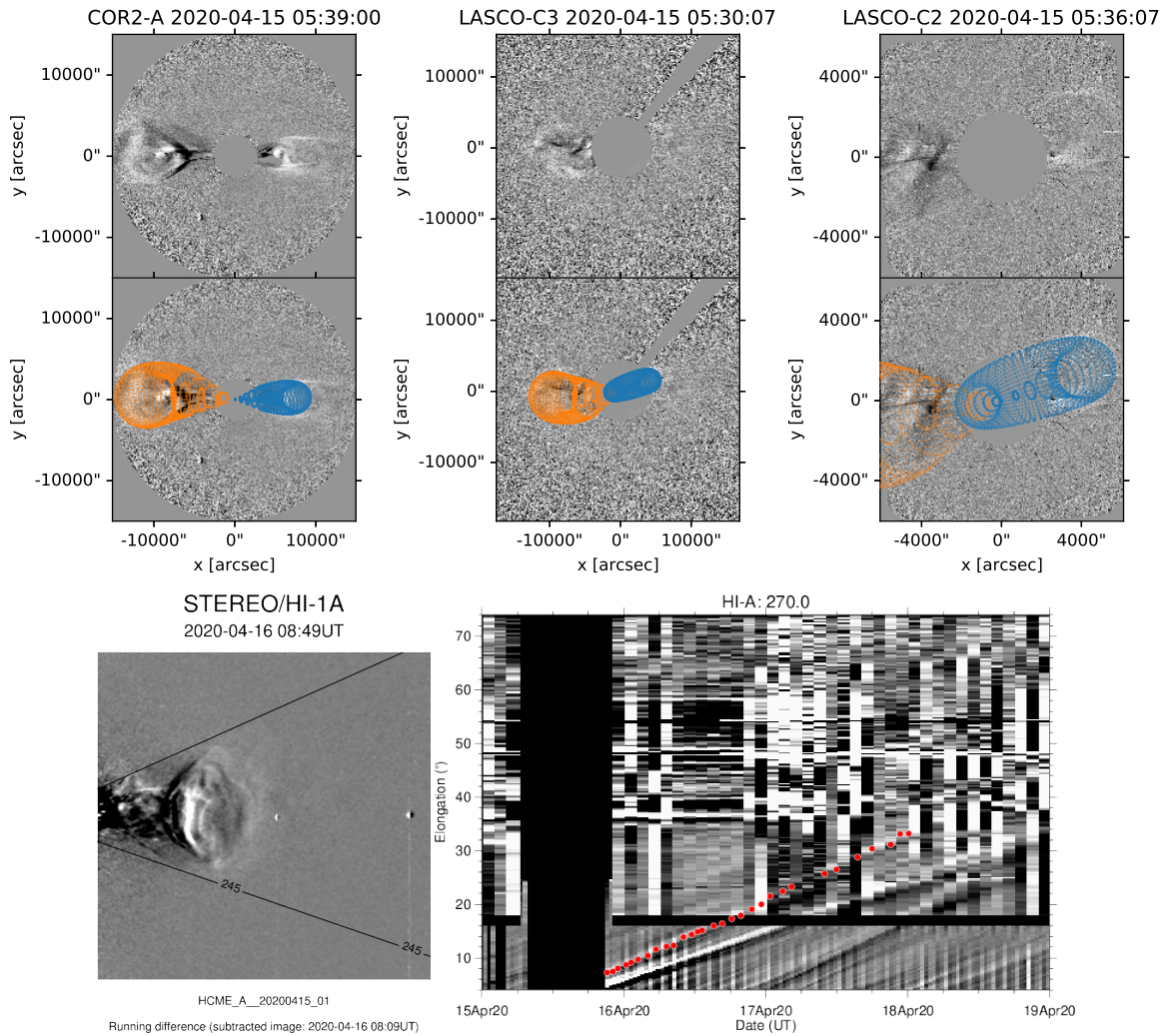


Fig. 8. Remote sensing observations of the CME. In the STEREO-A COR2 and SOHO LASCO C2 and C3 running difference images (top part), the GCS fitting was applied to derive the parameters R_0 and a_0 for the ForbMod model (see results in Table 2). The blue markings denote the Earth-directed CME we are investigating, while the CME fitted in orange is backsided and launched a few hours earlier. STEREO-A HI observations (bottom left) and time-elongation maps (bottom right) are provided by the HELCATS project.

is assumed to be constant over the course of the CME propagation, that is, the magnetic flux increases or decreases at the same rate. Thus, the inconsistency of the measured n_a values suggests that n_B must also have changed to keep x constant. So, we can derive $x = n_{B,\text{SolO-Wind}} - 2n_{a,\text{SolO-Wind}} = 0.55$, and then, under the assumption that $x = \text{const.}$, calculate a corresponding n_B for each of the measured n_a values. The results of this calculation are listed in Table 4. Of course, in the case of this event, $x = \text{const.}$ is a quite bold assumption to make considering the observed variation of n_a , but due to the lack of additional observations of n_B , there is no other way to derive the necessary input parameters from observations. We will discuss the possible implications of this in more detail in Sect. 5.

To summarize, we list all the parameters that are used for the application of ForbMod again in Table 3. We ran ForbMod for each of the n_a and n_B pairs that we calculated (Table 4), as well as for a “best fit” result reproducing the measured FD amplitudes at Solar Orbiter HET and CRaTER. Apart from the

response functions, transit times and radial distances, the ForbMod input parameters were always the same for both locations. It also must be noted that following the observed variation of n_a , the duration of the FD profile calculated with ForbMod was not derived from the $a(t)$ power law assumed by ForbMod (equation 2), but instead was fixed to the observed flux rope duration. The ForbMod best fit was obtained by calculating the FD amplitudes across the whole reasonable parameter space of n_a and n_B (while keeping all other parameters fixed) and then selecting the set of parameters that produced the lowest sum of squared residuals with respect to the two in situ measured amplitudes at HET and CRaTER (see Table 1).

The ForbMod results for the “best fit” parameters are shown in Fig. 9, where the time profile calculated using Equation 5 is plotted in red and the measurements in blue and gray (as previously shown in Figures 4 and 5). It can be seen that for these parameters, there is a good agreement between the model and observations: ForbMod aptly describes the relatively symmet-

Table 3. Input parameters for the ForbMod model

Parameter	Source	Section	Value
GCR spectrum	Force-field approximation, Gieseler et al. (2017)	3	Φ for June 2009
Diffusion coefficient D	Empirical function from Potgieter (2013) with parameters from Potgieter et al. (2014)	3	parameters for 2009
Detector response function	Geant4 simulation results	2.1, 2.2	See Fig. 3
Magnetic field B_c	B_{\max} in Wind data	4.1	$B_c = 16.2$ nT
expansion factors n_a, n_B	Calculation assuming $x = \text{const.}$ (Eq. 4) / best fit	4.3	see Table 4
Flux rope parameters R_0, a_0	GCS reconstruction	4.2	$R_0 = 9.64 R_\odot$, $a_0 = 1.93 R_\odot$
Diffusion time (\approx transit time)	In situ arrival time, Launch time: time of GCS fit	4.1, 4.2	$t_{\text{SolO}} = 99$ h, $t_{\text{Earth}} = 123$ h
Velocity profile	linear fit to in situ measurements at Wind	4.1	see Table 1

Table 4. Pairs of expansion factors n_a, n_B used for the ForbMod model, and resulting FD amplitudes at SolO HET, CRaTER and the South Pole neutron monitor.

Calculation	Sun → Wind	SolO → Wind	in situ @ Wind	best fit ^a
n_a	0.70	0.37	0.90	1.08
n_B	1.95 ^b	1.30	2.36 ^b	2.01
x^c	0.55	0.55	0.55	-0.15
$A_{\text{FD, SolO}} [\%]$	< 0.01	< 0.01	1.25	2.90
$A_{\text{FD, CRaTER}} [\%]$	< 0.01	< 0.01	0.50	2.00
$A_{\text{FD, SoPo}} [\%]$	< 0.01	< 0.01	0.03	0.44

Notes. Each column in the table corresponds to one set of input parameters n_a and n_B that was used with ForbMod. The modeled FD amplitude for the GSM data (10 GV) is < 0.01 % for all four sets of input parameters and not shown here.

^(a) Best fit was obtained by constraining the FD amplitudes at SolO and CRaTER. ^(b) These quantities were calculated assuming that $x = 0.55$ (see discussion in Sect. 4.3).

^(c) Calculated using Eq. 4.

ric Forbush decrease caused by the flux rope CME and reproduces the observed FD amplitudes. Of course, the second decrease caused by the SIR is not included in the model, which explains the obvious deviation of the measurements from the model after the flux rope passage. The effect of the spacecraft model included in the HET response function (see Sect. 2.1) is significant, applying ForbMod using the response function without the spacecraft would lead to a ~ 20 % larger FD (amplitude of 3.52 %, not shown here).

For the other parameters, n_a and n_B , derived from the observations, ForbMod results for the FD amplitude at SolO and CRaTER are shown in Table 4. With all these parameter sets, it can be seen that ForbMod underestimates the amplitude of the FD. The closest result is obtained using the in situ parameters

measured at Wind, but even in this case the modeled FD amplitude is less than half of the measurement. For the other sets of parameters, ForbMod predicts the flux rope to already be completely filled with GCRs by the time it reaches SolO and Earth, so that the FD amplitude is < 0.01 %.

In addition to SolO HET and CRaTER, we applied ForbMod at Earth with different response functions to model the FDs observed at the South Pole neutron monitor (SoPo) and in the GSM data. For the latter, we applied ForbMod monoenergetically at the fixed rigidity of 10 GV (corresponding to 9.1 GeV proton energy) that is used by GSM, while for the former we assume a constant response above a cutoff energy of 450 MeV (see Sect. 2.3). With these results, both the FDs at SoPo and GSM data are significantly underestimated, with a maximum amplitude of 0.44 % for SoPo and well below 0.01 % for GSM in all cases. To obtain the observed FD amplitude on the order of 1 % from the model, especially for the higher energy of GSM, the parameters n_a or n_B (or both) would need to be increased even more, which is not supported by observations or the previous observational constraints cited in Sect. 3.

5. Discussion and conclusions

In this study, we present in situ and remote sensing observations of the first flux rope CME that hit the Solar Orbiter spacecraft on April 19 and Earth on April 20, 2020. Furthermore, we study the Forbush decrease that it caused at both SolO and near Earth. This event is considered to be a “stealth CME” as it showed only weak signatures from the point of view of Earth in the EUV observations of the low corona. Remote sensing observations of this CME were only possible thanks to the ideal position of the STEREO-A spacecraft, which could track the CME from the outer corona until ~ 0.6 AU. At SolO and Earth, the CME was followed by a SIR, which is also clearly observed at both locations in the in situ magnetic field and cosmic ray signatures.

The largest FDs in terms of magnitude often require the presence and combined effect of the shock-sheath region and the following ejecta, both of which are necessary for deep GCR depressions (e.g., Papaioannou et al. 2020). Additionally, CMEs

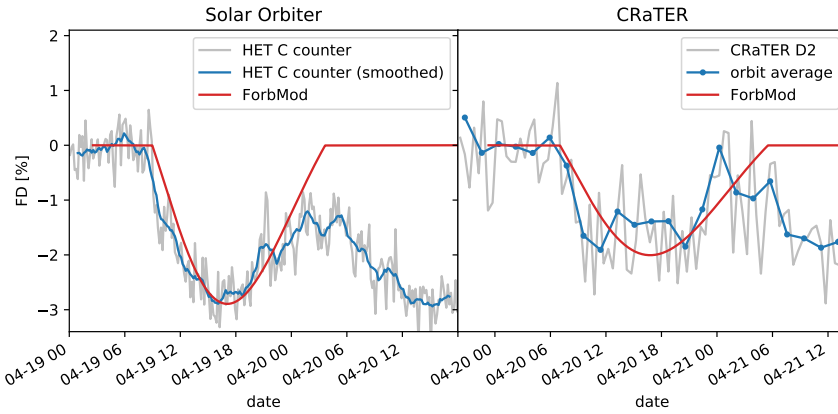


Fig. 9. ForbMod model results at Solar Orbiter and CRaTER, in comparison with the measured Forbush decreases at Solar Orbiter and CRaTER. The measurements are plotted in the same fashion as in Figures 4 and 5, but normalized to their pre-onset values to reflect the relative variation of the GCR count rate. Input parameters for ForbMod are listed in Tables 3 and 4. Also, n_a and n_B were used from the “best fit” result.

that are characterized as magnetic clouds (MCs) are more often associated with large FDs (Richardson & Cane 2011). However, although the CME studied in this work was associated with a shock and a clear MC observed at both SoLo and Earth, the resulting amplitude of the FD at Earth was relatively low, especially at higher GCR energies measured by neutron monitors and the GSM (only $\sim 1\%$). This may lead to the assumption that only the flank of the CME hit SoLo and Earth, but this is not supported by the in situ flux rope modeling in Sect. 4.1 and the remote sensing observations presented in Sect. 4.2. Instead, the slow propagation speed of the CME below 350 km/s led to a very weak shock and an extremely long propagation time of more than five days from the Sun to Earth, which made it possible for GCRs to diffuse into the MC and thus decrease the observed FD amplitude. This explanation relates well to the concept of the ForbMod model because the diffusion of GCRs into the flux rope over time is the basis for its calculations. Based on the timing of the FD, it seems that the shock only had a very weak effect on the GCR modulation, with the majority having been caused by the MC.

Using input parameters derived from the CME observations, we applied the ForbMod model to reproduce the FDs observed by the SoLo HET C detector counter and the LRO CRaTER D2 counter. The derivation for most of the parameters was relatively straightforward. Only the expansion factors n_a and n_B , which describe the evolution of the flux rope radius and its magnetic field (which the model is quite sensitive to) could not be unambiguously determined from observations, as they seem to vary significantly depending on where and how they are measured. In addition, while n_a could be measured for different locations, n_B could only be measured based on SoLo and Wind observations (i.e., there is no measurement of n_B from the Sun to Earth). One set of parameters, derived assuming that the expansion type x is constant and using the n_a value measured in situ near Earth, only produces an FD amplitude of 1.29% at SoLo compared to the measurement of $\sim 3\%$. A “best fit” set of parameters n_a and n_B , which closely reproduce the FD amplitudes measured at CRaTER and HET, was also calculated, with an even higher value of n_a , that is, a stronger expansion of the flux rope size not supported by the observations, and a lower value of x closer to zero corresponding to a conserved magnetic flux (see Dumbović et al. 2018). In this case, the faster expansion (larger n_a) counteracts the diffusion of GCRs into the flux rope, as described in Sect. 3, so that the FD amplitude becomes larger. However, even with the “best fit” parameter values, the higher-energy FD

measurements of the South Pole neutron monitor and the global survey method (GSM) could not be reproduced with ForbMod.

Using the observation of the flux rope evolution from SoLo to Earth in ForbMod yields FDs which do not agree with the observations. In addition, ForbMod best fit parameters yield global flux rope Sun-to-Earth evolutionary parameters, which are far from the values derived based on in situ measurement comparison between SoLo and Earth. This might indicate that Sun-to-Earth evolution of this CME was different from the SoLo-to-Earth evolution. A similar event, a slow stealth CME followed by a high speed stream was studied by He et al. (2018). The authors showed that the CME was compressed by the fast solar wind behind it, which caused an enhanced magnetic field and thus an unexpectedly high geoeffectiveness, and the same may have happened for this event. The inconsistent measured values of n_a , which correspond to a slower expansion of the flux rope between the Sun and 1 AU than suggested by the in situ measured velocity profile, can be a result of such a compression, thus indicating that the expansion behavior of this very slow CME may have changed during its propagation time. For instance, at some point during its propagation, the CME may have been slightly compressed by the SIR and expanded more freely at other times. Consequently, the assumption of ForbMod that the flux rope radius and its magnetic field follow power laws with constant indices n_a and n_B and that the resulting expansion type x , which describes the evolution of the magnetic flux, is also constant may not be valid in this more complex case. This may well be the reason why the model is not able to reproduce the higher energy FD measurements, even with a set of input parameters that fits the lower energy measurements of HET and CRaTER.

Another possible explanation for this discrepancy is that the energy dependence of the ForbMod-modeled FD amplitude may simply be overestimated for this event, resulting in too low FD amplitudes at higher energies. The reason for this, for example, could be that the empirical input parameters for the GCR spectrum and the energy dependence of the diffusion coefficient do not match the actual conditions at this time. This is an interesting result and should be investigated in more detail in future studies. For instance, a statistical validation of ForbMod against the results of the GSM, which has already been applied to a large catalog of FDs, may be helpful for examining whether this is a systematic problem in the description of the energy dependence for these higher GCR energies or whether this disagreement is a specific attribute of this CME event due to its low speed, very

long propagation time, and possible influence of the following SIR.

This study highlights the capabilities of the instruments on board the Solar Orbiter spacecraft, such as the high counting statistics of the HET C detector capable of detecting Forbush decreases. In addition, it shows that coordinated observations with Solar Orbiter and other spacecraft will be extremely important for the better understanding of space weather in the inner heliosphere. Spacecraft close to the Sun, such as Solar Orbiter and Parker Solar Probe, can serve as an upstream monitor to provide valuable information and early warning about CMEs. The CME in this case study also serves as an excellent example for a “stealth CME” that was still geoeffective due to its strong magnetic field even though it was not clearly seen in remote sensing observations from the point of view of Earth. This again highlights that the monitoring of Earth-directed CMEs requires in situ and remote sensing measurements at additional locations, for example, at Solar Orbiter and Parker Solar Probe as well as from STEREO-A or a future L5 mission. As the trajectory of Solar Orbiter moves closer to the Sun in the coming years and solar activity increases with the commencement of the Solar Cycle 25, space weather events during conjunctions with Earth as well as other spacecraft will become more probable, which will provide further exciting science opportunities.

Acknowledgements. J. v. F. thanks L. Seimetz and N. Lundt for their assistance in simulating the HET detector response functions. Additionally, we thank M. D. Looper and J. Wilson from the CRaTER team for providing the response functions of their instrument and helpful suggestions about the analysis of the CRaTER data. J. G. is supported by the Strategic Priority Program of the Chinese Academy of Sciences (Grant No. XDB41000000 and XDA15017300), the National Natural Science Foundation of China (Grant No. 42074222) and the CNSA pre-research Project on Civil Aerospace Technologies (Grant No. D020104). M. D. acknowledges support by the EU H2020 Grant Agreement 824135 (SOLARNET) and the Croatian Science Foundation under the Project 7549 (MSOC). A. P. acknowledges support by the TRACER project (<http://members.noa.gr/atpapaio/tracer/>) funded by the National Observatory of Athens (NOA) (Project ID: 5063) and from NASA/LWS project NNH19ZDA001N-LWS. M. A. and A. B. (IZMIRAN) are supported by the Russian Science Foundation under grant 20-72-10023. C. M., A. J. W., J. H., T. A. and M. B. thank the Austrian Science Fund (FWF): P31521-N27, P31659-N27, P31265-N27. This work, as well as the development of EPD on Solar Orbiter were supported by the German Federal Ministry for Economic Affairs and Energy, the German Space Agency (Deutsches Zentrum für Luft- und Raumfahrt e.V., DLR) under grants 50OT0901, 50OT1202, 50OT1702, and 50OT2002, by ESA under contract number SOL.ASTR.CON.00004, the University of Kiel and the Land Schleswig-Holstein, as well as by the Spanish Ministerio de Ciencia, Innovación y Universidades under grants FEDER/MCIU Agencia Estatal de Investigación/Projects ESP2105-68266-R and ESP2017-88436-R. The Solar Orbiter magnetometer was funded by the UK Space Agency (grant ST/T001062/1). Solar Orbiter EPD and MAG data are available in the Solar Orbiter Archive at <http://soar.esac.esa.int/soar/>. We acknowledge the NMDB database (<http://www.nmdb.eu>), funded under the European Union’s FP7 Programme (contract 213007), for providing data. The data from South Pole neutron monitor is provided by the University of Delaware with support from the U.S. National Science Foundation under grant ANT-0838839. LRO/CRaTER Level 2 data are archived in the NASA Planetary Data System’s Planetary Plasma Interactions Node at <https://pds-ppi.igpp.ucla.edu/> and also available through the CRaTER website at <https://crater-products.sr.unh.edu/data/inst/12/>. The Wind spacecraft solar wind and magnetic field data are provided on the Wind website at https://wind.nasa.gov/mfi_swe_plot.php. STEREO heliospheric imager observations and derived data are available on the HELCATS (<https://www.helcats-fp7.eu/>) and Helio4Cast (<https://helioforecast.space/arrcat>) websites. Graduated cylindrical shell reconstruction of CMEs was performed using version 0.2.0 of a new Python implementation of the GCS model (<https://doi.org/10.5281/zenodo.4443203>) available at https://github.com/johan12345/gcs_python, which is based on version 2.0.3 (<https://doi.org/10.5281/zenodo.4065067>) of the SunPy open source software package (The SunPy Community et al. 2020) and coronagraph images provided by the Helioviewer.org API (Müller et al. 2017).

References

- Abunin, A., Abunina, M., Belov, A., et al. 2013, in International Cosmic Ray Conference, Vol. 33, International Cosmic Ray Conference, 1618
- Abunina, M. A., Belov, A. V., Eroshenko, E. A., et al. 2020, *Sol. Phys.*, 295, 69
- Agostinelli, S., Allison, J., Amako, K., et al. 2003, *Nuclear Instruments and Methods in Physics Research Section A: Accelerators, Spectrometers, Detectors and Associated Equipment*, 506, 250
- Alzate, N. & Morgan, H. 2017, *The Astrophysical Journal*, 840, 103
- Appel, J. K. 2018, PhD thesis, University of Kiel
- Appel, J. K., Köhler, J., Guo, J., et al. 2018, *Earth and Space Science*, 5, 2
- Asvestari, E., Gil, A., Kovaltsov, G. A., & Usoskin, I. G. 2017, *Journal of Geophysical Research (Space Physics)*, 122, 9790
- Barnes, D., Davies, J. A., Harrison, R. A., et al. 2019, *Solar Physics*, 294
- Belov, A. 2000, *Space Sci. Rev.*, 93, 79
- Belov, A., Abunin, A., Abunina, M., et al. 2015, *Sol. Phys.*, 290, 1429
- Belov, A., Eroshenko, E., Yanke, V., et al. 2018, *Sol. Phys.*, 293, 68
- Belov, A. V., Blokh, I. L., Dorman, L. I., et al. 1974, *Akademiia Nauk SSSR Izvestiia Seriiia Fizicheskaiia*, 38, 1867
- Belov, A. V., Blokh, Y. A., Dorman, L. I., et al. 1973, in International Cosmic Ray Conference, Vol. 2, International Cosmic Ray Conference, 1247
- Bothmer, V. & Schwenn, R. 1998, *Annales Geophysicae*, 16, 1
- Brueckner, G. E., Howard, R. A., Koomen, M. J., et al. 1995, *Solar Physics*, 162, 357
- Cane, H. V. 2000, *Space Science Reviews*, 93, 55
- Cane, H. V., Richardson, I. G., von Rosenvinge, T. T., & Wibberenz, G. 1994, *Journal of Geophysical Research: Space Physics*, 99, 21429
- Clem, J. M. & Dorman, L. I. 2000, *Space Science Reviews*, 93, 335
- Corti, C., Potgieter, M. S., Bindi, V., et al. 2019, *The Astrophysical Journal*, 871, 253
- Davies, E., Möstl, C., Weiss, A. J., & et al. 2021, *Astronomy & Astrophysics*, submitted (not yet accepted)
- Davies, J. A., Harrison, R. A., Perry, C. H., et al. 2012, *The Astrophysical Journal*, 750, 23
- Démoulin, P. & Dasso, S. 2009, *A&A*, 498, 551
- Démoulin, P., Nakwacki, M. S., Dasso, S., & Mandrini, C. H. 2008, *Solar Physics*, 250, 347
- Dorman, L. 2009, *Cosmic Rays in Magnetospheres of the Earth and other Planets*, Vol. 358 (Springer)
- Dumbović, M., Heber, B., Vršnak, B., Temmer, M., & Kirin, A. 2018, *The Astrophysical Journal*, 860, 71
- Dumbović, M., Vršnak, B., Guo, J., et al. 2020, *Solar Physics*, 295, 104
- Forbush, S. E. 1937, *Phys. Rev.*, 51, 1108
- Freiherr von Forstner, J. L., Guo, J., Wimmer-Schweingruber, R. F., et al. 2020, *Journal of Geophysical Research: Space Physics*, 125, e2019JA027662
- Freiherr von Forstner, J. L., Guo, J., Wimmer-Schweingruber, R. F., et al. 2018, *Journal of Geophysical Research: Space Physics*, 123, 39
- Freiherr von Forstner, J. L., Guo, J., Wimmer-Schweingruber, R. F., et al. 2019, *Space Weather*, 17, 586
- Gieseler, J. & Heber, B. 2016, *Astronomy & Astrophysics*, 589, A32
- Gieseler, J., Heber, B., & Herbst, K. 2017, *Journal of Geophysical Research (Space Physics)*, 122, 10,964
- Gopalswamy, N. 2008, *Journal of Atmospheric and Solar-Terrestrial Physics*, 70, 2078, coupling of Solar Wind, Magnetosphere, Ionosphere and Upper Atmosphere
- Gulisano, A. M., Démoulin, P., Dasso, S., & Rodriguez, L. 2012, *A&A*, 543, A107
- Guo, J., Wimmer-Schweingruber, R. F., Dumbović, M., Heber, B., & Wang, Y. 2020, *Earth and Planetary Physics*, 4, 62
- Hassler, D. M., Zeitlin, C., Wimmer-Schweingruber, R. F., et al. 2012, *Space Science Reviews*, 170, 503
- He, W., Liu, Y. D., Hu, H., Wang, R., & Zhao, X. 2018, *The Astrophysical Journal*, 860, 78
- Horbury, T. S., O’Brien, H., Blazquez, I. C., et al. 2020, *Astronomy & Astrophysics*
- Howard, R. A., Moses, J. D., Vourlidis, A., et al. 2008, *Space Science Reviews*, 136, 67
- Howard, T. A. & Harrison, R. A. 2013, *Solar Physics*, 285, 269
- Janvier, M., Winslow, R. M., Good, S., et al. 2019, *Journal of Geophysical Research: Space Physics*, 124, 812
- Kilpua, E., Koskinen, H. E. J., & Pulkkinen, T. I. 2017, *Living Reviews in Solar Physics*, 14, 5
- Koldobskiy, S. A., Kovaltsov, G. A., & Usoskin, I. G. 2018, *Sol. Phys.*, 293, 110
- Krymsky, G. 1964, *Geomagn. Aeronomy*, 4, 763
- Krymsky, G., Altkhov, A., Kuzmin, A., & Skripin, G. 1966, *A New Method for Studying the Anisotropy of Cosmic Rays—Investigation of Geomagnetism and Aeronomy (Nauka, Moscow)*
- Kühl, P., Banjac, S., Heber, B., et al. 2015, *Central European Astrophysical Bulletin*, 39, 119

SUMMARY AND OUTLOOK

The goal of this thesis was to introduce observations at Mars as well as at Solar Orbiter (SolO) into the framework of space weather observations in the inner heliosphere, and to gain a better understanding of the radial evolution of interplanetary coronal mass ejections (ICMEs). This was achieved by making use of the Forbush decrease (FD) measurements available from the Radiation Assessment Detector (RAD) on Mars and from the High Energy Telescope (HET) onboard SolO.

In the first two publications, shown in Chapter 3, we have assembled two catalogs of ICME events that were associated with FDs at Mars, but were also observed from a second point — either in situ during oppositions of Mars with Earth or one of the STEREO spacecraft (Freiherr von Forstner et al., 2018), or remotely from the STEREO heliospheric imagers (HIs) (Freiherr von Forstner et al., 2019). These catalogs will serve as a useful resource for future studies and should be continued by including more recent events in the future. In the first article studying the events during opposition constellations, the cross-correlation function of the FD measurements allowed us to directly derive the transit times from 1 AU to Mars for a statistical study. The comparison of these transit times with the in situ measured ICME velocities at 1 AU allowed us to show for the first time that ICMEs can continue to decelerate beyond the Earth orbit and that this effect depends on the ICME's velocity relative to the ambient solar wind. This confirms that theoretical models based on this relative velocity, such as the drag-based model (DBM), are applicable even at larger distances from the Sun. The ICME arrival times were also compared to the results of the WSA-ENLIL+Cone magnetohydrodynamic (MHD) model, and we found that the mean deviations in the arrival time were comparable to those typically seen at other locations in the inner heliosphere. On the other hand, in the second publication, we used the FD observations at Mars to validate the HI-based arrival time estimations. The single-spacecraft reconstruction methods are not particularly precise, but their performance is in line with the results for other locations previously compiled by Möstl et al. (2017). Stereoscopic triangulation methods may improve these results, but the loss of connection to the STEREO-B spacecraft in 2014 (see Section 2.4) and the focus of the HI telescopes on the Earth-Sun line has prevented this for many Mars-directed events. In the future, data availability from the HI instruments onboard SolO and Parker Solar Probe (PSP) may make the application of such methods feasible again, and a recovery of STEREO-B in the coming years as it comes back closer to Earth would of course be beneficial as well.

With the study presented in Chapter 4, we shifted away from the mere analysis of arrival times to the investigation of other FD properties. Based on the catalog assembled in Freiherr von Forstner et al. (2019) as well as larger independent catalogs, we could reproduce a correlation of two FD parameters with the RAD measurements that was already known from previous studies at Earth, though the slope A of this relation (not to be confused with the steepness of the FDs them-

selves) was different at Mars than at Earth. Through the consultation of analytical **FD** models, we have found that this value A is likely independent of the particle energies observed by the different instruments and that it rather serves as a measure of the increase of the **ICME** or sheath structure's size between the two planets. This result was also supported by comparing the obtained ratio of A values with theoretical first-order approximations of the expected magnitude of this broadening. In future studies, this hypothesis should be further validated by analyzing large samples of **FDs** at other heliospheric locations in the same way.

In the two publications in **Chapter 5**, we have shown **RAD** measurements of the severe space weather events observed on the surface of Mars in September 2017. These consisted of a solar energetic particle (**SEP**) event as well as the merging of multiple **CMEs** en route to Mars, which caused an enormous **FD** following the **SEPs**. This serves as a case study of a complex space weather event seen at both Earth and Mars but should not be seen as a worst-case scenario, as the **SEP** source did not have direct magnetic connection to Mars, and the increased radiation dose during the event was coincidentally almost compensated by the following large **FD**.

Finally, **Chapter 6** introduced the measurement capabilities of the **HET** onboard the **Solo** mission, which launched in early 2020. While the measurement of **FDs** is not one of the main focuses of **Solo** and instruments for the direct measurement of **ICME** plasma and magnetic field are also available on the spacecraft, the first **FD** observations we obtained clearly show the high resolution with which such events can be captured by **HET**. The close alignment of **Solo** and Earth during this event also makes it a suitable candidate for multispacecraft studies, and this was pursued in the publication with the application of the **ForbMod** model to the **FDs** at **Solo** and Earth. The reason for the disagreement of **ForbMod** with the observations for this very slow **CME** needs to be examined in more detail in the future, but our initial investigations presented in the article suggest that it may be due to interaction with the following stream interaction region.

In a nutshell, this work, both in statistical and case-study form, has highlighted many different aspects of the propagation of **ICMEs** in the inner heliosphere. Still, there are numerous open questions in this field, and future studies building upon our results will undoubtedly be important contributions to the better understanding of space weather events as well as the development of enhanced forecasting capabilities.

BIBLIOGRAPHY

- Abunin, A. A. et al. (2012). “Forbush effects with a sudden and gradual onset.” In: *Geomagnetism and Aeronomy* 52.3, pages 292–299. doi: [10.1134/S0016793212030024](https://doi.org/10.1134/S0016793212030024).
- Agostinelli, S. et al. (2003). “Geant4—a simulation toolkit.” In: *Nuclear Instruments and Methods in Physics Research Section A: Accelerators, Spectrometers, Detectors and Associated Equipment* 506.3, pages 250–303. doi: [10.1016/S0168-9002\(03\)01368-8](https://doi.org/10.1016/S0168-9002(03)01368-8).
- Allen, R. C. et al. (2021a). “Energetic ions in the Venusian system: Insights from the first Solar Orbiter flyby.” In: *A&A*. in preparation.
- Allen, R. C. et al. (2021b). “Suprathermal particles from corotating interaction regions during the first perihelion pass of Solar Orbiter.” In: *A&A*. doi: [10.1051/0004-6361/202039870](https://doi.org/10.1051/0004-6361/202039870).
- Allison, J. et al. (2006). “Geant4 developments and applications.” In: *IEEE Transactions on Nuclear Science* 53.1, pages 270–278. doi: [10.1109/TNS.2006.869826](https://doi.org/10.1109/TNS.2006.869826).
- Annex, A. et al. (2020). “SpicePy: a pythonic wrapper for the SPICE toolkit.” In: *Journal of Open Source Software* 5.46, page 2050. doi: [10.21105/joss.02050](https://doi.org/10.21105/joss.02050).
- Antonucci, E. et al. (2020). “Metis: the Solar Orbiter visible light and ultraviolet coronal imager.” In: *A&A* 642, A10. doi: [10.1051/0004-6361/201935338](https://doi.org/10.1051/0004-6361/201935338).
- Appel, J. K. et al. (2018). “Detecting upward directed charged particle fluxes in the Mars Science Laboratory Radiation Assessment Detector.” In: *Earth and Space Science* 5.1, pages 2–18. doi: [10.1002/2016EA000240](https://doi.org/10.1002/2016EA000240).
- Appel, J. K. (2018). “Particle Flux Directionality and other Aspects of the Martian Radiation Environment: An Analysis of MSL/RAD Observation Data and Simulation Data.” PhD thesis. University of Kiel. URL: https://macau.uni-kiel.de/receive/diss_mods_00024576.
- Aran, A. et al. (2021). “The low-energy ion event on 19 june 2020 measured by solar orbiter.” In: *A&A*. in preparation.
- Belov, A. V. (2008). “Forbush effects and their connection with solar, interplanetary and geomagnetic phenomena.” In: *Proceedings of the International Astronomical Union* 4.S257, pages 439–450. doi: [10.1017/S1743921309029676](https://doi.org/10.1017/S1743921309029676).
- Belov, A. et al. (2018). “The global survey method applied to ground-level cosmic ray measurements.” In: *Solar Physics* 293.4, 68, page 68. doi: [10.1007/s11207-018-1277-6](https://doi.org/10.1007/s11207-018-1277-6).
- Berdermann, J. et al. (2018). “Ionospheric response to the X9.3 flare on 6 September 2017 and its implication for navigation services over europe.” In: *Space Weather* 16.10, pages 1604–1615. doi: [10.1029/2018SW001933](https://doi.org/10.1029/2018SW001933).
- Bland, E. C. et al. (2018). “SuperDARN radar-derived HF radio attenuation during the september 2017 solar proton events.” In: *Space Weather* 16.10, pages 1455–1469. doi: [10.1029/2018SW001916](https://doi.org/10.1029/2018SW001916).
- Burrell, A. G. et al. (2018). “Snakes on a spaceship—an overview of Python in heliophysics.” In: *Journal of Geophysical Research: Space Physics* 123.12, pages 10, 384–10, 402. doi: [10.1029/2018JA025877](https://doi.org/10.1029/2018JA025877).
- Cane, H. V. (2000). “Coronal mass ejections and Forbush decreases.” In: *Space Science Reviews* 93.1, pages 55–77. doi: [10.1023/A:1026532125747](https://doi.org/10.1023/A:1026532125747).
- Cargill, P. J. et al. (1996). “Magnetohydrodynamic simulations of the motion of magnetic flux tubes through a magnetized plasma.” In: *Journal of Geophysical Research: Space Physics* 101.A3, pages 4855–4870. doi: <https://doi.org/10.1029/95JA03769>.
- Clem, J. M. and L. I. Dorman (2000). “Neutron monitor response functions.” In: *Space Science Reviews* 93.1, pages 335–359. doi: [10.1023/A:1026508915269](https://doi.org/10.1023/A:1026508915269).

- Davies, E. E. et al. (2021). "In situ multi-spacecraft and remote imaging observations of the first CME detected by Solar Orbiter and BepiColombo." In: *A&A*. DOI: [10.1051/0004-6361/202040113](https://doi.org/10.1051/0004-6361/202040113).
- Davies, J. A. et al. (2009). "A synoptic view of solar transient evolution in the inner heliosphere using the heliospheric imagers on STEREO." In: *Geophysical Research Letters* 36.2. DOI: [10.1029/2008GL036182](https://doi.org/10.1029/2008GL036182).
- Davies, J. A. et al. (2012). "A self-similar expansion model for use in solar wind transient propagation studies." In: *The Astrophysical Journal* 750.1, page 23. URL: <http://stacks.iop.org/0004-637X/750/i=1/a=23>.
- Davies, J. A. et al. (2013). "Establishing a stereoscopic technique for determining the kinematic properties of solar wind transients based on a generalized self-similarly expanding circular geometry." In: *The Astrophysical Journal* 777.2, 167, page 167. DOI: [10.1088/0004-637X/777/2/167](https://doi.org/10.1088/0004-637X/777/2/167).
- Dumbović, M. et al. (2018a). "An analytical diffusion–expansion model for forrush decreases caused by flux ropes." In: *The Astrophysical Journal* 860.1, page 71. DOI: [10.3847/1538-4357/aac2de](https://doi.org/10.3847/1538-4357/aac2de).
- Dumbović, M. et al. (2018b). "The drag-based ensemble model (DBEM) for coronal mass ejection propagation." In: *The Astrophysical Journal* 854.2, page 180. DOI: [10.3847/1538-4357/aaa66](https://doi.org/10.3847/1538-4357/aaa66).
- Dumbović, M. et al. (2020). "Evolution of coronal mass ejections and the corresponding Forbush decreases: modeling vs. multi-spacecraft observations." In: *Solar Physics* 295.7, 104, page 104. DOI: [10.1007/s11207-020-01671-7](https://doi.org/10.1007/s11207-020-01671-7).
- Elftmann, R. (2020). "The High Energy Telescope on Solar Orbiter: Development and Validation of the Onboard Data Processing." PhD thesis. URL: https://macau.uni-kiel.de/receive/macau_mods_00000608.
- Eyles, C. J. et al. (2009). "The heliospheric imagers onboard the STEREO mission." In: *Solar Physics* 254.2, pages 387–445. DOI: [10.1007/s11207-008-9299-0](https://doi.org/10.1007/s11207-008-9299-0).
- Eyles, C. et al. (2003). "The Solar Mass Ejection Imager (SMEI)." In: *Solar Physics* 217.2, pages 319–347. DOI: [10.1023/B:SOLA.0000006903.75671.49](https://doi.org/10.1023/B:SOLA.0000006903.75671.49).
- Fisk, L. A. (1980). "Solar modulation of galactic cosmic rays." In: *The Ancient Sun: Fossil Record in the Earth, Moon and Meteorites*. Edited by R. O. Pepin, J. A. Eddy, and R. B. Merrill, pages 103–118.
- Forbes, T. G. (2000). "A review on the genesis of coronal mass ejections." In: *Journal of Geophysical Research: Space Physics* 105.A10, pages 23153–23165. DOI: <https://doi.org/10.1029/2000JA000005>.
- Forbush, S. E. (1937). "On the effects in cosmic-ray intensity observed during the recent magnetic storm." In: *Phys. Rev.* 51 (12), pages 1108–1109. DOI: [10.1103/PhysRev.51.1108.3](https://doi.org/10.1103/PhysRev.51.1108.3).
- Freeland, S. L. and B. N. Handy (1998). "Data analysis with the SolarSoft system." In: *Solar Physics* 182.2, pages 497–500. DOI: [10.1023/A:1005038224881](https://doi.org/10.1023/A:1005038224881).
- Freiherr von Forstner, J. L. (2018). "Tracking and validating ICMEs propagating towards Mars using STEREO Heliospheric Imagers combined with Forbush decreases detected by MSL/RAD." Master's thesis. University of Kiel.
- Freiherr von Forstner, J. L. et al. (2018). "Using Forbush decreases to derive the transit time of ICMEs propagating from 1 AU to Mars." In: *Journal of Geophysical Research: Space Physics* 123.1, pages 39–56. DOI: [10.1002/2017JA024700](https://doi.org/10.1002/2017JA024700).
- Freiherr von Forstner, J. L. et al. (2019). "Tracking and validating ICMEs propagating toward Mars using STEREO heliospheric imagers combined with Forbush decreases detected by MSL/RAD." In: *Space Weather* 17.4, pages 586–598. DOI: [10.1029/2018SW002138](https://doi.org/10.1029/2018SW002138).

- Freiherr von Forstner, J. L. et al. (2020). "Comparing the properties of ICME-induced Forbush decreases at Earth and Mars." In: *Journal of Geophysical Research: Space Physics* 125.5, e2019JA027662. DOI: [10.1029/2019JA027662](https://doi.org/10.1029/2019JA027662).
- Freiherr von Forstner, J. L. et al. (2021). "Radial evolution of the April 2020 stealth coronal mass ejection between 0.8 and 1 AU: A comparison of Forbush decreases at Solar Orbiter and Earth." In: *A&A*. DOI: [10.1051/0004-6361/202039848](https://doi.org/10.1051/0004-6361/202039848).
- Frissell, N. A. et al. (2019). "High-frequency communications response to solar activity in September 2017 as observed by amateur radio networks." In: *Space Weather* 17.1, pages 118–132. DOI: [10.1029/2018SW002008](https://doi.org/10.1029/2018SW002008).
- Geophysical Research Letters* (2018): *Impact of the Sept. 10, 2017, solar event on Mars*. URL: [https://agupubs.onlinelibrary.wiley.com/doi/toc/10.1002/\(ISSN\)1944-8007.MARS_SOLAR1](https://agupubs.onlinelibrary.wiley.com/doi/toc/10.1002/(ISSN)1944-8007.MARS_SOLAR1).
- Gómez-Herrero, R. et al. (2021). "First near-relativistic solar electron events observed by EPD onboard Solar Orbiter." In: *A&A*. DOI: [10.1051/0004-6361/202039883](https://doi.org/10.1051/0004-6361/202039883).
- Gopalswamy, N. et al. (2001). "Predicting the 1-AU arrival times of coronal mass ejections." In: *Journal of Geophysical Research: Space Physics* 106.A12, pages 29207–29217. DOI: <https://doi.org/10.1029/2001JA000177>.
- Gou, T. et al. (2020). "Solar flare–CME coupling throughout two acceleration phases of a fast CME." In: *The Astrophysical Journal* 897.2, page L36. DOI: [10.3847/2041-8213/ab9ec5](https://doi.org/10.3847/2041-8213/ab9ec5).
- Grotzinger, J. P. et al. (2012). "Mars Science Laboratory mission and science investigation." In: *Space Science Reviews* 170.1, pages 5–56. DOI: [10.1007/s11214-012-9892-2](https://doi.org/10.1007/s11214-012-9892-2).
- Guo, J. et al. (2015). "Variations of dose rate observed by MSL/RAD in transit to Mars." In: *A&A* 577, A58. DOI: [10.1051/0004-6361/201525680](https://doi.org/10.1051/0004-6361/201525680).
- Guo, J. et al. (2017a). "Dependence of the Martian radiation environment on atmospheric depth: modeling and measurement." In: *Journal of Geophysical Research: Planets* 122.2, 2016JE005206, pages 329–341. DOI: [10.1002/2016JE005206](https://doi.org/10.1002/2016JE005206).
- Guo, J. et al. (2017b). "Measurements of Forbush decreases at Mars: both by MSL on ground and by MAVEN in orbit." In: *Astronomy & Astrophysics*. DOI: [10.1051/0004-6361/201732087](https://doi.org/10.1051/0004-6361/201732087).
- Guo, J. et al. (2018). "Modeling the evolution and propagation of 10 September 2017 CMEs and SEPs arriving at Mars constrained by remote sensing and in situ measurement." In: *Space Weather* 16.8, pages 1156–1169. DOI: [10.1029/2018SW001973](https://doi.org/10.1029/2018SW001973).
- Guo, J. et al. (2019). "Ready functions for calculating the Martian radiation environment." In: *Journal of Space Weather and Space Climate* 9, A7, A7. DOI: [10.1051/swsc/2019004](https://doi.org/10.1051/swsc/2019004).
- Guo, J. et al. (2021). "Radiation environment for future human exploration on the surface of Mars: The current understanding based on MSL/RAD dose measurements." In: *The Astronomy and Astrophysics Review*. submitted.
- Haberle, R. M. et al. (2014). "Preliminary interpretation of the REMS pressure data from the first 100 sols of the MSL mission." In: *Journal of Geophysical Research: Planets* 119.3, pages 440–453. DOI: <https://doi.org/10.1002/2013JE004488>.
- Hassler, D. M. et al. (2012). "The Radiation Assessment Detector (RAD) investigation." In: *Space Science Reviews* 170.1, pages 503–558. DOI: [10.1007/s11214-012-9913-1](https://doi.org/10.1007/s11214-012-9913-1).
- Heinemann, S. G. et al. (2019). "CME-HSS interaction and characteristics tracked from Sun to Earth." In: *Solar Physics* 294.9, 121, page 121. DOI: [10.1007/s11207-019-1515-6](https://doi.org/10.1007/s11207-019-1515-6).
- Hess, V. F. and A. Demmelmair (1937). "World-wide effect in cosmic ray intensity, as observed during a recent magnetic storm." In: *Nature* 140, pages 316–317. DOI: [10.1038/140316a0](https://doi.org/10.1038/140316a0).
- Howard, R. A. et al. (2008). "Sun Earth Connection Coronal and Heliospheric Investigation (SECCHI)." In: *Space Science Reviews* 136.1, page 67. DOI: [10.1007/s11214-008-9341-4](https://doi.org/10.1007/s11214-008-9341-4).
- Howard, R. A. et al. (2020). "The Solar Orbiter heliospheric imager (SoloHI)." In: *A&A* 642, A13. DOI: [10.1051/0004-6361/201935202](https://doi.org/10.1051/0004-6361/201935202).

- Howard, T. A. et al. (2006). "Tracking halo coronal mass ejections from 0–1 AU and space weather forecasting using the solar mass ejection imager (SMEI)." In: *Journal of Geophysical Research: Space Physics* 111.A4. A04105. DOI: [10.1029/2005JA011349](https://doi.org/10.1029/2005JA011349).
- Janvier, M. et al. (2019). "Generic magnetic field intensity profiles of interplanetary coronal mass ejections at Mercury, Venus, and Earth from superposed epoch analyses." In: *Journal of Geophysical Research: Space Physics* 124.2, pages 812–836. DOI: [10.1029/2018JA025949](https://doi.org/10.1029/2018JA025949).
- Kahler, S. W. and D. F. Webb (2007). "V arc interplanetary coronal mass ejections observed with the Solar Mass Ejection Imager." In: *Journal of Geophysical Research: Space Physics* 112.A9. A09103. DOI: [10.1029/2007JA012358](https://doi.org/10.1029/2007JA012358).
- Köhler, J. et al. (2011). "Inversion of neutron/gamma spectra from scintillator measurements." In: *Nuclear Instruments and Methods in Physics Research B* 269.22, pages 2641–2648. DOI: [10.1016/j.nimb.2011.07.021](https://doi.org/10.1016/j.nimb.2011.07.021).
- Kollhoff, A. et al. (2021). "The first widespread sep event of the 25th solar cycle." In: *A&A*. in preparation.
- Kusano, K. et al. (2012). "Magnetic field structures triggering solar flares and coronal mass ejections." In: *The Astrophysical Journal* 760.1, page 31. DOI: [10.1088/0004-637x/760/1/31](https://doi.org/10.1088/0004-637x/760/1/31).
- Le Blancq, F. (2011). "Diurnal pressure variation: the atmospheric tide." In: *Weather* 66.11, pages 306–307. DOI: <https://doi.org/10.1002/wea.857>.
- Liu, Y. et al. (2010a). "Geometric triangulation of imaging observations to track coronal mass ejections continuously out to 1 AU." In: *The Astrophysical Journal Letters* 710.1, page L82. URL: <http://stacks.iop.org/2041-8205/710/i=1/a=L82>.
- Liu, Y. et al. (2010b). "Reconstructing coronal mass ejections with coordinated imaging and in situ observations: global structure, kinematics, and implications for space weather forecasting." In: *The Astrophysical Journal* 722.2, page 1762. URL: <http://stacks.iop.org/0004-637X/722/i=2/a=1762>.
- Lockwood, J. A. (1971). "Forbush decreases in the cosmic radiation." In: *Space Science Reviews* 12.5, pages 658–715. DOI: [10.1007/BF00173346](https://doi.org/10.1007/BF00173346).
- Lockwood, J. A., W. R. Webber, and H. Debrunner (1991). "The rigidity dependence of Forbush decreases observed at the Earth." In: *Journal of Geophysical Research: Space Physics* 96.A4, pages 5447–5455. DOI: [10.1029/91JA00089](https://doi.org/10.1029/91JA00089).
- Lugaz, N., A. Vourlidas, and I. I. Roussev (2009). "Deriving the radial distances of wide coronal mass ejections from elongation measurements in the heliosphere – application to CME-CME interaction." In: *Annales Geophysicae* 27.9, pages 3479–3488. DOI: [10.5194/angeo-27-3479-2009](https://doi.org/10.5194/angeo-27-3479-2009).
- Lugaz, N. et al. (2010). "Determining the azimuthal properties of coronal mass ejections from multi-spacecraft remote-sensing observations with stereo secchi." In: *The Astrophysical Journal* 715.1, page 493. URL: <http://stacks.iop.org/0004-637X/715/i=1/a=493>.
- Manchester IV, W. B. et al. (2005). "Coronal mass ejection shock and sheath structures relevant to particle acceleration." In: *The Astrophysical Journal* 622.2, pages 1225–1239. DOI: [10.1086/427768](https://doi.org/10.1086/427768).
- Mason, G. M. et al. (2020). "³He-rich solar energetic particle events observed on the first perihelion pass of Solar Orbiter." In: *A&A*. DOI: [10.1051/0004-6361/202039752](https://doi.org/10.1051/0004-6361/202039752).
- Mason, G. M. et al. (2021). "Quiet-time low energy ion spectra observed on solar orbiter during solar minimum." In: *A&A*. submitted.
- McDonald, F. B. and G. H. Ludwig (1964). "Measurement of low-energy primary cosmic-ray protons on IMP-1 satellite." In: *Physical Review Letters* 13.26, pages 783–785. DOI: [10.1103/PhysRevLett.13.783](https://doi.org/10.1103/PhysRevLett.13.783).
- Mewaldt, R. A. et al. (2001). "Long-term fluences of energetic particles in the heliosphere." In: *AIP Conference Proceedings* 598.1, pages 165–170. DOI: [10.1063/1.1433995](https://doi.org/10.1063/1.1433995).

- Moraal, H. (2013). "Cosmic-Ray Modulation Equations." In: *Space Science Reviews* 176.1-4, pages 299–319. DOI: [10.1007/s11214-011-9819-3](https://doi.org/10.1007/s11214-011-9819-3).
- Moraal, H., A. Belov, and J. M. Clem (2000). "Design and co-ordination of multi-station international neutron monitor networks." In: *Space Science Reviews* 93, pages 285–303. DOI: [10.1023/A:1026504814360](https://doi.org/10.1023/A:1026504814360).
- Möstl, C. et al. (2017). "Modeling observations of solar coronal mass ejections with heliospheric imagers verified with the Heliophysics System Observatory." In: *Space Weather* 15.7, pages 955–970. DOI: [10.1002/2017SW001614](https://doi.org/10.1002/2017SW001614).
- Müller, D. et al. (2020). "The Solar Orbiter mission — science overview." In: *A&A* 642, A1. DOI: [10.1051/0004-6361/202038467](https://doi.org/10.1051/0004-6361/202038467).
- O’Kane, J. et al. (2021). "Origins of a stealth CME detected at Solar Orbiter." In: *A&A*. submitted.
- Odstrcil, D., P. Riley, and X. P. Zhao (2004). "Numerical simulation of the 12 May 1997 interplanetary CME event." In: *Journal of Geophysical Research: Space Physics* 109.A2. A02116. DOI: [10.1029/2003JA010135](https://doi.org/10.1029/2003JA010135).
- OFCM (1995). "The National Space Weather Program: The strategic plan." In: *FCM-P30-1995*. URL: <http://www.ofcm.gov/publications/spacewx/nswpp30.pdf>.
- Ossing, D. A. et al. (2018). "The fall and rise of STEREO Behind." In: *2018 SpaceOps Conference*. DOI: [10.2514/6.2018-2565](https://doi.org/10.2514/6.2018-2565).
- Owens, M. and P. Cargill (2004). "Predictions of the arrival time of coronal mass ejections at 1AU: an analysis of the causes of errors." In: *Annales Geophysicae* 22.2, pages 661–671. DOI: [10.5194/angeo-22-661-2004](https://doi.org/10.5194/angeo-22-661-2004).
- Papaioannou, A. et al. (2019). "A catalogue of Forbush decreases recorded on the surface of Mars from 2012 until 2016: Comparison with terrestrial FDs." In: *Solar Physics* 294.6, page 66. DOI: [10.1007/s11207-019-1454-2](https://doi.org/10.1007/s11207-019-1454-2).
- Parker, E. (1958). "Dynamics of the interplanetary gas and magnetic fields." In: *The Astrophysical Journal* 128, page 664. DOI: [10.1086/146579](https://doi.org/10.1086/146579).
- Pomoell, J. and S. Poedts (2018). "EUHFORIA: European Heliospheric Forecasting Information Asset." In: *J. Space Weather Space Clim.* 8, A35. DOI: [10.1051/swsc/2018020](https://doi.org/10.1051/swsc/2018020).
- Ranyard, C. A. (1879). "Photographs and drawings of the corona." In: *Memoirs of the Royal Astronomical Society* 41, page 483.
- Reames, D. V. (1990). "Energetic particles from impulsive solar flares." In: *The Astrophysical Journal, Supplement* 73, page 235. DOI: [10.1086/191456](https://doi.org/10.1086/191456).
- Richardson, I. G. and H. V. Cane (1995). "Regions of abnormally low proton temperature in the solar wind (1965–1991) and their association with ejecta." In: *Journal of Geophysical Research: Space Physics* 100.A12, pages 23397–23412. DOI: [10.1029/95JA02684](https://doi.org/10.1029/95JA02684).
- (2010). "Near-earth interplanetary coronal mass ejections during solar cycle 23 (1996 - 2009): catalog and summary of properties." In: *Solar Physics* 264.1, pages 189–237. DOI: [10.1007/s11207-010-9568-6](https://doi.org/10.1007/s11207-010-9568-6).
- (2011). "Galactic cosmic ray intensity response to interplanetary coronal mass ejections/magnetic clouds in 1995 - 2009." In: *Solar Physics* 270.2, pages 609–627. DOI: [10.1007/s11207-011-9774-x](https://doi.org/10.1007/s11207-011-9774-x).
- Richardson, I. G. (2018). "Solar wind stream interaction regions throughout the heliosphere." In: *Living Reviews in Solar Physics* 15.1, 1, page 1. DOI: [10.1007/s41116-017-0011-z](https://doi.org/10.1007/s41116-017-0011-z).
- Rodríguez-Pacheco, J. et al. (2020). "The Energetic Particle Detector - energetic particle instrument suite for the Solar Orbiter mission." In: *A&A* 642, A7. DOI: [10.1051/0004-6361/201935287](https://doi.org/10.1051/0004-6361/201935287).
- Rouillard, A. P. et al. (2008). "First imaging of corotating interaction regions using the STEREO spacecraft." In: *Geophysical Research Letters* 35.10. DOI: [10.1029/2008GL033767](https://doi.org/10.1029/2008GL033767).
- Russell, C. T., editor (2008). *The STEREO Mission*. Springer New York. DOI: [10.1007/978-0-387-09649-0](https://doi.org/10.1007/978-0-387-09649-0).

- Russell, C. T., R. L. McPherron, and R. K. Burton (1974). "On the cause of geomagnetic storms." In: *Journal of Geophysical Research (1896-1977)* 79.7, pages 1105–1109. DOI: <https://doi.org/10.1029/JA079i007p01105>.
- Sato, H. et al. (2019). "Solar radio burst events on 6 September 2017 and its impact on GNSS signal frequencies." In: *Space Weather* 17.6, pages 816–826. DOI: [10.1029/2019SW002198](https://doi.org/10.1029/2019SW002198).
- Scolini, C. et al. (2019). "Observation-based modelling of magnetised coronal mass ejections with EUHFORIA." In: *A&A* 626, A122. DOI: [10.1051/0004-6361/201935053](https://doi.org/10.1051/0004-6361/201935053).
- Shea, M. A. and D. F. Smart (2001). "Vertical cutoff rigidities for cosmic ray stations since 1955." In: *International Cosmic Ray Conference*. Volume 10. International Cosmic Ray Conference, page 4063.
- Sheeley, N. R. et al. (1999). "Continuous tracking of coronal outflows: two kinds of coronal mass ejections." In: *Journal of Geophysical Research: Space Physics* 104.A11, pages 24739–24767. DOI: [10.1029/1999JA900308](https://doi.org/10.1029/1999JA900308).
- Simpson, J. A. (2000). "The cosmic ray nucleonic component: the invention and scientific uses of the neutron monitor - (keynote lecture)." In: *Space Science Reviews* 93, pages 11–32. DOI: [10.1023/A:1026567706183](https://doi.org/10.1023/A:1026567706183).
- Siscoe, G. and D. Odstrcil (2008). "Ways in which ICME sheaths differ from magnetosheaths." In: *Journal of Geophysical Research: Space Physics* 113.A9. DOI: [10.1029/2008JA013142](https://doi.org/10.1029/2008JA013142).
- Smart, D. and M. Shea (2008). "World grid of calculated cosmic ray vertical cutoff rigidities for epoch 2000.0." In: *Proceedings of the 30th International Cosmic Ray Conference*. Volume 1, pages 737–740.
- Space Weather* (2018): *Space Weather Events of 4-10 September 2017*. URL: [https://agupubs.onlinelibrary.wiley.com/doi/toc/10.1002/\(ISSN\)1542-7390.SW-SEPT2017](https://agupubs.onlinelibrary.wiley.com/doi/toc/10.1002/(ISSN)1542-7390.SW-SEPT2017).
- Steigies, C. T. (2009). "NMDB: towards a global neutron monitor database." In: *AGU Fall Meeting Abstracts*. Volume 2009, SH51B–1280.
- Sullivan, J. (1971). "Geometric factor and directional response of single and multi-element particle telescopes." In: *Nuclear Instruments and Methods* 95.1, pages 5–11. DOI: [10.1016/0029-554X\(71\)90033-4](https://doi.org/10.1016/0029-554X(71)90033-4).
- Tammen, J. et al. (2015). "Quenching comparison of BGO and BSO for heavy ions." In: *Nuclear Instruments and Methods in Physics Research Section B: Beam Interactions with Materials and Atoms* 360, pages 129–138. DOI: [10.1016/j.nimb.2015.07.127](https://doi.org/10.1016/j.nimb.2015.07.127).
- Temmer, M. et al. (2012). "Characteristics of kinematics of a coronal mass ejection during the 2010 August 1 CME–CME interaction event." In: *The Astrophysical Journal* 749.1, page 57. DOI: [10.1088/0004-637x/749/1/57](https://doi.org/10.1088/0004-637x/749/1/57).
- The SunPy Community et al. (2020). "The SunPy project: open source development and status of the version 1.0 core package." In: *The Astrophysical Journal* 890 (1), pages 68–. DOI: [10.3847/1538-4357/ab4f7a](https://doi.org/10.3847/1538-4357/ab4f7a).
- Thernisien, A. (2011). "Implementation of the graduated cylindrical shell model for the three-dimensional reconstruction of coronal mass ejections." In: *The Astrophysical Journal Supplement Series* 194.2, page 33. URL: <http://stacks.iop.org/0067-0049/194/i=2/a=33>.
- Thernisien, A., R. A. Howard, and A. Vourlidas (2006). "Modeling of flux rope coronal mass ejections." In: *The Astrophysical Journal* 652.1, page 763. URL: <http://stacks.iop.org/0004-637X/652/i=1/a=763>.
- Vourlidas, A. et al. (2016). "The wide-field imager for Solar Probe Plus (WISPR)." In: *Space Science Reviews* 204.1-4, pages 83–130. DOI: [10.1007/s11214-014-0114-y](https://doi.org/10.1007/s11214-014-0114-y).
- Vršnak, B. et al. (2014). "Heliospheric propagation of coronal mass ejections: comparison of numerical WSA-ENLIL+Cone model and analytical drag-based model." In: *The Astrophysical Journal Supplement Series* 213.2, page 21. URL: <http://stacks.iop.org/0067-0049/213/i=2/a=21>.

- Vršnak, B. et al. (2013). "Propagation of interplanetary coronal mass ejections: the drag-based model." In: *Solar Physics* 285.1, pages 295–315. doi: [10.1007/s11207-012-0035-4](https://doi.org/10.1007/s11207-012-0035-4).
- Wang, C., D. Du, and J. D. Richardson (2005). "Characteristics of the interplanetary coronal mass ejections in the heliosphere between 0.3 and 5.4 AU." In: *Journal of Geophysical Research: Space Physics* 110.A10. doi: <https://doi.org/10.1029/2005JA011198>.
- Wang, Y. et al. (2019). "CME arrival time prediction using convolutional neural network." In: *The Astrophysical Journal* 881.1, page 15. doi: [10.3847/1538-4357/ab2b3e](https://doi.org/10.3847/1538-4357/ab2b3e).
- Webb, D. F. and R. A. Howard (1994). "The solar cycle variation of coronal mass ejections and the solar wind mass flux." In: *Journal of Geophysical Research: Space Physics* 99.A3, pages 4201–4220. doi: [10.1029/93JA02742](https://doi.org/10.1029/93JA02742).
- Wibberenz, G. et al. (1998). "Transient effects and disturbed conditions." In: *Space Science Reviews* 83.1, pages 309–348. doi: [10.1023/A:1005083109827](https://doi.org/10.1023/A:1005083109827).
- Wimmer-Schweingruber, R. F. et al. (2006). "Understanding interplanetary coronal mass ejection signatures." In: *Coronal Mass Ejections*. New York, NY: Springer New York, pages 177–216. doi: [10.1007/978-0-387-45088-9_10](https://doi.org/10.1007/978-0-387-45088-9_10).
- Wimmer-Schweingruber, R. F. et al. (2021). "First year of energetic particle measurements in the inner heliosphere with solar orbiter." In: *A&A*. in preparation.
- Wimmer-Schweingruber, R. F. et al. (2020). "The Lunar Lander Neutron and Dosimetry (LND) experiment on Chang'E 4." In: *Space Science Reviews* 216.6. doi: [10.1007/s11214-020-00725-3](https://doi.org/10.1007/s11214-020-00725-3).
- Winslow, R. M. et al. (2015). "Interplanetary coronal mass ejections from MESSENGER orbital observations at Mercury." In: *Journal of Geophysical Research: Space Physics* 120.8, pages 6101–6118. doi: [10.1002/2015JA021200](https://doi.org/10.1002/2015JA021200).
- Xu, Z. et al. (2020). "First solar energetic particles measured on the lunar far-side." In: *The Astrophysical Journal* 902.2, page L30. doi: [10.3847/2041-8213/abbccc](https://doi.org/10.3847/2041-8213/abbccc).
- Zeitlin, C. et al. (2013). "Measurements of energetic particle radiation in transit to Mars on the Mars Science Laboratory." In: *Science* 340.6136, pages 1080–1084. doi: [10.1126/science.1235989](https://doi.org/10.1126/science.1235989).
- Zeitlin, C. et al. (2018). "Analysis of the radiation hazard observed by rad on the surface of mars during the September 2017 solar particle event." In: *Geophysical Research Letters* 45.12, pages 5845–5851. doi: [10.1029/2018GL077760](https://doi.org/10.1029/2018GL077760).
- Zhang, S. et al. (2020). "First measurements of the radiation dose on the lunar surface." In: *Science Advances* 6.39. doi: [10.1126/sciadv.aaz1334](https://doi.org/10.1126/sciadv.aaz1334).
- Žic, T., B. Vršnak, and M. Temmer (2015). "Heliospheric propagation of coronal mass ejections: drag-based model fitting." In: *The Astrophysical Journal Supplement Series* 218.2, page 32. URL: <http://stacks.iop.org/0067-0049/218/i=2/a=32>.
- Zurbuchen, T. H. and I. G. Richardson (2006). "In-situ solar wind and magnetic field signatures of interplanetary coronal mass ejections." In: *Coronal Mass Ejections*. New York, NY: Springer New York, pages 31–43. doi: [10.1007/978-0-387-45088-9_3](https://doi.org/10.1007/978-0-387-45088-9_3).

ACKNOWLEDGEMENTS

At this point, I would like to thank everyone who supported me during the course of my PhD studies and my work on MSL/RAD, Chang'E 4 LND as well as Solar Orbiter EPD.

First of all, I am grateful to my supervisor Prof. Robert Wimmer-Schweingruber for the opportunity to work on these exciting projects, and his helpful advice. He also made it possible that these results could be published in scientific journals and presented at many international conferences. Sincere thanks also to Prof. Jingnan Guo, who supported my work since my bachelor's thesis, and who I wish all the best for her new position in China.

Furthermore, thanks to all my colleagues in the three mission teams for their continued support and helpful discussions, including Zigong Xu, Alexander Kollhoff, and my officemate Christoph Terasa for the productive and enjoyable collaboration, e.g. on low- and high-level software for the Solar Orbiter mission, which will hopefully facilitate the EPD data analysis in the Kiel team for years to come, and to the rest of the Extraterrestrial Physics group at Kiel University. I also thank the group of Manuela Temmer and Astrid Veronig at the University of Graz and Mateja Dumbović at Hvar Observatory with whom I worked in close collaboration for many of the Forbush decrease studies, and who I enjoyed meeting regularly at the conferences in Vienna, Hvar and San Francisco.

I additionally want to thank the bachelor and master students who supported my work during their Hiwi positions, Charlotte Büschel and Niklas Lundt, and three secondary school students, Joana Wanger, Lukas Abegg and Markus Arndt, who contributed to the data sets used in my studies during their internships in the ET group.

I would like to thank Anne Fischer as well as Hanna Giese and Knud Schröter for their very thorough proofreading of this thesis and valuable suggestions, and my parents Kristina and Michael and my brother Julius for their moral support.

Last but not least, the data analysis presented in this thesis, the typesetting of the thesis itself and the generation of most of the figures were made possible by a number of open source software projects, including, but not limited to, the ones acknowledged below:

Rossum, G. van et al. (1991–). *Python programming language*.

Jones, E., T. Oliphant, P. Peterson, et al. (2001–). *SciPy: open source scientific tools for Python*. including NumPy, Pandas, and Matplotlib. URL: <http://www.scipy.org/>.

McKinney, W. (2011). "Pandas: a foundational Python library for data analysis and statistics." In: *Python for High Performance and Scientific Computing* 14.

Rasch, P. (2013–). *Spiceminer: A simple python wrapper for NASA's SPICE framework*.

Annex, A. et al. (2020). "SpiceyPy: a pythonic wrapper for the SPICE toolkit." In: *Journal of Open Source Software* 5.46, page 2050. DOI: [10.21105/joss.02050](https://doi.org/10.21105/joss.02050).

Köhler, J. et al. (2012–). *flight_tools: a collection of tools for MSL/RAD data parsing and evaluation*. URL: https://gitlab.physik.uni-kiel.de/mslrad/flight_tools.

- Freiherr von Forstner, J. L., J. C. Terasa, and S. Löffler (2019–). *ET SPICE: A wrapper around SpiceyPy that allows for easy access to often-used SPICE kernels*.
- Freiherr von von Forstner, J. L. et al. (2019–). *Solo Loader: Utilities to load and process Solar Orbiter EPD data*. URL: https://gitlab.physik.uni-kiel.de/solo/solo_loader.
- Lebigot, E. O. (2010-2016). *Uncertainties: a Python package for calculations with uncertainties*. URL: <https://pythonhosted.org/uncertainties/>.
- Lamport, L. et al. (1986). *LaTeX: a document preparation system*. Addison-Wesley Pub. Co.
- Lehman, P. et al. (2006–). *BibLaTeX: a sophisticated bibliography system for LaTeX users*. URL: <https://github.com/plk/biblatex>.
- Miede, A. (2006–). *classicthesis: a classic thesis style for LaTeX*. URL: <https://bitbucket.org/amiede/classicthesis>.
- Tantau, T. and C. Feuersänger (2005–). *PGF and TikZ – Graphic systems for TeX*.
- Wright, J. (2008–). *siunitx: a comprehensive SI units package for LaTeX*.
- Mumford, S. J. et al. (2020). *SunPy*. Version v2.0.4. DOI: [10.5281/zenodo.4275394](https://doi.org/10.5281/zenodo.4275394).

ISOTROPIC SIMULATION OF THE HIGH ENERGY TELESCOPE WITH THE SOLAR ORBITER SPACECRAFT MODEL

This chapter describes a simulation performed using the Geometry and Tracking 4 toolkit ([Geant4](#), Agostinelli et al., 2003) to model the response of the High Energy Telescope ([HET](#), [Section 2.2](#)) to an isotropic radiation field. [HET](#) is part of the Energetic Particle Detector ([EPD](#), Rodríguez-Pacheco et al., 2020) onboard Solar Orbiter ([SolO](#)), and [Geant4](#) is a software toolkit developed at CERN for Monte Carlo simulations of the interaction of particles with matter. [Geant4](#) is widely used in many different fields, such as high energy physics, medical physics and radiation protection, as well as astrophysics and space science (Allison et al., 2006). A [Geant4](#) simulation typically requires the definition of a particle source (e.g. a particle beam, a surface or volume source), a model of the geometry and materials of the experimental setup, and one or more sensitive detectors in which particle hits are detected. A so-called *physics list* describes all possible interaction processes and their probabilities, from which [Geant4](#) then chooses stochastically for each simulated particle. As a result, the trajectory of each particle and the detected particles in each detector can be stored and used to calculate e.g. the response function of a particle detector.

This simulation builds on top of the work by Elftmann (2020), who simulated the nominal data products of [HET](#) with [Geant4](#). In this case, particles were simulated only from a circular source in front of the A detector (see Elftmann, 2020, Figure 5.1), which fills the nominal field of view ([FOV](#)) of [HET](#). However, particles entering [HET](#) from outside its [FOV](#) may also play a role for certain data products, especially for the single-detector counters, which are sensitive to particles entering the telescope from all directions (e.g., through the housing, cf. [Figure 8](#)). These counters were used by Freiherr von Forstner et al. (2021) to observe Forbush decreases with [HET](#). Thus, it makes sense to simulate the [HET](#) detector in an isotropic particle flux to model its response to galactic cosmic rays ([GCRs](#)), and this will be done in [Section A.1](#).

For an isotropic particle flux, it is also important to take into account the [SolO](#) spacecraft on which [HET](#) is mounted. This is less relevant for the nominal [FOV](#), as the [HET](#) telescopes are mounted at an edge of the spacecraft body so that neither opening is obstructed by the spacecraft. But in the case of the single detector counters used by Freiherr von Forstner et al. (2021), the isotropic [GCR](#) flux is affected by the spacecraft body, as a significant part of the 4π solid angle is covered by the spacecraft. Thus, particles may be shielded away, or even generate secondary particles that are then detected within [HET](#). This will be investigated in [Section A.2](#).

A.1 ISOTROPIC SIMULATION OF HET

For the isotropic simulation, the geometric model of the **HET** instrument and its electronics box were reused from the simulation by Elftmann (2020). The reader is referred to this work for further details about its definition. The simulation setup was also very similar to the one from Elftmann (2020), using **Geant4** version 10.1.2 with the pre-defined general-purpose physics list **QGSP_BERT** and a power law spectrum for the energy-dependent intensity $I(E)$ of the input particles:

$$I(E) \sim E^{-1} \quad (5)$$

When the simulation results are later histogrammed over the primary particle energy with logarithmically spaced bins, the bin width at a certain energy is proportional to

$$\Delta E \propto \frac{d}{dE} \log(E) = E^{-1} = I(E) \quad (6)$$

This means that using this intensity profile, (approximately) the same number of particles are simulated in each primary energy bin, which facilitates the analysis of the simulation results (Section A.3). Only protons between 5 MeV and 100 GeV were simulated as input particles in this case, as other species were neglected in the modeling approach of Freiherr von Forstner et al. (2021). Still, all secondary particles generated by these primary protons are taken into account in the output of the simulation. Of course, other primary species such as electrons and heavy ions can be simulated in a similar fashion in the future, though in the case of heavy ions, the quenching model for the scintillator needs to be taken into account as described by Elftmann (2020, Section 5.4) and Tammen et al. (2015).

In contrast to the circular planar source surface used by Elftmann (2020), a spherical proton source with a radius of 15 cm (large enough to surround the model of **HET** and its electronics box) was defined, and particles were injected following a cosine-law angular distribution. This replicates an isotropic flux entering **HET** from all sides. The simulation was run for $N_{\text{total}} = 5 \times 10^8$ primary particles, and 1.6×10^7 particle hits (primary or secondary) were registered in the **HET** detectors (ratio: 3.2 %).

A.2 THE SPACECRAFT MODEL

To simulate how the interaction of **GCR** particles with the **Solo** spacecraft affects the **HET** measurements, the spacecraft needs to be included into the **Geant4** simulation. Creating an accurate model of a spacecraft for the purpose of such a simulation is notoriously difficult, as it consists of numerous components and information about their exact shape and composition is not always readily available. Thus, simulations taking into account spacecraft effects often need to make many assumptions and drastically simplify the geometry of the spacecraft (see e.g. Appel (2018) and Appel et al. (2018) for a similar simulation of the Mars Science Laboratory rover).

In the case of **Solo**, ESA has provided a computer-aided design (**CAD**) model of the spacecraft that can serve as a reference for simulations (D. Müller, 2020,

priv. comm.). This file (`dp17a1_bulk.bdf`) is provided in the BDF format of the NASTRAN software, a finite element analysis toolkit that was used for structural analysis of the spacecraft. The model contains the 3D geometry of the spacecraft, including material properties such as the density. Using the freeware software *FEX*¹, it is possible to inspect the model and measure the dimensions and total mass of certain structures.

As shown in [Figure 11](#), the model accurately represents the major structures of the *Solo* spacecraft, such as the main body, the solar panels, the heat shield, the instrument boom and various communications and radio wave antennae. However, not all parts are modeled in detail: Many small structures, such as the scientific payload and electronics within the spacecraft body, are replaced with mass points that are attached to the model (shown as colored tetrahedra in the image) for the purpose of structural analysis, and thus no information about their spatial extent and materials is provided. In addition, some parts of the spacecraft are constructed using composite materials, such as honeycomb structures instead of solid aluminium — in these cases, the material properties given in the [CAD](#) file do not include the correct densities, but are instead set to zero. Thus, the total mass of the spacecraft according to the [CAD](#) file is 1202 kg, which is significantly less than the total launch mass of ~ 1800 kg, or ~ 1600 kg without fuel (Müller et al., 2020).

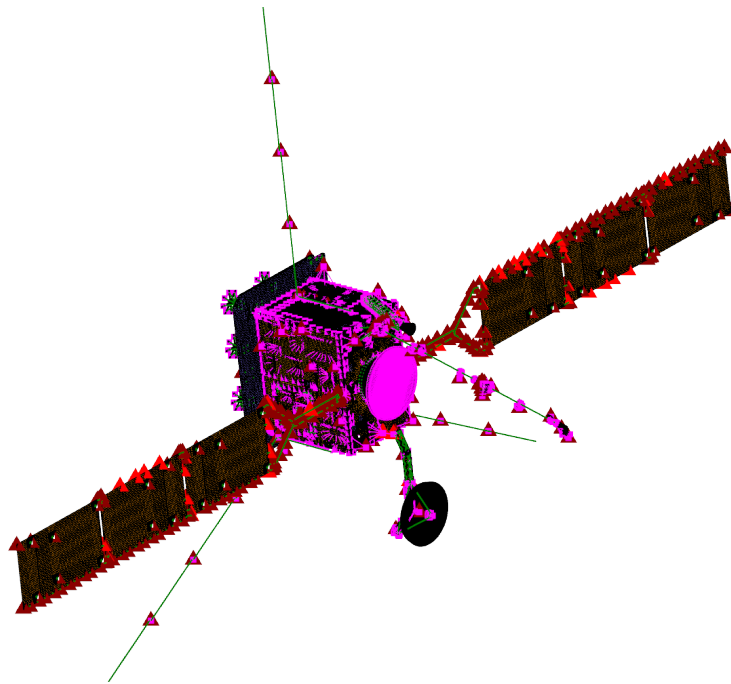


Figure 11: Density model of the *Solo* spacecraft as supplied by ESA. Colored tetrahedra correspond to mass points that are inserted into the model as a replacement for structures whose geometry is not modeled (e.g. scientific payload).

An automated conversion from the [CAD](#) file to a [Geant4](#)-compatible model (GDML) is challenging to implement and would also not be very meaningful due to the shortcomings of the [CAD](#) model described above. Also, such a detailed

¹ <http://www.f-e-x.com/>

geometry may cause the simulation to run very slowly. Therefore, as a first step towards implementing the spacecraft model in **Geant4**, the dimensions of the main box-shaped spacecraft body in the **CAD** file were measured to create a corresponding box in **Geant4**. This assumes that the additional structures besides the main body (e.g. the solar panels and other instruments) can be neglected. To estimate the mass of this box, the following assumptions are made: The total mass of the two solar panels in the **CAD** file is 110 kg, so the main spacecraft body (without solar panels) has a mass of $\sim 1100 \text{ kg} + 600 \text{ kg} = 1700 \text{ kg}$ (adding the 400 kg of mass that is “missing” in the **CAD** file as well as 200 kg of fuel). This value is used as the mass of the box in the **Geant4** model. With regard to the material, it is assumed that the mass is equally distributed throughout the volume of the box, with 200 kg of hydrazine fuel, and the remaining mass split 50:50 between electronics components and aluminium (750 kg each). Electronics were modeled using the printed circuit board (**PCB**) material taken from Appel et al. (2018) and Appel (2018). The dimensions and materials are summarized in **Table 2**.

Solo spacecraft body		PCB material	
X dimension	1812 mm	Cu	20 %
Y dimension	1461 mm	SiO ₂	15 %
Z dimension	2200 mm	PET	9.9 %
Mass	1700 kg	PP	4.8 %
Density	291.89 kg/m ³	Al	2 %
Composition	12 % hydrazine (N ₂ H ₄)	Pb	2 %
	44 % PCB material (see right table)	Ni	2 %
	44 % aluminium alloy (same as HET housing)	Fe	8 %
		Sn	4 %
		Mg	30 %

Table 2: Details of the spacecraft model used for the **HET** simulation. The left table shows the dimensions and composition of the box-shaped spacecraft body, while the right table shows the **PCB** material taken from Appel et al. (2018) and Appel (2018).

HET was then positioned next to the spacecraft body, at a location approximately derived from the position of the corresponding mass point of **HET 1** in the **CAD** file, and with the correct orientation relative to the Sun. This setup is shown in **Figure 12**. As both **HET 1** and **HET 2** are located near an edge of the spacecraft body, the difference between the positions of **HET 1** and **HET 2** is not expected to be significant for an isotropic radiation field — but of course, this may be verified with another simulation in the future. As a source, a cube of edge length 260 cm was used, which surrounds the spacecraft body and the **HET** sensor. Particles are again injected following a cosine-law distribution from the surface of this cube. Due to the large source size, the simulation needed to be run multiple times with different initialization values for **Geant4**’s random number generator to achieve a sufficient

amount of particles detected in HET. In total, $N_{\text{total}} = 1.6 \times 10^{10}$ primary particles were simulated, resulting in 5.6×10^6 hits in the HET detectors (ratio: 0.035%).

To speed up future simulations, the spacecraft model may also be replaced with smaller spherical shells of equivalent column density that are placed directly around the HET sensor head. In this case, the source size could be significantly reduced and thus the fraction of simulated particles that reach HET would increase. The simulation results with the actual spacecraft geometry could then be used to validate this approach.

A.3 ANALYSIS OF THE SIMULATION RESULTS

For the study presented in Freiherr von Forstner et al. (2021), the data analysis applied to the results of the simulations described in the previous two sections was fairly simple. To calculate the response function of the HET C detector single counters, the detected events were first filtered for hits in the C detector (detector ID 6 in the Geant4 simulation) with a deposited energy larger than a certain threshold E_{th} . The C detector single counters have threshold energies of 4 MeV for the low-gain channel and 10 MeV for the high-gain channel, so the calculation was done for both of these values. Next, the primary energy of the particles corresponding to these events was used to calculate a histogram with $k = 200$ logarithmically-spaced bins spanning the whole primary energy range. To calculate the energy-dependent geometric factor $G(E)$ for each primary energy from this histogram, the following formula (based on Sullivan, 1971, equation 18) was used:

$$G(E) = \frac{n(E)}{N(E)} \cdot G_{\text{source}} \quad (7)$$

where $n(E)$ is the number of hits in the C detector for primary particles of energy E , $N(E)$ is the number of primary particles simulated at this energy, and

$$G_{\text{source}} = \pi A_{\text{source}} \quad (8)$$

is the geometric factor of the particle source, which is calculated from the surface area of the spherical or cubical particle source (Sullivan, 1971, equation 6). $N(E)$ is easy to calculate due to the chosen input spectrum (Equation 5), which results in the same number of particles in each of the k energy bins, i.e.

$$N(E) = \frac{N_{\text{total}}}{k} \quad (9)$$

The resulting response function $G(E)$ is plotted in Figure 13. As explained by Freiherr von Forstner et al. (2021, Section 2.1), the narrow plateau below ~ 20 MeV corresponds to particles entering through the nominal field of view (i.e., through the A and B detectors), while the following increase is caused by particles that penetrate the HET housing. The effect of the spacecraft model on the response is as expected: A slight decrease for lower energies up to ~ 200 MeV due to shielding and a significant increase for high energies above 1 GeV due to the generation of secondaries in the spacecraft body.

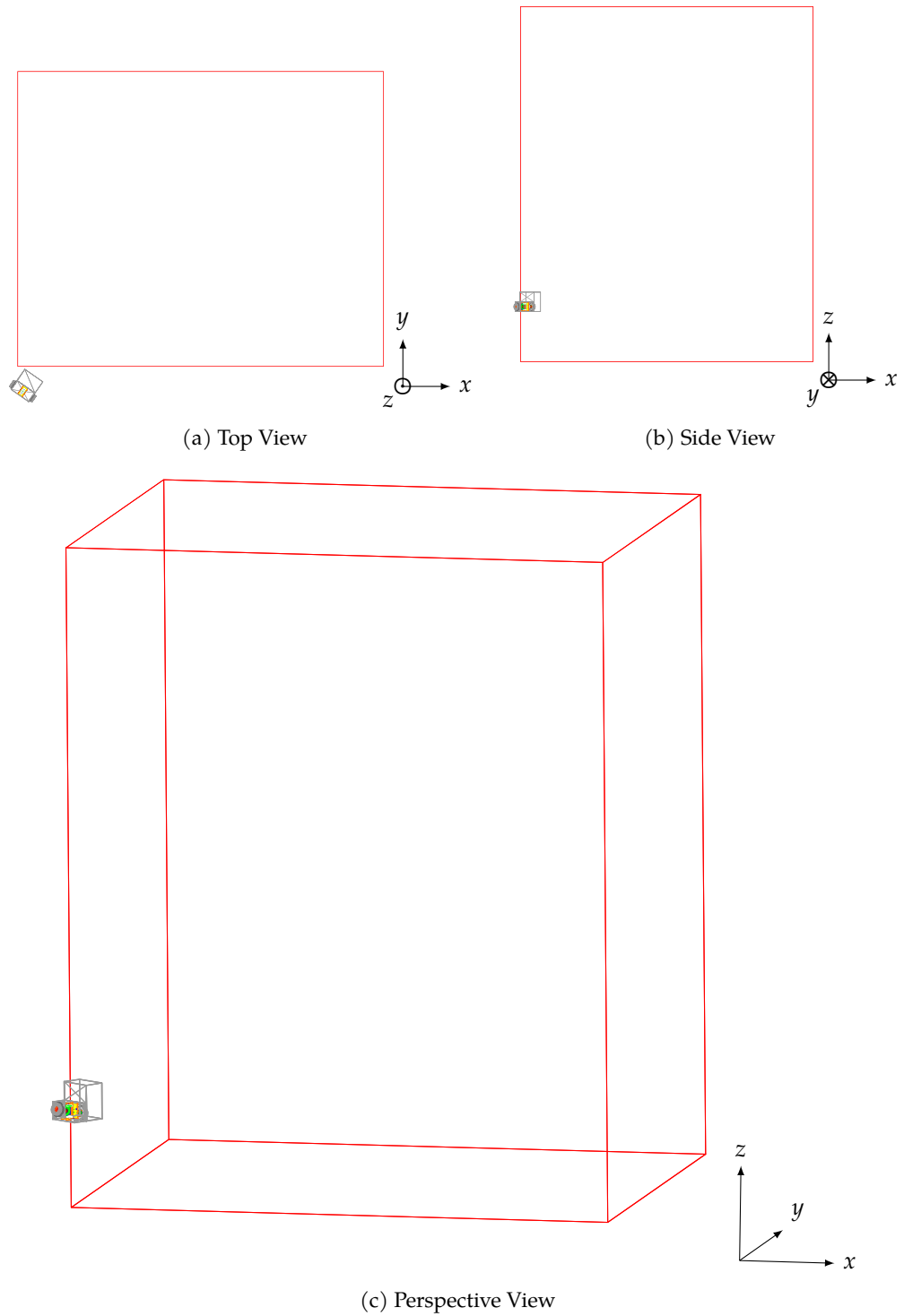


Figure 12: HET simulation setup with spacecraft model. The spacecraft (whose dimensions are given in Table 2) is drawn in red, and the HET sensor head and electronics box are shown in gray and other colors.

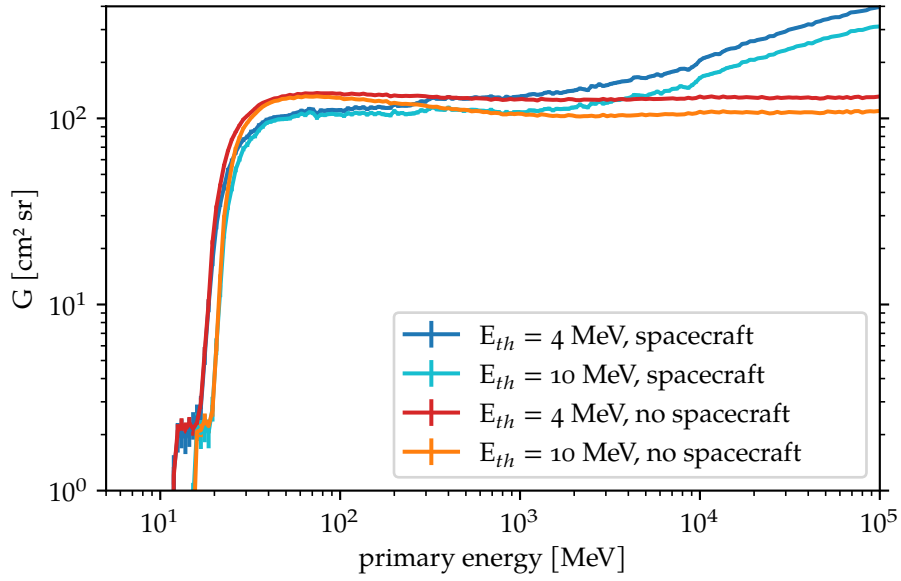


Figure 13: Response functions of HET C detector single counters, calculated from the Geant4 simulation.

In future studies, the isotropic simulation data presented in this chapter may also be used in conjunction with the simulated Level 3 trigger of HET to calculate the response functions of the other HET science data products. From these, one can derive the geometric factors for each data product, which can be used to validate the results obtained by Elftmann (2020). However, the number of particles in the simulation may need to be significantly increased for these results to be useful, as only a small fraction of the isotropic radiation enters HET from the nominal FOV.

IMPLEMENTATION OF THE GRADUATED CYLINDRICAL SHELL MODEL IN PYTHON

The graduated cylindrical shell model (GCS, Thernisien et al., 2006; Thernisien, 2011) is an empirical model that is commonly used to represent the three-dimensional structure of flux rope coronal mass ejections (CMEs) near the Sun. It defines a croissant-like 3D shape with conical legs whose ends are anchored to the center of the Sun, as shown in Figure 14.

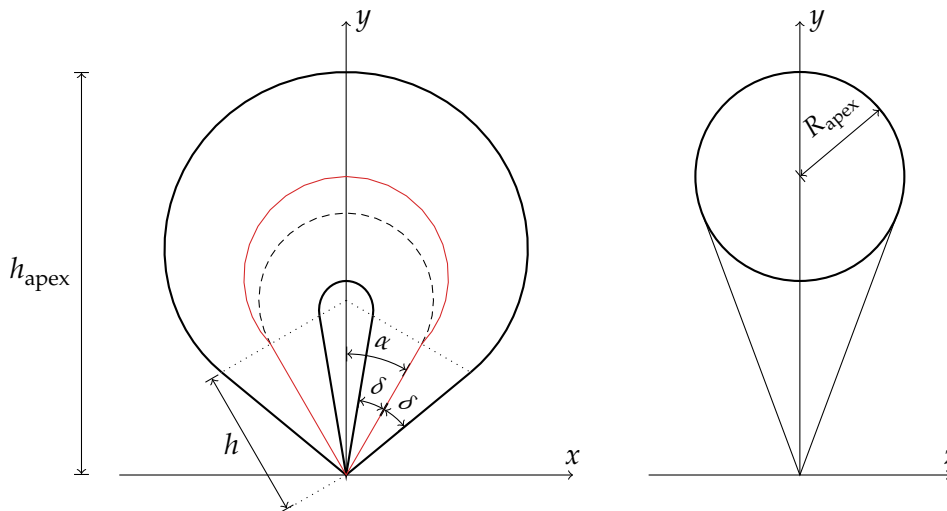


Figure 14: Illustration of the GCS model and definition of parameters h , h_{apex} , α , δ and R_{apex} , based on Thernisien (2011). In this example, the parameters are set to $\alpha = 30^\circ$ and $\kappa = 0.35$. The left panel shows a side view of the CME in the xy plane, where the thick black line marks the outer contour of the flux rope and the red line corresponds to its central axis. The dotted lines mark the boundary between the front section and the legs. The dashed line is a circular arc around the central point, showing that the front section does not have a constant radius. The right panel shows a cut in the perpendicular yz plane, where the cross section of the front is marked with a thick circle and the conical legs are indicated using the thin lines.

The GCS geometry is constrained using three main parameters: The CME apex height h_{apex} (or, alternatively, the leg height h), the angular half width α of the CME, and the so-called aspect ratio κ , which corresponds to the half angle δ of the leg cones:

$$\kappa = \sin \delta \quad (10)$$

The origin of the coordinate system shown in Figure 14 is fixed to the center of the Sun, with the y axis defining the propagation direction of the CME. Three additional parameters describe its orientation: The heliographic latitude θ and longitude ϕ (typically given in Stonyhurst or Carrington coordinates), and the tilt angle

γ , which defines the rotation around the y axis in [Figure 14](#). For a detailed description of the mathematical derivation of the [GCS](#) model, please refer to Thernisien ([2011](#)).

The [GCS](#) model is typically employed in a forward modelling approach, i.e., the model is visually compared to coronagraph observations of a [CME](#) and the input parameters are then iteratively adjusted by the scientist to achieve a good fit. This manual fitting process is ideally applied simultaneously to coronagraph images from multiple viewpoints, such as from the Solar and Heliospheric Observatory ([SOHO](#))/Large Angle and Spectrometric Coronagraph Experiment ([LASCO](#)) and Solar Terrestrial Relations Observatory ([STEREO](#))/Sun Earth Connection Coronal and Heliospheric Investigation ([SECCHI](#)) coronagraphs, to avoid ambiguity due to the line of sight effect. The resulting [GCS](#) parameters for the best fit can then be used for further evaluation, e.g. as input parameters for modeling the subsequent [CME](#) propagation. Additional properties of the flux rope, such as the radius at the apex R_{apex} (see [Figure 14](#)) can also be calculated from these parameters, as derived by (Thernisien, [2011](#)). When applied to a sequence of consecutive images, the [CME](#) kinematics can also be reconstructed.

The original implementation of the [GCS](#) model in the Interactive Data Language ([IDL](#))¹ and a corresponding graphical user interface ([GUI](#)) were developed by Thernisien et al. ([2006](#)) and are included in the SolarSoft software package (Freeland and Handy, [1998](#)) under the name `scraytrace`². SolarSoft is a collection of [IDL](#) software libraries that was originally developed in the 1990s by members of the Yohkoh and [SOHO](#) mission teams and the NASA Solar Data Analysis Center (SDAC), and some tools from other missions such as [STEREO](#) were also included later. Using this [GCS](#) implementation requires a license of [IDL](#), a local installation of SolarSoft and the corresponding database (SSWDB), which includes coronagraph images and calibration data. Obtaining and installing all these components is quite involved for scientists that are not familiar with [IDL](#) and SolarSoft. Additionally, the [GCS](#) implementation is only partially documented and not very flexible, as it was initially hard-coded to work with only [STEREO](#)-A and -B data, with support for [SOHO](#) being manually added later.

As described e.g. in the detailed review by Burrell et al. ([2018](#)), the Python programming language is becoming increasingly popular in the solar and heliospheric physics community, and consequently, various open source software libraries to assist with the associated data analysis are available. Python is a modern, general-purpose object-oriented programming language that is easy to learn and emphasizes code readability. According to the TIOBE Programming Community Index³, it has recently surpassed Java as the second most popular programming language in the world, and in contrast to [IDL](#), it is open source software (OSS) and available free of charge on all major operating systems.

SunPy (The SunPy Community et al., [2020](#)), a library for working with solar images from various missions, is one of the most widely-used Python toolkits for solar physics. However, it does not yet provide any models for [CME](#) reconstruction

¹ <https://www.l3harrisgeospatial.com/Software-Technology/IDL>

² <https://hesperia.gsfc.nasa.gov/ssw/stereo/secchi/idl/scraytrace>

³ <https://www.tiobe.com/tiobe-index/>

in coronagraph images. Thus, an open source Python implementation of the GCS model and a simple corresponding GUI application based on *SunPy* have been developed during the course of the study presented in Freiherr von Forstner et al. (2021). It can be used both as a standalone application as well as integrated into existing Python-based plotting routines. The source code is available on GitHub at https://github.com/johan12345/gcs_python, and is also mirrored at Kiel University under https://gitlab.physik.uni-kiel.de/ET/gcs_python. It can be easily installed with Python's pip package manager as follows:

```
pip3 install git+https://github.com/johan12345/gcs_python.git
```

(provided that Python 3.7 or above is already installed).

The following sections will describe the design and usage of this software package, and its validation against the original IDL version.

B.1 GCS GEOMETRY

The basic GCS geometry is implemented in the `gcs.geometry` module. This code is a close translation of the corresponding IDL routines from SolarSoft. Two basic functions are provided to calculate the geometry of the GCS structure based on the input parameters: The `skeleton` function (based on `shellskeleton.pro` in SolarSoft) calculates the shape of the central axis of the flux rope (thin solid line in Figure 14), which consists of two straight segments in the legs and a curved segment in the front. The desired resolution, i.e. the number of points along each part of the curve, can be passed to the function. This central axis, which lies in the xy plane, then needs to be used to generate the outer shell of the flux rope, which consists of circles that are perpendicular to the tangent vector at each point. For this purpose, the `skeleton` function also provides the orientation of this tangent vector as well as the radius of each circle. The `gcs_mesh` function (based on `cmeccloud.pro` in SolarSoft) then uses the output of the `skeleton` function to construct a 3D mesh by generating these circles around the central axis with the appropriate radius and orientation. The parameters of the `gcs_mesh` function are the half angle α , the CME height h_{apex} , and the aspect ratio κ , as well as the desired numbers of points along the straight segments, along the front, and along each circle in the mesh.

In addition to these basic routines to construct the GCS mesh, there is also a function `gcs_mesh_rotated`, which uses the three angles θ , ϕ , γ to rotate the CME cloud in 3D space, as well as the function `gcs_mesh_sunpy`, which converts the rotated GCS mesh into a *SunPy* `SkyCoord` object. This object then contains the necessary metadata about the coordinate system so that the model can directly be integrated into a *SunPy* plot.

B.2 GRAPHICAL USER INTERFACE

In addition to the implementation of the GCS geometry, a convenient GUI was created that can be used to fit the GCS model to coronagraph images. The GUI is based upon *SunPy*, which already provides functions to obtain coronagraph images and

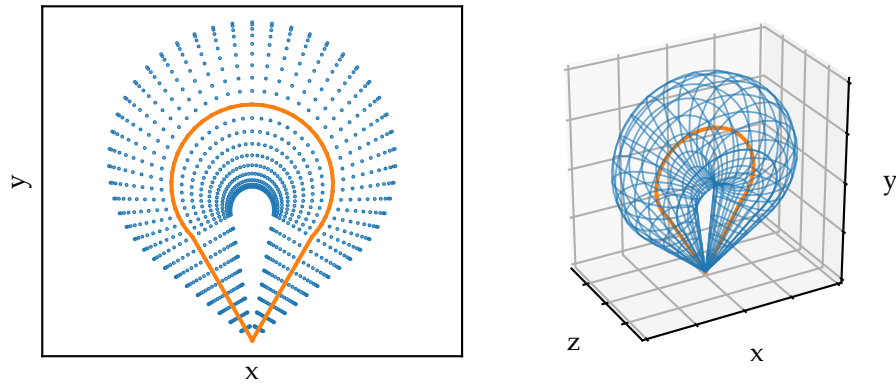


Figure 15: Results of the functions from the **GCS** Python implementation. The left panel shows the central axis of the flux rope, calculated using the `skeleton` function, in orange, and the surrounding circles generated by the `gcs_mesh` function in blue. The right panel shows a 3D wireframe representation of the same data. The input parameters α and κ are the same as in [Figure 14](#).

to perform the coordinate transformations necessary to overplot arbitrary points in space on these images. Thus, its implementation was relatively straightforward.

For starting the **GUI**, a command line interface is provided. For example,

```
gcs_gui "2013-05-13 16:54" STB SOHO STA
```

starts the **GCS GUI** with the closest available coronagraph images to the given date and time from **STEREO-B**, **SOHO** and **STEREO-A**. Additional command line options are available to set which coronagraph should be used (`-soho C2` or `C3`, and `-stereo C0R1` or `C0R2`) and whether to use running difference images (`-rd`) or direct images. Running difference images are calculated by subtracting a previous image (e.g. 1 h before) from the current one, so that moving features are highlighted.

The **GUI** components, e.g. sliders and text boxes for each input parameter, were implemented using the `PyQt5` library⁴, which provides Python bindings for the popular **GUI** framework `Qt`. The **GUI** is defined in the `gcs.gui` module as the `GCSGui` class. For embedding the solar images into the `Qt` window, it uses a plotting canvas provided by the `matplotlib` plotting package (`FigureCanvasQTAgg`).

When the user starts the **GUI**, it first retrieves the desired coronagraph images through the Internet. This is done using the `Helioviewer.org` Application Programming Interface (API)⁵, which directly provides images in `JPEG2000` format to which all necessary calibration and background subtraction routines were already applied on the server side. This drastically simplifies and speeds up the process compared to the **IDL** version, where images in `FITS` format need to be downloaded manually from the respective mission sites, and where the calibration procedure needs to be applied locally (requiring an installation of `SSWDB`). The `JPEG2000` images provided by `Helioviewer.org` also include additional metadata about the observer location and field of view, which are copied from the original `FITS` file

⁴ <https://riverbankcomputing.com/software/pyqt/>

⁵ <https://api.helioviewer.org/docs/v2/>

and are necessary to plot the images in the correct coordinate system (solar latitude and longitude).

When the images are downloaded, the **GCS GUI** plots them using *SunPy* and displays the result in the plotting canvas (see **Figure 16**). The **GCS** croissant mesh is then plotted on top of these images and the user can adjust the **GCS** parameters interactively with the six sliders and numerical input boxes on the right side of the window. Three additional controls are provided: A checkbox to show or hide the **GCS** mesh, a text view showing the calculated apex radius of the flux rope (R_{apex} , cf. **Figure 14**), and a button to save the **GCS** parameters to a file. These data are stored in the JavaScript Object Notation (**JSON**) format, a general-purpose data format that is human-readable and can be easily handled with most modern programming languages. On the upper edge of the **GCS** window, the standard *matplotlib* controls are also shown to allow zooming and panning in the images as well as saving the current set of images to a file.

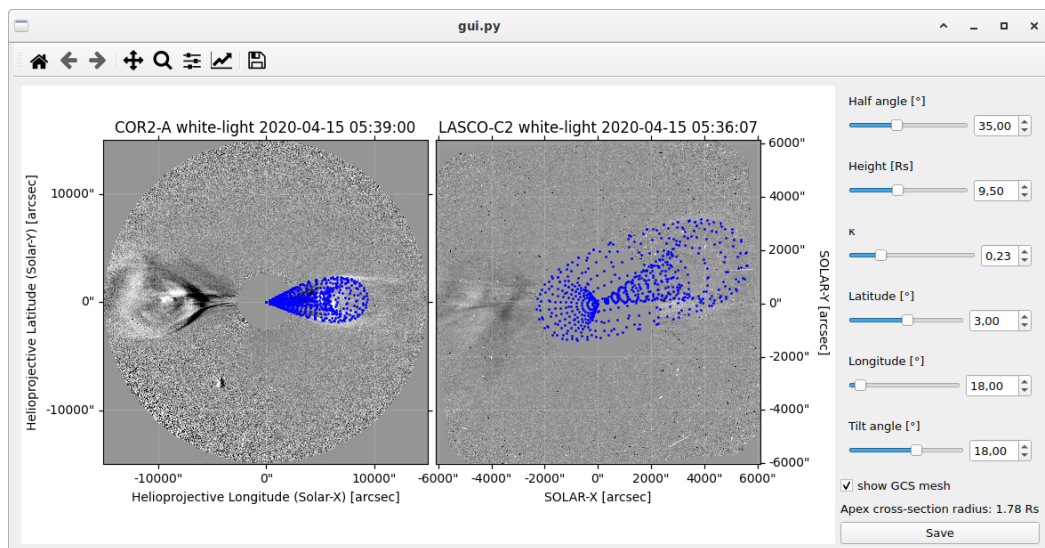


Figure 16: Screenshot of the **GCS** Python **GUI**. The left part of the window shows the plotting canvas with running difference coronagraph images of the April 15, 2020 **CME** (see Freiherr von Forstner et al., 2021). The user controls for the **GCS** parameters are shown on the right.

During the development of the **GCS GUI**, two problems with the data provided to *SunPy* by the Helioviewer.org Application Programming Interface (**API**) were discovered: First, the **STEREO-B** COR2 images were temporarily not available through the **API** in October 2020, an issue which has since been resolved by the Helioviewer.org team⁶. Second, there was an issue with the metadata included in the **SOHO**/LASCO files: The **SOHO** spacecraft performs a roll maneuver every three months to keep its high gain antenna oriented towards Earth. The files provided by Helioviewer.org already take this into account by rotating the images accordingly, so that the solar north pole is always pointing upwards. However, the metadata in the JPEG2000 files are not adjusted accordingly⁷, so *SunPy* still in-

⁶ <https://github.com/Helioviewer-Project/helioviewer.org/issues/288>

⁷ <https://github.com/sunpy/sunpy/issues/4553>

interprets these images as though they were rotated by 180° . This obviously caused the location of the GCS model results in the LASCO images to be incorrect. Thus, a workaround was implemented into the GCS GUI to reset the rotation metadata of the LASCO files and also submitted a patch⁸ to the *SunPy* project to address this issue, which is included in version 2.1 of *SunPy*.

Possible future improvements to the GCS GUI could include adding an option to calculate base difference images as an alternative to the current options of direct and running difference images, i.e. allowing the user to specify a fixed point in time that should be used for the subtraction. It may also be helpful to include additional controls for the user to adjust the contrast of the displayed images — this is already possible in the IDL implementation, but only before starting the fitting process, it cannot be changed interactively while already working on the fit. In addition, further tools could be provided to facilitate the fitting of time series so that the user can simply provide a start and end time, and the GUI would directly provide one image after another and store the fitting results for each time step in one file. The toolkit may also be easily extended to include support for additional data sources as soon as they are implemented in *SunPy*, such as the Wide-Field Imager onboard Parker Solar Probe (WISPR, Vourlidis et al., 2016), the Metis coronagraph onboard Solar Orbiter (Antonucci et al., 2020) and the Solar Orbiter Heliospheric Imager (SoloHI, Howard et al., 2020).

B.3 VALIDATION

To validate that the Python implementation of GCS yields the correct results, a set of CMEs were re-plotted with the Python GCS GUI that have previously been fitted using the IDL version to compare the resulting plots. One example of this is shown in Figure 17 for a CME launched on May 13, 2013 (originally reconstructed by Gou et al., 2020, Figure 2). The corresponding input parameters are shown in Table 3.

Parameter	Value
Stonyhurst Longitude ϕ [$^\circ$]	270
Heliographic Latitude θ [$^\circ$]	19
Tilt angle γ [$^\circ$]	35
Half angle α [$^\circ$]	28
Apex height R_{apex} [R_\odot]	10.8
Aspect ratio κ	0.35

Table 3: GCS parameters for the May 13, 2013 CME shown in Figure 17.

Similar comparisons were performed for other CMEs with different characteristics: The June 21, 2011 CME (originally reconstructed by Heinemann et al., 2019, Table 1), the May 25, 2014 CME (originally reconstructed by Dumbović et al., 2018a,

⁸ <https://github.com/sunpy/sunpy/pull/4561>

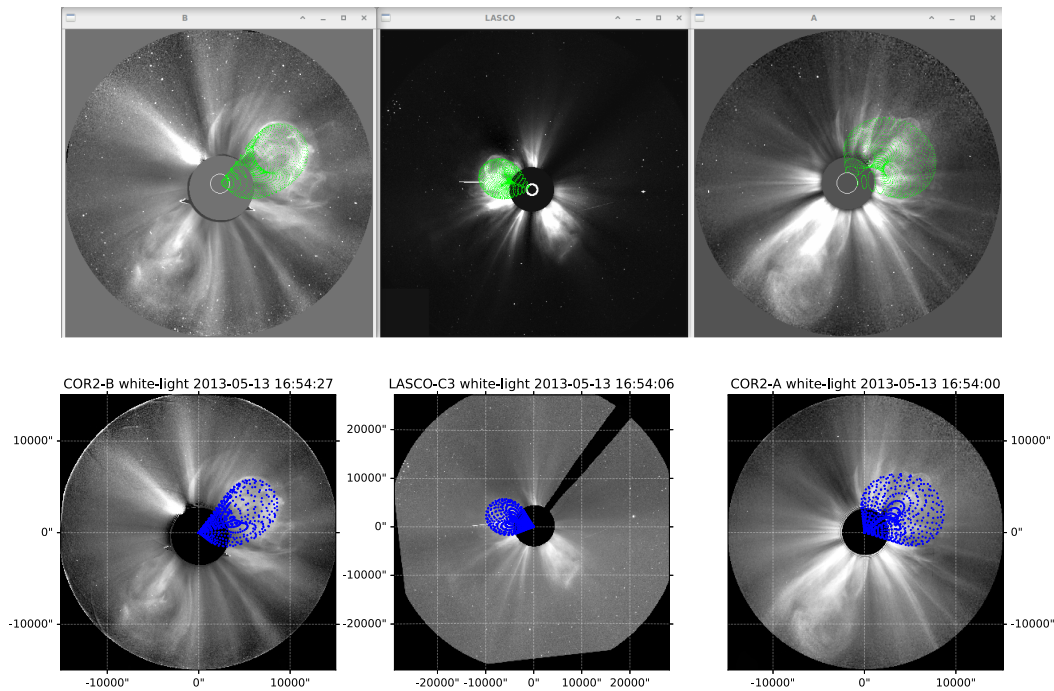


Figure 17: Validation of the **GCS** Python implementation. Both panels show the same **CME** on May 13, 2013, with the **GCS** parameters listed in [Table 3](#). The top image was generated by the **IDL** implementation of **GCS**, while the bottom panel shows the result of the new Python implementation.

Figure 5b), as well as the April 15, 2020 **CME** studied by Freiherr von Forstner et al. (2021). In all cases, the **GCS** 3D meshes generated by the Python implementation match the **CME** signatures in the coronagraph images as well as the original results from the **IDL** implementation. This shows that the Python version is implemented correctly and can be used for scientific purposes.

LIST OF PUBLICATIONS

This list shows all peer-reviewed publications that I have contributed to. Not all of these publications were included in this thesis, as they do not all fit into the logical flow of this thesis.

USING FORBUSH DECREASES TO DERIVE THE TRANSIT TIME OF ICMEs PROPAGATING FROM 1 AU TO MARS

Freiherr von Forstner, J. L., J. Guo, R. F. Wimmer-Schweingruber, D. M. Hassler, M. Temmer, M. Dumbović, L. K. Jian, J. K. Appel, J. Čalogović, B. Ehresmann, B. Heber, H. Lohf, A. Posner, C. T. Steigies, B. Vršnak, and C. J. Zeitlin, *Journal of Geophysical Research: Space Physics*, 123, 1, pages 39–56 (2018), DOI: [10.1002/2017JA024700](https://doi.org/10.1002/2017JA024700)

ANALYSIS OF THE RADIATION HAZARD OBSERVED BY RAD ON THE SURFACE OF MARS DURING THE SEPTEMBER 2017 SOLAR PARTICLE EVENT

Zeitlin, C., D. M. Hassler, J. Guo, B. Ehresmann, R. F. Wimmer-Schweingruber, S. C. R. Rafkin, **J. L. Freiherr von Forstner**, H. Lohf, T. Berger, D. Matthiä, and G. Reitz, *Geophysical Research Letters*, 45, 12, pages 5845–5851 (2018), DOI: [10.1029/2018GL077760](https://doi.org/10.1029/2018GL077760)

MODELING THE EVOLUTION AND PROPAGATION OF 10 SEPTEMBER 2017 CMEs AND SEPs ARRIVING AT MARS CONSTRAINED BY REMOTE SENSING AND IN SITU MEASUREMENT

Guo, J., M. Dumbović, R. F. Wimmer-Schweingruber, M. Temmer, H. Lohf, Y. Wang, A. Veronig, D. M. Hassler, L. M. Mays, C. Zeitlin, B. Ehresmann, O. Witasse, **J. L. Freiherr von Forstner**, B. Heber, M. Holmström, and A. Posner, *Space Weather*, 16, 8, pages 1156–1169 (2018), DOI: [10.1029/2018SW001973](https://doi.org/10.1029/2018SW001973)

TRACKING AND VALIDATING ICMEs PROPAGATING TOWARD MARS USING STEREO HELIOSPHERIC IMAGERS COMBINED WITH FORBUSH DECREASES DETECTED BY MSL/RAD

Freiherr von Forstner, J. L., J. Guo, R. F. Wimmer-Schweingruber, M. Temmer, M. Dumbović, A. Veronig, C. Möstl, D. M. Hassler, C. J. Zeitlin, and B. Ehresmann, *Space Weather*, 17, 4, pages 586–598 (2019), DOI: [10.1029/2018SW002138](https://doi.org/10.1029/2018SW002138)

SPICEYPY: A PYTHONIC WRAPPER FOR THE SPICE TOOLKIT

Annex, A., B. Pearson, B. Seignovert, B. Carcich, H. Eichhorn, J. Mapel, **J. L. Freiherr von Forstner**, J. McAuliffe, J. del Rio, K. Berry, K.-M. Aye, M. Stefko, M. de Val-Borro, S. Kulumani, and S.-y. Murakami, *Journal of Open Source Software*, 5, 46, page 2050 (2020), DOI: [10.21105/joss.02050](https://doi.org/10.21105/joss.02050)

COMPARING THE PROPERTIES OF ICME-INDUCED FORBUSH DECREASES AT EARTH AND MARS

Freiherr von Forstner, J. L., J. Guo, R. F. Wimmer-Schweingruber, M. Dumb-

ović, M. Janvier, P. Démoulin, A. Veronig, M. Temmer, A. Papaioannou, S. Dasso, D. M. Hassler, and C. J. Zeitlin, *Journal of Geophysical Research: Space Physics*, 125, 5, e2019JA027662 (2020), DOI: [10.1029/2019JA027662](https://doi.org/10.1029/2019JA027662)

THE LUNAR LANDER NEUTRON AND DOSIMETRY (LND) EXPERIMENT ON CHANG'E 4

Wimmer-Schweingruber, R. F., J. Yu, S. I. Böttcher, S. Zhang, S. Burmeister, H. Lohf, J. Guo, Z. Xu, B. Schuster, L. Seimetz, **J. L. Freiherr von Forstner**, A. Ravanbakhsh, V. Knierim, S. Kolbe, H. Woyciechowsky, S. R. Kulkarni, B. Yuan, G. Shen, C. Wang, Z. Chang, T. Berger, C. E. Hellweg, D. Matthiä, D. Hou, A. Knappmann, C. Büschel, X. Hou, B. Ren, and Q. Fu, *Space Science Reviews*, 216, 6 (2020), DOI: [10.1007/s11214-020-00725-3](https://doi.org/10.1007/s11214-020-00725-3)

FIRST MEASUREMENTS OF THE RADIATION DOSE ON THE LUNAR SURFACE

Zhang, S., R. F. Wimmer-Schweingruber, J. Yu, C. Wang, Q. Fu, Y. Zou, Y. Sun, C. Wang, D. Hou, S. I. Böttcher, S. Burmeister, L. Seimetz, B. Schuster, V. Knierim, G. Shen, B. Yuan, H. Lohf, J. Guo, Z. Xu, **J. L. Freiherr von Forstner**, S. R. Kulkarni, H. Xu, C. Xue, J. Li, Z. Zhang, H. Zhang, T. Berger, D. Matthiä, C. E. Hellweg, X. Hou, J. Cao, Z. Chang, B. Zhang, Y. Chen, H. Geng, and Z. Quan, *Science Advances*, 6, 39 (2020), DOI: [10.1126/sciadv.aaz1334](https://doi.org/10.1126/sciadv.aaz1334)

FIRST SOLAR ENERGETIC PARTICLES MEASURED ON THE LUNAR FAR-SIDE

Xu, Z., J. Guo, R. F. Wimmer-Schweingruber, **J. L. Freiherr von Forstner**, Y. Wang, N. Dresing, H. Lohf, S. Zhang, B. Heber, and M. Yang, *The Astrophysical Journal*, 902, 2, page L30 (2020), DOI: [10.3847/2041-8213/abbccc](https://doi.org/10.3847/2041-8213/abbccc)

³HE-RICH SOLAR ENERGETIC PARTICLE EVENTS OBSERVED ON THE FIRST PERIHELION PASS OF SOLAR ORBITER

Mason, G. M., G. C. Ho, R. C. Allen, J. Rodríguez-Pacheco, R. F. Wimmer-Schweingruber, R. Bučík, R. Gómez-Herrero, D. Lario, **J. L. Freiherr von Forstner**, G. B. Andrews, L. Berger, I. Cernuda Cangas, F. Espinosa Lara, W. J. Lees, C. Martín, D. Pacheco, M. Prieto, S. Sánchez-Prieto, C. E. Schlemm, H. Seifert, and K. Tyagi, *A&A* (2020), DOI: [10.1051/0004-6361/202039752](https://doi.org/10.1051/0004-6361/202039752)

RADIAL EVOLUTION OF THE APRIL 2020 STEALTH CORONAL MASS EJECTION BETWEEN 0.8 AND 1 AU: A COMPARISON OF FORBUSH DECREASES AT SOLAR ORBITER AND EARTH

Freiherr von Forstner, J. L., M. Dumbović, C. Möstl, J. Guo, A. Papaioannou, R. Elftmann, Z. Xu, J. C. Terasa, A. Kollhoff, R. F. Wimmer-Schweingruber, J. Rodríguez-Pacheco, A. J. Weiss, J. Hinterreiter, T. Amerstorfer, M. Bauer, A. V. Belov, M. A. Abunina, T. Horbury, E. E. Davies, H. O'Brien, R. C. Allen, G. B. Andrews, L. Berger, S. Boden, I. Cernuda Cangas, S. Eldrum, F. Espinosa Lara, R. Gómez-Herrero, J. R. Hayes, G. C. Ho, S. R. Kulkarni, W. J. Lees, C. Martín, G. M. Mason, D. Pacheco, M. Prieto Mateo, A. Ravanbakhsh, O. Rodríguez Polo, S. Sánchez Prieto, C. E. Schlemm, H. Seifert, K. Tyagi, and M. Yedla, *A&A* (2021), DOI: [10.1051/0004-6361/202039848](https://doi.org/10.1051/0004-6361/202039848)

FIRST NEAR-RELATIVISTIC SOLAR ELECTRON EVENTS OBSERVED BY EPD ONBOARD SOLAR ORBITER

Gómez-Herrero, R., D. Pacheco, A. Kollhoff, F. Espinosa Lara, **J. L. Freiherr von Forstner**, N. Dresing, D. Lario, L. Balmaceda, V. Krupar, O. E. Malandraki, A. Aran, R. Bučík, A. Klassen, K.-L. Klein, I. Cernuda Cangas, S. Eldrum, H. Reid, J. G. Mitchell, G. M. Mason, G. C. Ho, J. Rodríguez-Pacheco, R. F. Wimmer-Schweingruber, L. Berger, R. C. Allen, N. P. Janitzek, M. Laurenza, R. de Marco, N. Wijsen, Y. Y. Kartavykh, W. Dröge, T. S. Horbury, M. Maksimovic, C. J. Owen, A. Vecchio, X. Bonnin, O. Kruparova, D. Píša, J. Souček, P. Louarn, A. Fedorov, H. O'Brien, V. Evans, V. Angelini, P. Zucca, M. Prieto-Mateo, S. Sánchez-Prieto, A. Carrasco, J. J. Blanco, P. Parra, O. Rodríguez Polo, C. Martín, J. C. Terasa, S. Boden, S. R. Kulkarni, A. Ravanbakhsh, M. Yedla, Z. Xu, G. B. Andrews, C. E. Schlemm, H. Seifert, K. Tyagi, W. J. Lees, and J. Hayes, *A&A* (2021), doi: [10.1051/0004-6361/202039883](https://doi.org/10.1051/0004-6361/202039883)

SUPRATHERMAL PARTICLES FROM COROTATING INTERACTION REGIONS DURING THE FIRST PERIHELION PASS OF SOLAR ORBITER

Allen, R. C., G. M. Mason, G. C. Ho, J. Rodríguez-Pacheco, R. F. Wimmer-Schweingruber, G. B. Andrews, L. Berger, S. Boden, I. Cernuda Cangas, F. Espinosa Lara, R. Gómez-Herrero, S. R. Kulkarni, W. J. Lees, C. Martín, M. Prieto Mateo, D. Pacheco, O. Rodríguez Polo, A. Ravanbakhsh, S. Sánchez-Prieto, C. E. Schlemm, H. Seifert, J. C. Terasa, K. Tyagi, **J. L. Freiherr von Forstner**, Z. Xu, and M. Yedla, *A&A* (2021), doi: [10.1051/0004-6361/202039870](https://doi.org/10.1051/0004-6361/202039870)

ORIGINS OF A STEALTH CME DETECTED AT SOLAR ORBITER

O'Kane, J., L. M. Green, E. E. Davies, C. Möstl, J. Hinterreiter, **J. L. Freiherr von Forstner**, D. Long, and T. Amerstorfer, *A&A* (2021), submitted.

QUIET-TIME LOW ENERGY ION SPECTRA OBSERVED ON SOLAR ORBITER DURING SOLAR MINIMUM

Mason, G. M., G. C. Ho, R. C. Allen, Z. Xu, N. P. Janitzek, **J. L. Freiherr von Forstner**, A. Kollhoff, D. Pacheco, J. Rodríguez-Pacheco, R. F. Wimmer-Schweingruber, G. B. Andrews, C. E. Schlemm, H. Seifert, K. Tyagi, W. J. Lees, J. Hayes, R. Gómez-Herrero, M. Prieto, S. Sánchez-Prieto, F. Espinosa Lara, I. Cernuda Cangas, O. Rodríguez Polo, C. Martín, L. Berger, J. C. Terasa, S. Boden, S. R. Kulkarni, A. Ravanbakhsh, M. Yedla, and S. Eldrum, *A&A* (2021), submitted.

RADIATION ENVIRONMENT FOR FUTURE HUMAN EXPLORATION ON THE SURFACE OF MARS: THE CURRENT UNDERSTANDING BASED ON MSL/RAD DOSE MEASUREMENTS

Guo, J., R. F. Wimmer-Schweingruber, C. Zeitlin, D. M. Hassler, B. Ehresmann, **J. L. Freiherr von Forstner**, S. Khaksari, S. Rafkin, W. Liu, and Y. Wang, *The Astronomy and Astrophysics Review* (2021), submitted.

ENERGETIC IONS IN THE VENUSIAN SYSTEM: INSIGHTS FROM THE FIRST SOLAR ORBITER FLYBY

Allen, R. C., G. C. Ho, G. M. Mason, I. Cernuda Cangas, D. Pacheco, L. Berger, Z. Xu,

J. L. Freiherr von Forstner, J. Rodríguez-Pacheco, R. F. Wimmer-Schweingruber, S. K. Vines, Y. Khotyaintsev, T. Horbury, M. Maksimovic, L. Z. Hadid, M. Volwerk, A. Dimmock, L. Sorriso-Valvo, K. Stergiopoulou, G. B. Andrews, V. Angelini, S. Boden, S. I. Böttcher, T. Chust, S. Eldrum, P. P. Espada, F. Espinosa Lara, V. Evans, R. Gómez-Herrero, J. R. Hayes, A. M. Hellín, A. Kollhoff, V. Krasnoselskikh, M. Kretzschmar, P. Kühl, S. R. Kulkarni, W. J. Lees, E. Lorfèvre, C. Martín, H. O'Brien, D. Plettemeier, O. Rodríguez Polo, M. Prieto Mateo, A. Ravanbakhsh, S. Sánchez-Prieto, C. E. Schlemm, H. Seifert, J. Souček, M. Steller, Š. Štverák, J. C. Terasa, P. Trávníček, K. Tyagi, A. Vaivads, A. Vecchio, and M. Yedla, *A&A* (2021), in preparation.

THE LOW-ENERGY ION EVENT ON 19 JUNE 2020 MEASURED BY SOLAR ORBITER

Aran, A., D. Pacheco, N. Wijsen, E. Samara, D. Lario, L. Balmaceda, L. Rodriguez, R. Gómez-Herrero, M. Laurenza, S. Benella, B. Sanahuja, S. Poedts, **J. L. Freiherr von Forstner**, L. Berger, G. M. Mason, R. C. Allen, H. O'Brien, V. Evans, V. Angelini, T. S. Horbury, G. C. Ho, R. F. Wimmer-Schweingruber, J. Rodríguez-Pacheco, et al., *A&A* (2021), in preparation.

THE FIRST WIDESPREAD SEP EVENT OF THE 25TH SOLAR CYCLE

Kollhoff, A. et al., *A&A* (2021), in preparation.

FIRST YEAR OF ENERGETIC PARTICLE MEASUREMENTS IN THE INNER HELIOSPHERE WITH SOLAR ORBITER

Wimmer-Schweingruber, R. F., N. P. Janitzek, J. Rodríguez-Pacheco, G. M. Mason, G. C. Ho, D. Pacheco, **J. L. Freiherr von Forstner**, et al., *A&A* (2021), in preparation.

EIDESSTATTLICHE ERKLÄRUNG GEMÄSS §9 DER PROMOTIONSORDNUNG

Ich versichere an Eides statt, dass die vorliegende Abhandlung – abgesehen von der Beratung durch meinen Betreuer und der angegebenen Literatur – nach Inhalt und Form meine eigene Arbeit ist.

Ich versichere, dass die Arbeit weder ganz noch zum Teil schon einer anderen Stelle im Rahmen eines Prüfungsverfahrens vorgelegen hat. Teile dieser Arbeit wurden bereits in Fachzeitschriften veröffentlicht und sind als solche gekennzeichnet. Die Quellennachweise der jeweiligen Veröffentlichungen befinden sich ausschließlich in den zugehörigen Literaturverzeichnissen und werden nicht im Literaturverzeichnis dieser Abhandlung aufgeführt.

Ich versichere, dass die Arbeit unter Einhaltung der Regeln guter wissenschaftlicher Praxis der Deutschen Forschungsgemeinschaft entstanden ist.

Ich versichere, dass von mir noch kein früherer Promotionsversuch unternommen wurde und mir auch kein akademischer Grad entzogen wurde.

Kiel, Dezember 2020

Johan Lauritz Freiherr von Forstner